

Renormalization Group Investigations Of \mathcal{PT} -symmetric Quantum Many-Body Systems

A Thesis

Submitted for the Degree of
Doctor of Philosophy
in the Faculty of Science

by

Vinayak M Kulkarni



THEORETICAL SCIENCES UNIT
JAWAHARLAL NEHRU CENTRE FOR ADVANCED SCIENTIFIC
RESEARCH
Bangalore – 560 064
SEPTEMBER 2024

DECLARATION

I hereby declare that the matter embodied in the thesis entitled “**Renormalization Group Investigations Of \mathcal{PT} -symmetric Quantum Many-Body Systems**” is the result of investigations carried out by me at the Theoretical Sciences Unit, Jawaharlal Nehru Centre for Advanced Scientific Research, Bangalore, India under the supervision of Prof. N. S. Vidhyadhiraja and that it has not been submitted elsewhere for the award of any degree or diploma.

In keeping with the general practice of reporting scientific observations, due acknowledgment has been made whenever the work described is based on the findings of other investigators.



Vinayak M Kulkarni

CERTIFICATE

I hereby certify that the matter embodied in this thesis entitled “ **Renormalization Group Investigations Of \mathcal{PT} -symmetric Quantum Many-Body Systems**” has been carried out by Mr. Vinayak M Kulkarni at the Theoretical Sciences Unit, Jawaharlal Nehru Centre for Advanced Scientific Research, Bangalore, India under my supervision, and that it has not been submitted elsewhere for the award of any degree or diploma.



Prof. N. S. Vidhyadhiraja
(Research Supervisor)

To My Father

Acknowledgements

Heartfelt appreciation is extended to Prof. N.S. Vidhyadhiraja, my Ph.D. research supervisor, for the unwavering support, motivation, and guidance provided. Prof. Vidhyadhiraja's dedication to the field of science and tireless work ethic serve as a constant source of inspiration.

Sincere gratitude is expressed to Prof. Shobhan Narasimhan, Prof. Srikant Shastry, Prof. Swapan K. Pati, and Prof. Kavita Jain for their enlightening scientific discussions and invaluable insights shared during various courses, talks, and conferences.

Acknowledgment is extended to the GSAC committee members, Prof. Sundareshan A. and Prof. Swapan K. Pati, for their valuable contributions.

Prof. C. N. R. Rao and President Prof. G.U. Kulkarni deserve thanks for providing world-class facilities at the Institute.

Appreciation is conveyed to Prof. V.B. Shenoy and Prof. Subroto Mukharjee at IISc for their coursework and productive discussions.

Sincere appreciation is extended to Professor S. R. Hassan from the Institute of Mathematical Sciences (IMSc) for his significant contributions to my work boosting confidence through their inspiring teaching, technical training, and collaborative efforts.

Gratitude is also owed to Prof. Siddhartha Lal from IISER Kolkata for enlightening discussions and teachings on RG techniques.

Thanks go to Prof. Subir K. Das for his research project on criticality and teaching on statistical mechanics techniques.

Acknowledgment is extended to the past and present chairmen of the Theoretical Science Unit, Prof. Swapan K. Pati and Prof. Subir K. Das, for their invaluable support.

The entire faculty at JNCASR has been a constant source of inspiration with their advanced research.

Heartfelt thanks are extended to past teachers at the school and college levels for imparting their knowledge and providing support and encouragement.

Sincerest gratitude is extended to past and present labmates, including

Dr. Sudeshna Sen, Dr. Ruqsan Ul Haq, Dr. Wasim Raja Modal, Dr. Anirudha Mirmira, Mr. Gurshid Ali P, Ms. Gunjan Sharma, Mr. Sujan K. K., and Mr. Aashish Kumar, for their valuable discussions and for creating a warm and welcoming environment.

Efficient staff at the Library, Academic, and Administration sections are acknowledged for their prompt help and cooperation. Thanks are extended to the Hostel staff and Mess workers for providing a comforting atmosphere and delicious food during my stay at JNCASR.

Gratitude is expressed to friends, both within and outside JNCASR, for their constant support and companionship.

Lastly, heartfelt thanks are extended to all family members for their unconditional love, support, and encouragement, especially to my loving father, who has been a pillar of strength and guidance during challenging times.

Appreciation is extended to everyone for being part of this journey.

List of Publications

- Vinayak M. Kulkarni, Amit Gupta & Vidhyadhiraja, N. S., “Kondo effect in a non-Hermitian \mathcal{PT} -symmetric Anderson model with Rashba spin-orbit coupling”. Physical Review B, **106**, 075113 (2022).
- Vinayak M Kulkarni, N. S. Vidhyadhiraja”Flow Equation Analysis and Finite U Slave Boson” under preparation
- Vinayak M Kulkarni, N. S. Vidhyadhiraja ”Renormalization Analysis Of Complex \mathcal{DM} Interaction in Kondo Problem” under preparation

Synopsis

\mathcal{PT} -symmetric theories are an active area of research in studying open quantum systems, alongside various stochastic field theories and nonequilibrium theories. In the realm of many-body problems, the challenge lies in finding solutions that go beyond single-particle physics and approximate solutions. Various techniques have been employed to address this, including diagrammatic perturbation theory, Dynamical Mean Field theory, Renormalization techniques, conformal field theories, Bethe ansatz, and Slave-Boson method. The Bethe ansatz and Slave-Boson methods are particularly renowned in the field, providing closed-form solutions for various quantities.

In this thesis, we delve into the study of Open Quantum Systems from a fundamental perspective. Our primary focus is on the development and application of quantum many-body techniques for understanding the steady state of non-equilibrium systems, aiming to avoid the complexities and ambiguities associated with the Keldysh machinery. The reliance on Keldysh machinery often involves choosing an initial state, making numerous approximations, and computations, and can be numerically demanding.

Chapter 1 will present a literature survey of experimental realizations and theoretical investigations of non-Hermitian systems. This chapter will also present a brief, but self-contained background necessary for the consideration of such non-Hermitian Hamiltonians (nHH).

Chapter 2 begins with the derivation of an effective nHH from the quantum master equation which is then shown through simple transformations to be a non-Hermitian SIAM in chiral channels. We adapted standard techniques such as exact diagonalization, Green functions, and Slave Boson techniques with suitable modifications to explore this model. We have specifically focused on the interplay between non-Hermiticity, Rashba spin-orbit coupling, and strong correlations in a quantum dot connected to metallic leads.

Chapter 3 will focus on incorporating electron-electron (e-e) interaction

in nHH using finite-U Slave Boson and renormalization methods. In particular, we derive the Callan Symanzik renormalization equations from the impurity action in the Slave Boson representation. This approach was able to recover strong coupling and local moment phases in the Kondo problem, hence validating the method. We also show that these are general methods that can be used for lattice models and should serve to yield an unbiased simple description for incorporating e-e interactions in nHH. This is especially important since there are a limited number of analytical theories that are nonperturbative in both, the electron-electron interaction as well as QD-contacts coupling, and concomitantly have a straightforward generalization scheme. Secondly, the approach discussed in this chapter is analytical and, thus, will help to obtain closed-form expressions and reveal a physical picture underlying new and more complicated physical systems. Chapters 3 and 4 focus on the physics of a quantum dot connected through a parity-time symmetric, but non-Hermitian hybridization, to two metallic leads having Rashba spin-orbit coupling. The focus is on the interplay of non-Hermiticity, RSOC, and strong correlations, and the influence of such an interplay on exceptional and quantum critical points, as well as on new fixed points.

Chapter 4 of the thesis is dedicated to the investigation of the \mathcal{PT} -symmetric Dzyloashinski Moriya (\mathcal{DM}) interaction in the Kondo Problem. We employ the projection operator methods to derive a non-Hermitian Kondo model with complex \mathcal{DM} interaction. Subsequently, the model is investigated through an appropriately modified poorman's scaling formalism. The resulting RG equations up to second order are solved with which we obtain RG invariants, closed-form solutions, and critical points of the model. The rich physics resulting from the effect of the complex \mathcal{DM} interaction on Kondo physics is discussed.

Chapter 5 focuses on the interplay between Dresselhaus Spin-Orbit (DSO) and Rashba Spin-Orbit (RSO) coupling in the Hermitian and non-Hermitian single-impurity Anderson model. We derive the \mathcal{PT} -symmetric emergent spin-orbit coupling channels through angular momentum expansion in three dimensions. We utilize Kotliar and Ruckenstein Slave Boson's representation to rewrite the impurity action to derive saddle point equations to get the Kondo scale. RG calculations are performed in Kehrein's Flow Equations formalism by deriving the flow equations with different generators. we construct a comprehensive phase diagram that highlights the competition or cooperation between spin-orbit interactions and correlation in the non-Hermitian Kondo problem.

Chapter 6 explores the impact of non-linear dispersion in the conduction bath hosting topological states on the Kondo problem and its effect on electronic transport. An effective non-Hermitian Kondo model is derived by

analyzing a specially designed bath with a three-fold symmetry rotation in momentum. Combining anisotropic Dzyaloshinskii-Moriya (DM) interaction and non-linear dispersion leads to the surprising emergence of exceptional points in a Hermitian model. The chapter also investigates the effects of potential scattering and extends the model to a two-impurity Kondo system. Notably, our analysis reveals a "Sign Reversion" regime and the presence of out-of-phase RKKY oscillations.

A summary of the thesis along with a future outlook is provided in Chapter 7.

List of Figures

1.1	A schematic diagram distinguishing between Type-I and Type-II Exceptional Points (EPs) in various non-Hermitian models has been developed based on the discussions presented in Appendix B of Takanabu Taira's thesis ¹³ . Dotted lines represent imaginary weights of eigenvalues.	11
1.2	Plots demonstrating band touching points calculated from poles of $G(\omega)$ in k-space in 2 dimensions where above top plot for the Hermitian case(H_{Herm}) and bottom one is for Non-Hermitian($H_{non-Herm}^{PT}$), Note that the Dirac cones are rotated by 90 degrees and additionally there is Dirac cone at center in non-Hermitian case.	16
1.3	Emergent exceptional points at $Re(\epsilon_k) = \pm 1$ in the Hatano-Nelson Model with periodic perturbation, as discussed by Hebert et al. ⁴⁷	18
2.1	The inverse exceptional coupling, $g_{EP}^{-1} = \cot(\phi_{EP})$ as a function of (left panel) λ for various U values and (right panel) U for various λ values.	35
2.2	The lowest eight eigenvalues as a function of the non-Hermiticity parameter, ϕ , for $U = 4.0$, $\lambda = 1.2$, and $\epsilon_d = -U/2$. The cyan dot shows the first crossing of the ground state and the first excited state, and is thus identified as the quantum critical point.	36
2.3	The exceptional point phase diagram for the three-site model in the interacting regime is shown. The color bar shows the inverse exceptional coupling. The solid circles represent the line $\lambda = U/2$, on which the exceptional point remains at $\phi = \pi/4$ or $g = 1$. Everywhere else the exceptional point is strongly renormalized by interactions and SOC. In the dark regions (low U , high λ and high U , low λ), the inverse exceptional coupling vanishes, implying $g_{EP} \rightarrow \infty$, and hence \mathcal{PT} -symmetry is never violated.	37

2.4	Phase diagram in the ϕ – λ plane is shown for the non-interacting case ($U = 0$). The solid circles represent exceptional points, where certain real eigenvalues coalesce and complex conjugate eigenvalues emerge.	39
2.5	Dot density of states (DoS) as a function of frequency for various values of SOC (legends are the values of λ) and $\phi = \pi/5$ (left panel) and $\phi = \pi/3$ (right panel). In the top panel, the system does not violate \mathcal{PT} -symmetry for $\phi = \pi/5$ for any λ . The bottom panel is for $\phi = \pi/3$, for which $\lambda = 1.5$ represents the SOC value beyond which \mathcal{PT} -symmetry is restored.	42
2.6	The $U = 0$ Phase diagram in the $\phi - \lambda$ plane found through the norm violation condition of the Green's function. The solid symbols represent the line of exceptional points, where the spectral sum rule gets violated and the norm deviates from unity.	43
2.7	The sum of energies of all occupied causal states at a given ϕ measured from a reference value of $\phi = 0$ for various values of SOC. The ϕ value at which the discontinuity in total energy occurs is marked by arrows.	44
2.8	The phase diagram in the $\phi - \lambda$ plane, computed through an identification of the energy discontinuity (see text for details) showing the line of exceptional points (triangles). The shaded region represents the spontaneously broken \mathcal{PT} -symmetry broken regime, and the unshaded region represents the \mathcal{PT} -symmetry protected regime. The circles and squares represent the exceptional points derived through exact diagonalization and the spectral sum rule violation respectively. All the three conditions for determining exceptional points agree reasonably well.	45
2.9	T_K (black, solid) and the exponential fit (red-dashed) as a function of scaled dot-orbital energy, $\pi\epsilon_d/4\Delta_0$ for $\lambda = 0$ and $\phi = 0$	50
2.10	T_K (black, solid) and the exponential fit (red-dashed) as a function of spin-orbit coupling (λ).	50
2.11	T_K/T_{K0} for $\lambda = 0$ (black circles) and $\lambda = 1.5$ (red squares) and the respective fits (green-dashed and blue-dashed) for $\epsilon_d = -1.75$	51

2.12	The shaded region represents a parameter regime, where a finite Kondo scale is found. The Auxiliary Particle-boson results for the vanishing of T_K are shown by red crosses (ϕ -scan), and blue stars (λ -scan) and the dashed line represents a fit, and is a guide to the eye.	52
3.1	We have plotted ω roots given in equation 3.29 by varying Non-Hermitian strength (ϕ) for $\lambda = 0$	65
3.2	We have plotted ω roots given in equation 3.29 by varying Non-Hermitian strength (ϕ) $\lambda = 1.5$	66
3.3	Density of states from the Callan-Symmanzik Green's function by varying the bare NH hybridization and for $\lambda = 0$	66
3.4	We are plotting the computed form of flow equations β_{Δ_r} and $\beta_{\tilde{\epsilon}_d}$ given in equation 3.35 for $g < 1$	69
3.5	We are plotting the computed form of flow equations β_{Δ_r} and $\beta_{\tilde{\epsilon}_d}$ given in equation 3.35 for $g > 1$	70
3.6	Ground State computed from impurity action as a function of NH-Hybridization in the non-interacting case. Different colors represent computed ground state energy for different bare values of hybridization. Effective impurity action and Eq. 3.26 are utilized to compute free energy/ E_g	75
4.1	In equation 4.11, we demonstrate the fluctuations in the lowest eigenvalues E_{\pm} of the Kondo model by adjusting the strength of SOC (λ). The plots display thick lines for real eigenvalues and dotted lines for imaginary eigenvalues. The y-axis indicates $\frac{E}{J_0} - J_r$, which represents shifted eigenvalues.	83
4.2	Variation of Kondo scale with Non-Hermitian strength (g) and RSO (s) for the fixed bare value of the ratio $\frac{J}{J_r}$ in equation 4.27.	90
4.3	Flow diagrams illustrating the emergence of a new fixed point in the non-Hermitian (NH) case for $g \neq 0$ and $J_r \neq 0$. As the strength of the spin-orbit coupling (SOC) increases, the fixed point transitions from a stable state to a marginally stable state, ultimately vanishing when $J_r = 0$	91
4.4	Flow diagrams illustrate the evolution of a new spiral fixed point (black) to an unstable state (green) with \mathcal{PT} -symmetric coupling, along with the usual Kondo coupling J	93

4.5	The left flow diagram shows the absence of fixed points signaling there is no phase transition and the Kondo effect persists for $s \geq g$. The right flow diagram consists of 3 stable fixed points $s = g/2$ clear indication of phase transition. The red dot corresponds to the regime of irrelevant scattering, the grey dot corresponds to gamma diverging and the blue is the decoupled impurity.	96
5.1	The plot illustrates the roots of $A(\omega)$, which encompass both real and imaginary components, showcasing Exceptional Points (EPs). Solid lines in different colors represent real parts of the roots, while dotted lines depict the imaginary roots as functions of V_0 . Throughout these computations, we maintain a constant value of $\lambda_2 = 1.0$, and λ_1 can be adjusted. A higher λ_1 value signifies increased strength of V_0 and a greater likelihood of encountering EPs.	110
5.2	The figure displays a comparison between the original non-Hermitian resonant level Anderson model (NHAM) and the Anderson model after mapping. In plot (a), you can observe the eigenvalues of NHAM, while plot (b) showcases the eigenvalues of the mapped Anderson model.	122
5.3	The plot for comparing the original flow equations with the new generator flow equations when parity-time breaking interactions are absent.	129
5.4	The plot for comparing the original flow equations with the new generator flow equations when parity-time breaking interactions are absent.	129
5.5	To compare the flow equation results we derive flow equations from the new generator and then implement them in the standard algorithm as shown above.	130
5.6	Conventional flow equations are derived and implemented as shown in the above protocol.	130
6.1	The eigenvalues of the diagonalized model in equation 6.2 around the low k points represent the emergent chiral bands. In this case, we set $\beta = 0.3$, $\lambda = 1.0$, and $\theta = \frac{\pi}{3}$. We observed that larger β values flatten the bands.	137

- 6.2 The eigenvalues of the model (equation 6.17) with $J_0 = -2.0$ (above) and $J_0 = 1.0$ (below), along with the RG invariant $m = \pm 0.01$. For small values of m and two roots denoted as $J_0 < 0, J_0 > 0$, the eigenvalues are denoted from E_1 to E_4 for corresponding RG root. Topological transitions occur at $J_{k^3} = \pm 0.5$ and around $J_{k^3} = 0.75$. At smaller values of m , there will be small imaginary weights in the eigenvalues, but no exceptional points. These topological points remain at higher values of m , but the spectrum will be gapped due to higher J_0 values. 142
- 6.3 Eigenvalues of the equation 6.17 for resonant level cases (small J_0). For $J_0 = \pm 0.1$ and the RG invariant $m = \pm 4.0$. The labels E_1 to E_4 denote four different eigenvalues for positive and negative RG invariants, respectively. A Dirac cone appears in the impurity spectrum due to the topological properties of the local Hamiltonian. Larger values of m are required to observe exceptional points, and the gap in the spectrum widens with increasing J_0 143
- 6.4 Variation of the condition number with anisotropic \mathcal{DM} coupling J_{k^3} in the model in equation 6.14, using Fock-space diagonalization in the SS of the one-impurity problem. Diverging cusp-like points indicate high condition numbers denoted in graph implies defects in diagonalization found figure 6.2. 144
- 6.5 Variation of condition numbers in Fock space of the two-impurity model given in equation 6.24, and they show that the model is well conditioned for most values of K , except when K is 0. However, high condition numbers occur when the anisotropic coupling is non-zero, indicating that the model is not defective when J_{k^3} and J_k couplings are absent. 145
- 6.6 Left schematic representing two Anderson impurities in the edge states of the bath. Right one is regular hexagonal cell of bath to incorporate \mathcal{PC} symmetric potential scattering terms. The left and right scatterers are depicted with green and blue arrows, respectively. Here, $k_{\parallel} \rightarrow k$, $\sqrt{k_x^2 + k_y^2} \rightarrow k$ and $\theta \rightarrow \tan^{-1} \frac{k_y}{k_x}$. For derivations, see equations from 6.4 to 6.6. Electron and hole scatterings for (k, θ) to $(-k, \theta')$ are represented around the Dirac cone. Note that k is modulus of the vector and only its direction will decide the sign of momenta of hole or electron. 146

- 6.7 In these figures, we show the RG flow using the fixed values $g_{1k} = g_{1k^3} = 1$, which is invariant derived in the appendix B. Throughout our calculations, we use $J_{1k} = \frac{1}{2} \pm \frac{1}{2} \sqrt{1 + 4mJ_{1k^3}}$ alongside setting $m = -4$. The top row of the plots represents potential scattering, and the second row shows the real and imaginary parts of (J_{1k}) in both RG equations in x and y axes, where the notation (R^+, R^+) and $(R^+ I^+)$ denotes the real and imaginary parts on the x and y axes, respectively. Similarly, the third row is (I^-, R^-) and (I^-, I^-) . We observe at least two fixed points (FP) and two spiral points (SP) in the second row, while the third row shows one SP and one marginal point. The dotted lines in the second plot of the first row represent a family of FPs. The EP signatures figure 6.3 in RG flow can be observed here as parallel arrows at small J_0 and J_{k^3} values, representing unstable solutions. At these SP we found topological transitions in figures 6.2 and high condition numbers in figure 6.4 for $J_{k^3} = 0.5$ 147
- 6.8 We plot numerical solutions of the RG equations (6.22) at the fixed points in the flow diagrams. The x-axis corresponds to the flow parameter, and each plot is labeled at the top with the initial conditions for evolving RG ODE. Diverging solutions correspond to the strong coupling regimes, while cusp-like features changing sign abruptly correspond to dissipative regimes. The inset graph corresponds to a large negative RKKY, while the rest are set to small values as initial conditions. The plot depicts in order to renormalize RKKY all other coupling originating from bath are necessary, hence all flows to zero. . . . 151
- 6.9 In all plots above Dotted and thick lines correspond to real and imaginary coupling values. Sign reversion occurs in all couplings for imaginary weights at $J_{k^3} = -2.0$ in bottom plot. Between two sign-reversing phases top to bottom, various 2-pole and 3-pole regimes are observed. We verified that SR in imaginary weights in both one and two impurities occur at these dissipative fixed points. 152
- 6.10 Plot (a) shows the relaxation time for different values of the nonlinear parameter (β) , which is proportional to resistivity. Plot (b) is scaled from the first point of each curve shows a kink in the relaxation time (τ) . We show scaling collapse, and the kink disappear in plots (e) and (d) when those are scaled from two different roots respectively for both axes as $\tau_{\pm r}^{-1} = \tau^{-1} \times (1 \pm \sqrt{4D_{eff} + 1})$ and $D_{eff}^{\pm r} = D_{eff} \times (1 \pm \sqrt{4D_{eff} + 1})$. 154

6.11	We plot RKKY interaction as function of bandwidth ϵ , for a critical value of the chemical potential ($\mu = \pm 0.25$), J_Y^{odd} changes sign and goes out of phase as shown in the figure above. The RKKY interaction is amplified for a range of $0 < \beta < 1.0$ and approaches the ideal flat band limit for $\beta > 1.0$.	155
6.12	We plot the elliptic functions written in solution B.33. For negative chemical potential μ , there is discontinuity when bandwidth $\epsilon = -\mu = 0.25$ this correspond $q \rightarrow 0$ limit; elsewhere, we see exceptional points. The EPs start shifting for increasing positive μ , but there is no SR in the real part of these special functions. This odd channel shows EP or SR behavior, which is relevant in RG when dominant odd channel scattering emerges as complex FPs in such models.	156
A.1	$\delta\mathcal{J}$ represents couplings' RG equations and diagrams show 1-loop and 2-loop spin-flip possibilities.	172
B.1	RG flow of two impurity show the FP can be in different quadrants with $R_1 = -1$ and $R = 1.0$. We get around the SP($(J_Y = 1.0, J_0 = 3.0)$) existing SR regime in couplings.	186

List of Tables

2.1	Table showing the results of the fits of T_K <i>vs.</i> ϕ of figure 2.11, from which the critical ϕ has been obtained.	52
-----	---	----

Contents

Acknowledgements	vii
Synopsis	xi
1 Introduction	7
1.1 Early Development of Non-Hermitian Theories	8
1.2 Non-Hermitian Quantum Theories	9
1.3 Hermitianization and Metric Operators in Non-Hermitian Quantum Systems	10
1.4 Type I and Type II exceptional points	11
1.4.1 Example	11
1.5 Exceptional Points In Condensed matter	14
1.5.1 Example Of Non-Hermitian Dispersion in 2 dimensions	15
1.6 Non-Hermitian Condensed Matter Systems	17
1.7 The Hatano-Nelson Model with Periodic Potential	17
1.8 Non-Hermiticity and Strong Correlation	19
1.9 Perturbation Theory for Non-Hermitian Systems	19
1.10 Single and Two-Impurity Physics in the Anderson Model . . .	20
1.11 Overview of the thesis	21
2 Kondo effect in \mathcal{PT}-symmetric Anderson model with Rashba SO coupling	27
2.1 Introduction	28
2.2 Model and formalism	30
2.3 Three-site, zero bandwidth model in the chiral basis	32
2.3.1 Non-interacting case: $U = 0$	33
2.3.2 Interacting case: $U > 0$	35
2.4 Full model: Results and discussion	38
2.4.1 Exact Diagonalization of the non-interacting model . .	38
2.4.2 Spectral sum rule in the $U = 0$, non-interacting case . .	40
2.4.3 Total energy of the causal states ($U = 0$)	43

2.4.4	Auxiliary Particle boson mean-field solution	44
2.5	Discussion and Conclusions	53
3	Auxiliary Particle-Boson Methods for Non-Hermitian Models: Callan Symanzik Renormalization	57
3.1	Introduction	58
3.2	Auxiliary Particles-Boson Approaches in Non-Hermitian Systems	58
3.3	Renormalization and the CS Equation	59
3.3.1	Exceptional Points in Non-Interacting Problem	63
3.4	Exceptional Points in Strong Correlation	65
3.5	Finite U-Auxiliary ParticleBoson Analysis	68
3.6	Auxiliary Particle Method in Keldysh Field Theory	72
3.6.1	Current Calculation Within Mean Field Theory	74
3.7	Discussion and Conclusion	74
4	RG Analysis Of Complex \mathcal{DM} interaction in Kondo problem	77
4.1	Introduction	78
4.2	Projection Operator Method	79
4.3	Projection in the Chiral Basis	81
4.4	Poorman Scaling With Metric Operators	84
4.4.1	RG Invariants Identification	87
4.4.2	Comparison With earlier works	87
4.4.3	CFT scaling laws at two loops	88
4.4.4	Kondo Scale in one loop Poorman scaling	89
4.4.5	CFT scaling laws with finite γ and \mathcal{DM} -interactions	90
4.4.6	Non-Hermitian Phase renormalization	92
4.5	RG Flows And Critical Points	95
4.6	Discussion	97
4.7	Open Questions	98
5	Flow Equation and Finite-U Parton Boson Analysis of \mathcal{PT}-SIAM with RSO and DSO interactions	103
5.1	Introduction	104
5.2	Derivation of the Angular Momentum Basis Model	104
5.3	Emergence of \mathcal{PT} -bands in DSO case	105
5.4	Derivation of spectral function	107
5.4.1	Finite-U Auxiliary Particle -Boson Analysis	110
5.5	Illustration of Proposed Flow Generator for Diagonal Non-Hermiticity in a Simple Model	112

5.5.1	Deriving Flow Equations for Non-Hermitian Single Impurity Anderson Models using a Novel Generator . . .	113
5.6	Mapping of non-Hermitian model to isospectral Hermitian models	115
5.6.1	Unitary Operator for \mathcal{PT} -SIAM	119
5.6.2	Flow equations For Scaled PTSIAM	124
5.6.3	Conventional Flow Equations For Non-Hermitian SIAM	126
5.7	Discussion and Conclusion	128
6	Anderson Impurities In Edge States with Nonlinear Dispersion	133
6.1	Introduction	134
6.2	Model and Formalism	135
6.3	Effective Model Derivation And Poorman Scaling	138
6.4	Emergence Of Complex Solution	139
6.4.1	Condition Number In Fock Space	141
6.5	Renormalization With Potential Scattering	141
6.6	Generalization to Two Impurities	146
6.6.1	Eigenspectrum connection to fixed points	148
6.7	Solutions for RG ODE	150
6.7.1	RG Equations Zeros and Poles Analysis	150
6.8	Impurity Transport Calculation	150
6.8.1	Scaling Collapse In $\frac{1}{\tau}$	153
6.9	Results and Discussion	153
7	Conclusions and Future perspectives	161
7.1	Summary of the Thesis	162
7.2	Future Perspectives	164
7.3	Time Evolution of Non-Hermitian Systems	164
7.3.1	Lie Algebra and Renormalization Group (RG) Invariants	165
7.4	Exploration of \mathcal{DM} interaction forms And their Group structures	166
7.5	DMFT for non-Hermitian systems	166
7.6	NRG for non-Hermitian systems	166
7.7	Self-consistency and Green's functions	167
7.8	Real-time dynamics	167
A	Derivation Of Metric Operator and RG Equations	169
A.1	Metric Operator in spin basis	169
A.1.1	Poorman scaling	173
A.1.2	One loop solution with γ	174

A.1.3	Analytical Solution at third order non-linearity	174
A.1.4	Regime $s/g \rightarrow \infty$	175
A.1.5	Regime $g \rightarrow \infty$	175
A.2	Resistivity Calculation	175
B	Derivations for The Chapter 6	177
B.1	Projection details for deriving effective sd model	177
B.2	Including the potential scattering	182
B.3	Analytic Solution of RG Equations	184
B.4	RKKY Interaction	187
B.5	Impurity Transport Calculation	187
C	Derivation Of Effective Model From Lindbladian	191
C.1	Appendix-Development of a non-Hermitian Hamiltonian . . .	191
C.2	Lindbladian Derivation	192

Chapter 1

Introduction

1.1 Early Development of Non-Hermitian Theories

The contemporary formulation of quantum mechanics in a closed system is based on the axioms which can be traced back to the mathematical formulation of quantum mechanics, proposed by Paul Dirac¹ in 1930 and John von Neumann² in 1932. Below we present the axioms of quantum mechanics generally found in standard quantum mechanics textbooks³⁻⁵.

- State vector ψ is the element in infinite dimensional Hilbert space \mathcal{H} . ψ satisfies all the criteria of vector space.

$$\psi = \lambda_1 \psi_1 + \lambda_2 \psi_2 \quad (1.1)$$

where λ_1 and λ_2 are arbitrary complex numbers. ψ can be shown it is square integrable:

$$\begin{aligned} |\psi|^2 &= |\lambda_1|^2 |\psi_1|^2 + |\lambda_2|^2 |\psi_2|^2 + \lambda_1^* \lambda_2 \psi_1^* \psi_2 + \lambda_1 \lambda_2^* \psi_1 \psi_2^* \\ &\leq |\lambda_1| |\lambda_2| (|\psi_1|^2 + |\psi_2|^2) \end{aligned} \quad (1.2)$$

ψ spans vector space hence square-integrable and $|\psi|^2$ is smaller than a function whose integral converges.

- Scalar product is defined as $(\phi, \psi) = \int d\tau \phi^* \psi$ and has following properties:

$$\begin{aligned} (\phi, \psi) &= (\psi, \phi)^* \\ (\phi, \lambda_1 \psi_1 + \lambda_2 \psi_2) &= \lambda_1 (\phi, \psi_1) + \lambda_2 (\phi, \psi_2) \\ (\lambda_1 \phi_1 + \lambda_2 \phi_2, \psi) &= \lambda_1^* (\phi_1, \psi) + \lambda_2^* (\phi_2, \psi) \end{aligned} \quad (1.3)$$

The scalar product is linear and if $(\phi, \psi) = 0$ then ϕ and ψ are orthogonal, and $(\psi, \psi) = \int d\tau |\psi|^2$ is a real positive number and it is only zero when ψ is zero. All the vectors in Hilbert space obey the Schwartz inequality:

$$|(\psi_1, \psi_2)| \leq \sqrt{(\psi_1, \psi_1)} \sqrt{(\psi_2, \psi_2)} \quad (1.4)$$

- Self-adjoint ($A^\dagger = A$) or Hermitian operators satisfies the relation $(\phi|A|\psi) = (\psi|A|\phi)^*$ and action of operator "A" $A|\psi\rangle = |\psi'\rangle$ and It is worth noting that ψ' is also a part of the Hilbert space.

- Completeness or closure relation can be defined as $\sum_i P_i = \mathcal{I}$ and projection operators are $P_i = |\psi_i\rangle\langle\psi_i|$.
- When the physical quantity $\langle\psi|A|\psi\rangle$ on a normalized state ψ the probability of obtaining non-degenerate eigenvalue a_n is $\mathbb{P}(a_n)$ is given by $\mathbb{P}(a_n) = |\langle u_n|\psi\rangle|^2$ where $|u_n\rangle$ is normalized and its eigenvalue is a_n .
- Time Evolution in the standard formulation is unitary and can be stated as,

$$i\hbar\frac{d}{dt}|\psi(t)\rangle = H(t)|\psi(t)\rangle$$

These standard axioms will be modified in the case of Non-Hermitian quantum theories; here, we present an overview of the early formulation and a few pioneering works. Carl Bender's article⁶ in 1998 sheds light on a certain class of Non-Hermitian Hamiltonians. Complex Hamiltonians were used in dissipative systems as early as 1928, where an imaginary part of the model was used to explain the lifetime of the resonance state. The fundamental difference between the various types of complex Hamiltonians lies in the inner products of the states^{7;8}.

1.2 Non-Hermitian Quantum Theories

The theories involving Non-Hermitian Hamiltonians, which are not necessarily self-adjoint and can lead to complex eigenvalues. The study of Non-Hermitian quantum theories is motivated by the desire to understand the properties of systems that standard Hermitian quantum mechanics does not describe. Some research areas in this field include the study of Non-Hermitian phase transitions, the behavior of Non-Hermitian systems in the presence of dissipation, and the investigation of Non-Hermitian quantum gravity models⁹.

It is important to note that Non-Hermitian systems are still poorly understood, and many open questions in this field are ripe for investigation⁹. The development of Non-Hermitian theories in the early stage was focused on complex theories like the ϕ^3 and $i\phi^3$ and wrong sign " $-\phi^4$ " models. The nhQFT host-bound states were first shown by Carl M. Bender et al⁹., opening up new possibilities for studying bound states and resonances in Non-Hermitian systems⁹. Since then, research in this area has grown, and

the exploration of NH theories has expanded to include a wide range of topics⁹.

There have been several attempted extensions of well-known theories like the Non-Hermitian Standard Model or Non-Hermitian extensions of other gauge theories⁹. These extensions could involve studying the impact of non-Hermitian terms on particle interactions, symmetries, and the dynamics of the system. Additionally, it is worth investigating the implications of Non-Hermitian quantum field theories in the context of quantum information theory and quantum computing. Understanding the effects of Non-Hermitian terms on quantum entanglement and quantum information processing could have practical applications in quantum technologies.

1.3 Hermitianization and Metric Operators in Non-Hermitian Quantum Systems

In the first formulation with an indefinite inner product¹⁰, Mark S. Swanson introduced a mapping known as the Dyson map, represented as $\eta(z)H\eta^{-1}(z)$, which transforms a given non-Hermitian Hamiltonian H to that of a harmonic oscillator, denoted as $h = \frac{1}{2}\mu(z)p^2 + \frac{1}{2}\nu(z)x^2$. The Dyson map relies on the concept of Hermitianization, expressed as $\eta^{-1}A\eta = (\eta^{-1}A\eta)^\dagger \implies A\eta^\dagger\eta = \eta^\dagger\eta A^\dagger \implies \eta^\dagger\eta = \rho$. Swanson's work has shown observable effects in various regimes, revealing the connection between Non-Hermitian quantum systems and Harmonic Oscillators¹⁰. This mapping provides valuable insights into the behavior of Non-Hermitian systems by relating them to well-understood and tractable harmonic oscillators, facilitating their study and analysis in different physical scenarios. The approach has implications in a wide range of quantum systems, and its applications continue to be explored in the field of theoretical physics.

In studies involving NHH, one typically seeks metric operators to map models to Hermitian form or define meaningful inner products and averages. The selection of metric operators can vary depending on the particular model and the type of non-Hermiticity involved. For instance, in a generalized Harmonic Oscillator model, Musumbu et al.¹¹ demonstrated that there are multiple options for choosing a metric operator.

In the conventional quantum formulation, it is a requirement that the inner product must be bounded from below, meaning that $\langle\psi_n|\psi_m\rangle$ should be both finite and positive, with the added condition that $\langle\psi_n|\psi_m\rangle < \infty$. However, in the context of non-Hermitian systems, the inner product must

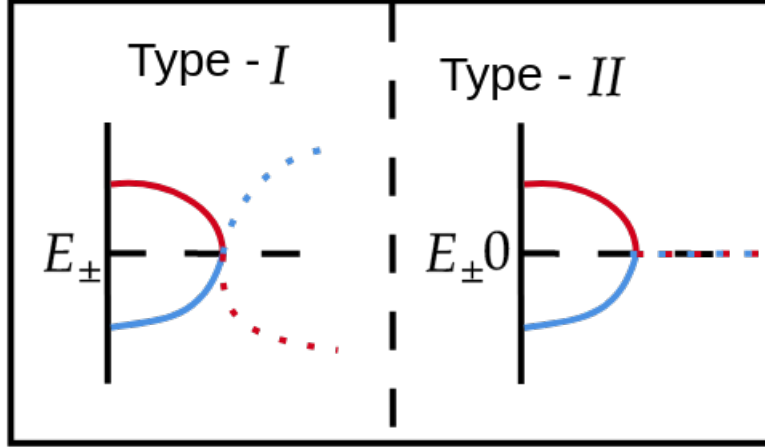


Figure 1.1: A schematic diagram distinguishing between Type-I and Type-II Exceptional Points (EPs) in various non-Hermitian models has been developed based on the discussions presented in Appendix B of Takanabu Taira's thesis¹³. Dotted lines represent imaginary weights of eigenvalues.

be taken over an appropriate basis using metric operators. Several works^{9;12} have demonstrated that in these non-Hermitian scenarios, the probability is not conserved, and it exhibits oscillatory behavior in regimes involving imaginary eigenvalues.

1.4 Type I and Type II exceptional points

In non-Hermitian quantum mechanics, exceptional points (EPs) are singular points in a system's parameter space. Two types of EPs, Type-I and Type-II as shown in figure 1.1, can occur. Takanobu and Andreas Fring's work¹³ offers insights into obtaining distinct solutions for different types of EPs.

The concept of complex scaling of an operator, originally introduced by Dyson, has found practical use in nuclear reactions and can be adjusted for use in complex scaling within the context of \mathcal{PT} -symmetric systems⁷.

1.4.1 Example

A three-site problem can be considered as a demonstration of the Dyson Map. Let's illustrate the concept of complex scaling of operators using this

example in second quantization.

$$H = \epsilon_{-1}c_{-1}^\dagger c_{-1} + \epsilon_0 c_0^\dagger c_0 + \epsilon_1 c_1^\dagger c_1 + re^{-i\theta}(c_{-1}^\dagger c_0 + hc) + re^{-i\theta}(c_1^\dagger c_0 + hc) \quad (1.5)$$

We can write this in the following matrix form,

$$H = \begin{pmatrix} c_{-1}^\dagger & c_0^\dagger & c_1^\dagger \end{pmatrix} \begin{pmatrix} \epsilon_{-1} & re^{-i\theta} & 0 \\ re^{-i\theta} & \epsilon_0 & re^{i\theta} \\ 0 & re^{i\theta} & \epsilon_1 \end{pmatrix} \begin{pmatrix} c_{-1} \\ c_0 \\ c_1 \end{pmatrix} \quad (1.6)$$

In order to find a metric operator that satisfies the quasi/pseudo-Hermitian condition $\eta H \eta^{-1} = H^\dagger$, we can observe the following symmetry operations on the Hamiltonian H:

$$\begin{aligned} \mathcal{P}c_j\mathcal{P}^{-1} &= c_{-j} \\ \mathcal{T}i\mathcal{T}^{-1} &= -i \\ \mathcal{C}c_j\mathcal{C}^{-1} &= ic_j^\dagger \end{aligned} \quad (1.7)$$

We can construct a metric operator by using the symmetry operations outlined in Equation 1.7, which include \mathcal{P} for parity, \mathcal{T} for time reversal, and \mathcal{C} for charge conjugation. These operations were also discussed by Bender et al.⁹ in their work on a model in first quantization:

$$\begin{aligned} \begin{pmatrix} c_{-1} \\ c_0 \\ c_1 \end{pmatrix} &\xrightarrow{\mathcal{PT}} \begin{pmatrix} c_1 \\ c_0 \\ c_{-1} \end{pmatrix} \\ \begin{pmatrix} c_{-1} \\ c_0 \\ c_1 \end{pmatrix} &= \begin{pmatrix} 0 & 0 & 1 \\ 0 & 1 & 0 \\ 1 & 0 & 0 \end{pmatrix} \begin{pmatrix} c_1 \\ c_0 \\ c_{-1} \end{pmatrix} \\ \therefore \eta &= \begin{pmatrix} c_1^\dagger & c_0^\dagger & c_{-1}^\dagger \end{pmatrix} \begin{pmatrix} 0 & 0 & 1 \\ 0 & 1 & 0 \\ 1 & 0 & 0 \end{pmatrix} \begin{pmatrix} c_1 \\ c_0 \\ c_{-1} \end{pmatrix} \\ &= c_1^\dagger c_{-1} + c_0^\dagger c_0 + c_{-1}^\dagger c_1 \end{aligned} \quad (1.8)$$

With the metric operator provided in Equation 4.20, it is possible to demonstrate that $\eta H \eta^\dagger = H^\dagger$, which satisfies the condition for pseudohermiticity. Subsequently, we can determine the left-right eigenstates of the model along with their corresponding eigenvalues.

$$\lambda_0 = \epsilon, \quad \lambda_{\pm} = \frac{\epsilon + \epsilon_0}{2} \pm \sqrt{\frac{(\epsilon_0 - \epsilon)^2}{4} + 2r^2 \cos 2\theta} \quad (1.9)$$

We can verify the completeness with bi-vector formalism¹⁴⁻¹⁶ that is $\sum_{\alpha, \alpha=0, \pm 1} |\alpha\rangle_{LR} \langle \alpha'| = \delta_{\alpha, \alpha'}$,

$$\begin{aligned}
|\pm\rangle_R &= \frac{1}{\sqrt{N_{\pm}}} \begin{pmatrix} \pm \frac{e^{-i\theta}}{\sqrt{2 \cos 2\theta}} \\ 1 \\ \pm \frac{e^{i\theta}}{\sqrt{2 \cos 2\theta}} \end{pmatrix}, \quad \langle \pm|_L = \frac{1}{\sqrt{N_{\pm}}} \begin{pmatrix} \pm \frac{e^{-i\theta}}{\sqrt{2 \cos 2\theta}} & 1 & \pm \frac{e^{i\theta}}{\sqrt{2 \cos 2\theta}} \end{pmatrix} \\
|0\rangle_R &= \frac{1}{\sqrt{N_0}} \begin{pmatrix} e^{i\theta} \\ 0 \\ -e^{-i\theta} \end{pmatrix}, \quad \langle 0|_L = \frac{1}{\sqrt{N_0}} (e^{i\theta} \quad 0 \quad -e^{-i\theta}) \\
N_{\pm} &= \frac{2 + 2 \cos 2\theta}{2 \cos 2\theta}, \quad N_0 = 2, \quad N = 2 \cos 2\theta \\
\text{where } N &= {}_L \langle \pm, 0 | \pm, 0 \rangle_R, \quad N_{\pm, 0} = {}_R \langle \pm, 0 | \pm, 0 \rangle_R
\end{aligned} \tag{1.10}$$

The completeness for this problem can be verified as the following,

$$\begin{aligned}
|+\rangle_{LR} \langle +| + |0\rangle_{LR} \langle 0| + |-\rangle_{LR} \langle -| &= I \\
|\pm\rangle_R \langle \pm|_L &= \frac{1}{N} \begin{pmatrix} \frac{e^{-2i\theta}}{2 \cos 2\theta} & \pm \frac{e^{-i\theta}}{\sqrt{2 \cos 2\theta}} & \frac{1}{2 \cos 2\theta} \\ \pm \frac{e^{-i\theta}}{\sqrt{2 \cos 2\theta}} & 1 & \pm \frac{e^{i\theta}}{\sqrt{2 \cos 2\theta}} \\ \frac{1}{2 \cos 2\theta} & \pm \frac{e^{i\theta}}{2 \cos 2\theta} & \frac{e^{2i\theta}}{2 \cos 2\theta} \end{pmatrix} \\
|0\rangle_R \langle 0|_L &= \frac{1}{2} \begin{pmatrix} e^{-2i\theta} & 0 & -1 \\ 0 & 0 & 0 \\ -1 & \frac{e^{i\theta}}{2 \cos 2\theta} & \frac{e^{2i\theta}}{2 \cos 2\theta} \end{pmatrix}
\end{aligned} \tag{1.11}$$

complex scaled operators can map the \mathcal{PT} -Hamiltonian as a Hermitian model, which is a Dyson map in this case,

$$\begin{aligned}
\tilde{c}_{-1} &= f(\theta) e^{-i\theta} c_{-1}, \quad \tilde{c}_1 = f(\theta) e^{i\theta} c_1, \quad f(\theta) = \sqrt{2 \cos 2\theta} \\
\epsilon_- &= \frac{\epsilon_{-1}}{\sqrt{2 \cos 2\theta}} e^{-2i\theta}, \quad \epsilon_+ = \frac{\epsilon_{+1}}{\sqrt{2 \cos 2\theta}} e^{2i\theta}
\end{aligned} \tag{1.12}$$

Using the above complex scaling for operators and parameters, we get a mapped Hamiltonian having the same spectrum as the original one until we reach the exceptional point,

$$\tilde{H} = \epsilon_- \tilde{c}_{-1}^\dagger \tilde{c}_{-1} + \epsilon_+ \tilde{c}_1^\dagger \tilde{c}_1 + \epsilon_0 \tilde{c}_0^\dagger \tilde{c}_0 + r \sqrt{\cos 2\theta} (\tilde{c}_{-1}^\dagger \tilde{c}_0 + \tilde{c}_1^\dagger \tilde{c}_0 + hc) \tag{1.13}$$

The time evolution of the operators will follow the conventional equation of motion,

$$\dot{\tilde{c}}_{\pm 1, 0}(t) = \frac{i}{\hbar} [\tilde{H}, \tilde{c}_{\pm 1, 0}] \tag{1.14}$$

Green's functions for the scaled operators and exceptional point analysis will differ from conventional ones,

$$\begin{aligned}\tilde{\mathcal{G}}_{\tilde{c}_{\pm 1}^\dagger \tilde{c}_{\pm 1}} &= \left(\omega^+ - \epsilon_{\pm} - \frac{r^2 \cos 2\theta}{\omega^+ - \epsilon_{\pm} - \frac{r^2 \cos 2\theta}{\omega^+ - \epsilon_{\pm}}} - \frac{r^3 \cos^{\frac{3}{2}} 2\theta}{(\omega^+ - \epsilon_{\pm})(\omega^+ - \epsilon_{\pm} - \frac{r^2 \cos 2\theta}{\omega^+ - \epsilon_{\pm}})} \right)^{-1} \\ \tilde{\mathcal{G}}_{\tilde{c}_0^\dagger \tilde{c}_0} &= \left(\omega^+ - \epsilon_0 - \sum_{\alpha} \frac{r^2 \cos 2\theta}{\omega^+ - \epsilon_{\alpha}} \right)^{-1}\end{aligned}\tag{1.15}$$

Substituting the ϵ_{\pm} we can show these Green functions will not have causality violation as follows,

$$\tilde{\mathcal{G}}_{\tilde{c}_{\pm 1}^\dagger \tilde{c}_{\pm 1}} = \left(\omega^+ - \epsilon_{\pm} - \frac{r^2 \cos 2\theta}{\omega^+ - \epsilon_{\pm} - \frac{r^2 \cos 2\theta}{\omega^+ - \epsilon_{\pm}}} - \frac{r^3 \cos^{\frac{3}{2}} 2\theta}{(\omega^+ - \epsilon_{\pm})(\omega^+ - \epsilon_{\pm} - \frac{r^2 \cos 2\theta}{\omega^+ - \epsilon_{\pm}})} \right)^{-1}\tag{1.16}$$

This demonstrates that the Dyson map produces all spectral functions that adhere to the Lehmann representation, until the point where the Non-Hermitian parameter changes the sign of the quantity $\cos 2\theta$. This mapping can be likened to a problem involving oscillators by Mark S. Swanson^{17–19}. Subsequent chapters of the thesis will delve deeply into this issue, exploring it through different renormalization techniques.

The article by Ashida et al²⁰ in 2020 provides an overview of theoretical investigations into various Non-Hermitian theories. Since these processes can have diverse physical origins, they necessitate distinct theoretical approaches.

1.5 Exceptional Points In Condensed matter

In condensed matter physics, exceptional points (EPs) are singularities where a system's Hamiltonian eigenvalues and eigenvectors converge^{21;22;22–28}. EPs occur across electronic systems^{21–23}, photonic^{24–26}, and mechanical systems^{22;27;28}.

In electronic systems, EPs alter energy spectra, impacting topological properties crucial for understanding quantum phases and transport^{21–23}. Similarly, in photonic systems, EPs affect eigenmodes, influencing phenomena like lasing and emission suppression^{24–26}.

1.5.1 Example Of Non-Hermitian Dispersion in 2 dimensions

In order to showcase exceptional points in Non-Hermitian dispersion, we use a straightforward model with a specific type of spin-momentum coupled interaction. We compare this model in both Hermitian and Non-Hermitian problems, highlighting the importance of exploring Green's functions in the appropriate basis for Non-Hermitian problems. This topic is further discussed in Chapter 2.

$$H_{Herm} = \sum_{k,\sigma} (\cos k_x + \cos k_y) c_{k\sigma}^\dagger c_{k\sigma} + i \sum_k \psi_k^\dagger (\vec{\epsilon}_{k_x, k_y} \times \vec{\sigma})_z \psi_k \quad (1.17)$$

In the above model (1.17) index $k = \sqrt{k_x^2 + k_y^2}$, the eigenvector is represented in spin-momentum coupled interaction as:

$$\psi_k^\dagger = \begin{pmatrix} c_{k\uparrow}^\dagger & c_{k\downarrow}^\dagger \end{pmatrix}$$

where $\vec{\epsilon}_{k_x, k_y} = \cos k_x \hat{i} + \cos k_y \hat{j}$ and $\vec{\sigma} = \sigma_x \hat{i} + \sigma_y \hat{j} + \sigma_z \hat{k}$ and $k = \sqrt{k_x^2 + k_y^2}$. The Green's function for the model can be derived as follows:

$$G(\omega)_{\{c_\sigma^\dagger, c_\sigma\}} = \left(\omega^+ - \cos k_x - \cos k_y - \frac{\cos^2 k_x + \cos^2 k_y}{\omega^+ - \cos k_x - \cos k_y} \right)^{-1} \quad (1.18)$$

Now we consider a spin-dependent gauge that can be used to construct the non-Hermitian model and show the differences between the Hermitian and non-Hermitian cases particularly at band touching points.

$$H_{Non-Herm}^{PT} = \sum_{k\sigma} |\vec{\epsilon}_{k_x, k_y}| e^{i\sigma\theta} c_{k\sigma}^\dagger c_{k\sigma} + \left((\cos k_x - \cos k_y) c_{k\uparrow}^\dagger c_{k\downarrow} + (\cos k_x + \cos k_y) c_{k\downarrow}^\dagger c_{k\uparrow} \right) \quad (1.19)$$

where in the above model 1.19 $\theta = \tan^{-1} \frac{\cos k_y}{\cos k_x}$ and Green's functions for the above model can be derived as follows,

$$G^{PT}(\omega)_{\{c_\sigma^\dagger, c_\sigma\}} = \left(\omega^+ - \sigma \cos k_x - \sigma \cos k_y - \frac{\cos^2 k_x - \cos^2 k_y}{\omega^+ - \sigma \cos k_x - \sigma \cos k_y} \right)^{-1} \quad (1.20)$$

In the above equation, in the limit as $\omega^+ = (\omega + i\eta) \rightarrow \omega$, which is essentially equivalent to taking $\eta \rightarrow 0$, the roots of the denominator of the corresponding Green's function (denoted as G) are plotted in Figure 1.2. This figure illustrates subtle differences between the symmetry-preserved regime of a non-Hermitian model and a Hermitian model.

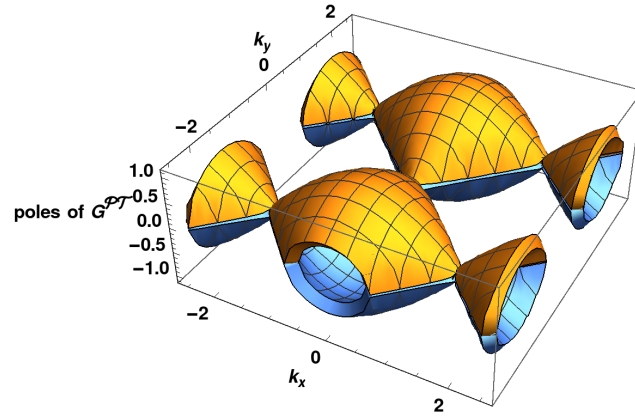
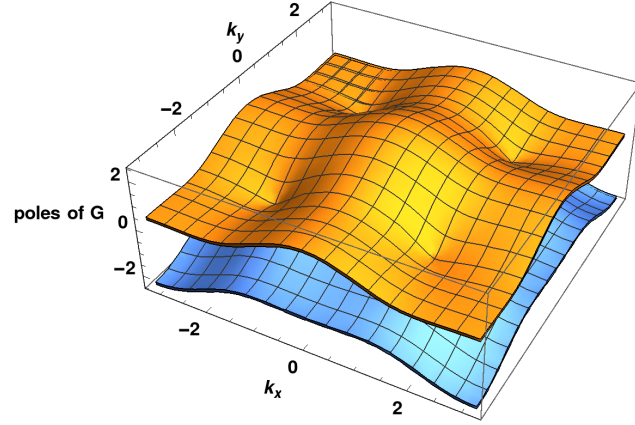


Figure 1.2: Plots demonstrating band touching points calculated from poles of $G(\omega)$ in k -space in 2 dimensions where above top plot for the Hermitian case(H_{Herm}) and bottom one is for Non-Hermitian($H_{non-Herm}^{PT}$), Note that the Dirac cones are rotated by 90 degrees and additional there is Dirac cone at center in non-Hermitian case.

1.6 Non-Hermitian Condensed Matter Systems

The study of open quantum systems often involves master equation techniques with various noise terms²⁹. Quantum criticality in \mathcal{PT} -symmetric effective field theories has been explored in the sine-Gordon model, describing the transition from a Mott insulator to a Tomonaga-Luttinger liquid^{30;31}. Similar critical behavior has been observed in classical systems and in classical spin chains with imaginary fields^{12;32}. Non-Hermitian Hamiltonians have been studied in experiments with balanced gain and loss in open systems, as observed in recent experiments with cold atoms^{33–36}.

Conventional Kondo-type systems, like impurities coupled to baths, have been realized in controlled environments such as atoms in harmonic traps^{37–42}. In experiments with synthetically generated Rashba-type spin-orbit coupling, induced artificial magnetic fields break parity and time reversal symmetries. Exceptional points may lead to sensitive sensors, where any perturbation of strength ϵ leads to a splitting of the levels proportionate to the n^{th} root of ϵ ^{43;44}.

Achieving Exceptional Points (EPs) in physical systems is challenging and can be engineered by manipulating dissipation, employing gain and loss elements, or applying external fields. Different systems such as electronic, photonic, mechanical, and microwave systems can be used to realize EPs. It is essential to confirm the characteristics of EPs, such as the degeneracy of eigenvalues and eigenvectors, and the appearance of new modes of vibration.

Recent discoveries include the creation of topologically protected lasers through unique lattice constructions in geometrically designed lasing cavities^{45;46}. The presence of nitrogen vacancies and carbon isotope substitution can lead to intriguing non-Hermitian phenomena in these systems.

1.7 The Hatano-Nelson Model with Periodic Potential

The Hatano-Nelson model is a well-studied quantum mechanical model in second quantization that describes the motion of a quantum particle in a disordered lattice with a periodic potential. Introduced in 1996 by Hatano and Nelson as a simplified version of the Anderson model, it is widely used to study quantum localization transitions. The Hamiltonian of the Hatano-Nelson model is given by:

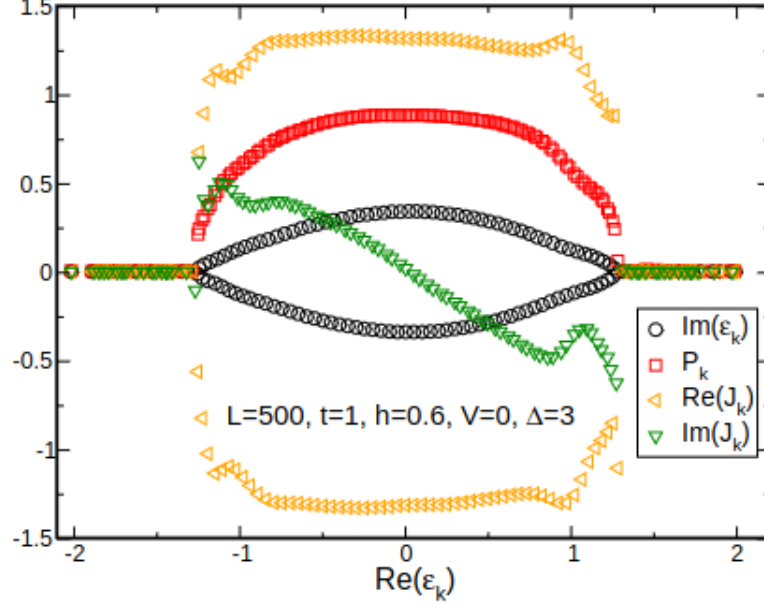


Figure 1.3: Emergent exceptional points at $Re(\epsilon_k) = \pm 1$ in the Hatano-Nelson Model with periodic perturbation, as discussed by Hebert et al.⁴⁷.

$$H_{HN} = \sum_n \left[-t \left(e^h c_n^\dagger c_{n+1} + e^{-h} c_{n+1}^\dagger c_n \right) + \mu_n c_n^\dagger c_n \right] + \sum_n V \cos n\pi$$

where c_n^\dagger and c_n are the creation and annihilation operators at site n , t is the hopping amplitude between neighboring sites, h introduces anisotropy in hopping probabilities, and μ_n is the on-site potential with site disorder following a uniform distribution $\mu_n \in [-\Delta/2, \Delta/2]$. Figure 1.3 illustrates the emergent exceptional points (EPs) for a particular set of parameters, despite the model not being inherently \mathcal{PT} -symmetric.

The Hatano-Nelson model exhibits several key phenomena of interest in quantum systems:

- **Anderson Localization:** The model captures Anderson localization, where quantum particles become localized due to disorder, resulting in the absence of diffusive transport⁴⁸.
- **Quantum Phase Transition:** It undergoes a quantum phase transition between localized and delocalized phases as disorder or the ratio of hopping to potential strength is varied, characterized by a critical point separating the phases⁴⁹.

- **Self-duality:** The model exhibits self-duality, a property that links the behavior in both phases, providing insights into its critical behavior⁵⁰.

1.8 Non-Hermiticity and Strong Correlation

Non-Hermitian systems exhibit unique behaviors, including exceptional points (EPs) and novel phenomena when interactions are introduced. This interplay is important in fields like quantum computing and topological phases of matter. Techniques like master equations and renormalization group calculations are often used to study these effects²⁹.

Quantum criticality in PT-symmetric field theories has been explored in models like the sine-Gordon model, while classical systems have shown similar transitions^{12;30–32;51}. Non-Hermitian effects in strongly correlated systems lead to complex phenomena, including the emergence of EPs and non-Hermitian topological phases^{52;53}.

Non-Hermiticity can also contribute to the formation of topological phases, characterized by robust, quantized properties. This interplay adds complexity to the study of quantum materials and their behavior in strongly correlated systems.

1.9 Perturbation Theory for Non-Hermitian Systems

Diagrammatic perturbation theory represents particle interactions through diagrams, with vertex contraction techniques simplifying calculations. Bilinear operators in momentum enable these contractions, while Poorman’s scaling reveals anomalous second-loop corrections. These methods extend to time-dependent scenarios and spectral function computations.

In non-Hermitian systems, time-dependent perturbation theory shows asymmetric corrections to ground states in two- and three-level systems⁵⁴. The concepts of pseudo-Hermiticity and geometric dynamics emphasize the topological nature of these systems¹⁶. Symmetries and unitary evolution are also explored⁵⁵, and Carlström introduces a diagram technique for correlation effects in steady-state non-Hermitian systems⁵⁶.

Pseudo-Hermitian (PHH) operators clarify claims about \mathcal{PT} -symmetry and observables in these systems, with time-independent PHH operators addressing spectral consequences of anti-linear symmetries. Time-dependent PHH operators face challenges related to unitarity and observability, which

Mostafazadeh addresses through a geometric interpretation of the energy operator¹⁶.

Longhi extends time-dependent perturbation theory to non-Hermitian systems, revealing asymmetric transition probabilities under non-Hermitian perturbations⁵⁴. This theory predicts exact transition probabilities, even in strong interactions, and explores phenomena like the breakdown of the adiabatic theorem and exceptional point encircling.

1.10 Single and Two-Impurity Physics in the Anderson Model

The Anderson model serves as a fundamental framework for studying single impurity behavior, particularly regarding the Kondo effect. At low temperatures, conduction electrons form spin-singlet states with the impurity, effectively screening its magnetic moment. This screening phenomenon is characterized by the Kondo temperature (T_K), below which a many-body Kondo singlet emerges due to antiferromagnetic interactions between conduction electrons and the impurity. Physical properties such as magnetic susceptibility and specific heat exhibit universal scaling behavior near T_K , with impurity spin dynamics significantly influenced by conduction electrons, resulting in non-Fermi liquid behavior.

In systems with multiple impurities, direct and indirect interactions mediated by conduction electrons become prominent. Each impurity can individually exhibit the Kondo effect, leading to the formation of localized "Kondo clouds." However, competition between Kondo screening processes introduces complex phenomena, including magnetic phases and intricate ground state configurations. Multi-impurity systems can undergo quantum phase transitions, depending on impurity concentration, temperature, and external magnetic fields. Experimental techniques, such as scanning tunneling microscopy (STM), provide valuable insights into these interactions and emergent behaviors.

Extending the framework, the non-Hermitian Anderson model incorporates complex potentials, resulting in non-unitary dynamics, exceptional points, and non-reciprocal transport. These characteristics break symmetries and modify electronic and transport properties, offering a rich platform to explore dissipation, topological phases, and non-equilibrium dynamics. In this thesis, it is shown that the non-Hermitian Anderson model exhibits many-body level crossings reminiscent of the quantum Zeno effect, with scaling behavior disappearing at the exceptional point. In the two-impurity case,

the destruction of the Kondo effect leads to chaotic renormalization group (RG) trajectories and limit cycles, underscoring the non-Hermitian nature of the system.

1.11 Overview of the thesis

In Chapter 2, we derived an effective Non-Hermitian Anderson model using the quantum master equation and solved the model using Fock space diagonalization, Green's functions techniques, and Auxiliary Particle-Boson methods. Our focus was on the two limits: noninteracting and infinite interaction in the thermodynamic limit. We also considered finite interaction in Fock-Space diagonalization for finite systems.

In Chapter 3, we addressed the issue of incorporating interactions in NHH models using Auxiliary Particle-Boson Methods and derived Callan-Symmanzik Equations to perform RG.

Subsequently, in Chapter 4, we projected the model studied in the earlier chapter 2 to obtain a low energy singly occupied sub-space by preserving the symmetry. This resulted in the spin-spin interaction Hamiltonian. We performed perturbative renormalization calculations on this model to obtain the RG flows for couplings and critical points specific to this model. These calculations were compared with the conformal field theory results.

In Chapter 5, we studied the Hermitian and Non-Hermitian models using non-perturbative techniques, namely finite-U Auxiliary Particle Boson and flow equation approaches. These complemented the perturbative ones to investigate the exceptional points in strong and weak correlation. We derived the scale and response in the new representation.

In Chapter 6, we studied the One and Two-Impurity problem in a topological system with nonlinear perturbation. We derived the Lie algebra for computing RG equations from CFT and compared it with Poorman scaling analysis. We also presented a transport study for these problems.

Bibliography

- [1] P. A. M. Dirac, *The principles of quantum mechanics*, 27 (Oxford university press, 1981).
- [2] J. Von Neumann, *Mathematical foundations of quantum mechanics: New edition* (Princeton university press, 2018).

- [3] J. J. Sakurai, *Advanced quantum mechanics* (Pearson Education India, 2006).
- [4] J. J. Sakurai and E. D. Commins, “Modern quantum mechanics, revised edition,” (1995).
- [5] C. Cohen-Tannoudji, B. Diu, and F. Laloe, *Quantum Mechanics* **1**, 898 (1986).
- [6] C. M. Bender and S. Boettcher, *Phys. Rev. Lett.* **80**, 5243 (1998).
- [7] N. Moiseyev, *Non-Hermitian quantum mechanics* (Cambridge University Press, 2011).
- [8] K. Kawabata, K. Shiozaki, M. Ueda, and M. Sato, *Physical Review X* **9**, 041015 (2019).
- [9] C. M. Bender, S. Boettcher, H. Jones, P. N. Meisinger, and M. Şimşek, *Physics Letters A* **291**, 197 (2001).
- [10] M. Froissart, *Nuovo Cimento (Italy) Divided into Nuovo Cimento A and Nuovo Cimento B* **10** (1959).
- [11] D. Musumbu, H. Geyer, and W. Heiss, *Journal of Physics A: Mathematical and Theoretical* **40**, F75 (2006).
- [12] C. M. Bender and D. W. Darg, *Journal of mathematical physics* **48**, 042703 (2007).
- [13] T. Takanobu, *Non-Hermitian Quantum Field Theory*, Ph.D. thesis, City, University of London (2021).
- [14] A. Mostafazadeh, *Journal of Mathematical Physics* **43**, 205 (2002).
- [15] A. Mostafazadeh, *Journal of Mathematical Physics* **43**, 205 (2002).
- [16] A. Mostafazadeh, *Entropy* **22**, 471 (2020).
- [17] M. S. Swanson, *Journal of Mathematical Physics* **45**, 585 (2004).
- [18] M. S. Swanson, *Path integrals and quantum processes* (Courier Corporation, 2014).
- [19] R. Sohn and M. S. Swanson, *Journal of Physics A: Mathematical and General* **38**, 2511 (2005).

- [20] Y. Ashida, Z. Gong, and M. Ueda, *Advances in Physics* **69**, 249 (2020).
- [21] H. Zhou, C. Peng, Y. Yoon, C. W. Hsu, K. A. Nelson, L. Fu, J. D. Joannopoulos, M. Soljačić, and B. Zhen, *Science* **359**, 1009 (2018).
- [22] T. Stehmann, W. Heiss, and F. Scholtz, *Journal of Physics A: Mathematical and General* **37**, 7813 (2004).
- [23] M. Sakhdari, M. Hajizadegan, Q. Zhong, D. Christodoulides, R. El-Ganainy, and P.-Y. Chen, *Physical review letters* **123**, 193901 (2019).
- [24] M.-A. Miri and A. Alu, *Science* **363**, eaar7709 (2019).
- [25] Ş. K. Özdemir, S. Rotter, F. Nori, and L. Yang, *Nature materials* **18**, 783 (2019).
- [26] M. Król, I. September, P. Oliwa, M. Kdziora, K. Lempicka-Mirek, M. Muszyński, R. Mazur, P. Morawiak, W. Piecek, P. Kula, *et al.*, *Nature Communications* **13**, 5340 (2022).
- [27] W. Heiss, *Journal of Physics A: Mathematical and Theoretical* **45**, 444016 (2012).
- [28] A. Krasnok, N. Nefedkin, and A. Alù, *IEEE Antennas and Propagation Magazine* **63**, 110 (2021).
- [29] M. B. Plenio and P. L. Knight, *Rev. Mod. Phys.* **70**, 101 (1998).
- [30] Y. Ashida, S. Furukawa, and M. Ueda, *Nature communications* **8**, 15791 (2017).
- [31] B.-B. Wei and L. Jin, *Scientific reports* **7**, 7165 (2017).
- [32] O. A. Castro-Alvaredo and A. Fring, *Journal of Physics A: Mathematical and Theoretical* **42**, 465211 (2009).
- [33] J. Schindler, A. Li, M. C. Zheng, F. M. Ellis, and T. Kottos, *Phys. Rev. A* **84**, 040101 (2011).
- [34] C. E. Rüter, K. G. Makris, R. El-Ganainy, D. N. Christodoulides, M. Segev, and D. Kip, *Nature physics* **6**, 192 (2010).
- [35] S. Krinner, T. Esslinger, and J.-P. Brantut, *Journal of Physics: Condensed Matter* **29**, 343003 (2017).

- [36] I. Rotter, Journal of Physics A: Mathematical and Theoretical **42**, 153001 (2009).
- [37] L. Riegger, N. Darkwah Oppong, M. Höfer, D. R. Fernandes, I. Bloch, and S. Fölling, Phys. Rev. Lett. **120**, 143601 (2018).
- [38] M. Kanász-Nagy, Y. Ashida, T. Shi, C. u. u. u. P. m. c. Moca, T. N. Ikeda, S. Fölling, J. I. Cirac, G. Zaránd, and E. A. Demler, Phys. Rev. B **97**, 155156 (2018).
- [39] R. Zhang, Y. Cheng, P. Zhang, and H. Zhai, Nature Reviews Physics **2**, 213 (2020).
- [40] Y. Nishida, Physical Review A **93**, 011606 (2016).
- [41] M. Nakagawa and N. Kawakami, Physical review letters **115**, 165303 (2015).
- [42] J. Bauer, C. Salomon, and E. Demler, Physical review letters **111**, 215304 (2013).
- [43] J. L. Miller, Physics Today **70**, 23 (2017).
- [44] J. Wiersig, Photonics Research **8**, 1457 (2020).
- [45] W. Zhang, X. Ouyang, X. Huang, X. Wang, H. Zhang, Y. Yu, X. Chang, Y. Liu, D.-L. Deng, and L.-M. Duan, Phys. Rev. Lett. **127**, 090501 (2021).
- [46] Z. Li, X.-W. Luo, D. Lin, A. Gharajeh, J. Moon, J. Hou, C. Zhang, and Q. Gu, Phys. Rev. Lett. **131**, 023202 (2023).
- [47] F. Hébert, M. Schram, R. Scalettar, W. Chen, and Z. Bai, The European Physical Journal B **79**, 465 (2011).
- [48] L. G. Molinari, Journal of Physics A: Mathematical and Theoretical **42**, 265204 (2009).
- [49] W. Wang and Z. Ma, Physical Review B **106**, 115306 (2022).
- [50] T. Liu and X. Xia, Physical Review B **105**, 054201 (2022).
- [51] N. Hatano and D. R. Nelson, Physical Review Letters **77**, 570 (1996).
- [52] H. Gao, H. Xue, Q. Wang, Z. Gu, T. Liu, J. Zhu, and B. Zhang, Physical Review B **101**, 180303 (2020).

- [53] C. Wu, N. Liu, G. Chen, and S. Jia, Physical Review A **106**, 012211 (2022).
- [54] S. Longhi and G. Della Valle, Annals of Physics **385**, 744 (2017).
- [55] P. D. Mannheim, Philosophical Transactions of the Royal Society A: Mathematical, Physical and Engineering Sciences **371**, 20120060 (2013).
- [56] J. Carlström, Physical Review Research **2**, 013078 (2020).

Chapter 2

Kondo effect in \mathcal{PT} -symmetric Anderson model with Rashba SO coupling

The non-interacting and non-Hermitian, parity-time (\mathcal{PT})-symmetric Anderson model exhibits an exceptional point (EP) at a non-Hermitian coupling $g = 1$, which remains unrenormalized in the presence of interactions (Lourenco et al, Phys. Rev. B **98**, 085126 (2018)), where the EP was shown to coincide with the quantum critical point (QCP) for Kondo destruction. In this work, we consider a quantum dot hybridizing with metallic leads having Rashba spin-orbit coupling (λ). We show that for a non-Hermitian hybridization, λ can renormalize the exceptional point even in the non-interacting case, stabilizing \mathcal{PT} -symmetry beyond $g = 1$. Through exact diagonalization of a zero-bandwidth, three-site model, we show that the quantum critical point and the exceptional point bifurcate, with the critical point for Kondo destruction at $g_c = 1$, and the exceptional coupling being $g_{EP} > 1$ for all $U \neq 0$ and $\lambda \geq 0$; $\lambda \neq U/2$. On the line $\lambda = U/2$, the critical point and the EP again coincide at $g_c = g_{EP} = 1$. The full model with finite bandwidth leads is investigated through the Auxiliary Particle-boson approach, using which we show that, in the strong coupling regime, λ and interactions co-operate in strongly reducing the critical point associated with Kondo destruction, below the $\lambda = 0$ value.

*This work has been published in PhysRevB.106.075113
Copyright (2022) by American Physical Society*

2.1 Introduction

Conventional quantum theory postulates that every physical observable may be represented by a Hermitian operator since Hermiticity ensures that the eigenvalues of the corresponding operators would be real. A generalization to the existing quantum postulates can be made with consideration of \mathcal{PT} -symmetric orthonormal set of eigenstates^{1;2}. These states preserve the norm and form a complete set which also allows for an unambiguous definition of expectation of physical observables. Physically, non-Hermitian models represent open quantum systems³⁻⁵. These models can exhibit eigenvalue degeneracies at certain values of non-Hermitian parameters, called exceptional points (EPs), which correspond to quantum phase transitions of the level-crossing type. Concomitantly, these points also show a breakdown of \mathcal{PT} -symmetry. Beyond such exceptional points, the eigenvalues develop finite imaginary parts, and the norm of the corresponding eigenvector is not conserved. Hence, probabilities of eigenstates oscillate with a decay factor as a function of non-Hermitian strength. The emergence of imaginary eigenvalues may be associated with a loss of bound states and a crossover to scattering states of open quantum systems⁶⁻⁸.

Many theoretical studies of non-Hermitian Hamiltonians have been motivated by experiments that realize such models in open systems with balanced gain and loss^{3;9-12}. Recent experiments in cold atoms have observed level crossing-like transitions even though many-body interactions are present in the system. The observations of gain and loss due to the depletion of atoms have been attributed to the phenomenon of continuous quantum Zeno effect¹³⁻¹⁶. Conventional Kondo-type systems such as impurities coupled to baths have been realized in controlled environments like atoms in harmonic traps¹⁷⁻²², where the small number of excited states mimic magnetic impurities and the atoms in the ground state provide the bath. In experiments where Rashba-type spin-orbit coupling is generated synthetically, induced artificial magnetic fields break parity and time reversal symmetries. It is important to note that when both of these symmetries break, $SU(2)$ symmetry will also be violated. Exceptional points may also lead to exceptionally sensitive sensors^{23;24} since for an EP of order n , any perturbation of strength ϵ leads to a splitting of the levels (Δ_L) that is proportional to the n^{th} root of ϵ , which is in contrast to that of a diabolic point where $\Delta_L \sim \epsilon$.

Open quantum systems are generally investigated through master equation techniques with various kinds of noise terms as discussed by Plenio and Knight²⁵. Quantum criticality in \mathcal{PT} -symmetric effective field theories have been studied in the sine-Gordon model²⁶ which has been shown to describe

the transition between a Mott-insulator to a Tomonaga-Luttinger liquid²⁷. The \mathcal{PT} -symmetry breaking transition has also been studied in a classical system, where critical behavior, similar to that found in quantum systems, has been observed through numerical calculations²⁸. Classical spin chains with imaginary fields also exhibit similar phase transitions²⁹. Another work in interacting quantum many-body systems discusses a novel way of doing path integrals for such systems to capture the Anderson localisation transition with non-Hermitian disorder³⁰.

Lourenco et al³¹ considered a real-space parity-time symmetric model comprising a correlated impurity connected to left and right leads through a non-hermitian hybridization coupling. They have employed perturbative renormalization group (RG) approach to investigate the exceptional points in the strong coupling regime. The non-interacting exceptional point was shown to coincide with the critical point for Kondo destruction and also found to remain invariant under RG flow. Nakagawa et al³² have considered a non-Hermitian (NH) Kondo model that is not \mathcal{PT} -symmetric. It is an extension of the standard Kondo model to one with complex spin exchange couplings and the justification for these non-Hermitian terms is given through Lindbladian dynamics. Standard two-loop poorman RG yields a phase transition, as seen through RG reversion, which occurs at a very small value of the complex coupling since there is no symmetry and there is a local-moment type fixed point. These results have been further supported through Bethe ansatz calculations.

Our interest is to explore exceptional and quantum critical points in a non-hermitian quantum many-body system subjected to a decohering term such as the Rashba spin-orbit coupling (RSOC). The interplay of RSOC and interactions has been investigated extensively in the Hermitian case using RG methods such as poorman scaling and numerical renormalization group^{33–37}. Other special, but Hermitian, cases such as an impurity in graphene, nanoribbons, and an impurity in a topological insulator have been considered^{37;38} and through a mapping onto the pseudogap Anderson model, a quantum phase transition has been shown to occur. The SO coupling, particularly the Rashba type, breaks parity symmetry in conventional models represented by an angular momentum basis. Concomitantly, this also leads to the generation of \mathcal{PT} symmetric channels and hence a Dzyaloshinskii-Moriya (DM) interaction in the effective model of impurity subspace, which leads us to consider interesting possibilities. If we consider NH coupling to these \mathcal{PT} channels, there is an emergent parity-time breaking DM interaction which may modify the exceptional points of the NH model. In the conventional Hermitian case, closed systems may exhibit phase transitions as a function of SO interactions only for some special lattices like a honeycomb lattice as

seen in e.g. Bi_2Se_3 and Bi_2Te_3 . However, in NH systems, one can expect phase transitions driven by the imaginary interaction generically irrespective of the lattice. With the prospect of the above possibilities, we ask the following questions: (a) Can RSOC renormalize the exceptional point in the non-interacting case? (b) What is the combined effect of interactions and RSOC on Kondo destruction and the exceptional points? For investigating these, we have considered a single level quantum dot connected to a bath which has RSOC (which is important for realizing \mathcal{PT} symmetry^{17;39}). The model is also motivated by recent experiments¹⁷ where singlet and triplet scales in open conditions have been measured.

We set up the full, non-Hermitian, single impurity Anderson model, and establish \mathcal{PT} -symmetry, first in a simplified zero-bandwidth, three-site model, and subsequently in the full model. Using exact diagonalization, we show the emergence of distinct quantum critical and exceptional points in the three-site model. Subsequently, the full model in the non-interacting case is solved through exact diagonalization, Green's functions methods, and total energy calculations. In order to understand the effect of interactions, we utilise the Auxiliary Particle-boson method, and show the co-operative interplay of non-Hermitian coupling and RSOC (λ) in inducing Kondo destruction. We show that a finite λ protects \mathcal{PT} -symmetry by pushing the exceptional point beyond the $\lambda = 0$ value. In the strong coupling regime, a quantum phase transition occurs between a Kondo screened phase and an unscreened moment at a critical non-Hermitian coupling $g_c = 1$ for $\lambda = 0$. With increasing λ , the critical coupling decreases monotonically showing a strong renormalization of the QCP due to RSOC.

The chapter is organized as follows: The following section introduces the model and formalism. Section III introduces a simplified three-site, zero-bandwidth model using which \mathcal{PT} -symmetry is analyzed and exceptional points are found in closed form. Through exact diagonalization of the interacting three-site model in Fock space, we show the bifurcation of the exceptional point and the quantum critical point. We present the results and discussion for the full, finite bandwidth leads, model in section IV, and conclude in the final section with a short discussion and open questions.

2.2 Model and formalism

As mentioned in the introduction, we have chosen to work with a single impurity Anderson model (SIAM) comprising a single non-degenerate level

quantum dot system connected to an electron reservoir, for which the Hamiltonian, H , is given in standard notation as

$$H_{SIAM} = H_0 + H_d + H_{hyb}, \quad (2.1)$$

where the two-dimensional conduction band reservoir may be represented by $H_0 = \sum_{\mathbf{k}\sigma} \epsilon_{\mathbf{k}} c_{\mathbf{k}\sigma}^\dagger c_{\mathbf{k}\sigma}$ and the isolated quantum dot is given by $H_d = \sum_{\sigma} \epsilon_d d_{\sigma}^\dagger d_{\sigma} + U n_{d\uparrow} n_{d\downarrow}$. The hybridization term is given by $H_{hyb} = \sum_{\mathbf{k}\sigma} V_{\mathbf{k}\sigma} (c_{\mathbf{k}\sigma}^\dagger d_{\sigma} + \text{h.c.})$.

The presence of spin-orbit coupling in a two-dimensional conduction electron bath has been considered previously by several groups^{34–37}. In this work, we have investigated the interplay of Rashba-type spin-orbit coupling (SOC) with the presence of non-Hermitian, but PT-symmetric terms in the Hamiltonian. Defining $\psi_{\mathbf{k}} = (c_{\mathbf{k}\uparrow} \ c_{\mathbf{k}\downarrow})^T$, the SOC term is given by:

$$\begin{aligned} H_{\text{RSO}} &= \lambda \sum_{\mathbf{k}} \psi_{\mathbf{k}}^\dagger (\mathbf{k} \times \vec{\sigma})_z \psi_{\mathbf{k}} \\ &= \lambda \sum_{\mathbf{k}} k \left(e^{i\theta_{\mathbf{k}}} c_{\mathbf{k}\uparrow}^\dagger c_{\mathbf{k}\downarrow} + \text{h.c.} \right) \end{aligned} \quad (2.2)$$

where $k = |\mathbf{k}|$ and $\theta_{\mathbf{k}} = \tan^{-1}(-k_x/(-k_y))$. The action of the parity operator is:

$$\mathcal{P} : \sigma_x \psi_{\mathbf{k}} \implies c_{\mathbf{k}\uparrow} \rightarrow c_{\mathbf{k}\downarrow}, \quad (2.3)$$

and using the above, we see that H_{RSO} is not invariant under parity transformation.

The conduction band terms, namely H_0 and H_{RSO} may be combined³⁴, which leads to the emergence of chiral conduction bands. This is accomplished using an angular momentum expansion for the conduction band operators, followed by a unitary transformation as:

$$c_{\mathbf{k}\sigma} = c_{k_x k_y \sigma} = \frac{1}{\sqrt{2\pi k}} \sum_{m=-\infty}^{\infty} c_{km\sigma} \exp(-im\theta_{\mathbf{k}}), \quad (2.4)$$

where $k = |\mathbf{k}|$. The inverse transform is defined as $c_{km\sigma} = \sqrt{\frac{k}{2\pi}} \int_0^{2\pi} d\theta_{\mathbf{k}} c_{\mathbf{k}\sigma} e^{im\theta_{\mathbf{k}}}$. Substituting the above expansion³⁴ (equation 2.4) into the Hamiltonian, and assuming an isotropic dispersion, which depends only on $k = |\mathbf{k}|$, such that $\epsilon_{\mathbf{k}} = \epsilon_k$, the H_0 becomes:

$$H_0 = \sum_{\mathbf{k}\sigma} \epsilon_{\mathbf{k}} c_{\mathbf{k}\sigma}^\dagger c_{\mathbf{k}\sigma} = \sum_{km\sigma} \tilde{\epsilon}_k c_{km\sigma}^\dagger c_{km\sigma} \quad (2.5)$$

where $\tilde{\epsilon}_k = \epsilon_k/k$. Further, with the same transformation, the RSO term transforms to:

$$H_{\text{RSO}} = \lambda \sum_{km} \left(c_{km\uparrow}^\dagger c_{k\,m+1\downarrow} + \text{h.c.} \right) \quad (2.6)$$

In Appendix-C, we develop a non-Hermitian Anderson model Hamiltonian by combining the above terms and a few extra terms invoking Lindladian dynamics, and the resulting Hamiltonian has the following form:

$$\begin{aligned} H = & \sum_{kh\eta} \tilde{\epsilon}_{kh} c_{kh\eta}^\dagger c_{kh\eta} + \sum_{k\eta h} X_{k\eta h} \left(c_{k\eta h}^\dagger d_h + \text{h.c.} \right) \\ & + \epsilon_d \sum_h n_{dh} + U n_{d+} n_{d-} \end{aligned} \quad (2.7)$$

where h is a 'chiral' quantum number and can be thought of as a pseudospin index, $\eta \in \{L, R\}$ is the channel index, which is, in fact, the $j_m = m + \sigma$ index in the angular momentum representation. The hybridization coefficients are $X_{kLh} = \sqrt{2}|X_k|e^{i\phi_k}$ and $X_{kRh} = -hX_{kLh}^*$. The model obtained in the rotated basis above has the interpretation of a dot connected to two leads, and appears very similar to the *real-space* model considered by Lourenco et al³¹. The main difference is that the real-space model had non-Hermitian coupling to just two sites directly connected to the dot. In our case, the hybridization elements, $X_{k\eta}$, being complex, render the Hamiltonian non-hermitian when $\phi_k \neq 0, \pi$ and for all k .

Before we investigate the full model in equation 2.7, we have considered a three-site, zero-bandwidth model with a very similar structure to equation 2.7. We will see that the symmetry class, exceptional points etc can be obtained easily and exactly, and hence is very instructive. Furthermore, generalizing the symmetry analysis to the full model will be straightforward.

2.3 Three-site, zero bandwidth model in the chiral basis

Consider simplifying the above model (equation 2.7), where single sites replace the leads with two orbitals each.

$$\begin{aligned} H = & \sum_{h\eta} \epsilon_h c_{h\eta}^\dagger c_{h\eta} + \sum_{\eta h} X_{\eta h} \left(c_{\eta h}^\dagger d_h + \text{h.c.} \right) \\ & + \epsilon_d \sum_h n_{dh} + U n_{d+} n_{d-} \end{aligned} \quad (2.8)$$

where $\epsilon_h = \epsilon + h\lambda$, $X_{Lh} = Ve^{i\phi}$, $X_{Rh} = -hX_{Lh}^*$ and V is a real number ($V \in \mathcal{R}$). The exceptional points may be found in terms of ϕ or a coupling g defined as the ratio of the imaginary part to the real part of the hybridization, which is simply $g = \tan \phi$. Using $\psi = (c_{L+} \ c_{R+} \ d_+ \ d_- \ c_{L-} \ c_{R-})^T$, we can write the above Hamiltonian as

$$H = \psi^\dagger \mathcal{H} \psi + U n_{d+} n_{d-} \quad (2.9)$$

where

$$\mathcal{H} = \begin{pmatrix} \epsilon_+ & 0 & X_{L+} & 0 & 0 & 0 \\ 0 & \epsilon_+ & X_{R+} & 0 & 0 & 0 \\ X_{L+} & X_{R+} & \epsilon_d & 0 & 0 & 0 \\ 0 & 0 & 0 & \epsilon_d & X_{L-} & X_{R-} \\ 0 & 0 & 0 & X_{L-} & \epsilon_- & 0 \\ 0 & 0 & 0 & X_{R-} & 0 & \epsilon_- \end{pmatrix} \quad (2.10)$$

This matrix is block-diagonal, since the chiral channels do not mix in the absence of interaction, i.e for $U = 0$. It is also non-Hermitian, but symmetric, i.e $\mathcal{H}^\dagger \neq \mathcal{H}$, but $\mathcal{H}^T = \mathcal{H}$. Now, we explore the non-interacting case first, before moving on to $U \neq 0$.

2.3.1 Non-interacting case: $U = 0$

Keeping $X_{\eta h}$ general, we want to find conditions so that the eigenvalues are real. The eigenvalues of the above Hamiltonian (Λ) (for the special case of $\epsilon = \epsilon_d = 0$ and $U = 0$), are given by:

$$\begin{aligned} \Lambda &= \pm \lambda \\ \Lambda^2 - (\pm \lambda)\Lambda - (X_{L\pm}^2 + X_{R\pm}^2) &= 0 \end{aligned} \quad (2.11)$$

Thus the condition that determines real eigenvalues is

$$\cos 2\phi \geq -\frac{\lambda^2}{8V^2} \quad (2.12)$$

which reduces to $\phi \leq \pi/4$ in the absence of RSOC, while if $\lambda \neq 0$, the condition is as given above, so RSOC stabilizes \mathcal{PT} -symmetry by increasing the range of ϕ to beyond $\pi/4$. And if $\lambda \geq 2\sqrt{2}V$, \mathcal{PT} -symmetry can not be broken for any ϕ . Thus, for $\lambda \leq 2\sqrt{2}V$, the exceptional point is given by,

$$\phi_{EP} = \pi/4 + \frac{1}{2} \sin^{-1} \frac{\lambda^2}{8V^2}, \quad (2.13)$$

or equivalently in terms of g , the EP is given by

$$g_{EP} = \tan \phi_{EP} = \sqrt{\frac{1 + \lambda^2/8V^2}{1 - \lambda^2/8V^2}}. \quad (2.14)$$

So, the minimal condition necessary for real eigenvalues is $X_{Rh}^2 + X_{Lh}^2 \in \mathcal{R}$ for $h = \pm$. From an inspection of the Hamiltonian, a mapping that yields $\mathcal{H} \rightarrow \mathcal{H}^\dagger$ is

$$\psi = \begin{pmatrix} c_{L+} \\ c_{R+} \\ d_+ \\ d_- \\ c_{L-} \\ c_{R-} \end{pmatrix} \rightarrow \begin{pmatrix} -c_{R+} \\ -c_{L+} \\ d_+ \\ d_- \\ c_{R-} \\ c_{L-} \end{pmatrix} \quad (2.15)$$

This implies that the matrix representation of the metric operator, η , that should yield this transformation should be

$$\eta = \begin{pmatrix} 0 & -1 & 0 & 0 & 0 & 0 \\ -1 & 0 & 0 & 0 & 0 & 0 \\ 0 & 0 & 1 & 0 & 0 & 0 \\ 0 & 0 & 0 & 1 & 0 & 0 \\ 0 & 0 & 0 & 0 & 0 & 1 \\ 0 & 0 & 0 & 0 & 1 & 0 \end{pmatrix} \quad (2.16)$$

such that $\eta^2 = \mathbf{I}$, and thus $\eta^\dagger = \eta^{-1} = \eta$, which is unitary. Indeed, we find that

$$\eta \mathcal{H} \eta^{-1} = \mathcal{H}^\dagger \quad (2.17)$$

implying that H is pseudohermitian. Since \mathcal{H} is also symmetric, i.e $\mathcal{H}^T = \mathcal{H}$, the pseudohermiticity is identical to \mathcal{PT} -symmetry⁴⁰. We can also make a statement about the left (Ψ_L) and right eigenvectors (Ψ_R), as follows. Since $\mathcal{H}\Psi_{\alpha R} = E_\alpha \Psi_{\alpha R}$, where E_α is the α^{th} eigenvalue, and given the property 2.17, we can see that

$$\mathcal{H}^\dagger(\eta\Psi_{\alpha R}) = E(\eta\Psi_{\alpha R}) \quad (2.18)$$

and hence the left eigenvector corresponding to the complex conjugate eigenvalue E_α^* would be $\Psi_{\alpha L} = \eta\Psi_{\alpha R}$. We can also construct the metric operator in the second quantized form, as

$$\begin{aligned} \hat{\eta} &= \psi^\dagger \eta \psi \\ &= - \left(c_{R+}^\dagger c_{L+} + \text{h.c} \right) + \left(c_{R-}^\dagger c_{L-} + \text{h.c} \right) \\ &\quad + \left(d_+^\dagger d_+ + d_-^\dagger d_- \right) \end{aligned} \quad (2.19)$$

For the Hamiltonian to be pseudoHermitian, it is easy to see from equation 2.17 that the condition to be satisfied is

$$[H + H^\dagger, \hat{\eta}] = 0 \quad (2.20)$$

and indeed we see that this condition is satisfied as shown below.

$$\begin{aligned} [H, \hat{\eta}] = & (X_{L+} + X_{R+}) \left((c_{L+}^\dagger + c_{R+}^\dagger) d_+ - \text{h.c} \right) \\ & + (X_{L-} - X_{R-}) \left((c_{L-}^\dagger - c_{R-}^\dagger) d_- - \text{h.c} \right) \end{aligned} \quad (2.21)$$

With the above result, we see that the condition for pseudohermiticity (equation 2.20) is satisfied since

$$\text{Re}(2X_{Lh} + X_{R+} - X_{R-}) = 0 \quad (2.22)$$

Thus, with the combination of pseudohermiticity and symmetric form, we establish \mathcal{PT} -symmetry.

2.3.2 Interacting case: $U > 0$

We perform exact diagonalization of the three-site model for $U \neq 0$ (equation 2.8) in the Fock space to get an insight into the combined effect of U , λ and non-hermiticity on the phase diagram. The exceptional point is found as usual from the emergence of a non-zero imaginary part in the eigenvalues of the Hamiltonian, while a quantum phase transition would be signaled by a crossing of the real-valued ground state and the first excited state eigenvalues.

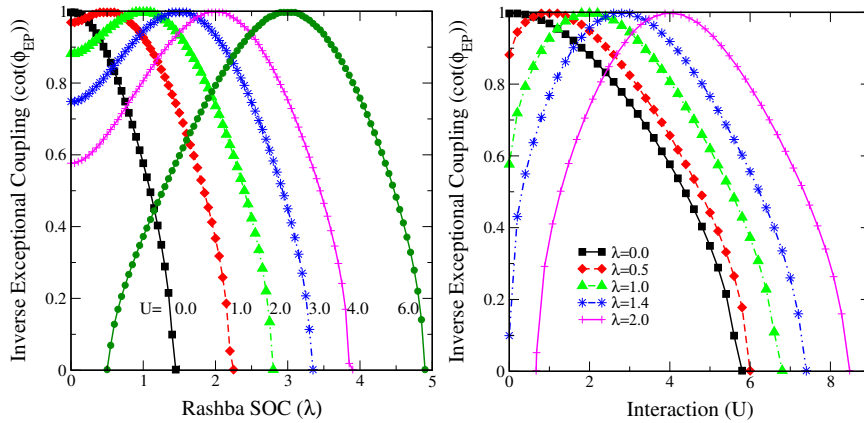


Figure 2.1: The inverse exceptional coupling, $g_{EP}^{-1} = \cot(\phi_{EP})$ as a function of (left panel) λ for various U values and (right panel) U for various λ values.

We have seen in the non-interacting case (refer equation 2.12) that the spin-orbit coupling stabilizes \mathcal{PT} -symmetry, in the sense that ϕ_{EP} increases from $\pi/4$ at $\lambda = 0$ to $\pi/2$ at $\lambda_c = 2\sqrt{2}V$ beyond which the exceptional point does not arise, implying that the \mathcal{PT} -symmetry does not break. As mentioned before, the non-Hermitian coupling at the exceptional point defined as $g_{EP} = \tan(\phi_{EP})$ increases from 1 to ∞ . Now, we can investigate the exceptional points in the presence of U and λ .

The top panel of figure 2.1 shows the inverse exceptional coupling, i.e $g_{EP}^{-1} = \cot(\phi_{EP})$ as a function of λ for various U values, while the bottom panel shows the same as a function of U for various λ values. We see that for $U = 0$, the exceptional points shift to higher values ($\phi_{EP} > \pi/4$ or $g > 1$) upon increasing λ , which is consistent with that found in the non-interacting case. The effect of finite interactions is to enhance the critical λ beyond which \mathcal{PT} -symmetry is violated. Eventually for large U , the \mathcal{PT} -symmetry is unbroken upto a critical λ . Interestingly, we notice that at $\lambda = U/2$, the exceptional point reverts back to $\phi_{EP} = \pi/4$, which is just the same as the non-interacting value, thus negating the effect of λ and U completely. The implication is that, for a fixed U , if $\lambda = U/2$, the exceptional point is the same as that in the non-interacting, and zero SOC case, and is hence unrenormalized. The bottom panel shows a similar behavior as the top panel, with the roles of U and λ reversed, and again the $\lambda = U/2$ points are seen to be special unrenormalized points.

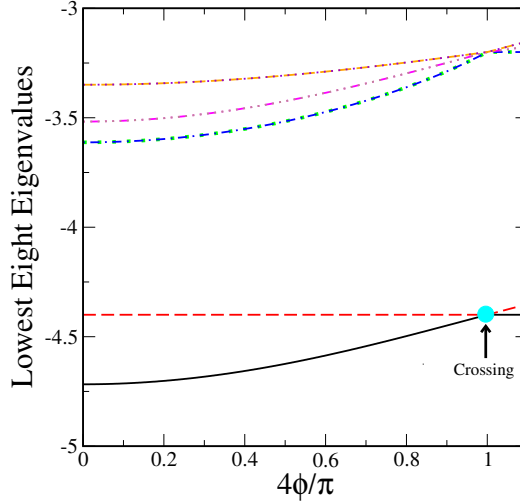


Figure 2.2: The lowest eight eigenvalues as a function of the non-Hermiticity parameter, ϕ , for $U = 4.0$, $\lambda = 1.2$, and $\epsilon_d = -U/2$. The cyan dot shows the first crossing of the ground state and the first excited state, and is thus identified as the quantum critical point.

In figure 2.2, we have shown the eight lowest eigenvalues as a function of ϕ for $U = 4.0$, $\epsilon_d = -U/2$, $\lambda = 1.2$, in the \mathcal{PT} -symmetry unbroken regime. The ground state, being adiabatically continuous with the hermitian case ($\phi = 0$) is identified as the Kondo screened phase. This is also confirmed by examining the ground state eigenvector in the Fock space. The first crossing of the ground state and the first excited state eigenvalue, identified as the quantum critical point of the many-body level crossing type, remains at $\phi = \pi/4$ or $g = 1$ for all $U \neq 0$ and any λ . We have confirmed through an eigenstate analysis also that the QCP represents a transition from a Kondo-screened singlet phase to a local moment phase.

The exceptional point phase diagram in the $U - \lambda$ plane is shown in figure 2.3. The colour represents inverse exceptional coupling, g_{EP}^{-1} . The extent of renormalization of the exceptional point due to interactions and SOC is indicated by the darkness of the colour. As mentioned above, the solid circles represent the line $\lambda = U/2$, where the exceptional point is completely unrenormalized with respect to $\lambda = U = 0$. Finally, in the $U - \lambda$ plane,

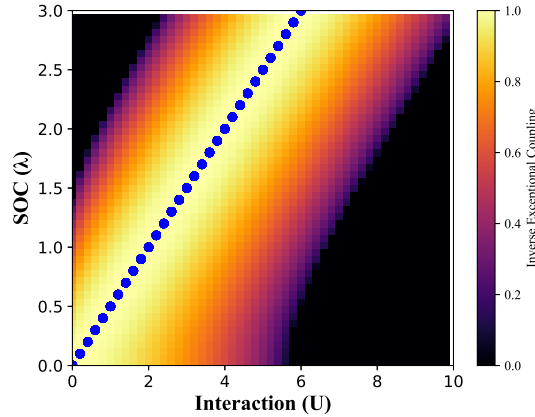


Figure 2.3: The exceptional point phase diagram for the three-site model in the interacting regime is shown. The color bar shows the inverse exceptional coupling. The solid circles represent the line $\lambda = U/2$, on which the exceptional point remains at $\phi = \pi/4$ or $g = 1$. Everywhere else the exceptional point is strongly renormalized by interactions and SOC. In the dark regions (low U , high λ and high U , low λ), the inverse exceptional coupling vanishes, implying $g_{EP} \rightarrow \infty$, and hence \mathcal{PT} -symmetry is never violated.

the Kondo destruction critical point for all $U \neq 0$ and any λ coincides with the exceptional point for $\lambda = U/2$, while the exceptional point gets strongly renormalized away from this line, and does not even exist for $U/\lambda \gg 1$ and

$$U/\lambda \ll 1.$$

2.4 Full model: Results and discussion

Taking cues from the solution of the three-site model, we can now explore the eigenvalues, and the symmetry of the full model, i.e equation 2.7. Again, using the representation $\psi_k = (c_{kL+} \ c_{kR+} \ d_+ \ d_- \ c_{kL-} \ c_{kR-})^T$, we can write the Hamiltonian of equation 2.7 as

$$H = \sum_k \psi_k^\dagger \mathcal{H}_k \psi_k + \epsilon_d \sum_h n_{dh} + U n_{d+} n_{d-} \quad (2.23)$$

where

$$\mathcal{H}_k = \begin{pmatrix} \epsilon_{kL+} & 0 & X_{kL+} & 0 & 0 & 0 \\ 0 & \epsilon_{kR+} & X_{kR+} & 0 & 0 & 0 \\ X_{kL+} & X_{kR+} & 0 & 0 & 0 & 0 \\ 0 & 0 & 0 & 0 & X_{kL-} & X_{kR-} \\ 0 & 0 & 0 & X_{kL-} & \epsilon_{kL-} & 0 \\ 0 & 0 & 0 & X_{kR-} & 0 & \epsilon_{kR-} \end{pmatrix} \quad (2.24)$$

We observe from the form of the matrix above that the metric operator can be generalized from the case of the three-site model as

$$\begin{aligned} \hat{\eta} &= \sum_k \psi_k^\dagger \eta \psi_k \\ &= \sum_k \left[- \left(c_{kR+}^\dagger c_{kL+} + \text{h.c} \right) + \left(c_{kR-}^\dagger c_{kL-} + \text{h.c} \right) \right] \\ &\quad + \left(d_+^\dagger d_+ + d_-^\dagger d_- \right) \end{aligned} \quad (2.25)$$

which will again yield

$$[H + H^\dagger, \hat{\eta}] = 0, \quad (2.26)$$

thus showing that the Hamiltonian is pseudohermitian even for $U \neq 0$, and since $H = H^T$, we can identify the symmetry as being equivalent to \mathcal{PT} symmetry.

2.4.1 Exact Diagonalization of the non-interacting model

For $U = 0$, $\epsilon_{kLh} = \epsilon_{kRh}$ and the hybridization elements assumed to be k -independent, the characteristic polynomial that yields the eigenvalues is found to be:

$$(\epsilon_d - \Lambda) - \sum_k \frac{(X_{Lh}^2 + X_{Rh}^2)}{\epsilon_{kh} - \Lambda} = 0 \quad \text{for } h = \pm. \quad (2.27)$$

Thus the possibility of real eigenvalues exists if $(X_{Lh}^2 + X_{Rh}^2) \in \mathcal{R}$. However, equation 2.27 is not suitable (numerically) to find all the eigenvalues, especially if some of these are complex, hence we create the Hamiltonian matrix for the two chiral channels separately (since they do not mix for $U = 0$) using equation 2.23 and the basis, $\psi_h = (c_{k_1 Lh} \ c_{k_1 Rh} \ \dots \ c_{k_N Lh} \ c_{k_N Rh} \ d_h)^T$. Using a uniformly spread sequence of N ϵ_k values between $-D$ to D , we get a Hamiltonian matrix of size $N + 1$. We then directly diagonalize the Hamiltonian matrix using numerical diagonalization methods (HTDQLS[?]) for general complex symmetric, but non-Hermitian matrices. In practice, we have used $D = 1$ and have tested our results for various sizes of the Hamiltonian matrices, and the results reported here (figure 2.4) are for $N = 100$ values of ϵ_k . The phase diagram for $U = 0$ in the $\phi - \lambda$ plane is shown in figure 2.4.

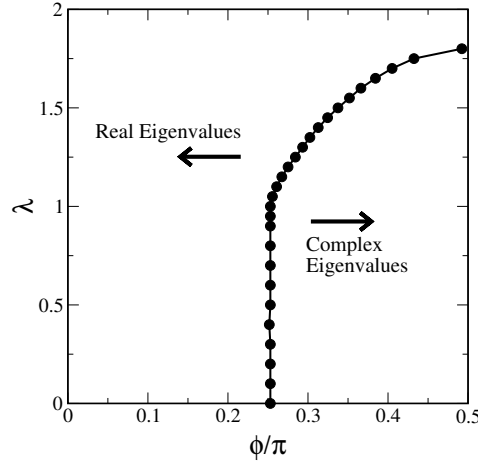


Figure 2.4: Phase diagram in the $\phi - \lambda$ plane is shown for the non-interacting case ($U = 0$). The solid circles represent exceptional points, where certain real eigenvalues coalesce and complex conjugate eigenvalues emerge.

The solid curve is the line of exceptional points, which shows that increasing spin-orbit coupling enhances the range of ϕ within which real eigenvalues are obtained, and hence SOC stabilizes \mathcal{PT} symmetry. The exceptional point for $\lambda = 0$ is at $\phi = \pi/4$. It is interesting to see that for even an infinitesimal $\phi > \pi/4$, the SOC needed to restore \mathcal{PT} symmetry is $\lambda \sim \mathcal{O}(1)$. This is in contrast to the three site model where the line of exceptional points was given by $\phi - \pi/4 \propto \lambda^2$ for $\lambda \rightarrow 0$. The reason for the discrepancy is that the full model has a conduction band, and we find that the minimum spin-orbit coupling needed to restore \mathcal{PT} symmetry is of the order of bandwidth, which is $\mathcal{O}(1)$ in the present case, and was zero in the three-site model.

2.4.2 Spectral sum rule in the $U = 0$, non-interacting case

Since the model is PT-symmetric, and the eigenvalues of the Hamiltonian are real in a finite range of the parameter space, the time evolution of operators will be unitary, for $\phi < \phi_{EP}$, where the latter represents the exceptional point. Hence, we can use the equation of motion (EoM) method to find the retarded Green's functions ($G_B^A(t, t') = -i\langle \Psi_G^L | \{A_H(t), B_H^\dagger(t') | \Psi_G^R \rangle \theta(t - t')$) in the unbroken \mathcal{PT} -symmetry regime⁴¹. The Green's function is defined with respect to the left and right (L/R) eigenstates of the full Hamiltonian. The equations of motion are given by

$$\begin{aligned} \omega^+ G_B^A(\omega) &= \langle \{A, B\} \rangle + G_B^{[A, H]-}(\omega) \\ &= \langle \{A, B\} \rangle + G_{[H, B]-}^A(\omega) \end{aligned} \quad (2.28)$$

In order to gain insight into the interplay of PT-symmetry and SOC, we investigate the non-interacting case ($U = 0$). We first find the retarded Green's function for the dot operators in the chiral basis, i.e G_{hh}^{dd} . The following equation is obtained for the dot Green's functions,

$$G_{hh}^{dd} = [\omega^+ - \epsilon_d - \Gamma_h(\omega)]^{-1} \quad (2.29)$$

where the hybridization function is given as

$$\Gamma_h(\omega) = \sum_k \frac{X_{kLh}^2 + X_{kRh}^2}{\omega^+ - \tilde{\epsilon}_{kh}} \quad (2.30)$$

Using $X_{Lk+} = X_{Lk-} = |X_k|e^{i\phi_k}$, so that $X_{kR+} = -|X_k|e^{-i\phi_k} = -X_{kR-}$, the diagonal dot Green's functions are obtained as (for $U = 0$):

$$G_{hh}^{dd}(\omega) = \frac{1}{\omega^+ - \epsilon_d - 2 \sum_k \frac{|X_k|^2 \cos(2\phi_k)}{\omega^+ - \tilde{\epsilon}_{kh}}} \quad (2.31)$$

The Green's function is causal, as long as either (i) $\phi_k \leq \pi/4$, $\forall k$ or (ii) if the imaginary part of hybridization is zero. The spectral density is guaranteed to be positive definite in this regime. Interestingly, although the Hamiltonian is non-Hermitian for $\phi_k \neq 0$, the Green's function, being exactly the same as for a single impurity Anderson model with a renormalized hybridization ($V_k^2 \rightarrow 2|X_k|^2 \cos(2\phi_k)$), is fully causal, and has the same analytic structure of the usual Green's functions. We also see that the eigenvalue equation (2.27) is identical to the equation obtained for the zeroes of the denominator of

the Green's function (2.31). This is not surprising, since the non-interacting Green's function is given by $\hat{G} = [\omega^+ \mathbf{1} - \hat{H}]^{-1}$.

Taking $X_k = X_0$ and $\phi_k = \phi$ to be independent of k , the k -sum in the hybridization can be converted to a density of states integral, which is then given by

$$\Gamma_h(\omega) = \Gamma_0 \cos(2\phi_0) H_T[\omega^+ - h\lambda], \quad (2.32)$$

where $\Gamma_0 = 2X_0^2$ and $H_T[z]$ is the Hilbert transform defined by

$$H_T[z] = \int_{-\infty}^{\infty} d\epsilon \frac{\rho_0(\epsilon)}{z - \epsilon}. \quad (2.33)$$

The exact diagonalization calculation required us to choose energy values, ϵ_k , distributed in a certain way, and for convenience, we chose a uniform distribution. The density of states accordingly for the Green's function calculation has been chosen to be a flat band, namely $\rho_0(\epsilon) = \sum_k \delta(\epsilon - \tilde{\epsilon}_{kh}) = \theta(D - |\epsilon_{kh}|)/(2D)$, for which the Hilbert transform may be obtained in a straightforward way as:

$$H_{Th}[\omega^+] = \frac{1}{2D} \ln \left| \frac{\omega - h\lambda + D}{\omega - h\lambda - D} \right| - i \frac{\pi}{2D} \theta(D - |\omega - h\lambda|) \quad (2.34)$$

The spectral function is given by

$$D_h(\omega) = -\frac{1}{\pi} \text{Im} G_{hh}^{dd} = -\frac{1}{\pi} \text{Im} (\omega^+ - \epsilon_d - \Gamma_h(\omega))^{-1}. \quad (2.35)$$

For a representative set of parameters $\Gamma_0 = 1/4$, we show the spectral function of the chiral index summed Green's function ($G_d = 0.5 \sum_h G_{hh}^{dd}$) in figure 2.5. The numbers mentioned in the legends are values of the SOC(λ). Both panels show the dot density of states (DoS) in the non-Hermitian case of $\phi = 0.2\pi < \pi/4$ (top) and $\phi = \pi/3 > \pi/4$ (bottom). The top panel shows that for $\lambda = 0$, the DoS is a Lorentzian, as expected, while for higher λ , the DoS splits into two peaks. These peaks grow in intensity, while becoming narrower as $\lambda \gg 1$. In fact, in the latter limit, it is easy to show that the DoS reduces to just two poles at $\omega = \pm 2\Gamma_0 \cos 2\phi/|\lambda|$. We see that for any value of λ in the top panel, the DoS preserves the spectral sum rule, and is hence causal. The bottom panel shows the DoS for $\phi = \pi/3$, which is greater than $\pi/4$, so for $\lambda = 0$, the DoS should be expected to be acausal. Indeed, we see that for $\lambda = 1.4$ (and all lower values), the DOS is negative and acausal, but for all $\lambda > 1.5$, we recover causality, in the sense that the integrated spectral weight or the spectral norm is one. But as the figure shows, the DoS does become negative over a finite frequency range, albeit, the negative weight is

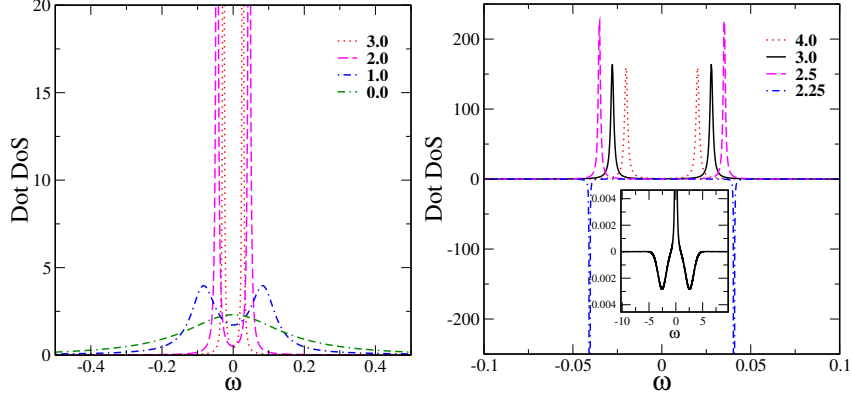


Figure 2.5: Dot density of states (DoS) as a function of frequency for various values of SOC (legends are the values of λ) and $\phi = \pi/5$ (left panel) and $\phi = \pi/3$ (right panel). In the top panel, the system does not violate \mathcal{PT} -symmetry for $\phi = \pi/5$ for any λ . The bottom panel is for $\phi = \pi/3$, for which $\lambda = 1.5$ represents the SOC value beyond which \mathcal{PT} -symmetry is restored.

compensated by the positive part, preserving the total spectral norm. The density of states being negative is of course not physical in a conventional Hermitian picture; but for a non-Hermitian system considered here, such a result can be speculated to imply states that are not stationary and are either lossy or amplifying. We note that further studies are required to find the correct interpretation of the negative density of states. The inference from the above investigation is that higher λ values restore \mathcal{PT} -symmetry that was broken spontaneously at lower λ , and hence SOC protects \mathcal{PT} -symmetry.

In the hermitian case, the spectral function is positive-definite and causal, i.e., normalized to one ($\int d\omega D_h(\omega) = 1$). We will explore the violation of causality by computing the deviation of the norm from unity as a function of ϕ and λ . The most interesting feature about the phase diagram, computed through the violation of spectrum sum rule condition, and shown in figure 2.6, is that although the hybridization, being proportional to $\cos(2\phi)$ has an acausal imaginary part beyond $\phi > \pi/4$, the spectral function sum rule is not violated above a certain value of the spin-orbit coupling, λ . The critical λ for $\phi = \pi/4$ is found to be equal to the effective bandwidth of the conduction band. Since λ shifts the center of the conduction band away from $\omega = 0$ for each 'chiral' index, this implies that if the imaginary part of hybridization is either vanishingly small or negative definite (causal) at $\omega = 0$, the spectral function norm is preserved. Thus, the inference is, as found through exact diagonalization in Sec.IVA, spin-orbit coupling stabilizes \mathcal{PT} -symmetry.

We note that such a conclusion is sensitive to the choice of the conduction

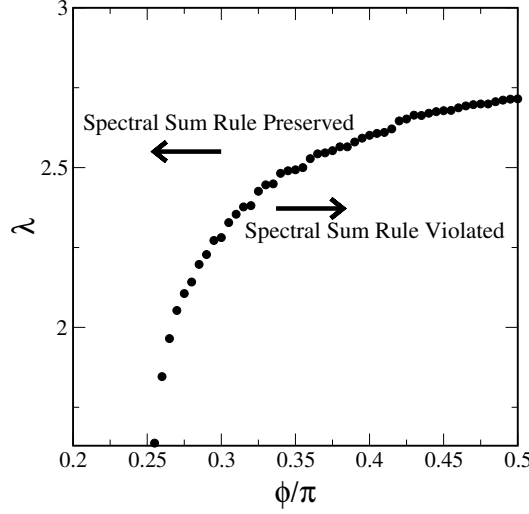


Figure 2.6: The $U = 0$ Phase diagram in the $\phi - \lambda$ plane found through the norm violation condition of the Green's function. The solid symbols represent the line of exceptional points, where the spectral sum rule gets violated and the norm deviates from unity.

band density of states. For example, the choice of an infinitely wide flat band will result in the exceptional point being $\phi_{EP} = \pi/4$ or $g_{EP} = 1$ for any value of the spin-orbit coupling, λ . We will find the trace of the Hamiltonian in the next section, and identify the violation of \mathcal{PT} -symmetry from the dependence of total energy on ϕ and λ .

2.4.3 Total energy of the causal states ($U = 0$)

A violation of \mathcal{PT} -symmetry introduces complex conjugate eigenvalues into the eigenspectrum. Thus, if we measure the energy of the system as the trace over the occupied states of the real part of the eigen-spectrum, we should observe some form of singular behavior such as discontinuity or non-differentiability, when one or more pairs of real eigenvalues become complex. From the exact diagonalization done in section IV.A, we have the eigenvalues of the Hamiltonian. Now, we consider a sum of all the real eigenvalues that are below the chemical potential (which is zero in our case), and denote that as E_{tot} . As shown in figure 2.7, the quantity $(E_{\text{tot}}(\phi) - E_{\text{tot}}(0))$, where $E_{\text{tot}}(0)$ is the corresponding quantity for $\phi = 0$, is discontinuous at specific ϕ values, that depend on the value of the SOC, and the discontinuities are marked by arrows. Such a discontinuity provides an alternate measure of the exceptional point. It is also interesting to see that the total energy is conserved below

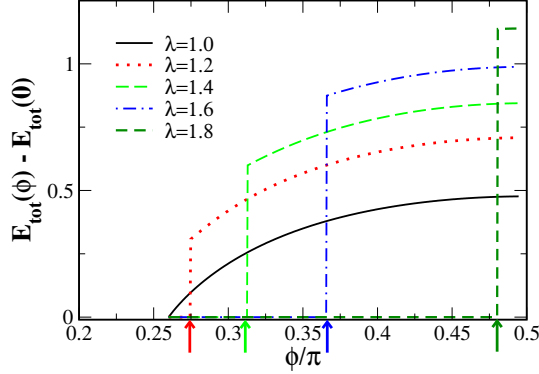


Figure 2.7: The sum of energies of all occupied causal states at a given ϕ measured from a reference value of $\phi = 0$ for various values of SOC. The ϕ value at which the discontinuity in total energy occurs is marked by arrows.

the exceptional point, while for $\phi > \phi_{EP}$, since some of the states develop imaginary eigenvalues, they would be excluded from $(E_{tot}(\phi) - E_{tot}(0))$, and this quantity, which is a fictitious energy in the \mathcal{PT} -symmetry broken regime, then appears to increase with increasing ϕ . Figure 2.8 shows the phase diagram computed through the energy discontinuity superimposed on the phase diagrams obtained through exact diagonalization and the spectrum sum rule violation. The three criteria for finding the exceptional points match reasonably well. Thus, we establish that *the \mathcal{PT} -violation as seen by the exact diagonalization of the Hamiltonian is also indicated to a good extent by causality violation of the Green's function, and by the energy discontinuity condition.*

Until now, we have restricted ourselves to the non-interacting case ($U = 0$). In the following subsection, we will investigate the other extreme, i.e the $U \rightarrow \infty$ limit using the Auxiliary Particle boson formalism.

2.4.4 Auxiliary Particle boson mean-field solution

The Hamiltonian in equation 2.7 may be rewritten in the $U \rightarrow \infty$ case using Coleman bosons⁴² as

$$\begin{aligned}
 H = H_0 + \sum_{k\eta h} X_{k\eta h} \left(c_{k\eta h}^\dagger b_\eta d_h + \text{h.c.} \right) \\
 + \epsilon_d \sum_h n_{dh} + \zeta \left(\sum_\eta b_\eta^\dagger b_\eta + \epsilon_d \sum_h n_{dh} - 1 \right)
 \end{aligned} \tag{2.36}$$

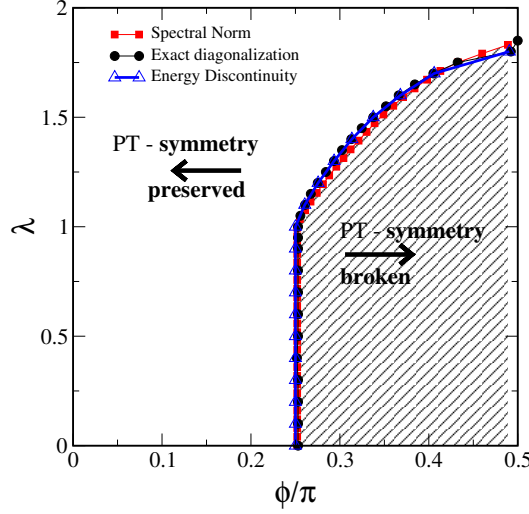


Figure 2.8: The phase diagram in the $\phi - \lambda$ plane, computed through an identification of the energy discontinuity (see text for details) showing the line of exceptional points (triangles). The shaded region represents the spontaneously broken \mathcal{PT} -symmetry broken regime, and the unshaded region represents the \mathcal{PT} -symmetry protected regime. The circles and squares represent the exceptional points derived through exact diagonalization and the spectral sum rule violation respectively. All the three conditions for determining exceptional points agree reasonably well.

where $H_0 = \sum_{kh\eta} \tilde{\epsilon}_{kh} c_{kh\eta}^\dagger c_{kh\eta}$, and ζ is the Lagrange multiplier which enforces the constraint that the total filling (fermions + bosons) is one. Note that the two channels, namely L and R have been associated with two different bosons as a general possibility. Hence, with the mean-field approximation, $\langle b_L^\dagger \rangle = \langle b_L \rangle = re^{i\theta}$ and $\langle b_R^\dagger \rangle = \langle b_R \rangle = re^{-i\theta}$ implying that the total mean boson number will be $\langle b_L^\dagger b_L + b_R^\dagger b_R \rangle = 2r^2 \cos(2\theta)$, the mean-field Hamiltonian becomes

$$\begin{aligned}
 H_{MF} = H_0 &+ \sum_{k\eta h} \tilde{X}_{k\eta h} \left[c_{k\eta h}^\dagger d_h + \text{h.c.} \right] \\
 &+ \tilde{\epsilon}_d \sum_h n_{dh} + \zeta (2r^2 \cos(2\theta) - 1)
 \end{aligned} \tag{2.37}$$

where $\tilde{X}_{kLh} = re^{i\theta} X_{kLh} = \sqrt{2}r|X_k|e^{i(\phi+\theta)}$, $\tilde{X}_{kRh} = \bar{h}re^{-i\theta} X_{kRh} = \sqrt{2}\bar{h}r|X_k|e^{-i(\phi+\theta)}$ and $\tilde{\epsilon}_d = \epsilon_d + \zeta$. The parameters r, ζ and θ may be found self-consistently by minimizing $\langle H_{MF} \rangle$. Since the Auxiliary Particle boson mean-field Hamiltonian has exactly the same form as the non-interacting Hamiltonian, equation 2.7, we will find the expression

for the total energy in the $U = 0$ case, and generalize it to the Auxiliary Particle-boson case.

For finding the expectation value of the Hamiltonian in equation 2.7, we need Green's functions other than the one computed before (equation 2.31). These are listed below:

$$G_{k\eta h}^{k\eta h} = \frac{1}{\omega^+ - \tilde{\epsilon}_{kh}} + \frac{X_{k\eta h}^2}{(\omega^+ - \tilde{\epsilon}_{kh})^2} G_{dh}^{dh} \quad (2.38)$$

$$G_{k\eta h}^{dh} = G_{dh}^{k\eta h} = \frac{X_{k\eta h}}{\omega^+ - \tilde{\epsilon}_{kh}} G_{dh}^{dh} \quad (2.39)$$

Using these to find the expectation value of the Hamiltonian, equation 2.7, we get

$$E_{tot} = \int_{-\infty}^{\infty} d\omega f(\omega) \tilde{D}(\omega) \quad (2.40)$$

where

$$\begin{aligned} \tilde{D}(\omega) &= -\frac{1}{\pi} \text{Im} \sum_h \tilde{G}_h(\omega) \\ &= -\frac{1}{\pi} \text{Im} \left[\sum_{kh\eta} \left(\tilde{\epsilon}_{kh} G_{kh\eta}^{kh\eta} + 2X_{kh\eta} G_{k\eta h}^{dh} \right) + \epsilon_d \sum_h G_{dh}^{dh} \right] \end{aligned} \quad (2.41)$$

and,

$$\begin{aligned} \tilde{G}_h(\omega) &= \left(-\sum_{k\eta} \right) + \left(\omega^+ \sum_{k\eta} \frac{1}{\omega^+ - \tilde{\epsilon}_{kh}} \right) \\ &+ G_{dh}^{dh} \left(\epsilon_d + \sum_{k\eta} \frac{X_{kh\eta}^2}{\omega^+ - \tilde{\epsilon}_{kh}} + \omega^+ \sum_{k\eta} \frac{X_{kh\eta}^2}{(\omega^+ - \tilde{\epsilon}_{kh})^2} \right) \end{aligned} \quad (2.42)$$

which when simplified yields

$$\begin{aligned} \tilde{D}_h(\omega) &= \omega D_{c0}(\omega - h\lambda) + \epsilon_d D_{d0h}(\omega) \\ &- \frac{1}{\pi} \text{Im} \left[G_{dh}^{dh} \left(\Gamma_h - \omega \frac{d\Gamma_h}{d\omega} \right) \right] \end{aligned} \quad (2.43)$$

The first term contributes to the conduction electron energy, and depends

on λ as follows:

$$\begin{aligned}
E_{c0} &= \sum_h \int_{-\infty}^0 \omega D_{c0}(\omega - h\lambda) d\omega \\
&= 2 \int_{-\infty}^0 \omega D_{c0}(\omega) d\omega + 2 \int_0^\lambda (\omega - \lambda) D_{c0}(\omega) d\omega \\
&= E_0 + 2 \int_0^\lambda (\omega - \lambda) D_{c0}(\omega) d\omega
\end{aligned} \tag{2.44}$$

where E_0 is independent of λ , and we have assumed that $D_{c0}(\omega)$ is symmetric about $\omega = 0$. The second term yields a contribution proportional to the dot occupancy. Thus

$$\begin{aligned}
E_{tot} - E_0 &= 2 \int_0^\lambda (\omega - \lambda) D_{c0}(\omega) d\omega + \epsilon_d \sum_h n_{dh0} \\
&\quad - \sum_h \int_{-\infty}^0 d\omega \frac{1}{\pi} \text{Im} \left[G_{dh}^{dh} \left(\Gamma_h - \omega \frac{d\Gamma_h}{d\omega} \right) \right]
\end{aligned} \tag{2.45}$$

A Gaussian conduction band is chosen for convenience for bath dos as $\rho_0(\epsilon) = \sum_k \delta(\epsilon - \tilde{\epsilon}_k) = \exp(-\epsilon^2/2t_*^2)/\sqrt{(\pi)t_*}$ (with $t_* = 1$ as the unit of energy), for which the Hilbert transform may be written in terms of the Faddeeva function, $w(z)$ as $H_T[z] = (-i\sqrt{\pi}/t_*)w(z/\sqrt{2}t_*)$ if $\text{Im}(z) > 0$. With a Gaussian DoS, the hybridization function, $\Gamma_h(\omega)$ is given by (equation 2.32)

$$\begin{aligned}
\Gamma_h(\omega) &= \Gamma_0 \cos(2\phi) H_T[z_h] \\
&= \Gamma_0 \cos(2\phi) (-is\sqrt{\pi} \exp(-z_h^2) \text{erfc}(-isz_h))
\end{aligned} \tag{2.46}$$

where $z_h = \omega^+ - h\lambda$, $s = \text{sgn}(\text{Im}z_h) = +1$, and $\text{erfc}(z)$ is the complementary error function. The derivative of the hybridization function is given by

$$\begin{aligned}
\frac{d\Gamma_h}{d\omega} &= \Gamma_0 \cos(2\phi) \frac{dH_T(z)}{dz} \\
&= 2\Gamma_0 \cos(2\phi) (1 - z_h H_T[z_h])
\end{aligned} \tag{2.47}$$

The total energy expression 2.45 shows that the first term is the conduction electron contribution, and the second and third terms are the contributions due to the dot and the hybridization respectively. If $\lambda = 0$, and $\phi = \pi/4$, then for $\epsilon_d = 0$, the total energy is just zero. In fact, the third term, being proportional to $\cos(2\phi)$ will yield zero for any λ and ϵ_d at $\phi = \pi/4$.

The Auxiliary Particle-boson mean-field Hamiltonian may be treated exactly as the non-interacting limit, and the average energy $\tilde{E}_{\text{tot}} = \langle H_{MF} \rangle$ is

obtained as

$$\begin{aligned} \tilde{E}_{tot} - E_0 &= 2 \int_0^\lambda (\omega - \lambda) D_{c0}(\omega) d\omega + \tilde{\epsilon}_d \sum_h \tilde{n}_{dh0} \\ &\quad - \sum_h \int_{-\infty}^0 d\omega \frac{1}{\pi} \text{Im} \left[\tilde{G}_{dh}^{dh} \left(\tilde{\Gamma}_h - \omega \frac{d\tilde{\Gamma}_h}{d\omega} \right) \right] \\ &\quad + \zeta (2r^2 \cos(2\theta) - 1) \end{aligned} \quad (2.48)$$

where the renormalized dot Green's functions and hybridizations are given by

$$\tilde{G}_{dh}^{dh}(\omega) = \left[\omega^+ - \tilde{\epsilon}_d - \tilde{\Gamma}_h(\omega) \right]^{-1}, \quad (2.49)$$

$$\tilde{\Gamma}_h(\omega) = 4r^2 |X_0|^2 \cos(2\phi + 2\theta) \mathcal{H}_T[z_h], \quad (2.50)$$

and the Hilbert transform is defined by the Faddeeva function given above equation 2.46. We observe that the first term in equation 2.48 does not depend on r, ζ or θ , and hence will not affect the minimization.

In order to investigate the effect of finite bandwidth and SOC in the strong coupling limit, we go back to equation 2.48, and minimize the total energy for a Gaussian band and for finite SOC. We will find the equations for the determination of $r^2, \tilde{\epsilon}_d$ and θ , and solve them numerically. The derivatives of the total energy are

$$\frac{\partial \tilde{E}_{tot}}{\partial \zeta} = \mathcal{A}(\tilde{\epsilon}_d, r^2, \theta) + 2r^2 \cos 2\theta - 1 \quad (2.51)$$

$$\frac{\partial \tilde{E}_{tot}}{\partial r^2} = \frac{1}{r^2} \mathcal{B}(\tilde{\epsilon}_d, r^2, \theta) + 2\zeta \cos 2\theta \quad (2.52)$$

$$\frac{\partial \tilde{E}_{tot}}{\partial \theta} = -2 \left[\tan(2(\phi + \theta)) \mathcal{B}(\tilde{\epsilon}_d, r^2, \theta) + 2\zeta r^2 \sin 2\theta \right], \quad (2.53)$$

where

$$\begin{aligned} \mathcal{A}(\tilde{\epsilon}_d, r^2, \theta) &= -\frac{1}{\pi} \text{Im} \int_{-\infty}^0 \sum_h \mathcal{F}_h(\omega) d\omega \\ \mathcal{B}(\tilde{\epsilon}_d, r^2, \theta) &= -\frac{1}{\pi} \text{Im} \int_{-\infty}^0 \sum_h \mathcal{G}_h(\omega) d\omega \end{aligned} \quad (2.54)$$

and

$$\begin{aligned}
\mathcal{F}_h(\omega) &= \left(\tilde{G}_{dh}^{dh}\right)^2 \left(\tilde{\epsilon}_d + \tilde{\Gamma}_h - \omega \frac{d\tilde{\Gamma}_h}{d\omega}\right) + \tilde{G}_{dh}^{dh} \\
\mathcal{G}_h(\omega) &= \left(\tilde{G}_{dh}^{dh}\right)^2 \tilde{\Gamma}_h \left(\tilde{\epsilon}_d + \tilde{\Gamma}_h - \omega \frac{d\tilde{\Gamma}_h}{d\omega}\right) \\
&\quad + \tilde{G}_{dh}^{dh} \left(\tilde{\Gamma}_h - \omega \frac{d\tilde{\Gamma}_h}{d\omega}\right)
\end{aligned} \tag{2.55}$$

Using the above expressions, and the definitions we get the following self-consistent nonlinear equations:

$$\mathcal{A}(\tilde{\epsilon}_d, r^2, \theta) = 1 - 2r^2 \cos(2\theta) \tag{2.56}$$

$$\mathcal{B}(\tilde{\epsilon}_d, r^2, \theta) = -2\zeta r^2 \cos(2\theta) \tag{2.57}$$

$$\tan(2\phi + 2\theta)\mathcal{B}(\tilde{\epsilon}_d, r^2, \theta) = -2\zeta r^2 \sin(2\theta). \tag{2.58}$$

Since equations 2.57 and 2.58 yield the result that $\theta \neq 0$ only if $\phi = 0$, we conclude that the Auxiliary Particle-boson equations do not renormalize the non-Hermitian coupling strength, which is non-zero only if $\phi \neq 0$. Thus, we restrict ourselves to $\theta = 0$, and solve equations 2.56 and 2.57 to determine $\tilde{\epsilon}_d = \epsilon_d + \zeta$ and r^2 . Again, we choose a Gaussian density of states for the bare conduction band. The numerical solution proceeds with the choice of a parameter, $a = r^2/\tilde{\epsilon}_d$, and using this, the equation 2.56 can be transformed to a single variable non-linear equation, and hence can be solved easily. Given both r^2 and $\tilde{\epsilon}_d$, we can substitute in equation 2.57 and get ζ , and hence ϵ_d . For vanishing SOC ($\lambda \rightarrow 0$), we expect to find a Kondo scale that has a dependence similar to the conventional Hermitian case. Defining $\Delta_0 = \pi X_0^2 \rho_0(0)$ which is equal to $\sqrt{\pi} X_0^2/t_*$ for the Gaussian DoS, figure 2.9 shows that the Kondo scale, $T_K/D = r^2 \sqrt{\Delta_0^2 + \tilde{\epsilon}_d^2}/D$, found with the Gaussian density of states, is indeed exponentially dependent on $\pi\epsilon_d/\Delta_0$, but with an exponent, that is slightly different than the one obtained for the flat band case. With increasing SOC, since the hybridization value at $\omega = 0$ decreases, we may expect the Kondo scale to decrease. A countereffect is provided by a concomitant increase in the total bandwidth. However, since λ affects $\Gamma_h(\omega = 0)$ exponentially (Gaussian DoS), the Kondo scale decreases exponentially with an increase in SOC as shown in figure 2.10. This finding must be contrasted with that of the flat band case^{43;44}, where, since the $\Gamma_h(\omega = 0)$ does not change with varying λ , the bandwidth becomes the only controlling parameter, and the scale increases linearly with increasing SOC in the flat band case.

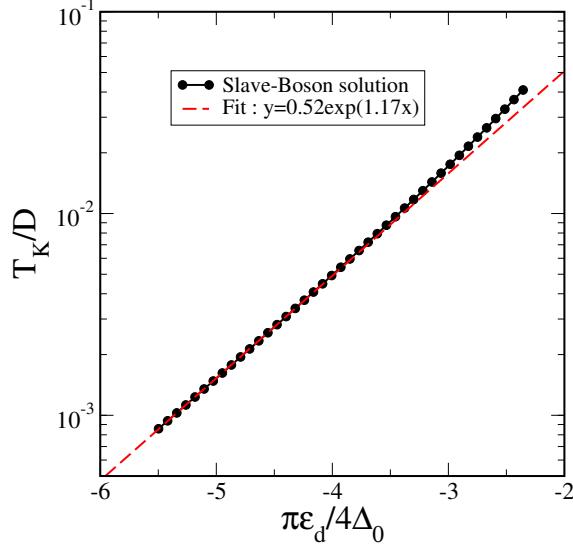


Figure 2.9: T_K (black, solid) and the exponential fit (red-dashed) as a function of scaled dot-orbital energy, $\pi\epsilon_d/4\Delta_0$ for $\lambda = 0$ and $\phi = 0$.

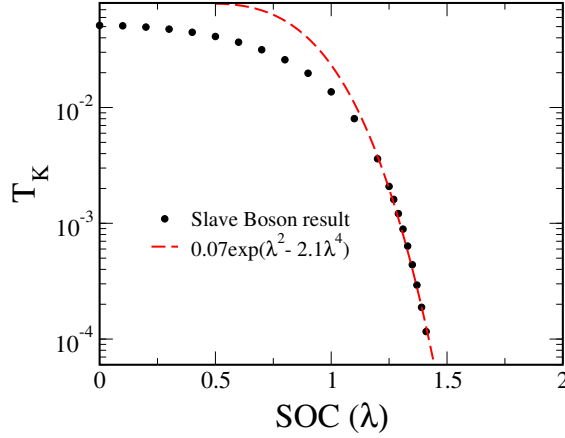


Figure 2.10: T_K (black, solid) and the exponential fit (red-dashed) as a function of spin-orbit coupling (λ).

Now, we investigate the variation of the scale with increasing non-hermitian strength for fixed SOC and ϵ_d in the strong coupling regime. To recapitulate the results from the non-interacting case, we had found that for $\lambda = 0$, the exceptional point was at $\phi_{EP} = \pi/4$. And increasing λ , increased the ϕ_{EP} to beyond $\pi/4$, showing that SOC stabilized \mathcal{PT} -symmetry for $U = 0$. In the zero bandwidth, three-site model, we found that the exceptional point ($g_{EP} > 1$) and the quantum critical point ($g_c = 1$) become distinct in the

$U - \lambda$ plane except on the $\lambda = U/2$ line, where $g_{EP} = g_c = 1$. With the Auxiliary Particle-boson calculation, we will be able to extract the Kondo scale, T_K , and hence the quantum critical point will be identified through the vanishing of T_K . However, we may not be able to identify the exceptional point since the zero bandwidth case indicates that \mathcal{PT} -symmetry breaks spontaneously at a non-hermitian coupling, $g \geq 1$, which is always greater than or equal to the QCP ($g = 1$); while the Auxiliary Particle boson mean-field vanishes at the QCP, and the theory may not even be valid beyond the QCP. Now, we discuss the Auxiliary Particle-boson results.

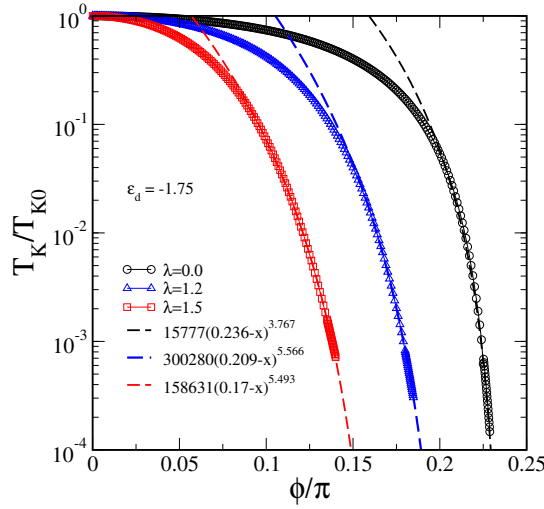


Figure 2.11: T_K/T_{K0} for $\lambda = 0$ (black circles) and $\lambda = 1.5$ (red squares) and the respective fits (green-dashed and blue-dashed) for $\epsilon_d = -1.75$.

Defining T_{K0} as the Kondo scale for $\phi = 0$, in figure 2.11, we show T_K/T_{K0} vs. ϕ for $\epsilon_d = -1.75$ and $\lambda = 0, 1.2$ and 1.5 . The scale decreases sharply with increasing ϕ , and is seen to vanish at a critical ϕ (as seen by the power law fits). The critical values of ϕ and the non-Hermitian coupling $g = \tan(\phi)$ for various λ are given in table 2.1. It is observed that the critical coupling decreases sharply with increasing λ , and at some value of $\lambda = \lambda_c$, the critical ϕ will vanish, which implies that the model will not have a Kondo screened state for any finite value of the non-Hermitian coupling if $\lambda > \lambda_c$. The results shown in table 2.1 also consolidate the inference that interactions and SOC cooperate in reducing the value of the quantum critical non-Hermitian strength.

Using the above results in figure 2.11, we can draw a phase diagram in the $\phi - \lambda$ plane. The shaded region in figure 2.12 represents the parameter

λ	ϕ_c	$g_c = \tan(\phi_c)$
0.0	0.236π	0.916
1.2	0.209π	0.771
1.5	0.17π	0.591

Table 2.1: Table showing the results of the fits of T_K vs. ϕ of figure 2.11, from which the critical ϕ has been obtained.

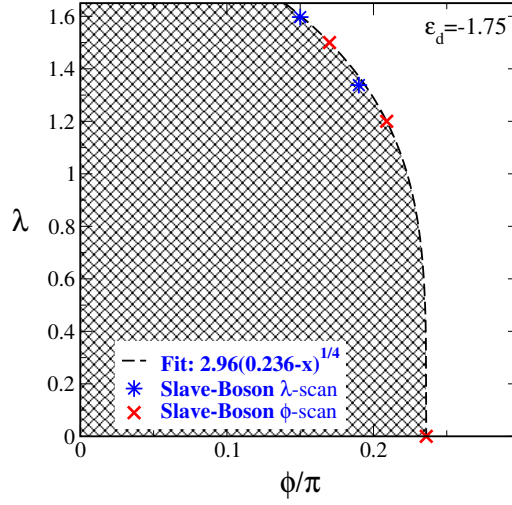


Figure 2.12: The shaded region represents a parameter regime, where a finite Kondo scale is found. The Auxiliary Particle-boson results for the vanishing of T_K are shown by red crosses (ϕ -scan), and blue stars (λ -scan) and the dashed line represents a fit, and is a guide to the eye.

regime where the Kondo scale is finite, while the dashed line is where the scale vanishes. The red crosses are the actual Auxiliary Particle-boson results found through the analysis shown in figure 2.11, where for a fixed λ , we have found the T_K vs ϕ . This will be called ϕ -scan. In order to validate the phase diagram, we have carried out λ -scans for fixed ϕ , and the blue stars shown in figure 2.12 are found to lie on the same curve as the red crosses. The fit shows that the critical λ_c discussed above is given by $\lambda_c = 2.96(0.236)^{1/4} = 2.06$, beyond which the model does not support the Kondo screened state for any finite ϕ .

2.5 Discussion and Conclusions

In this work, we have considered the interplay of interactions, Rashba spin-orbit coupling and non-Hermitian coupling to the baths on the Kondo effect and preservation or violation of \mathcal{PT} -symmetry. We begin with a derivation of the model of an interacting quantum dot hybridizing through non-Hermitian couplings with non-interacting leads having Rashba spin-orbit coupling using Lindbladian dynamics. A simplification of the full model in terms of a zero bandwidth, three-site model is considered, which yields a wealth of information including the demonstration of \mathcal{PT} -symmetry, the dependence of quantum critical points and exceptional points on Rashba spin-orbit coupling and interactions etc. Our analysis shows that the exceptional point at $g_{EP} = 1$ in the non-interacting case coincides with the Kondo destruction critical point, g_c for all $\lambda = U/2, U \neq 0$, but the two bifurcate significantly everywhere else in the $U - \lambda$ phase diagram. The quantum critical point remains at $g_c = 1$ for all $U \neq 0$ and λ . The phase diagram of this simple, three-site system shows that U and λ protect \mathcal{PT} symmetry in the $U/\lambda \gg 1$ and $U/\lambda \ll 1$ regime for any strength of the non-Hermitian coupling, but in the neighborhood of $\lambda = U/2$, the exceptional point occurs at a finite coupling strength.

A detailed analysis of the full, finite bandwidth model, in the non-interacting case using exact diagonalization (ED), Green's functions and Hamiltonian trace calculation is used to establish that exceptional points may be deduced from the ED calculations, or equivalently from the violation of the spectral sum rule of the Green's functions or the energy discontinuity condition. Finally, the strong coupling regime is investigated using a Auxiliary Particle-boson approach, which, by construction is valid for $U \rightarrow \infty$. The mean-field equations were derived through Green's function approach. We have shown earlier (in section IV-A) that the spectral function is positive definite and norm preserving for all $\phi < \pi/4$, while only beyond $\pi/4$, the spectral function became negative over certain frequency regions. Since the Kondo destruction critical point has been found for all λ to lie at $\phi_c < \pi/4$, the derived mean-field equations are valid. The exceptional points could not be found within this approach since the solution to the Auxiliary Particle-boson mean-field equations yields a vanishing boson mean field implying a Kondo destruction quantum critical point before the \mathcal{PT} -symmetry is violated. The quantum critical points for the finite bandwidth case get significantly renormalized below the $\lambda = 0$ value of $g_c = 1$ by the SOC. A critical value of λ is also found beyond which the model does not support the Kondo-screened singlet state for any finite value of the non-hermitian coupling. Lourenco et al³¹

had considered a real-space non-hermitian model that was similar to what we have considered, and through RG, the authors had found that the exceptional point and the critical point coincide at $g_c = 1$, and the RG flow does not renormalize the critical point. This is of course, contrary to our findings, and the discrepancy could be due to the subtle differences between their model and our model. We are working on trying to understand the origin of these discrepancies through RG-based approaches. Further, the solution of the Auxiliary Particle boson equations beyond the Kondo destruction critical point is being attempted. We believe that the Auxiliary Particle boson mean field could take on negative or complex values implying complex values of the boson mean fields.

Bibliography

- [1] H. Zhao, S. Longhi, and L. Feng, Scientific reports **5**, 17022 (2015).
- [2] O. Rosas-Ortiz and K. Zelaya, Annals of Physics **388**, 26 (2018).
- [3] I. Rotter, Journal of Physics A: Mathematical and Theoretical **42**, 153001 (2009).
- [4] S. Echeverri-Arteaga, H. Vinck-Posada, and E. A. Gómez, Optik **180**, 505 (2019).
- [5] H. Wang, Y. Qin, J. Ma, H. Shen, Y. Hu, and X. Jia, Chinese Physics B **30**, 050301 (2021).
- [6] C. M. Bender, Reports on Progress in Physics **70**, 947 (2007).
- [7] A. Matzkin, Journal of Physics A: Mathematical and General **39**, 10859 (2006).
- [8] H. Jones, Physical Review D **76**, 125003 (2007).
- [9] J. Schindler, A. Li, M. C. Zheng, F. M. Ellis, and T. Kottos, Phys. Rev. A **84**, 040101 (2011).
- [10] C. E. Rüter, K. G. Makris, R. El-Ganainy, D. N. Christodoulides, M. Segev, and D. Kip, Nature physics **6**, 192 (2010).
- [11] S. Krinner, T. Esslinger, and J.-P. Brantut, Journal of Physics: Condensed Matter **29**, 343003 (2017).
- [12] S. Longhi, EPL (Europhysics Letters) **120**, 64001 (2018).

- [13] N. Syassen, D. M. Bauer, M. Lettner, T. Volz, D. Dietze, J. J. Garcia-Ripoll, J. I. Cirac, G. Rempe, and S. Dür, *Science* **320**, 1329 (2008).
- [14] B. Zhu, B. Gadway, M. Foss-Feig, J. Schachenmayer, M. L. Wall, K. R. A. Hazzard, B. Yan, S. A. Moses, J. P. Covey, D. S. Jin, J. Ye, M. Holland, and A. M. Rey, *Phys. Rev. Lett.* **112**, 070404 (2014).
- [15] G. Barontini, R. Labouvie, F. Stubenrauch, A. Vogler, V. Guarrera, and H. Ott, *Phys. Rev. Lett.* **110**, 035302 (2013).
- [16] M. J. Mark, E. Haller, K. Lauber, J. G. Danzl, A. Janisch, H. P. Büchler, A. J. Daley, and H.-C. Nägerl, *Phys. Rev. Lett.* **108**, 215302 (2012).
- [17] L. Riegger, N. Darkwah Oppong, M. Höfer, D. R. Fernandes, I. Bloch, and S. Fölling, *Phys. Rev. Lett.* **120**, 143601 (2018).
- [18] M. Kanász-Nagy, Y. Ashida, T. Shi, C. P. Moca, T. N. Ikeda, S. Fölling, J. I. Cirac, G. Zaránd, and E. A. Demler, *arXiv preprint arXiv:1801.01132* (2018).
- [19] R. Zhang, Y. Cheng, P. Zhang, and H. Zhai, *Nature Reviews Physics* **2**, 213 (2020).
- [20] Y. Nishida, *Physical Review A* **93**, 011606 (2016).
- [21] M. Nakagawa and N. Kawakami, *Physical review letters* **115**, 165303 (2015).
- [22] J. Bauer, C. Salomon, and E. Demler, *Physical review letters* **111**, 215304 (2013).
- [23] J. L. Miller, *Physics Today* **70**, 23 (2017).
- [24] J. Wiersig, *Photonics Research* **8**, 1457 (2020).
- [25] M. B. Plenio and P. L. Knight, *Rev. Mod. Phys.* **70**, 101 (1998).
- [26] Y. Ashida, S. Furukawa, and M. Ueda, *Nature communications* **8**, 15791 (2017).
- [27] B.-B. Wei and L. Jin, *Scientific reports* **7**, 7165 (2017).
- [28] C. M. Bender and D. W. Darg, *Journal of mathematical physics* **48**, 042703 (2007).

- [29] O. A. Castro-Alvaredo and A. Fring, Journal of Physics A: Mathematical and Theoretical **42**, 465211 (2009).
- [30] N. Hatano and D. R. Nelson, Physical Review Letters **77**, 570 (1996).
- [31] J. A. S. Lourenço, R. L. Eneas, and R. G. Pereira, Phys. Rev. B **98**, 085126 (2018).
- [32] M. Nakagawa, N. Kawakami, and M. Ueda, Phys. Rev. Lett. **121**, 203001 (2018).
- [33] J. Malecki, Journal of Statistical Physics **129**, 741 (2007).
- [34] M. Zarea, S. E. Ulloa, and N. Sandler, Phys. Rev. Lett. **108**, 046601 (2012).
- [35] D. Mastrogiuseppe, A. Wong, K. Ingersent, S. E. Ulloa, and N. Sandler, Phys. Rev. B **90**, 035426 (2014).
- [36] M. Zarea and N. Sandler, Phys. Rev. B **79**, 165442 (2009).
- [37] R. Žitko, Phys. Rev. B **81**, 241414 (2010).
- [38] F. Hu, T. Ma, H.-Q. Lin, and J. E. Gubernatis, Physical Review B **84**, 075414 (2011).
- [39] A. Nejati, K. Ballmann, and J. Kroha, Physical review letters **118**, 117204 (2017).
- [40] H. Shackleton and M. S. Scheurer, Phys. Rev. Research **2**, 033022 (2020).
- [41] N. Moiseyev, *Non-Hermitian quantum mechanics* (Cambridge University Press, 2011).
- [42] D. Newns and N. Read, Advances in Physics **36**, 799 (1987).
- [43] T. I. Ivanov, Phys. Rev. B **86**, 155429 (2012).
- [44] R. Žitko and J. Bonča, Phys. Rev. B **84**, 193411 (2011).

Chapter 3

Auxiliary Particle-Boson Methods for Non-Hermitian Models: Callan Symanzik Renormalization

In this chapter, we will discuss techniques for analyzing EPs in both equilibrium and non-equilibrium settings, focusing on non-Hermitian models. We will introduce an analytical method that involves deriving Callan-Symanzik equations as a simple approach for integrating interactions into the study of non-Hermitian systems. Additionally, we will provide a brief overview of modified Auxiliary Particle Boson methods tailored constraints and Lagrange multipliers to incorporate interactions in non-Hermitian systems.

3.1 Introduction

The Callan-Symanzik equation is a differential equation primarily used to study the renormalization of correlation functions and describe physical observables' scale dependence. Deriving the Callan-Symanzik equation¹⁻⁴ in the context of non-Hermitian or non-equilibrium systems involves adapting this equation with modifications to boson-fermion fields, incorporating suitable constraints to account for interactions. Generally, the complexity of incorporating interactions involves perturbation expansion. However, as discussed earlier, the ambiguity in the choice of the basis in Green's functions to evaluate the perturbation series makes this problem challenging. We bypass this task using mean-field Green's functions with the flow of boson-fermion weights with scale.

Now, we briefly introduce these mean-field methods, which can be used to derive the Callan-Symanzik form of equations to trace the quasiparticle weights as a function of momentum. These methods are very similar to minimization techniques used in variational problems or self-consistent solutions in the auxiliary particle method. In such problems, the initial condition is crucial to achieving the convergence.

3.2 Auxiliary Particles-Boson Approaches in Non-Hermitian Systems

Extending auxiliary particle-boson theories to non-Hermitian systems introduces significant challenges, not only due to gain and loss terms in the Hamiltonian but also because of convergence issues arising from the presence of complex terms. These complexities disrupt conventional perturbation theory, requiring the development of new techniques like the renormalization group (RG) to study novel phase transitions, including exceptional points and spontaneous symmetry breaking. Despite these difficulties, the auxiliary particle-boson method remains valuable for representing impurity actions and enforcing charge conservation, while simplifying the system by eliminating high-energy degrees of freedom. This approach facilitates the study of how coupling constants evolve with energy scale, providing insights into the system's parameter flow and convergence behavior in non-Hermitian contexts.

In the large interaction limit, impurity operators are expressed as fermions and bosons as following,

$$d^\dagger = f^\dagger b \tag{3.1}$$

A total number conservation constraint is used as following,

$$\sum_{\sigma} n_{f\sigma} + n_b = 1 \quad (3.2)$$

We use this representation to derive the effective model and identify the fixed points from the CS-RG analysis. These will serve as initial conditions for boson and fermion weights to achieve minimization.

3.3 Renormalization and the CS Equation

The Callan-Symanzik(CS) equation serves as a tool for analyzing the interactions of a theory and RG flows across the phases with energy scale. Here we use the Auxiliary Particle-Boson theory, for mean field Green functions and analogous analysis will be done by separating the beta functions.

The analysis only includes the impurity Green's function, which depends on the re-normalized parameters. The impurity Green functions are evaluated by integrating out the bath degrees of freedom using the mean field decomposition, this serves as a starting point of RG.

Using Auxiliary Particle-Boson RG methods combined with the CS equation provides a framework for understanding the flow of coupling constants in the system. This approach allows us to explore the system's critical behavior and properties as the energy scale changes, shedding light on the underlying physics. We particularly focus on the derivation by Parameshwaran et al.⁵ of RG beta functions. It involves renormalized Green function \tilde{G} by setting its derivative with respect to the scale cutoff parameter Λ to zero, denoted as $\frac{d\tilde{G}}{d\Lambda} = 0$.

This analysis focuses on the renormalized Green function \tilde{G} , transforming it into a function G that depends on parameters such as r^2 (boson weight), θ (non-Hermitian parameter), and $\tilde{\epsilon}_d$ (the renormalized site energy). The expression for G is given by:

$$G = \langle \{d_{\sigma}^{\dagger}, d_{\sigma}\} \rangle \quad (3.3)$$

We express this equation in terms of the renormalized parameters, referring to the earlier chapter where d_{σ} operators are transformed into chiral ones with left-right bosons. Consequently, the trace of \tilde{G} can be written as:

$$\tilde{G} = \langle \{b_L f_L^{\dagger}, b_L f_L\} \rangle + \langle \{b_R f_R^{\dagger}, b_R f_R\} \rangle \quad (3.4)$$

By scaling the operators, this equation can be reformulated as:

$$\tilde{G} = \langle \{r e^{-i\theta} \sqrt{\zeta} d_\sigma^\dagger, r e^{-i\theta} d_\sigma\} \rangle + \langle \{r e^{i\theta} \sqrt{\zeta} d_\sigma^\dagger, r e^{i\theta} \sqrt{\zeta} d_\sigma\} \rangle \quad (3.5)$$

This yields the renormalized impurity Green function:

$$\begin{aligned} \tilde{G} &= r^2 \cos(2\theta) \zeta \langle \{d_\sigma^\dagger, d_\sigma\} \rangle \\ &= r^2 \cos(2\theta) \zeta G_0 \end{aligned} \quad (3.6)$$

The constraints for the Lagrange multipliers ζ , θ , and r^2 are given by:

$$\langle b_L^\dagger b_L \rangle + \langle b_R^\dagger b_R \rangle + \langle f_L^\dagger f_L \rangle + \langle f_R^\dagger f_R \rangle = 1 \quad (3.7)$$

This can be modified to:

$$r^2 \cos(2\theta) + \zeta = 1 \quad (3.8)$$

The site energy is then modified as $\tilde{\epsilon}_d = \epsilon_d + i\zeta$. We can now write the Callan-Symanzik (CS) equation for the above Green function as follows:

$$\begin{aligned} \Lambda \left(\frac{\partial}{\partial \Lambda} + \frac{\partial \tilde{\epsilon}_d}{\partial \Lambda} \frac{\partial}{\partial \tilde{\epsilon}_d} + \frac{\partial r^2}{\partial \Lambda} \frac{\partial}{\partial r^2} + \frac{\partial \theta}{\partial \Lambda} \frac{\partial}{\partial \theta} \right) \tilde{G} &= 0 \\ \beta_{\tilde{\epsilon}_d} &= \Lambda \frac{\partial \tilde{\epsilon}_d}{\partial \Lambda}, \quad \beta_{r^2} = \Lambda \frac{\partial r^2}{\partial \Lambda}, \quad \beta_\theta = \Lambda \frac{\partial \theta}{\partial \Lambda} \end{aligned} \quad (3.9)$$

The effective action, a functional that describes the dynamics of a system in terms of its degrees of freedom, can be written for the impurity action in the auxiliary particle-Boson representation as follows:

$$\mathcal{S}_{eff} = \int d\tau \left(\sum_{h=L,R} \bar{d}_h \tilde{G}^{-1} d_h + \zeta (r^2 \cos(2\theta) - 1) \right) \quad (3.10)$$

In earlier chapter we studied with spin-orbit interactions ,here we set the Spin-Orbit (SO) interaction to zero and it consist of the NH interaction with \mathcal{PT} symmetry. By integrating out the Fermionic degrees of freedom, we are obtaining a saddle point (SP) solution for effective action.This involves taking derivatives with the Lagrange multipliers in average action.

It is to note that \mathcal{PT} symmetry (Parity-time) can be present in the both

Hermitian as well as the non-Hermitian systems.

$$\begin{aligned}
\mathcal{S}'_{eff} &= \int d\tau \ln(\tilde{G}^{-1}(\zeta(r^2 \cos(2\theta) - 1))) \\
\langle \frac{\partial \mathcal{S}'_{eff}}{\partial \zeta} \rangle &= -\frac{1}{\tilde{G}} \frac{\partial \tilde{G}}{\partial \zeta} + \frac{1}{\zeta} \\
\langle \frac{\partial \mathcal{S}'_{eff}}{\partial r^2} \rangle &= -\frac{1}{\tilde{G}} \frac{\partial \tilde{G}}{\partial r^2} + \frac{\cos(2\theta)}{r^2 \cos(2\theta) - 1} \\
\langle \frac{\partial \mathcal{S}'_{eff}}{\partial \theta} \rangle &= -\frac{1}{\tilde{G}} \frac{\partial \tilde{G}}{\partial \theta} - \frac{2r^2 \sin(2\theta)}{(r^2 \cos(2\theta) - 1)}
\end{aligned} \tag{3.11}$$

Now using above functional derivatives to zero will give one set of equations. Form the cs equation 3.9 we can arrive at the following by considering the ,

$$\frac{d\tilde{G}}{d\Lambda} = 0 \tag{3.12}$$

We can expand the complete derivative as partial ones for the above particularly the left-hand side as following,

$$\frac{d\tilde{G}}{d\Lambda} = \frac{\partial \tilde{G}}{\partial \Lambda} + \frac{\partial \zeta}{\partial \Lambda} \frac{\partial \tilde{G}}{\partial \zeta} + \frac{\partial \theta}{\partial \Lambda} \frac{\partial \tilde{G}}{\partial \theta} + \frac{\partial r^2}{\partial \Lambda} \frac{\partial \tilde{G}}{\partial r^2} \tag{3.13}$$

Now above equation can further expanded by substituting $\tilde{G} = r^2 \cos 2\theta \zeta G_0$ as the following,

$$\begin{aligned}
\frac{d\tilde{G}}{d\Lambda} &= -r^2 2 \sin 2\theta \frac{\partial \theta}{\partial \Lambda} \zeta G_0 + r^2 \cos 2\theta \frac{\partial \zeta}{\partial \Lambda} G_0 + \cos 2\theta \frac{\partial r^2}{\partial \Lambda} \zeta G_0 \\
&+ \frac{\partial \tilde{\epsilon}_d}{\partial \Lambda} \frac{\partial \tilde{G}}{\partial \tilde{\epsilon}_d} + \frac{\partial \theta}{\partial \Lambda} \frac{\partial \tilde{G}}{\partial \theta} + \frac{\partial r^2}{\partial \Lambda} \frac{\partial \tilde{G}}{\partial r^2}
\end{aligned} \tag{3.14}$$

In above equation we can express all G_0 terms to \tilde{G} particularly in first 3 terms,

$$\begin{aligned}
\frac{d\tilde{G}}{d\Lambda} &= -2 \tan 2\theta \frac{\partial \theta}{\partial \Lambda} \tilde{G} + \frac{1}{\zeta} \frac{\partial \zeta}{\partial \Lambda} \tilde{G} + \frac{1}{r^2} \frac{\partial r^2}{\partial \Lambda} \tilde{G} \\
&+ \frac{\partial \tilde{\epsilon}_d}{\partial \Lambda} \frac{\partial \tilde{G}}{\partial \tilde{\epsilon}_d} + \frac{\partial \theta}{\partial \Lambda} \frac{\partial \tilde{G}}{\partial \theta} + \frac{\partial r^2}{\partial \Lambda} \frac{\partial \tilde{G}}{\partial r^2}
\end{aligned} \tag{3.15}$$

Left-hand side of the above is basically zero since it is an invariance condition. So, if we divide throughout by \tilde{G} , we get the following.

$$\begin{aligned}
0 &= -2 \tan 2\theta \frac{\partial \theta}{\partial \Lambda} + \frac{1}{\zeta} \frac{\partial \zeta}{\partial \Lambda} + \frac{1}{r^2} \frac{\partial r^2}{\partial \Lambda} \\
&+ \frac{1}{\tilde{G}} \frac{\partial \tilde{\epsilon}_d}{\partial \Lambda} \frac{\partial \tilde{G}}{\partial \tilde{\epsilon}_d} + \frac{1}{\tilde{G}} \frac{\partial \theta}{\partial \Lambda} \frac{\partial \tilde{G}}{\partial \theta} + \frac{1}{\tilde{G}} \frac{\partial r^2}{\partial \Lambda} \frac{\partial \tilde{G}}{\partial r^2}
\end{aligned} \tag{3.16}$$

From equation 3.11 the derivatives of effective action averages can be equated to zero as a saddle-point(SP) or minimization procedure,

$$\begin{aligned} & -2 \tan(2\theta) \frac{\partial \theta}{\partial \Lambda} + \frac{1}{r^2} \frac{\partial r^2}{\partial \Lambda} + \frac{1}{\zeta} \frac{\partial \zeta}{\partial \Lambda} + \frac{\partial \zeta}{\partial \Lambda} \left(\frac{1}{\zeta} \right) \\ & + \frac{\partial r^2}{\partial \Lambda} \left(\frac{\cos(2\theta)}{r^2 \cos(2\theta) - 1} \right) - \frac{\partial \theta}{\partial \Lambda} \left(\frac{2r^2 \sin(2\theta)}{(r^2 \cos(2\theta) - 1)} \right) = 0 \end{aligned} \quad (3.17)$$

It is convenient to use variable separable method for deriving the flow equations for the above,

$$\begin{aligned} & 2 \tan(2\theta) \frac{\partial \theta}{\partial \Lambda} + \frac{\partial \theta}{\partial \Lambda} \left(\frac{2r^2 \sin(2\theta)}{(r^2 \cos(2\theta) - 1)} \right) = \Lambda_{cutoff} \\ & \frac{1}{\zeta} \frac{\partial \zeta}{\partial \Lambda} + \frac{1}{\zeta} \frac{\partial \zeta}{\partial \Lambda} = \Lambda_{cutoff} \\ & \frac{1}{r^2} \frac{\partial r^2}{\partial \Lambda} + \frac{\partial r^2}{\partial \Lambda} \left(\frac{\cos(2\theta)}{r^2 \cos(2\theta) - 1} \right) = \Lambda_{cutoff} \end{aligned} \quad (3.18)$$

Now with the above flow equations, we can work out the ratio of the one another to get how they flow with each other as follows,

$$\begin{aligned} & \zeta \tan(2\theta) \frac{d\theta}{d\zeta} + \zeta \frac{d\theta}{d\zeta} \left(\frac{r^2 \sin 2\theta}{r^2 \cos 2\theta - 1} \right) = 1 \\ & \frac{\zeta}{2r^2} \frac{dr^2}{d\zeta} + \frac{\zeta}{2} \frac{dr^2}{d\zeta} \left(\frac{\cos 2\theta}{r^2 \cos 2\theta - 1} \right) = 1 \end{aligned} \quad (3.19)$$

Deviding above equations we get the following,

$$\frac{d\theta}{dr^2} = \frac{2r^2 \cos 2\theta - 1}{2r^2(2r^2 \sin 2\theta - \tan 2\theta)} \quad (3.20)$$

This will yield a solution as $\theta = \pm \frac{1}{2} \arccos \frac{e^{-2C_1}}{r^2}$ this implies $r^2 \cos 2\theta \rightarrow$ invariant, using this solution we find the ζ and θ renormalization. We get another solution as $r^2 = \zeta^{2\frac{g-1}{2g-1}}$ now using these solution we can rewrite the renormalized Green functions to solve for Kondo scale,

$$\begin{aligned} \tilde{G}^{-1}(\omega) &= (\omega^+ - \tilde{\epsilon}_d - \tilde{\Gamma}(\omega)) \\ \tilde{\Gamma}(\omega) &= \sum_k \frac{4r^2 |X_0|^2 \cos 2\theta}{\omega^+ - \epsilon_k} \end{aligned} \quad (3.21)$$

Using the invariance condition $\frac{d\tilde{G}}{d\Lambda} = 0$ we get $\frac{d\tilde{\epsilon}_d}{d\Lambda} + \int_{-D}^D \frac{4r^2 |X_0|^2 \cos 2\theta}{\omega^+ - D} d\omega = 0$ Now we can solve for the above equations for different cases imaginary and

real (r^2, θ) values to get the scales as the following,

$$\begin{aligned}
\ln \frac{\zeta}{\sqrt{\cos 2\theta} e^{\frac{4g^2}{(g^2-1)^{3/2}}\theta}} &\rightarrow \text{invariant} \\
\frac{\zeta}{\sqrt{1-g^2}} e^{-\frac{4g^2}{(g^2-1)^{3/2}}\theta} &\rightarrow \text{nh-scale for real } \theta \\
\frac{\zeta}{\sqrt{1+g^2}} e^{\frac{4g^2}{(g^2+1)^{3/2}}\theta} &\rightarrow \text{nh-scale for -im } \theta
\end{aligned} \tag{3.22}$$

In above equation depending on θ real for \mathcal{PT} -symmetric case. It can be chosen as imaginary θ correspond to exponentially decaying Boson weight. We can see scale either vanishes or diverges depending on the choice of Lagrange multipliers. For $g = r^2 \cos 2\theta$, we used the previous solution, which is invariant.

3.3.1 Exceptional Points in Non-Interacting Problem

We are considering the problem of a single impurity connected to a parity symmetric bath which is flip terms

$$\mathcal{Z} = \int \mathcal{D}\bar{\xi} \int \mathcal{D}\xi \int \mathcal{D}\bar{\Lambda} \int \mathcal{D}\Lambda e^{-S}, \tag{3.23}$$

where the total action can be written as a sum of the actions corresponding to the left lead, right lead, dot and the hybridization terms, i.e. $S = S_L + S_R + S_{dot} + S_{hyb}$ and the individual terms are given by

$$\begin{aligned}
S_L &= \sum_{nkh} \bar{\Lambda}_{khLn} (-i\omega_n + \epsilon_{kh}) \Lambda_{khLn} \\
S_R &= \sum_{nkh} \bar{\Lambda}_{khRn} (-i\omega_n + \epsilon_{kh}) \Lambda_{khRn} \\
S_{dot} &= \sum_{n\sigma} \bar{\xi}_{n\sigma} (-i\omega_n + \epsilon_d) \xi_{n\sigma} + \frac{U}{\beta} \sum_{\{n_i\}} \bar{\xi}_{n_1\uparrow} \xi_{n_2\uparrow} \bar{\xi}_{n_3\downarrow} \xi_{n_4\downarrow} \delta_{n_1+n_3, n_2+n_4} \\
S_{hyb} &= \sum_{nk} X_k (\bar{\Lambda}_{k+Ln} \xi_{n\uparrow} + \bar{\Lambda}_{k-Ln} \bar{\xi}_{n\uparrow} + gc) + \sum_{nk} X_k^* (\bar{\Lambda}_{k+Ln} \xi_{n\downarrow} + \bar{\Lambda}_{k-Ln} \bar{\xi}_{n\downarrow} + gc) \\
&\quad \sum_{nk} X_k (\bar{\Lambda}_{k+Rn} \xi_{n\downarrow} - \bar{\Lambda}_{k-Rn} \bar{\xi}_{n\downarrow} + gc) + \sum_{nk} X_k^* (\bar{\Lambda}_{k+Rn} \xi_{n\uparrow} - \bar{\Lambda}_{k-Rn} \bar{\xi}_{n\uparrow} + gc)
\end{aligned} \tag{3.24}$$

We first integrate out the Grassmann variables corresponding to the leads $(\{\Lambda\})$, Grassmann variables in impurities $(\{\xi\})$ and obtain an effective dot

action as

$$\begin{aligned}
S_{dot}^{eff} &= \sum_n \bar{\xi}_{n\sigma} \left(\Delta_{-i\omega_n} + \frac{4}{\Delta_{-i\omega_n}} \sum_{kh} M_{kh} \sum_{k'h'} M_{k'h'} \right) \xi_{n\sigma} \\
&+ \frac{U}{\beta} \sum_{\{n_i\}} \bar{\xi}_{n_1\uparrow} \xi_{n_2\uparrow} \bar{\xi}_{n_3\downarrow} \xi_{n_4\downarrow} \delta_{n_1+n_3, n_2+n_4} \\
\text{where } M_{kh} &= \frac{hX_k}{(-i\omega_n + \epsilon_{kh})^2}, \quad \Delta_{-i\omega_n} = -i\omega_n + \epsilon_d + \sum_{kh} \frac{2X_k^2 \cos(2\phi)}{-i\omega_n + \epsilon_{kh}}
\end{aligned} \tag{3.25}$$

We found EP's from the zeros of the denominators of the retarded G as the following for zero bandwidth, we show the eigenvalues are real from discriminant properties of the cubic equation of inverse G.

$$\begin{aligned}
G &= \left(\omega - \epsilon_d - \frac{4\omega X_0^2 \cos(2\phi)}{\omega^2 - \lambda^2} \right. \\
&\quad \left. - \frac{4}{\omega - \epsilon_d - \frac{4\omega X_0^2 \cos(2\phi)}{\omega^2 - \lambda^2}} \sum_{kh} \frac{\lambda X_k^2 \cos(2\phi)}{\omega - \epsilon_{kh}} \sum_{k'h'} \frac{\lambda X_{k'}^2 \cos(2\phi)}{\omega - \epsilon_{k'h'}} \right)^{-1} \\
G^{-1} &= \Delta_{-i\omega_n} - \frac{4}{\Delta_{-i\omega_n}} \sum_{kh} M_{kh} \sum_{k'h'} M_{k'h'} = 0
\end{aligned} \tag{3.26}$$

we rewrite the above equation in real frequency as the following;

$$\Delta_\omega - \frac{4}{\Delta_\omega} \sum_h M_{0h} \sum_{h'} M_{0h'} = 0 \tag{3.27}$$

Where in the above G we have restricted ourselves to analyzing local EP's and summing over chiral channels yield terms $\Delta_\omega = \omega - \epsilon_d - \frac{4\omega X_0^2 \cos(2\phi)}{\omega^2 - \lambda^2}$ and $\sum_h M_{0h} = \frac{-2\lambda X_0^2 \cos(2\phi)}{\omega^2 - \lambda^2}$ substituting these in the above gives polynomial in ω :

$$((\omega^2 - \lambda^2)(\omega - \epsilon_d) - 4\omega X_0^2 \cos(2\phi))^2 - 16X_0^4 \cos^2(2\phi)\lambda^2 = 0 \tag{3.28}$$

We get roots of ω for the above equations from Cardano's method of cubic equation solution as the following,

$$\begin{aligned}
\omega_1 &= -\lambda \\
\omega_2 &= \frac{1}{2} \left(\epsilon + \lambda - \sqrt{16X^2 \cos(2\phi) + \lambda^2 + \epsilon^2 - 2\lambda\epsilon} \right) \\
\omega_3 &= \frac{1}{2} \left(\epsilon + \lambda + \sqrt{16X^2 \cos(2\phi) + \lambda^2 + \epsilon^2 - 2\lambda\epsilon} \right)
\end{aligned} \tag{3.29}$$

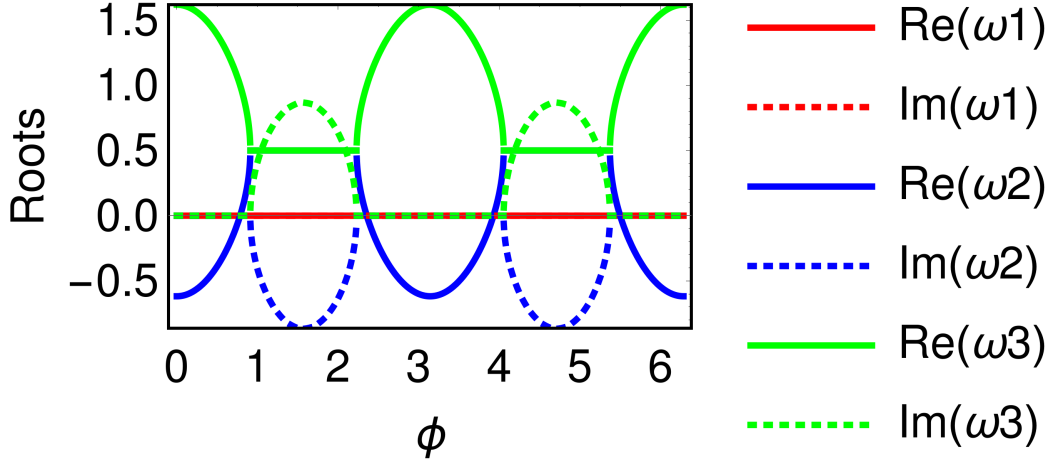


Figure 3.1: We have plotted ω roots given in equation 3.29 by varying Non-Hermitian strength (ϕ) for $\lambda = 0$

There will be another set of roots which are obtained simply by replacing in above by $\lambda \rightarrow -\lambda$. These 6 roots will be doubly degenerate 3 roots for $\epsilon = 0$ which is \mathcal{PT} symmetry case, and $\lambda = 0$. We expect peaks in spectral functions for these points of $\omega = -4X\sqrt{\cos(2\phi)}, 0, 4X\sqrt{\cos(2\phi)}$ as we tune the nh-strength these will coalesce to zero i.e., non-interacting limit, we observed this feature in impurity DOS. Also, the spectral function peaks correspondence with the eigenvalues. The above retarded Green's function in effective action 3.25 captures the physics of the exceptional points and \mathcal{PT} -transition in the non-interacting limit for $U = 0$.

3.4 Exceptional Points in Strong Correlation

Strong correlation effects on the exceptional points can be investigated from Auxiliary Particle-Boson calculations. We have seen in earlier section \mathcal{PT} -nh model retarded Green's function can be derived from the equation of motion or the path integral approach corresponding diagonal G^{-1} for the impurity states in the \mathcal{PT} -channels. We use the following representation for dot operators $\xi_{n\sigma}$ as auxiliary particles Fermion f_σ and Boson b with a charge Q conservation constraint.

$$\xi_\sigma = f_\sigma b^\dagger, \quad Q = b^\dagger b + \sum_\sigma f_\sigma^\dagger f_\sigma = 1 \quad (3.30)$$

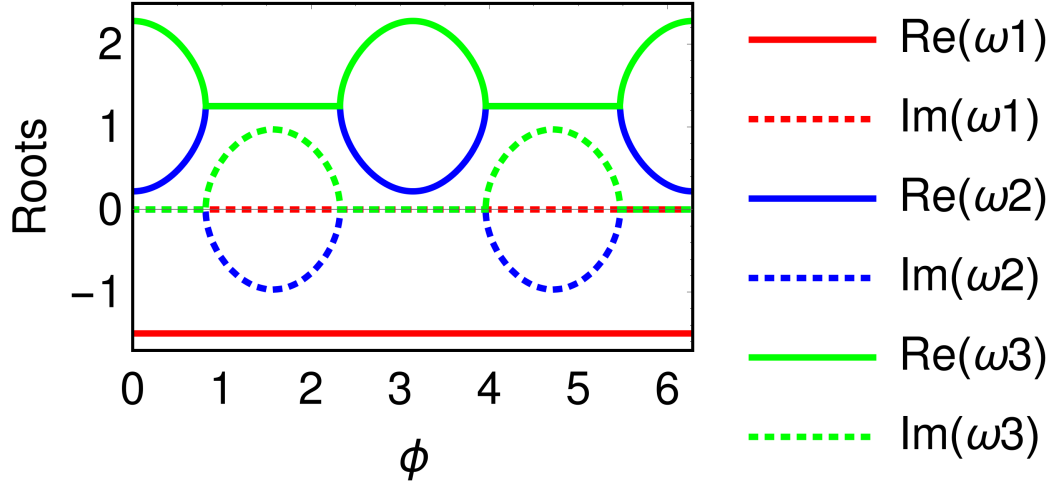


Figure 3.2: We have plotted ω roots given in equation 3.29 by varying Non-Hermitian strength (ϕ) $\lambda = 1.5$

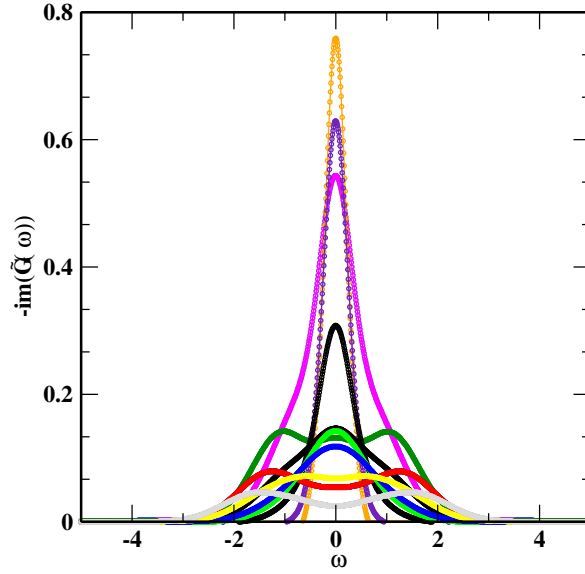


Figure 3.3: Density of states from the Callan-Symmanzik Green's function by varying the bare NH hybridization and for $\lambda = 0$.

We will use the representation given equation 3.30 for the action 3.25 and without decoupling the interaction term. Th we find the following renormalized action.

$$\begin{aligned}
 S_{SB}^{\text{eff}} = & \sum_{n\sigma} \bar{\xi}_{n\sigma} (-i\omega_n + \tilde{\epsilon}_d + \tilde{\Gamma}_1(i\omega_n)) \xi_{n\sigma} \\
 & + \sum_{n\sigma} \left(\bar{\xi}_{n\sigma} (\tilde{\Gamma}_2(i\omega_n) \xi_{n\sigma} + g.c) + i\delta(r^2 - 1) \right) \\
 \text{where } \tilde{\Gamma}_1 = & \sum_{kh} \frac{X_{kh}^2 + (X_{kh}^*)^2}{i\omega_n - \epsilon_{kh}}, \quad \tilde{\Gamma}_2 = \sum_{kh} \frac{X_{kh}^2 - (X_{kh}^*)^2}{i\omega_n - \epsilon_{kh}}
 \end{aligned} \tag{3.31}$$

The representation and constraints of the Auxiliary Particle-Boson can be applied to the actions derived in equations 3.25 and 3.31. Once all dot operators are integrated out, both actions result in the same free energy, as the flip contributions disappear. Since we are dealing with a non-Hermitian system, we separate the real and imaginary components of the Boson field to analyze their effects on the ground state, which provides valuable information at the EP for interacting cases. We derive the saddle point equations from the action to find a consistent solution for the Boson field. The role of the Lagrange multiplier (δ) in the path integral is extensively discussed in references⁶⁻⁸. It has been demonstrated that the Fermionic degrees of freedom can be integrated out in the Auxiliary Particle-Boson method due to the bilinear nature of the action in Fermion numbers, simplifying the calculations. However, treating the Lagrange multipliers as dynamical variables in this method is impractical, as it would introduce additional diagrams in the perturbation theory, making the calculations more complex. By performing unitary operations, we can demonstrate that the action is diagonal and use the Fermionic action to integrate out the emergent pseudo-Fermion variables to obtain the scale. This results in the following free energy from the path integral.

$$\langle F \rangle = -\frac{1}{N} \int_{-D}^D \ln((\omega^+ - \epsilon_d - \tilde{\Gamma}_1)^2 - \tilde{\Gamma}_2^2) d\omega + i\delta(r^2 - 1) \quad (3.32)$$

Due to the meromorphic property of Green functions, we can readily see the real part of the integral vanishes in any symmetric limits integral, since it is anti-symmetric. This reduces to the following,

$$\langle F \rangle = -\frac{i}{N} \int_{-D}^D \tan^{-1} \left(\frac{\text{Im}((\omega^+ - \tilde{\epsilon}_d - \tilde{\Gamma}_1)^2 - \tilde{\Gamma}_2^2)}{\text{Re}((\omega^+ - \tilde{\epsilon}_d - \tilde{\Gamma}_1)^2 - \tilde{\Gamma}_2^2)} \right) + i\delta(r^2 - 1) \quad (3.33)$$

where in equation 3.33 $\omega^+ = \omega + i\eta$, for simplicity we can drop η in the ω^+ but we retain it in hybridization. Following saddle point equations can be derived.

$$\begin{aligned} \int_{-D}^D \frac{\Delta_r \Delta'_i - \Delta_i \Delta'_r}{\Delta_r^2 + \Delta_i^2} d\omega + |r|^2 &= 0 \\ \int_{-D}^D \frac{\Delta_r(\omega - \tilde{\epsilon}_d)}{\Delta_r^2 + \Delta_i^2} d\omega - 2\tilde{\epsilon}_d r_i &= 0 \\ \int_{-D}^D \frac{\Delta_i(\omega - \tilde{\epsilon}_d)}{\Delta_r^2 + \Delta_i^2} d\omega + 2\tilde{\epsilon}_d r_r &= 0 \end{aligned} \quad (3.34)$$

The above equation 3.34 contains terms $\Delta' = \frac{\partial \Delta_i}{\partial \omega}$, and $\Delta_{i,r}$ representing imaginary and real parts. To gain qualitative understanding from the Auxiliary Particle-Boson perspective, we need to solve the above equations exactly, but for simplicity, we use some approximations to obtain a closed-form solution. Deriving RG equations from eq 3.34 gives the following:

$$\frac{\partial \tilde{\Delta}_r}{\partial \tilde{\epsilon}_d} = \frac{(1 - g^2)\tilde{\epsilon}_d - 2\tilde{\Delta}_r}{\tilde{\Delta}_r^2 \tilde{\epsilon}_d} \text{ where } g = \frac{\Delta_i}{\Delta_r} \quad (3.35)$$

Figure 3.4 shows that a diverging Auxiliary Particle field implies that the system flows towards the non-interacting fixed point. Additionally, for $g > 1$, the diverging Boson field is purely due to an imaginary interaction. The red and blue curves in the figure represent the critical trajectories from the analytic solution of the Auxiliary Particle-Boson method, the red curve is for $\tilde{\Delta}_r, \tilde{\epsilon}_d < 0$ and the blue curve is for $\tilde{\Delta}_r, \tilde{\epsilon}_d > 0$. Figure 3.5 shows the flow towards the strong coupling (SC) fixed point for values of g less than 1. This is an indication that the system is in the Kondo phase. The g parameter can be tuned to move across the NKK regime. This will serve as an additional handle to move across the conventional Kondo-NKK regime by tuning the g parameter providing important information about the behavior of the system and the nature of the phase transitions.

Conventional perturbation theories, in conjunction with the Callan-Symanzik equation, can be employed to investigate the renormalization group (RG) flows of the system by introducing corrections to the system's effective action as a response to variations in the scale parameter.

In the Kondo model, the parameter $\tilde{\epsilon}_d$ scales as $1/J$. A diverging Auxiliary Particlefield corresponds to the non-interacting fixed point. If the Auxiliary Particlefield flows to zero, as shown in figure 3.5, it indicates a strong coupling fixed point corresponding to the Kondo state.

3.5 Finite U-Auxiliary ParticleBoson Analysis

We use the rotational invariant Auxiliary Particle-Boson (SB) representation to derive the mean-field Hamiltonian for the non-Hermitian single impurity model. This involves expressing the Hamiltonian in terms of the Auxiliary ParticleBosonic fields and their conjugate momenta and applying a mean field approximation to decouple the interactions between the fields. The resulting mean-field Hamiltonian, which is a quadratic form in the Auxiliary

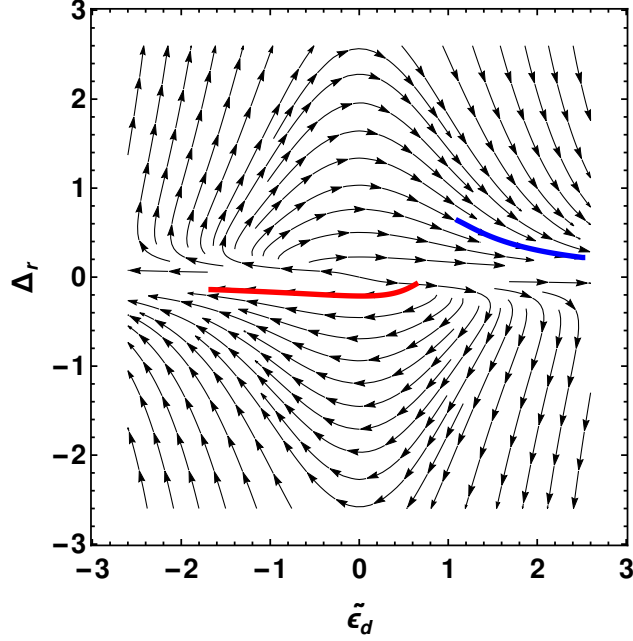


Figure 3.4: We are plotting the computed form of flow equations β_{Δ_r} and $\beta_{\tilde{\epsilon}_d}$ given in equation 3.35 for $g < 1$

ParticleBosonic fields and their conjugate momenta, also includes a term that enforces the constraint that the Auxiliary ParticleBosons represent the sites either empty or doubly occupied states. This Hamiltonian can be used to study the non-Hermitian single impurity model's behavior and calculate various physical properties.

$$\begin{aligned}
 H_{bath} &= \sum_{\eta kh} \epsilon_{\eta kh} c_{\eta kh}^\dagger c_{\eta kh} \quad H_{lead-dot} = \sum_{k\sigma} X_{\eta kh} \left(z^\dagger d_h^\dagger c_{\eta kh} + hc \right) \\
 H_{dot} &= \sum_h \epsilon_h n_{dh} + U d^\dagger d + \lambda^{(1)} P + \lambda_h^{(2)} Q_h
 \end{aligned} \tag{3.36}$$

where the constraints are given by the following with a modification for chiral Bosons,

$$\begin{aligned}
 z &= \frac{(e^\dagger p + p^\dagger d)}{(\sqrt{1 - d^\dagger d - p^\dagger p})(\sqrt{1 - e^\dagger e - p^\dagger p})} \\
 P &= e^\dagger e + \sum_h p_h^\dagger p_h + d^\dagger d - 1 = 0 \\
 Q_h &= n_{dh} - p_h^\dagger p_h - d^\dagger d = 0
 \end{aligned} \tag{3.37}$$

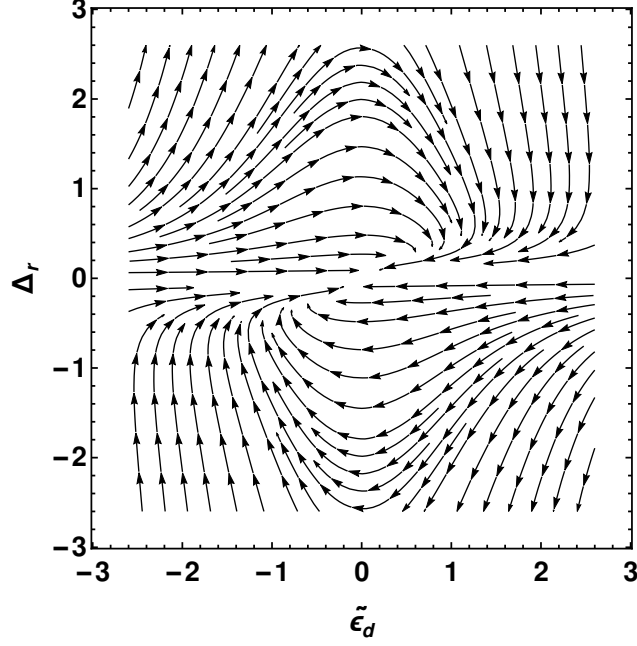


Figure 3.5: We are plotting the computed form of flow equations β_{Δ_r} and $\beta_{\tilde{\epsilon}_d}$ given in equation 3.35 for $g > 1$

Using the constraints above we write the following action,

$$\begin{aligned} \mathcal{S}^h = \int d\tau \left[\left(\frac{\partial}{\partial \tau} - \epsilon_{kh} \right) c_{\eta kh}^\dagger c_{\eta kh} + \sum_{\eta kh} X_{\eta kh} (z^\dagger d_h^\dagger c_{\eta kh} + hc) \right. \\ \left. + \sum_h \left(\frac{\partial}{\partial \tau} - \epsilon_h \right) z^\dagger d_h^\dagger d_h z + U d^\dagger d + \lambda^{(1)} P + \lambda_h^{(2)} Q_h \right] \end{aligned} \quad (3.38)$$

After integrating out bath operators we get the following effective action,

$$\mathcal{S}_{eff}^h = \int d\tau \left(\frac{\partial}{\partial \tau} - \epsilon_h + \lambda_h^{(2)} + \sum_{\eta k} \frac{X_{\eta kh}^2}{\frac{\partial}{\partial \tau} - \epsilon_{\eta kh}} \right) z^\dagger d_h^\dagger d_h z + U d^\dagger d + \lambda^{(1)} P + \lambda_h^{(2)} Q_h \quad (3.39)$$

The chiral channel-dependent Green's function and the Boson will introduce the effective action as follows,

$$\mathcal{S}_{eff} = \int d\tau \ln \tilde{G}_{0+} \ln \tilde{G}_{0-} + U d^\dagger d + \lambda^{(1)} P + \lambda_h^{(2)} Q_h \quad (3.40)$$

Free energy of the system can be written as the following,

$$f_0 = \ln \left(\prod_h \tilde{G}_{0h}^{-1} \right) + U d^2 + \lambda^{(1)} P + \lambda_h^{(2)} Q_h \quad (3.41)$$

The saddle point solution with $\lambda_{1,2}$

$$\begin{aligned}
\frac{\partial f_0}{\partial \lambda^{(1)}} &= \int d\omega \frac{1}{(\prod_h \tilde{G}_{0h}^{-1})} \sum_h \tilde{G}_{0h}^{-1} \frac{\partial \tilde{G}_{0h}}{\partial \lambda^{(1)}} + P = 0 \\
\frac{\partial f_0}{\partial \lambda_h^{(2)}} &= \int d\omega \frac{1}{(\prod_h \tilde{G}_{0h}^{-1})} \sum_h \tilde{G}_{0h}^{-1} \frac{\partial \tilde{G}_{0h}}{\partial \lambda_h^{(2)}} + Q_h = 0 \\
\frac{\partial f_0}{\partial d^2} &= \int d\omega \frac{1}{(\prod_h \tilde{G}_{0h}^{-1})} \sum_h \tilde{G}_{0h}^{-1} \frac{\partial \tilde{G}_{0h}}{\partial d^2} + U + \lambda^{(1)} \frac{\partial P}{\partial d^2} + \lambda^{(2)} \frac{\partial Q_h}{\partial d^2} = 0 \\
\frac{\partial f_0}{\partial e^2} &= \int d\omega \frac{1}{(\prod_h \tilde{G}_{0h}^{-1})} \sum_h \tilde{G}_{0h}^{-1} \frac{\partial \tilde{G}_{0h}}{\partial e^2} + \lambda^{(1)} \frac{\partial P}{\partial e^2} + \lambda^{(2)} \frac{\partial Q_h}{\partial e^2} = 0
\end{aligned}$$

where $\tilde{G}_{0h} = \left(\frac{\partial}{\partial \tau} - \epsilon_h + \lambda_h^{(2)}(1 + Q_h) + \sum_{\eta k} \frac{X_{\eta kh}^2}{\frac{\partial}{\partial \tau} - \epsilon_{\eta kh}} \right) z^2$

(3.42)

For flat band the d^2 equation given in 3.42 can be solved and we get the following,

$$0 = U + \sum_h \int_{-D}^D d\omega f(\omega) \arctan \left(\frac{\Delta_h}{\epsilon_f - \omega} \right) \frac{\partial Q_h}{\partial d^2} \quad (3.43)$$

integrating by parts we have the following,

$$\begin{aligned}
0 &= U + I \frac{\partial Q_h}{\partial d^2} - \int_{-D}^D I \frac{d \frac{\partial Q_h}{\partial d^2}}{d\omega} d\omega \\
I &= \left(- \sum_h \Delta_h + \epsilon_f \sum_h \arctan \frac{\Delta_h}{\epsilon_f} + \sum_h \frac{\Delta_h}{2} \ln \left(\frac{\sqrt{\epsilon_f^2 + \Delta_h^2}}{D^2} \right) \right) \\
&= \left(- \sum_h \Delta_h + \epsilon_f \arctan \frac{\sum_h \Delta_h}{\epsilon_f(1 - \Delta_- \Delta_+)} \right. \\
&\quad \left. + \ln \left(\frac{\sqrt{\epsilon_f^2 + \Delta_+^2}}{D^2} \right)^{\Delta_+} \left(\frac{\sqrt{\epsilon_f^2 + \Delta_-^2}}{D^2} \right)^{\Delta_-} \right)
\end{aligned} \quad (3.44)$$

Main contribution of the above integral will be at $\omega^+ \rightarrow 0$ and $\epsilon \rightarrow D$ (bandwidth) hence this will reduce to the following,

$$I_0 = -\frac{2DX_0^2 \cos 2\phi_0}{D^2 - \lambda^2} + \epsilon_f \tan^{-1} \frac{2D}{\epsilon_f^2(d^2 - \lambda^2) - X_0^2 \cos 2\phi} + \ln \left(\frac{\epsilon_f}{D^2} \right)^{\frac{2DX_0^2 \cos 2\phi_0}{D^2 - \lambda^2}} \quad (3.45)$$

The analysis of the RG equations leads to the conclusion that the arctan function at the lowest ω point is significant and the scaling behavior can be derived from it.,

$$D_{eff} = D \left(1 + \frac{U}{\Delta} \right), \text{ where } \Delta = \frac{2DX_0^2 \cos 2\phi_0}{D^2 - \lambda^2} \quad (3.46)$$

$$\lambda_c = \pm \left(\frac{U - 2X_0 \cos(2\phi_0)}{U} \right)^{1/2}$$

3.6 Auxiliary Particle Method in Keldysh Field Theory

Consider the Grassmann variables $\bar{\xi}_\sigma, \xi_\sigma$ for the dot degrees of freedom and $\bar{\Lambda}_{k\eta h}, \Lambda_{k\eta h}$ for the conduction electron degrees of freedom. The partition function \mathcal{Z} for the Hamiltonian is given by

$$\mathcal{Z} = \int \mathcal{D}\bar{\xi}_\sigma \int \mathcal{D}\xi_\sigma \int \mathcal{D}\bar{\Lambda}_{k\eta h} \int \mathcal{D}\Lambda_{k\eta h} e^{-S}, \quad (3.47)$$

where the total action S is decomposed as $S = S_L + S_R + S_{\text{dot}} + S_{\text{hyb}}$ with

$$S = \int (\mathcal{L}_L + \mathcal{L}_R + \mathcal{L}_{\text{dot}} + \mathcal{L}_{\text{hyb}}) dt, \quad (3.48)$$

and

$$\mathcal{L}_L = \sum_{kh} \bar{\Lambda}_{khL} (i\partial_t - \epsilon_{kh}) \Lambda_{khL}, \quad (3.49)$$

$$\mathcal{L}_R = \sum_{kh} \bar{\Lambda}_{khR} (i\partial_t - \epsilon_{kh}) \Lambda_{khR}, \quad (3.50)$$

$$\mathcal{L}_{\text{dot}} = \sum_{\sigma} \bar{\xi}_\sigma (i\partial_t - \epsilon_d) \xi_\sigma + U \bar{\xi}_\uparrow \bar{\xi}_\downarrow \xi_\downarrow \xi_\uparrow, \quad (3.51)$$

$$\mathcal{L}_{\text{hyb}} = \sum_{kh} \tilde{V}_k (\bar{\Lambda}_{khL} \xi_\uparrow + h \bar{\Lambda}_{khR} \xi_\downarrow + gc). \quad (3.52)$$

In the auxiliary particle-boson representation, the complex fermionic field is expressed as $\xi_\sigma = \bar{b} f_\sigma$. To enforce total charge conservation on the Keldysh contour, a Lagrange multiplier field is introduced, leading to the partition function evaluation by path integration over all fields.

Applying the Keldysh rotation transforms the bosonic and fermionic fields into real fields:

$$b_c = \frac{b_1 + b_2}{\sqrt{2}}, \quad b_q = \frac{b_1 - b_2}{\sqrt{2}}, \quad (3.53)$$

$$f_c = \frac{f_1 + f_2}{\sqrt{2}}, \quad f_q = \frac{f_1 - f_2}{\sqrt{2}}, \quad (3.54)$$

where b_1 , b_2 and f_1 , f_2 are the bosonic and fermionic fields on the forward and backward branches of the Keldysh contour, respectively.

Rewriting the action in terms of the rotated fields:

$$\begin{aligned} S &= S_{\text{bath}} + S_f + S_b + S_{\text{hyb}} + \sqrt{2}\delta_2, \\ S_{\text{bath}} &= \int_0^\infty dt \sum_{kh\eta} \begin{pmatrix} \Lambda_1^\dagger & \Lambda_2^\dagger \end{pmatrix} \begin{pmatrix} i\partial_t - \epsilon_{kh} - \delta\mu & 0 \\ 0 & i\partial_t - \epsilon_{kh} - \delta\mu \end{pmatrix} \begin{pmatrix} \Lambda_1 \\ \Lambda_2 \end{pmatrix}, \\ S_f &= \int_0^\infty dt \sum_\sigma \begin{pmatrix} f_{1\sigma}^\dagger & f_{2\sigma}^\dagger \end{pmatrix} \begin{pmatrix} i\partial_t - \epsilon_f - \frac{\delta_1}{\sqrt{2}} & -\frac{\delta_2}{\sqrt{2}} \\ -\frac{\delta_2}{\sqrt{2}} & i\partial_t - \epsilon_f - \frac{\delta_1}{\sqrt{2}} \end{pmatrix} \begin{pmatrix} f_{1\sigma} \\ f_{2\sigma} \end{pmatrix}, \\ S_b &= \int_0^\infty dt \sum_{kh\eta} \begin{pmatrix} b_1^\dagger & b_2^\dagger \end{pmatrix} \begin{pmatrix} -\frac{\delta_2}{\sqrt{2}} & i\partial_t - \frac{\delta_1}{\sqrt{2}} \\ i\partial_t - \frac{\delta_1}{\sqrt{2}} & -\frac{\delta_2}{\sqrt{2}} \end{pmatrix} \begin{pmatrix} b_1 \\ b_2 \end{pmatrix}, \\ S_{\text{hyb}} &= \sum_{kh} \tilde{V}_k \left(f_{1\uparrow}^\dagger (b_1 \Lambda_{1Lkh} + b_2 \Lambda_{2Lkh}) + f_{2\uparrow}^\dagger (b_1 \Lambda_{2Lkh} + b_2 \Lambda_{1Lkh}) + gc \right) \\ &\quad + \sum_{kh} h \tilde{V}_k \left(f_{1\downarrow}^\dagger (b_1 \Lambda_{1Rkh} + b_2 \Lambda_{2Rkh}) + f_{2\downarrow}^\dagger (b_1 \Lambda_{2Rkh} + b_2 \Lambda_{1Rkh}) + gc \right). \end{aligned} \quad (3.55)$$

By integrating out the bath and impurity operators (Λ , f), the partition function simplifies to $\mathcal{Z}_{\text{eff}} = \int [b, \delta] e^{-S_{\text{eff}}}$. The saddle point equations are derived by setting $\langle \delta S_{\text{eff}} / \delta b_{1,2} \rangle = 0$ and $\langle \delta S_{\text{eff}} / \delta \delta_{1,2} \rangle = 0$:

$$\begin{aligned} 0 &= \sum_{\alpha=1,2} \left[\left(i\partial_t - \frac{\delta_\alpha}{\sqrt{2}} \right) b_{\bar{\alpha}} - \frac{\delta_{\bar{\alpha}}}{\sqrt{2}} b_\alpha \right. \\ &\quad \left. - \frac{1}{\sqrt{2}} \sum_{kh} \tilde{V}_{kh} \left(\langle \Lambda_{\alpha Lkh}^\dagger f_{\alpha\uparrow} \rangle + \langle \Lambda_{\bar{\alpha} Lkh}^\dagger f_{\bar{\alpha}\uparrow} \rangle - h \langle \Lambda_{\alpha Rkh}^\dagger f_{\alpha\downarrow} \rangle - h \langle \Lambda_{\bar{\alpha} Rkh}^\dagger f_{\bar{\alpha}\downarrow} \rangle \right) \right], \\ \sum_\sigma \left(\langle f_{1\sigma}^\dagger f_{1\sigma} \rangle + \langle f_{2\sigma}^\dagger f_{2\sigma} \rangle \right) + \langle b_1^\dagger b_2 \rangle + \langle b_2^\dagger b_1 \rangle &= 0, \\ \sum_\sigma \left(\langle f_{1\sigma}^\dagger f_{2\sigma} \rangle + \langle f_{2\sigma}^\dagger f_{1\sigma} \rangle \right) + \langle b_1^\dagger b_1 \rangle + \langle b_2^\dagger b_2 \rangle - 2 &= 0. \end{aligned} \quad (3.56)$$

In the steady state, setting $b_2 = \delta_2 = 0$, we obtain:

$$\begin{aligned} \frac{\delta_1}{\sqrt{2}}b_1 + \sum_{kh} \tilde{V}_{kh} \langle \Lambda_{2Lkh}^\dagger f_{1\uparrow} \rangle &= 0, \\ \sum_{\sigma} \langle f_{2\sigma}^\dagger f_{1\sigma} \rangle + b_1^\dagger b_1 - 2 &= 0. \end{aligned} \quad (3.57)$$

The Kondo scale T_K is expressed as:

$$T_K = c_N (D - \mu + \lambda)^{1/N} (D + \mu - \lambda)^{1-1/N} e^{\frac{(D^2 - \lambda^2)(\epsilon_d - \mu)}{A_N \rho_0 V^2}}, \quad (3.58)$$

and in the large- N limit:

$$T_K \approx (D + \mu - \lambda) e^{\frac{(D^2 - \lambda^2)(\epsilon_d - \mu)}{2D A_N \rho_0 V^2}}. \quad (3.59)$$

3.6.1 Current Calculation Within Mean Field Theory

In the Keldysh field theory framework, the current J_L through the system is derived from the lesser Green's function $G_{\{O_1, O_2\}}^<$, using the relation between the retarded and lesser Green's functions:

$$J_L = \int d\omega \frac{2e}{\hbar} \sum_{kh} \text{FT} \left(u_{kh} v_{kh}^* f(E_{kh+}) e^{-iE_{kh+}(t-t')} - u_{kh} v_{kh}^* f(E_{kh-}) e^{-iE_{kh-}(t-t')} \right), \quad (3.60)$$

with the final expression:

$$J_L = \sum_h \oint \frac{\sqrt{\frac{3}{4} - \frac{V^2}{\epsilon}} \rho(\epsilon)}{\omega - \frac{2+2V^2}{\epsilon}} d\epsilon_k. \quad (3.61)$$

3.7 Discussion and Conclusion

We have come-up with a technique which serves as a initial conditions for self-consistency or convergence in complex valued coupled equation minimization by identifying the fixed points of the Callan-Symmanzik equation. Exploring non-Hermitian systems often leads discrepancies between methods due to the presence different type of dissipation. These differences often arise from the inherent model properties or method's assumptions in each approach, leading to qualitative variations in the outcomes.

For instance, the Auxiliary Particle-Boson Renormalization Group (RG) method is effective in capturing the local moment and Kondo regimes in non-Hermitian settings. However, it may fail to detect phenomena such as RG

reversion, where the system reverts towards the non-interacting fixed point after initially deviating from it. This observation contrasts with findings from other perturbative RG methods, which report a complete reversal in RG behavior, often referred to as a "Violation of the g-theorem." Such outcomes are consistent with results from Poorman scaling methods, as noted in several references^{9–12}. Despite its limitations, particularly in fully capturing the system's behavior, the Auxiliary Particle-Boson RG method remains valuable as a low-energy effective field theory. This necessitates the more advanced techniques such as the NRG to understand phenomena like RG reversion, ground state properties and the steady states of a non-equilibrium/driven system.

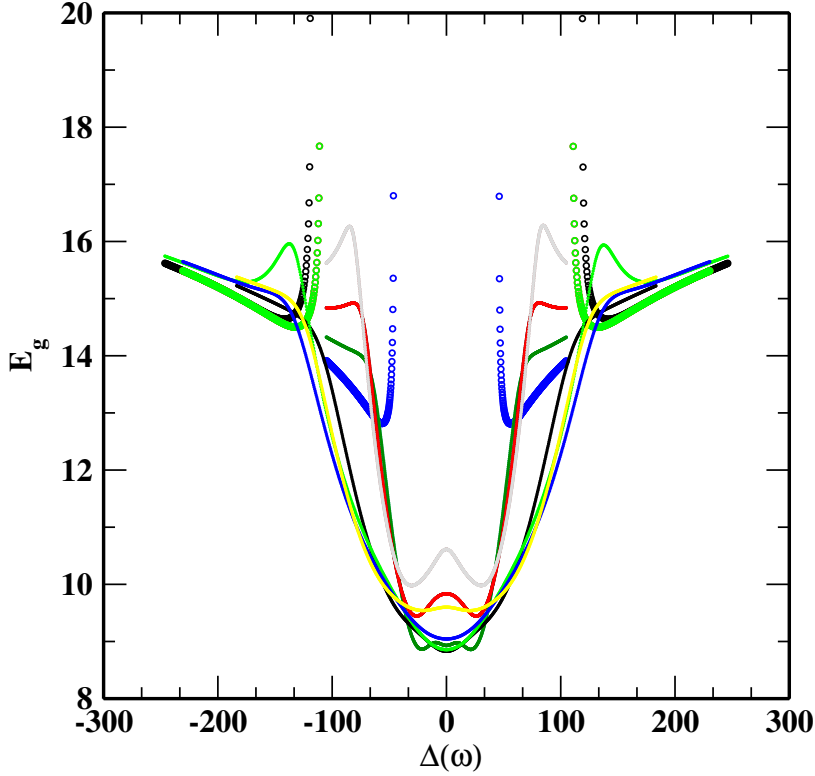


Figure 3.6: Ground State computed from impurity action as a function of NH-Hybridization in the non-interacting case. Different colors represent computed ground state energy for different bare values of hybridization. Effective impurity action and Eq. 3.26 are utilized to compute free energy/ E_g .

Bibliography

- [1] J. Braun, Y.-r. Chen, W.-j. Fu, A. Geißel, J. Horak, C. Huang, F. Ihssen, J. M. Pawłowski, M. Reichert, F. Rennecke, *et al.*, SciPost Physics Core **6**, 061 (2023).
- [2] L. Fritz, S. Florens, and M. Vojta, Phys. Rev. B **74**, 144410 (2006).
- [3] D. D. Scherer and H. Gies, Phys. Rev. B **85**, 195417 (2012).
- [4] L. Tincani, R. M. Noack, and D. Baeriswyl, Phys. Rev. B **79**, 165109 (2009).
- [5] S. Parameswaran, R. Shankar, and S. L. Sondhi, Physical Review B **82**, 195104 (2010).
- [6] R. Frésard, M. Dzierzawa, and P. Wölfle, EPL (Europhysics Letters) **15**, 325 (1991).
- [7] R. Frésard and T. Kopp, Annalen der Physik **524**, 175 (2012).
- [8] R. Frésard, H. Ouerdane, and T. Kopp, EPL (Europhysics Letters) **82**, 31001 (2008).
- [9] M. Nakagawa, N. Kawakami, and M. Ueda, Phys. Rev. Lett. **121**, 203001 (2018).
- [10] J. A. S. Lourenço, R. L. Eneias, and R. G. Pereira, Phys. Rev. B **98**, 085126 (2018).
- [11] V. M. Kulkarni, arXiv preprint arXiv:2211.00333 (2022).
- [12] V. M. Kulkarni, arXiv preprint arXiv:2303.10731 (2023).

Chapter 4

RG Analysis Of Complex \mathcal{DM} interaction in Kondo problem

The chapter focuses on the study of \mathcal{PT} -transitions in a many-body Hamiltonian with finite interactions. It investigates the complex physics arising from the interplay between correlation, parity-breaking interactions, and non-Hermiticity. Specifically, renormalization calculations are performed on the projected low-energy, singly-occupied subspace, revealing the diverse physics and the emergence of a Kondo-non-Kondo phase diagram. The competition between correlations and non-Hermitian interactions leads to the formation of many-body singlets and unique phenomena, such as the decoupling of the impurity in the Kondo problem. The chapter sheds light on the intricate behavior of systems with finite interactions, providing insights into the scaling properties and the transition between different magnetic phases.

Manuscript under preparation

4.1 Introduction

The investigation of non-Hermitian (NH) interactions in cold atom systems has gained significant attention in recent years. These NH interactions arise from the continuous Zeno effect, which occurs due to the depletion of atoms in a subsystem. We propose to study the NonKondo-Kondo(NKK) transition in ^{171}Yb and ^{173}Yb atoms¹⁻⁴ to investigate NH interactions, specifically focusing on the internal degrees of freedom caused by spin-orbit interactions in a system with a balance of loss and gain.

Experimental observations have shown that transitions between different atomic states, such as $^1s_0 \rightarrow ^3P_0$, and $^3P_0 \rightarrow ^3s_1$, are allowed in these cold atom systems. In a balanced gain-loss scenario, the stable state is found to be 3P_0 , and there is a possibility of Kondo cloud formation in the strong coupling, anti-ferromagnetic regime. Our study aims to trace the origin of NH interactions to the bath channels and develop an effective impurity model that incorporates an imaginary \mathcal{DM} interaction. This interaction plays a stabilizing role in the triplet ground state within the symmetry-preserved regime. Recent experimental findings have observed a stable triplet ground state in a pumping-repumping situation, and our explanation involves the imaginary \mathcal{DM} interaction and potential scattering terms⁵.

Spin-orbit (SO) interactions are known to play a crucial role in various lattice problems, such as impurities in graphene and nanoribbons⁶⁻¹⁰. In these systems, SO interactions, particularly of the Rashba type, break parity symmetry. However, despite this symmetry breaking, it is still possible to have \mathcal{PT} -symmetric channels and \mathcal{DM} interaction in the effective impurity model through the influence of SO interactions. Renormalization group (RG) methods, including Numerical Renormalization Group (NRG), Poorman scaling, and Dynamical Mean Field Theory (DMFT), have been successfully employed to study the effects of SO interactions in conventional problems. Additionally, Anderson impurities in topological insulators, such as honeycomb lattices, Bi_2Se_3 , and Bi_2Te_3 , have shown phase transitions with strong SO interactions.

However, in the context of non-Hermitian (NH) systems, the physics and role of SO interactions may differ from conventional systems. In NH systems, phase transitions can be driven by imaginary interactions that are independent of the lattice structure. It becomes important to investigate the interplay between SO interactions and NH effects. While the conventional closed systems exhibit phase transitions with strong SO interactions in certain lattice structures, in NH systems, phase transitions can occur even in

the absence of a specific lattice structure, solely driven by imaginary interactions^{11;12}.

Therefore, our proposed study aims to explore the role of SO interactions in the presence of NH effects, specifically in the context of the NKK transition in ^{171}Yb and ^{173}Yb atoms. By studying these NH systems with a balance of loss and gain, we aim to understand how the internal degrees of freedom, influenced by spin-orbit interactions, contribute to the NH interactions and the formation of stable ground states. The investigation of the interplay between SO interactions and NH effects will provide valuable insights into the unique physics of NH systems and contribute to our understanding of the broader field of condensed matter physics.

In the context of our study, we place particular emphasis on the perturbative renormalization group (RG) approach. As a result, we refer to the literature that discusses perturbation theory applied to non-Hermitian systems.

4.2 Projection Operator Method

The projection operator method divides the Hilbert space into subspaces: one containing the relevant states and another with irrelevant states. By projecting onto these subspaces, we obtain a reduced Hamiltonian that captures the essential physics of the system. Several works address non-Hermitian projection in first-quantization^{13–16}.

For the Kondo problem, this method allows us to focus on the relevant singly occupied states while excluding doubly occupied and unoccupied states, simplifying the system for renormalization.

However, in cases such as non-number conserving models or systems with \mathcal{PT} -symmetry breaking, the completeness of the projected subspace may be violated. This issue will be further explored in subsequent sections.

The completeness relation $\sum_i P_i = \sum_i |\psi_i\rangle\langle\psi_i| = \mathbf{I}$ allows the construction of projection operators. Inserting identity operators into the Schrödinger equation $H\psi = E\psi$, we have:

$$\left(\sum_{i=0}^2 |\psi_i\rangle\langle\psi_i|\right) H \left(\sum_{i=0}^2 |\psi_i\rangle\langle\psi_i|\right) \psi = E \left(\sum_{i=0}^2 |\psi_i\rangle\langle\psi_i|\right) \psi$$

The identity operators can be written as projectors for the unoccupied, singly occupied, and doubly occupied subspaces, which are orthogonal.

$$\left(\sum_{i=0}^2 |\psi_i\rangle\langle\psi_i|\right) H \left(\sum_{i=0}^2 |\psi_i\rangle\langle\psi_i|\right) \left(\sum_{i=0}^2 |\psi_i\rangle\langle\psi_i|\right) \psi = E \left(\sum_{i=0}^2 |\psi_i\rangle\langle\psi_i|\right) \psi \quad (4.1)$$

These identity operators can be written as the projectors for $(0, 1, 2)$, which correspond to not occupied, singly occupied, and doubly occupied subspaces, and are orthogonal.

$$\begin{pmatrix} H_{00} & H_{01} & H_{02} \\ H_{10} & H_{11} & H_{12} \\ H_{20} & H_{21} & H_{22} \end{pmatrix} \begin{pmatrix} \psi_0 \\ \psi_1 \\ \psi_2 \end{pmatrix} = E \begin{pmatrix} \psi_0 \\ \psi_1 \\ \psi_2 \end{pmatrix} \quad (4.2)$$

where $P_m P_n = \delta_{mn} P_{m=n}$ and $P^k = P$

An effective Hamiltonian can be derived from the above for different subspaces by eliminating the respective wave function in favor of the other.

$$H_\alpha^{eff} = H_{\alpha\alpha} + \sum_{\alpha' \neq \alpha} H_{\alpha\alpha'} \frac{1}{E - H_{\alpha'\alpha'}} H_{\alpha'\alpha} \quad (4.3)$$

The Hermitian problem will have the $H_{\alpha\alpha'}^\dagger = H_{\alpha'\alpha}$; However for preserving pseudoHermiticity we need to have $\mathcal{PT} H \mathcal{PT}^\dagger = H^\dagger$, where the \mathcal{PT} operator is the metric operator, denoted as $\hat{\eta}$ in the previous chapter. Additionally, excitations from the unoccupied to the doubly occupied sector and vice-versa are absent (due to the structure of the Hamiltonian), hence $H_{02} = H_{20} = 0$. We use Projection operators for the SOC coupled non-Hermitian Anderson model studied in our previous work¹⁷. In this work, we start with the model in the spin basis of impurity operators and project it onto the low-energy subspace.

$$\begin{aligned} H = & \sum_{k\eta h} \epsilon_{k\eta h} c_{kh\eta}^\dagger c_{kh\eta} + \epsilon_d n_{d\sigma} + U n_{d\uparrow} n_{d\downarrow} \\ & + \sum_{kh} X_k \left[c_{kLh}^\dagger d_\uparrow + h c_{kRh}^\dagger d_\downarrow + h.c. \right] \\ & + \sum_{kh} X_k^* \left[c_{kLh}^\dagger d_\downarrow + h c_{kRh}^\dagger d_\uparrow + h.c. \right] \end{aligned} \quad (4.4)$$

This model in the eqn 6.1 is borrowed from appendix eqn (B9) of the earlier work¹⁷, and it is shown to be Anderson Model in chiral basis as the following,

$$H = \sum_{kh\eta} \tilde{\epsilon}_{kh} c_{kh\eta}^\dagger c_{kh\eta} + \sum_{k\eta h} X_{k\eta h} \left(c_{k\eta h}^\dagger d_h + h.c. \right) + \epsilon_d \sum_h n_{dh} + U n_{d+} n_{d-} \quad (4.5)$$

In the model, the parameters X_{kRh} and X_{kLh} are given by $X_{kRh} = -h(V + \omega e^{i\phi})$ and $X_{kLh} = -hX_{Rh}^*$, respectively. The projection operators in the chiral basis are defined as $P_0 = (1 - n_+)(1 - n_-)$ for unoccupied states, $P_1 = n_+(1 - n_-) + n_-(1 - n_+)$ for singly occupied states, and $P_2 = n_+n_-$ for doubly occupied states. For the Projection operator method (POM) to apply to non-Hermitian systems, it must satisfy the pseudo-Hermiticity condition, which is discussed in Appendix A. The model expressed in chiral operators can be transformed back to the original operators using an inverse mapping given by $\{O_{kh}, O_h\} \rightarrow \{O_{km\sigma}, O_\sigma\}$ that is nothing but $O_{kh} = \frac{1}{\sqrt{2}}(O_{k\uparrow} + hO_{k\downarrow})$ similarly for impurity operators $O_h = \frac{1}{\sqrt{2}}(O_\uparrow + hO_\downarrow)$, where O_{kh} and O_h represent the bath and impurity operators, respectively.

4.3 Projection in the Chiral Basis

The SOC-coupled model can now be written as the new Anderson model in chiral operators. We show here projection on the same basis to compare with the earlier results.

$$H_{10} = \sum_{\eta kh} X_{k\eta h} d_h^\dagger (1 - n_{\bar{h}}) c_{k\eta h}, \quad H_{12} = \sum_{kh} X_{k\eta h} d_h^\dagger n_{\bar{h}} c_{k\eta h} \quad (4.6)$$

Remaining components are $H_{00} = \sum_{k\alpha} \epsilon_{k\alpha} c_{k\alpha}^\dagger c_{k\alpha} P_0 + \sum_{\sigma} \epsilon_d n_{\sigma} P_0$ and $H_{22} = \sum_{k\alpha} \epsilon_{k\alpha} c_{k\alpha}^\dagger c_{k\alpha} P_2 + \sum_{\sigma} \epsilon_d n_{\sigma} P_2 + U n_{\uparrow} n_{\downarrow} P_2$. Now we have all the components to calculate the effective models in various sub-spaces (0, 1, 2) as in equation 4.3. The effective model in singly occupied subspace can largely be divided into $\eta = \eta'$ and $\eta \neq \eta'$ Hamiltonian where η here refers to left or right lead. We detail the derivation as follows,

$$\begin{aligned} [H_{eff}^1] &= [Rh, Rh'] + [Lh, Lh'] + [Lh, Rh'] + [Rh, Lh'] \\ &= \sum_{kk'hh'} X_{Rkh} X_{Rk'h'} M_h \mathbf{S}_{kk'}^{RR} + \sum_{kk'hh'} X_{Lkh} X_{Lk'h'} M_h \mathbf{S}_{kk'}^{LL} \\ &\quad + \sum_{kk'hh'} X_{Rkh} X_{Lk'h'} M_h \mathbf{S}_{kk'}^{RL} + \sum_{kk'hh'} X_{Lkh} X_{Rk'h'} M_h \mathbf{S}_{kk'}^{LR} \end{aligned} \quad (4.7)$$

where in above equation 4.7 $X_{kLh} = \sqrt{2}|X_k|e^{i\phi_k}$ and $X_{kRh} = -hX_{kLh}^*$. It is important to note that when $\lambda = 0$, the M_h elements are the same for all, but they become $M_h = M_{kk'}(1 + h\lambda M_{kk'})$ and the matrix elements are $M_{kk'} = \frac{1}{\epsilon_{k'} - \epsilon_d} + \frac{1}{\epsilon_{k'} + \epsilon_d + U}$ can be approximated to $M = \frac{1}{-\epsilon_d} + \frac{1}{\epsilon_d + U}$ at Fermi-level ($\epsilon_k = \epsilon_{k'} = \epsilon_f = 0$). Model in equation 4.7 exhibits pseudo-Hermiticity,

with non-Hermitian terms appearing only in the RR and LL Kondo models, while the LR and RL blocks are real.

$$\begin{aligned}
H_{eff}^1 = & \sum_{kk'h} |X_k|^2 e^{i(\phi_k + \phi_{k'})} M_h \mathbf{S} \cdot \mathbf{s}_{kk'}^{RR} + \sum_{kk'h} |X_k|^2 e^{i(\phi_k + \phi_{k'})} M_{\bar{h}} \mathbf{S} \cdot \mathbf{s}_{kk'}^{RR} \\
& \sum_{kk'h} |X_k|^2 e^{-i(\phi_k + \phi_{k'})} M_h \mathbf{S} \cdot \mathbf{s}_{kk'}^{LL} + \sum_{kk'h} |X_k|^2 e^{-i(\phi_k + \phi_{k'})} M_{\bar{h}} \mathbf{S} \cdot \mathbf{s}_{kk'}^{LL} \\
& - \sum_{kk'h} |X_k|^2 e^{i(\phi_k - \phi_{k'})} M_h \mathbf{S} \cdot \mathbf{s}_{kk'}^{RL} + \sum_{kk'h} |X_k|^2 e^{i(\phi_k - \phi_{k'})} M_{\bar{h}} \mathbf{S} \cdot \mathbf{s}_{kk'}^{RL} \\
& - \sum_{kk'h} |X_k|^2 e^{i(\phi_k - \phi_{k'})} M_h \mathbf{S} \cdot \mathbf{s}_{kk'}^{LR} + \sum_{kk'h} |X_k|^2 e^{i(\phi_k - \phi_{k'})} M_{\bar{h}} \mathbf{S} \cdot \mathbf{s}_{kk'}^{LR}
\end{aligned} \tag{4.8}$$

In the above equation 4.8, the model is expanded over chiral index h . This can be simplified and can be written as follows,

$$\begin{aligned}
H_{eff}^1 = & \sum_{kk'\eta\eta'} X_{\eta+} X_{\eta'+} M S^z \cdot s_{kk'}^{z\eta\eta'} + \sum_{kk'\eta\eta'} X_{\eta-} X_{\eta'-} M S^z \cdot s_{kk'}^{z\eta\eta'} \\
& + \sum_{kk'\eta\eta'} X_{\eta+} X_{\eta'-} M S^+ s_{kk'}^{-\eta\eta'} + \sum_{kk'\eta\eta'} X_{\eta-} X_{\eta'+} M s_{kk'}^{+\eta\eta'} S^- \\
& + \lambda M^2 \sum_{kk'\eta\eta'} X_{\eta+} X_{\eta'-} (-S^+ s_{kk'}^{-\eta\eta'} + s_{kk'}^{+\eta\eta'} S^-)
\end{aligned} \tag{4.9}$$

In the above equation 4.9 we can notice the term $(-S^+ s_{kk'}^{-\eta\eta'} + S^- s_{kk'}^{+\eta\eta'}) = i(S^x s_{kk'}^{y\eta\eta'} - s_{kk'}^{x\eta\eta'} S^y) = 2i(S \times s_{kk'}^{\eta\eta'})_z$ which is the \mathcal{DM} -interaction in chiral operators. We can write the above model as the following using Lie matrices which are written with $SU(2)$ matrices which are also given in works^{18–20}. These matrices were employed to do diagonalization in parallel to the CFT work²⁰.

$$\begin{aligned}
H_{eff} = & H_0 + M(\psi^\dagger \Sigma \psi \cdot S + iX_i \psi^\dagger \Omega \psi \cdot S - X_r \psi^\dagger \Gamma \psi \cdot S) \\
& + 2i\lambda M^2 \left((\psi^\dagger \Sigma \psi + X_i^2 \psi^\dagger \Omega \psi - X_r^2 \psi^\dagger \Gamma \psi) \times S \right)_z + H_{pot}
\end{aligned} \tag{4.10}$$

Using the Spinor $\psi^\dagger = (c_{kR+}^\dagger \quad c_{kR-}^\dagger \quad c_{kL+}^\dagger \quad c_{kL-}^\dagger)$ We drop potential scattering terms to diagonalize later these terms will be considered in Poorman scaling,

$$\begin{aligned}
H_{eff} = & H_0 + M(|X|^2 \psi^\dagger \Sigma \psi \cdot S + iX_i^2 \psi^\dagger \Omega \psi \cdot S - X_r^2 \psi^\dagger \Gamma \psi \cdot S) \\
& + 2i\lambda M^2 \left((|X| \psi^\dagger \Sigma_x \psi + X_i^2 i \psi^\dagger \Omega_x \psi - X_r^2 \psi^\dagger \Gamma_x \psi) S_y \right. \\
& \left. - S_x (\psi^\dagger \Sigma_y \psi + X_i^2 i \psi^\dagger \Omega_y \psi - X_r^2 \psi^\dagger \Gamma_y \psi) \right)
\end{aligned} \tag{4.11}$$

We diagonalize the above model in equation 4.11 by rewriting couplings as $J_0 = M|X|^2$, $J_r = \text{Re}(X_r^2 M)$, $J_i = X_i^2 M$, and the ratio $g = \frac{J_i}{J_0}$ and the results are shown in figure 4.1. As the strength of the SOC increases, the exceptional point of the eigenvalues in the (1,1) sector of the Kondo model continues to decrease. We have a good comparison to CFT work²⁰ for $\lambda = 0.0$ and in intermediate λ we have coalescence in imaginary eigenvalues as well, for example, see plot $\lambda = 0.4$. For higher λ we have nontrivial topology in complex eigenvalues see $\lambda = 0.99$.

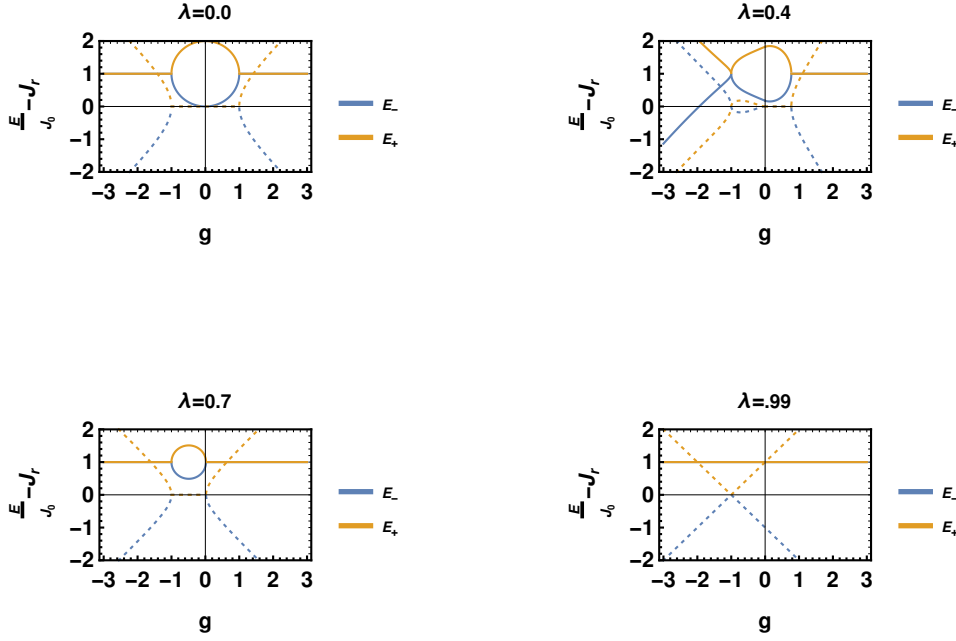


Figure 4.1: In equation 4.11, we demonstrate the fluctuations in the lowest eigenvalues E_{\pm} of the Kondo model by adjusting the strength of SOC (λ). The plots display thick lines for real eigenvalues and dotted lines for imaginary eigenvalues. The y-axis indicates $\frac{E}{J_0} - J_r$, which represents shifted eigenvalues.

Now we show that the projected model is consistent with the zarea⁷ et al. by transforming back to the spin operators. The key difference between the above chiral model to the spin basis one is a different form of the potential scattering. we get the following effective model after inverting relations in terms of spin operators.

$$\begin{aligned}
H_{eff} = & H_K + \sum_{kk'\sigma} (J_r + \sigma i J_i) S^z c_{k\sigma}^{0\dagger} c_{k'\sigma}^0 + H_{\mathcal{DM}} + \sum_{kk'} \gamma \mathbf{S} \cdot \mathbf{s}_{kk'}^\gamma + H_{pot} \\
& + \sum_{kk'} \Lambda \cdot (e^{2i\phi_k} \mathbf{s}_{kk'}^+ \times \mathbf{S} + e^{-2i\phi_k} \mathbf{s}_{kk'}^- \times \mathbf{S})
\end{aligned} \tag{4.12}$$

Where in the above equation the couplings J_r and J_i correspond to real and imaginary parts originating from NH hybridization. These couplings in the above model may be explicitly written as $J_r = \text{Re}(X_k^* X_{k'} M_{kk'})$, $J_i = \text{Im}(X_k^* X_{k'} M_{kk'})$, $\Lambda = |X_k^* X_{k'}| \lambda_{SO} M_{kk'}$ and $\gamma = |X_k^* X_{k'}| M_{kk'}$. The Kondo model in a rotated bath is described by the Hamiltonian:

$$H_K = \sum_{k,m,\sigma} \tilde{\epsilon}_{k\sigma} c_{km\sigma}^\dagger c_{km\sigma} + \sum_{k,k'} J_0 \mathbf{S} \cdot \mathbf{s}_{kk'} \quad (4.13)$$

Here, $\tilde{\epsilon}_{k\sigma} = \epsilon_k + h\lambda$ represents the energy dispersion in the rotated bath, where ϵ is the dispersion of the original bath and $h\lambda$ is a Zeeman-like term.

The Hamiltonian also includes a Hermitian Dzyaloshinskii-Moriya (\mathcal{DM}) term given by:

$$H_{\mathcal{DM}} = \sum_{k,k'} \Lambda. (\mathbf{s}_{kk'}^\Lambda \times \mathbf{S}) \quad (4.14)$$

In addition, there is a non-Hermitian \mathcal{DM} term denoted as $H_{\mathcal{DM}}^{\mathcal{PT}}$, which is expressed as:

$$H_{\mathcal{DM}}^{\mathcal{PT}} = \sum_{k,k'} \Lambda. (e^{2i\phi} \mathbf{s}_{kk'}^+ \times \mathbf{S} + e^{-2i\phi} \mathbf{s}_{kk'}^- \times \mathbf{S}) \quad (4.15)$$

These spinors, denoted by $\mathbf{s}_{kk'}$, represent Abrikosov's conduction electron spin²¹. The term $H_\gamma = \sum_{k,k'} \gamma \mathbf{s}_{kk'}^\gamma \cdot \mathbf{S}$ arises from the projection to an effective model, which involves scattering between the $m = 1$ to $m = -1$ bath states.

The expressions for the spinors are as follows:

$$\mathbf{s}_{kk'} = c_s^{0\dagger} \tau_{ss'} c_{s'}^0 \quad (4.16)$$

$$\mathbf{s}_{kk'}^\gamma = c_{ks}^{-1\dagger} \tau_{ss'} c_{k'-s'}^1 \quad (4.17)$$

$$\mathbf{s}_{kk'}^- = c_{k-s}^{0\dagger} \tau_{ss'} c_{ks'}^{-1} + c_{ks}^{-1\dagger} \tau_{ss'} c_{k-s'}^0 \quad (4.18)$$

Finally, the term $H_{\text{pot}} = \sum_{k,k'} k_\gamma \mathbf{S} \cdot \mathbf{s}_{kk'}^\gamma$ represents potential scattering terms in the Hamiltonian, and γ denotes the scattering channel. The presence of potential scattering terms contributes in a non-trivial way to the overall dynamics and behavior of the system.

4.4 Poorman Scaling With Metric Operators

In earlier work by Kulkarni et al.¹⁷, the concept of Pseudo Hermiticity of the Hamiltonian (PHH) was discussed, primarily using metric operators in the spin basis to confirm the condition $(\hat{\mathcal{PT}})H(\hat{\mathcal{PT}})^\dagger = H^\dagger$. To ensure

PHH is maintained consistently across every perturbation order, we have extended this operation to each vertex. This guarantees that PHH is satisfied at all levels of the perturbation theory. This operation is executed with the operator $\hat{\mathcal{PT}} = -e^{i\theta}c_{-\frac{1}{2}\uparrow}^\dagger c_{\frac{1}{2}\uparrow} - e^{-i\theta}c_{-\frac{1}{2}\downarrow}^\dagger c_{\frac{1}{2}\downarrow} + hc + \sum_{\sigma} n_{\sigma}$. Alternatively, we have used $\hat{\eta}$ in the chiral basis, in contrast to Chapter 2.

Using canonical relations $O_{\eta h} = \frac{1}{\sqrt{2}}(O_{\pm\frac{1}{2}\uparrow} + hO_{\pm\frac{1}{2}\downarrow})$ where O can be either bath operators or impurity operators, and generic phase factors to avoid ambiguity from angular momentum channel states, we get the $\hat{\mathcal{PT}}$ operator. These obey the algebra with impurity operators and bath operators (here, phase factors are dropped for notational convenience for details, refer to Appendix A) as the following,

$$\begin{aligned} [S_z, \hat{\mathcal{PT}}] &= 0, \quad [S_{\pm}, \hat{\mathcal{PT}}] = -S_{\mp} \\ [c_{k\sigma}^{0\dagger} c_{k\sigma}^0, \hat{\mathcal{PT}}] &= 0, \quad [c_{k\sigma}^{0\dagger} c_{k\bar{\sigma}}^0, \hat{\mathcal{PT}}] = -c_{k\sigma}^{0\dagger} c_{k\sigma}^0 \\ [c_{k\sigma}^{m\dagger} c_{k\sigma'}^{m'}, \hat{\mathcal{PT}}] &= (1 - \delta_{m,m'} \delta_{\sigma\sigma'}) c_{k\sigma}^{m\dagger} c_{k\sigma'}^{m'} \end{aligned} \quad (4.19)$$

The metric operator ($\hat{\mathcal{PT}}$) in the $(\eta h) \rightarrow (m\sigma)$ basis can be written as the following,

$$\begin{aligned} \{\hat{\mathcal{PT}}, n_{\sigma} + c_{\pm\frac{1}{2}\sigma}^\dagger c_{\pm\frac{1}{2}\sigma}\} &= 2(\hat{\mathcal{PT}} - n_{\sigma}) + 2\hat{\mathcal{PT}} n_{\sigma} \\ \left[\hat{\mathcal{PT}}, n_{\sigma} + c_{\pm\frac{1}{2}\sigma}^\dagger c_{\pm\frac{1}{2}\sigma} \right] &= -2(\hat{\mathcal{PT}} - n_{\sigma}) \end{aligned} \quad (4.20)$$

The method involving the insertion of metric operators at each vertex, coupled with the algebra elucidated in equations 4.19 and 4.20, plays a crucial role in maintaining the global number, particularly when dealing with the emergence of flip terms during the evaluation of Feynman diagrams for one- and two-spin flip processes. This approach effectively ensures the preservation of symmetry throughout the calculation. Electron-hole scattering can introduce symmetry-breaking corrections to the unperturbed propagators. The perturbation theory for non-Hermitian problems often poses challenges in getting the corrections hence we argue that it is crucial to preserve the symmetry at every vertex by inserting the metric operators¹⁷. We show at the one-loop level, the clear comparison with the earlier works^{7;20} (for limits $\lambda \rightarrow 0$ and $\phi \rightarrow 0$ respectively) can be made and discussed in later sections. At higher loops, the particle number conserving diagrams are essential for the flow and renormalization of the non-Hermitian phase within Poorman scaling. A natural extension of the usual formalism²² can be represented as follows,

$$\begin{aligned} T_{kk'} &= V_{kk'} + V_{k'q} \hat{\mathcal{PT}} G_0(\omega, q) \hat{\mathcal{PT}}^\dagger T_{qk} \\ &+ V_{k'q} \hat{\mathcal{PT}} G_0(\omega, q) \hat{\mathcal{PT}}^\dagger T_{q,q'} \hat{\mathcal{PT}} G_0(\omega, q') \hat{\mathcal{PT}}^\dagger T_{q',k} + \dots \end{aligned} \quad (4.21)$$

A comprehensive proof of the aforementioned statement can be exceedingly intricate for a general case. Instead, we offer a demonstration by considering a select number of vertices, thereby affirming the validity of the Pseudo-Hermiticity condition. To show the algebra we consider all bath states are in angular momentum basis i.e. $\eta = L/R, j_m = \pm \frac{1}{2}\sigma$ the η represents emergent parity. We show the PHH condition at a vertex V satisfying the operation $\mathcal{PTV}\mathcal{PT}^\dagger = V^\dagger$ as follows.

$$\begin{aligned} & (\hat{\mathcal{PT}})(e^{i\phi}c_{+\frac{1}{2}\uparrow}^\dagger d_{\uparrow}^\dagger d_{\downarrow}c_{+\frac{1}{2}\downarrow} + e^{-i\phi}c_{-\frac{1}{2}\downarrow}^\dagger d_{\downarrow}^\dagger d_{\uparrow}c_{-\frac{1}{2}\uparrow})(\hat{\mathcal{PT}})^\dagger \\ &= e^{i\phi}c_{-\frac{1}{2}\uparrow}^\dagger d_{\uparrow}^\dagger d_{\downarrow}c_{-\frac{1}{2}\downarrow} + e^{-i\phi}c_{+\frac{1}{2}\downarrow}^\dagger d_{\downarrow}^\dagger d_{\uparrow}c_{+\frac{1}{2}\uparrow} \end{aligned} \quad (4.22)$$

The following RG equations can be derived from the algebra after expanding over the vertices of the impurity and various AM channels. Apart from the topologically distinct contributions remaining, all other contributions vanish; these are also discussed in various articles^{23–26}. After computing diagrams, it is common to apply Poorman’s approximation²⁷, which involves setting $k = k'$ and modifying the bandwidth D to $D' = D(1 + \lambda/D)$. This approximation simplifies the calculations and allows us to capture the renormalization effects effectively. However, in certain cases where specific symmetries are being broken, such as in the current context, it is necessary to consider the potential scattering terms. These terms, which may be irrelevant in particle-hole symmetry, become relevant in the presence of symmetry-breaking interactions and need to be taken into account for a comprehensive analysis.

$$\frac{dJ}{d\log D'} = J(J - J_r) + \Lambda^2 + J^3 + J_r^2 J + J_i^2 J + \Lambda^2 J \quad (4.23a)$$

$$\frac{d\Lambda}{d\log D'} = \Lambda \left((J - J_r) + \gamma + J_r^2 + J^2 + J\gamma + \gamma^2 + \Lambda^2 \right) \quad (4.23b)$$

$$\frac{dJ_i}{d\log D'} = J_i \left((J - J_r) + \gamma + J^2 + J_r^2 + J\gamma + \gamma^2 + J_i^2 + \Lambda^2 \right) \quad (4.23c)$$

$$\frac{dJ_r}{d\log D'} = J_i^2 - J_r^2 + \Lambda J_i + \Lambda^2 - J_r^3 + J_i^2 (J_r + \gamma + \Lambda) \quad (4.23d)$$

$$\frac{d\gamma}{d\log D'} = \gamma^2 + \Lambda^2 - J_r\gamma + J_r^2\gamma + \gamma^3 + J_i^2\gamma + \Lambda^2\gamma \quad (4.23e)$$

In the equations presented above, the subscripts i and r serve to distinguish between the real and imaginary components of the bare couplings. These Renormalization Group (RG) equations stand as the central outcome of our novel perturbation theory, and we proceed to analyze and delve deeper into these equations in subsequent sections of this work.

4.4.1 RG Invariants Identification

To determine the invariants, we can perform algebraic operations on the equations. For example, subtracting equation 4.23e from equation 4.23a and taking the ratio of equation 4.23c, we obtain the invariant g . Similarly, subtracting equation 4.23e from equation 4.23a and taking the ratio of equation 4.23b, we obtain the invariant s . The explicit expressions for these invariants can be derived, and presented as follows:

$$\frac{\frac{dJ_i}{d \ln D'}}{\frac{dJ}{d \ln D'} - \frac{d\gamma}{d \ln D'}} = \frac{J_i(J - J_r + \gamma + J^2 + J_r^2 + J\gamma + \gamma^2 + J_i^2 + \Lambda^2)}{(J - \gamma)(J - J_r + \gamma + J^2 + J_r^2 + J\gamma + \gamma^2 + J_i^2 + \Lambda^2)} \quad (4.24a)$$

$$\therefore \int \frac{dJ_i}{J_i} = \int \frac{d(J - \gamma)}{(J - \gamma)} \quad (4.24b)$$

$$\log \frac{J_i}{(J - \gamma)} = \text{constant} \quad (4.24c)$$

$$\implies \frac{J_i}{(J - \gamma)} = g \quad (4.24d)$$

$$\frac{\frac{d\Lambda}{d \ln D'}}{\frac{dJ}{d \ln D'} - \frac{d\gamma}{d \ln D'}} = \frac{\Lambda(J - J_r + \gamma + J_r^2 + J^2 + J\gamma + \gamma^2 + \Lambda^2)}{(J - \gamma)(J - J_r + \gamma + J^2 + J_r^2 + J\gamma + \gamma^2 + \Lambda^2)} \quad (4.24e)$$

$$\int \frac{d\Lambda}{\Lambda} = \int \frac{d(J - \gamma)}{(J - \gamma)} \quad (4.24f)$$

$$\log \frac{\Lambda}{(J - \gamma)} = \text{constant} \quad (4.24g)$$

$$\implies \frac{\Lambda}{(J - \gamma)} = s \quad (4.24h)$$

From equations 4.24a and 4.24e, we can identify certain RG invariants that capture the underlying symmetries of the system. For \mathcal{PT} -symmetry, the parameter g serves as the invariant, while for parity (\mathcal{P})-symmetry, the invariant is given by the parameter s . Additionally, the potential scattering coupling γ acts as an asymmetry parameter that can be used to tune the system across different symmetry-breaking regimes.

4.4.2 Comparison With earlier works

Zarea's work⁷ investigated the behavior of a Kondo impurity within a Hermitian context, utilizing the Schrieffer Wolff Transformation (SWT) and Poorman scaling method. An important outcome of their study was the identification of a crossover from a two-channel Kondo (2CK) to a single-channel

Kondo (1CK) behavior in an isotropic dispersion regime. The presence of potential scattering shows the existence of two channels however these will flow to a single channel at a strong coupling fixed point.

Lourenço's work²⁰, on the other hand, delved into the non-Hermitian Anderson problem using the framework of conformal field theory (CFT). Their study derived scaling equations at the one-loop level. In the context of our analysis, we demonstrate the comprehensiveness of our approach by encompassing both of these distinct scenarios. Precisely, our analysis captures the essence of both RG equations, effectively accounting for the absence of spin-orbit interaction in comparison to Lourenço's work²⁰ and the absence of non-Hermiticity in comparison to Zarea's work⁷.

4.4.3 CFT scaling laws at two loops

In parallel to the work by Lourenco et al.²⁰ we derive the scaling laws at two loops to make clear algebraic comparison with the perturbative scaling equations derived in our work.

The current-current correlators in conformal field theory (CFT) algebra for the Kondo problem and two impurity problems were originally done in the work by I. Affleck²⁸.

Along with the general Pauli-matrix algebra, a third-order perturbation theory was employed in the study using the $SU(2)$ commutation relations are worked out below. These commutation relations provide the necessary algebraic structure to investigate the scaling behavior of the model.

A pivotal distinction in Conformal Field Theory (CFT) lies in the fact that perturbations carried out within the Kondo coupling framework are inherently local field-theoretic expansions. Consequently, this local nature of the perturbation ensures the preservation of symmetry, a characteristic that is intrinsic to the matrix algebra outlined above.

In the context of our analysis, it's worth noting that a diagrammatic expansion of third-order perturbation theory has been elaborated upon in the works of I. Affleck^{18;19;28}. Furthermore, natural extensions of these diagrams for Bose-Fermi Kondo models have been extensively detailed in subsequent works^{23–25;28;29}. At the third order of perturbation theory, we derive the

following Renormalization Group (RG) equations.

$$\begin{aligned}
\frac{dJ}{d \log D} &= J(J - J_r) + J^3 + J_r^2 J + J_i^2 J \\
\frac{dJ_i}{d \log D} &= J_i \left((J - J_r) + J^2 + J_r^2 + J_i^2 \right) \\
\frac{dJ_r}{d \log D} &= J_i^2 - J_r^2 - J_r^3 + J_i^2 J_r
\end{aligned} \tag{4.25}$$

Poorman scaling equations in 4.23 derived from our perturbation theory reduces to these equations in 4.23 in the limits of $\gamma \rightarrow 0$, $\Lambda \rightarrow 0$ validating our method.

4.4.4 Kondo Scale in one loop Poorman scaling

We initially focus on one-loop contributions without considering scattering effects to derive the Kondo scale. The inclusion of potential scattering terms will be addressed in a comprehensive analysis.

$$\begin{aligned}
\frac{dJ}{d \ln D'} &= J(J - J_r), \quad \frac{d\Lambda}{d \ln D'} = \Lambda(J - J_r) \\
\frac{dJ_i}{d \ln D'} &= J_i(J - J_r), \quad \frac{dJ_r}{d \ln D'} = J_i^2 - J_r^2 + \Lambda J_i + \Lambda^2
\end{aligned} \tag{4.26}$$

We analytically solve the equations in 4.26 by introducing substitutions, specifically $g = \frac{J_i}{J_0}$ and $s = \frac{\Lambda}{J_0}$. This simplifies the problem to a single differential equation: $\frac{dJ}{dJ_r} = \frac{J(J - J_r)}{g^2 J^2 - J_r^2 + s g J^2 + s^2 J^2}$, which possesses the following analytic solution.

$$\begin{aligned}
J_r &= C \left(-\alpha \frac{J_0}{J_r} + 1 \right)^{\alpha-1} \left(\frac{J_0}{J_r} \right)^{-\alpha} e^{\frac{J_r}{J_0}} \\
\text{where } C &= \frac{\tilde{J}}{\tilde{J}_r} = -\frac{\ln T_K}{J_r}, \quad \alpha = (g^2 + s^2 + g s) \\
T_K &= \exp \left\{ -\frac{J_r^2}{\left(-\alpha \frac{J_0}{J_r} + 1 \right)^{\alpha-1} \left(\frac{J_0}{J_r} \right)^{-\alpha}} e^{-\frac{J_r}{J_0}} \right\}
\end{aligned} \tag{4.27}$$

A plot of the Kondo Scale (T_K) for equation 4.27 is shown in figure 4.2 for varying NH invariants and a fixed Rashba Spin-Orbit Coupling (RSO) strength. The interchangeability of g and s in equation 4.27 implies that

Kondo destruction is always present, and a small increase in the Kondo scale can be observed over a range of g or s values while fixing the other invariant. At one loop level, two phases can be qualitatively observed, where a small increase in scale corresponds to the Kondo phase and the scale vanishing point corresponds to QCP. Zarea et al.⁷ also found that the Kondo scale increases with RSO while NH interaction is absent.

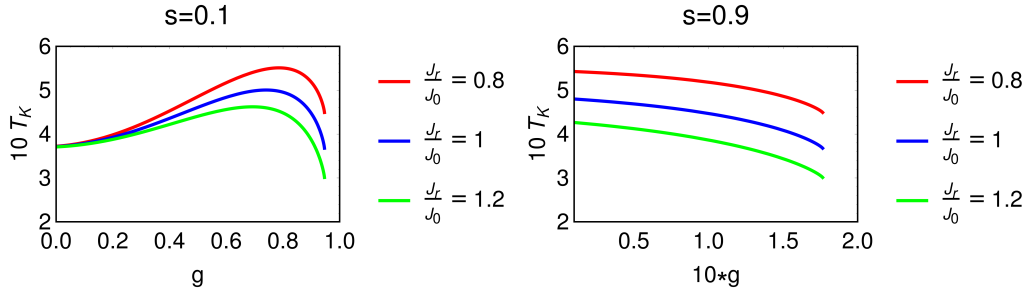


Figure 4.2: Variation of Kondo scale with Non-Hermitian strength (g) and RSO (s) for the fixed bare value of the ratio $\frac{J}{J_r}$ in equation 4.27.

We solve the RG equations in 4.23 which are the central results of the work highlighting the validity of the perturbation theory employed in parallel to the earlier results and establishing the existence of new fixed points. The figures in 4.3 show the existence of a new stable critical point in the non-Hermitian case, which is denoted by the color green, and for vanishing nh coupling, we have conventional 1CK Kondo problem which is consistent with Zarea et al.⁷. The separatrix line corresponds to diagonalization line where local moment survive and in regimes where J and γ diverge we have Kondo effect. We emphasize that the new fixed point will only be stabilized with the non-zero \mathcal{PT} - symmetric coupling and NH strength g .

4.4.5 CFT scaling laws with finite γ and \mathcal{DM} -interactions

We established the algebraic consistency between our employed perturbation theory and the algebraic framework of Conformal Field Theory and elucidated through third-order perturbation diagrams. Our findings align with prior research by Lourenco et al.²⁰, showcasing the RG flow's congruence, particularly in scenarios devoid of potential scattering and \mathcal{DM} interactions. Furthermore, our results are in accordance with the observations made by Sandler et al.⁷ when considering the presence of \mathcal{DM} interactions.

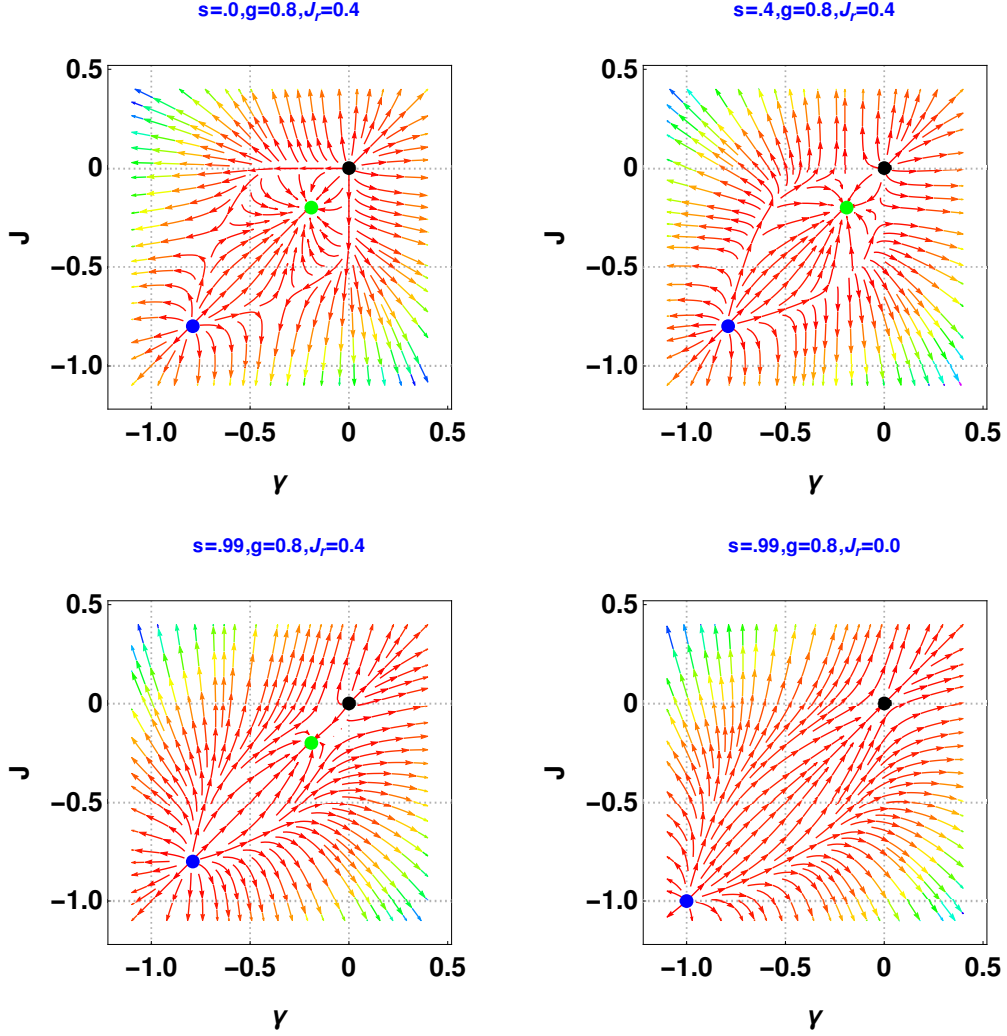


Figure 4.3: Flow diagrams illustrating the emergence of a new fixed point in the non-Hermitian (NH) case for $g \neq 0$ and $J_r \neq 0$. As the strength of the spin-orbit coupling (SOC) increases, the fixed point transitions from a stable state to a marginally stable state, ultimately vanishing when $J_r = 0$.

Remarkably, we have observed the emergence of a fixed point in the \mathcal{PT} -symmetry preserved regime. Notably, a complete reversion of the RG flow occurs at higher invariant strengths, as illustrated in Figure 4.4. This result carries significant implications, indicating that both γ and \mathcal{DM} interactions exert substantial influence on the Kondo problem. Importantly, we've demonstrated that this fixed point can manifest prior to the breaking of \mathcal{PT} -symmetry, offering an avenue for more efficient tuning of the NKK phases by increasing the invariant strengths.

It is worth highlighting that one of the primary motivations behind our work was to establish a sound perturbation theory for the \mathcal{PT} -symmetric non-Hermitian problem, and this objective has been met. Furthermore, we have provided insights into the renormalization of Exceptional Points (EPs), contrasting with the Slave-Boson solution presented in Chapter 2.

In our study, we have made an intriguing observation: the inclusion of higher-order corrections beyond the one-loop level has led to the emergence of a spiral fixed point while retaining the parameter 'g' in its original form. This finding stands in contrast to the outcomes of previous work on Conformal Field Theory (CFT) in parity channels²⁰.

We have found the existence of a stable fixed point that appears prior to the breaking of \mathcal{PT} -symmetry. The phenomenon of Renormalization Group (RG) reversion, observed in both ferromagnetic (FM) and antiferromagnetic (AFM) scenarios, is shifted to higher coupling strengths. It's worth noting that when the NH strength 'g' reaches 1.0, the black dot and red dot coincide, aligning with earlier results from Auxiliary-Particle(SB) theory where the Kondo scale vanishes before reaching an exceptional point (EP).

The red dot represents a trivial fixed point within the model, while the green dot corresponds to the regime where the Kondo scale diverges, accompanied by the breaking of \mathcal{PT} -symmetry.

4.4.6 Non-Hermitian Phase renormalization

Another significant motivation for this work was to explore the impact of interactions on Exceptional Points (EPs). Earlier research in Chapter 2 demonstrated that the interaction effect on EPs from Slave-Boson calculation was inconclusive. Therefore, our goal was to investigate how interactions might influence EPs and, in doing so, illustrate the renormalization process of the non-Hermitian (NH) phase. In Appendix A, we provide the analytical solution at the one-loop level. Here, we present the closed forms 'sol1' and 'Sol2' in terms of $w = \frac{J}{\gamma}$ we have obtained and derive the expression for the renormalization of non-Hermitian phase ϕ in terms of the model parameters

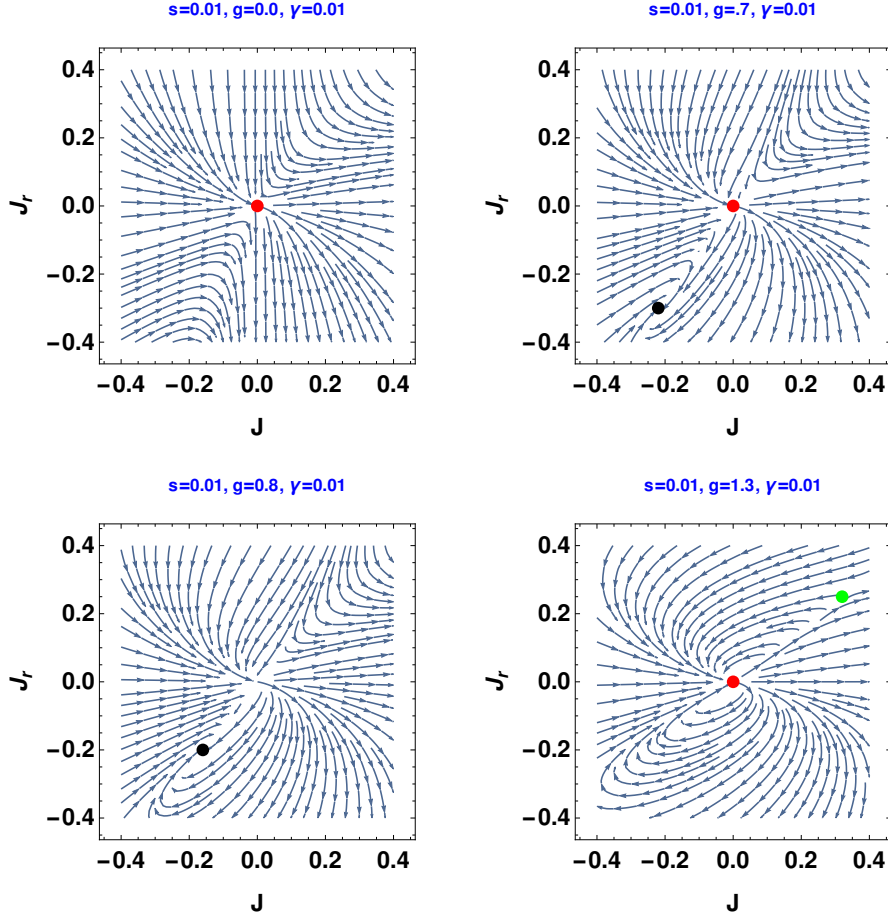


Figure 4.4: Flow diagrams illustrate the evolution of a new spiral fixed point (black) to an unstable state (green) with \mathcal{PT} -symmetric coupling, along with the usual Kondo coupling J .

as follows:

$$\begin{aligned}
Sol_1 : \log \left(w(w - \frac{2}{s^2} - \zeta)^{\frac{4a}{s^2}} (w - \frac{2}{s^2} + \zeta)^{\frac{4b}{s^2}} \right) &= \log \gamma^k, \\
Sol_2 : \gamma &= \left(\frac{\frac{J_r}{\gamma} - \zeta_1}{\frac{J_r}{\gamma}} \right)^{-\frac{1}{\zeta_1}} \\
\Rightarrow \left(\frac{\frac{J_r}{\gamma} - \zeta_1}{\frac{J_r}{\gamma}} \right)^{-\frac{k}{\zeta_1}} &= w(w - \frac{2}{s^2} - \zeta)^{\frac{4a}{s^2}} (w - \frac{2}{s^2} + \zeta)^{\frac{4b}{s^2}} \\
\therefore \frac{\gamma}{J_r} &= \frac{1 - f(w)^{-\frac{\zeta_1}{k}}}{\zeta_1}, \quad 1 + \cot^2(\phi_{k_f}) = 2 \frac{w^2 M_{k_f}}{\gamma} \frac{1 - f(w)^{-\frac{\zeta_1}{k}}}{\zeta_1} \\
\cot^2(\phi_{k_f}) &= \left| 2 \frac{\omega^2 M_{k_f}}{\gamma} \frac{1 - f(w)^{-\frac{\zeta_1}{k}}}{\zeta_1} - 1 \right| \\
M_{k_f} &= \frac{1}{-\epsilon_d} + \frac{1}{\epsilon_d + U}
\end{aligned} \tag{4.28}$$

The exceptional inverse coupling parameter, denoted as $\cot(\phi)$, can be determined through a self-consistent calculation that considers finite U and γ , effectively renormalizing the exceptional point (EP). The RG procedure outlined above provides the matrix elements for the Spin-Orbit Coupling (SOC), given by $\Lambda = \lambda M_{kk'} e^{i(\phi_k + \phi_{k'})}$. In the Poorman scaling approach, when we set $k = k' = k_f$, this expression simplifies to $\Lambda \sim \lambda M_{k_f} e^{2i\phi_{k_f}}$. Further details of this calculation can be found in Appendix A. As found in equation 4.28 NH phase renormalization with J, γ can be worked out as following,

$$\begin{aligned} \phi_{k_f} &= \frac{1}{2} \sec^{-1} \left(\frac{1 - f(w)^{\frac{-\zeta_1}{k}}}{\zeta_1} \right), \quad \frac{J}{\gamma} = w \\ f(w) &= \left(w \left(w - \frac{2}{s^2} - \zeta \right)^{\frac{4a}{s^2}} \left(w - \frac{2}{s^2} + \zeta \right)^{\frac{4b}{s^2}} \right) \\ \zeta &= \left(\frac{4}{s^4} - \frac{4}{s^2} \right)^{\frac{1}{2}}, \quad \zeta_1 = \left(\frac{4\alpha^2}{s^2} - 1 \right), \\ a &= \frac{1}{2\zeta \left(\frac{2}{s^2} + \zeta \right)}, \quad b = \frac{-1}{2\zeta \left(\frac{2}{s^2} - \zeta \right)}, \quad \alpha^2 = (g^2 + s^2 + gs) \end{aligned} \quad (4.29)$$

The EP $\theta_{k_f} = \frac{\pi}{4}$ correspond to $g = \frac{s}{2}$ in the RG context as $\zeta_1 \rightarrow 0$ we have the separatrix which coincides with our Exact diagonalization calculation in the work¹⁷.

$$\begin{aligned} g = \frac{s}{2} &\implies \frac{X_{im}^2 M_{k_f}}{X_0^2 M_{k_f}} = \frac{\lambda}{2} \frac{M_{k_f}^2}{X_0^2 M_{k_f}} \\ \frac{|X|_{im}^2}{|X|_0^2} &= \frac{\lambda}{2} \left(\frac{1}{U + \epsilon_d - \epsilon_{k_f}} + \frac{1}{\epsilon_{k_f} - \epsilon_d} \right) \end{aligned} \quad (4.30)$$

At particle-hole symmetry and for zero bandwidth case $\epsilon_{k_f} = 0$ we have the following,

$$\begin{aligned} \frac{|X|_{im}^2}{|X|_0^2} &= \frac{\lambda}{2} \frac{4}{U} \implies \lambda = \frac{U}{2} \frac{|X|_{im}^2}{|X|_0^2} \\ |X|_{im}^2, |X|_0^2 &\text{ magnitude of bare coupling} \end{aligned} \quad (4.31)$$

We captured the critical line from ED calculations for zero bandwidth through the full analytic solution of nonlinear RG-equations. We also diagonalized the effective model in equation 4.12 to explore the nontrivial topology which is also found in CFT model diagonalization. The figures ?? show the existence of exceptional points from exact diagonalization at particle-hole symmetry and the left panel(a and c) is for the small U limit and the right panel(b,d)

is for the large U limit. Each of the eigenenergies is for the non-Hermitian Kondo model with Rashba coupling $\lambda = 0.5$. The plots c and d correspond to particle-hole symmetry, similarly, a and b correspond to away from PH symmetry $\epsilon_d < -\frac{U}{2}$. Where the parameter ϕ is in the units of π .

4.5 RG Flows And Critical Points

To address the topological aspect and further validate the results of the spin Hamiltonian using the ED method, we take the approach of separating the two channels of the Kondo model. We then explore the various fixed points within these parameter planes, specifically the $J + \gamma$ versus $J - \gamma$ plane. Our goal is to construct an RG flow diagram similar to the one presented in the work of Gil Young Cho et al.³⁰. The emergent coupling γ in the Kondo model will separate the two channels as $J_1 = J - \gamma$ and $J_2 = J + \gamma$, if γ does not renormalize to zero then we don't have a conventional 1CK fixed point. However, this is unique to the non-Hermitian model, particularly the considered model. Transforming the system of equations given in 4.23 into the context of two channels, we observe that out of the five interconnected nonlinear equations, Two invariants lead to a reduction of two equations, leaving us with three remaining differential equations. The remaining equations involving parameters such as J , J_2 , and γ can be expressed as follows.

$$\begin{aligned} \frac{dJ_1}{d \log D'} &= J_1 J_2 - J_r J_1 + J_r^2 J_1 + \\ &\quad g^2 J_1^3 + J_1 (J_1^2 - \frac{3}{4} J_2^2) \\ \frac{dJ_2}{d \log D'} &= J_2^2 - \frac{(J_1^2 - J_2^2)}{2} - J_r J_1 + J_r^2 J_2 + 2s^2 J_1^2 \\ &\quad + g^2 J_2^3 + J_2^3 - \frac{3}{4} J_2 (J_1^2 - J_2^2) \end{aligned} \tag{4.32}$$

The coupled nonlinear equations presented in 4.32 possess analytic solutions in various limits, particularly when $\frac{s}{g} \rightarrow \infty$ or $g \rightarrow \infty$. These analytic solutions are then compared with the computed flow diagrams. Using a method of variable separation and a substitution $k = \frac{J_2^3}{3J_1^2}$ we solve the above set of equations and analyze the solution in the following limits.

$$\begin{aligned} \frac{g^2 k^{2/3} {}_2F_1\left(\frac{2}{3}, 1; \frac{5}{3}; -\frac{3g^2 k}{2s^2}\right)}{4s^2} &= -\frac{3}{4} J_1^{-\frac{4}{3}} + \text{const} \\ \text{where } k &= \frac{J_2^3}{3J_1^2}, \text{ for } \frac{s}{g} \rightarrow \infty \end{aligned} \tag{4.33}$$

Where in the above equation 4.33 ${}_2F_1$ is Gauss Hypergeometric function. The above regime clearly shows that these two channels do not mix in the symmetry-preserved regime as shown in figures 4.5. Particularly in the figure showing the channels are asymptotically stable along the separatrix which indicates $J_1 = J_2$ showing the irrelevance of γ -potential scattering terms in the limit $s \geq g$.

$$\frac{2}{J_1^2} - \frac{2}{J_2^2} = \text{const}, \text{ for } g \rightarrow \infty \quad (4.34)$$

This shows the Kondo problem in the inverse couplings of the channels which clearly indicate symmetry breaking.

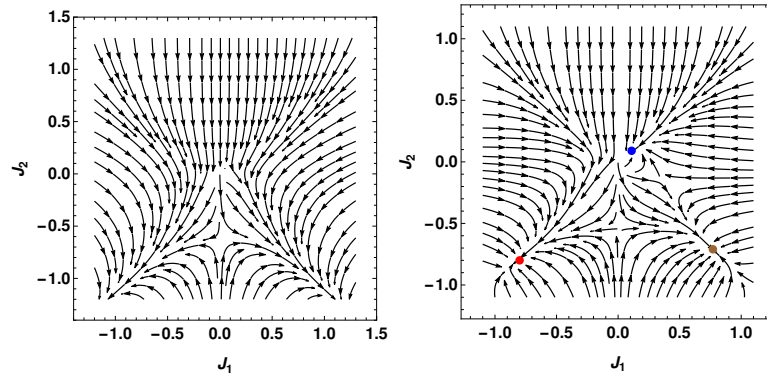


Figure 4.5: The left flow diagram shows the absence of fixed points signaling there is no phase transition and the Kondo effect persists for $s \geq g$. The right flow diagram consists of 3 stable fixed points $s = g/2$ clear indication of phase transition. The red dot corresponds to the regime of irrelevant scattering, the grey dot corresponds to gamma diverging and the blue is the decoupled impurity.

In Appendix A, we have provided specific details for a comparison with the RG flows discussed in Loure's CFT paper²⁰ and Zarea's presentation of the Hermitian case⁷. These fixed points correspond to three distinct regimes. For instance, the red dot corresponds to the scenario where γ renormalizes to zero. The brown point represents the situation where γ diverges in ferromagnetic coupling. The blue dot corresponds to the case where $J = J_r$, signifying symmetry breaking and the emergence of unconventional RG behavior. The other two points are associated with symmetry-preserved transitions. The RG flow diagram reveals three stable fixed points, including a non-interacting marginally relevant fixed point and two stable single-channel fixed points, as illustrated in Figure 4.5.

Mapping to Anisotropic Hermitian Models and Quantum Phase Transitions

Of notable importance is the realization that the \mathcal{PT} -symmetric Kondo model can be elegantly mapped to an anisotropic Hermitian model. This mapping enables the resolution of physical theories within open conditions and unveils the enhanced Kondo scale, as demonstrated in Zarea et al.'s work⁷ for the Poorman scaling method. In contrast, the PartonBoson (SB) method yields a linear enhancement. Furthermore, our exploration uncovers a quantum phase transition point denoted as (E_p) . Below this threshold, the system assumes the typical behavior associated with Kondo interactions. Beyond the exceptional point, a phase emerges, akin to the local moment phase, as the \mathcal{PT} coupling diminishes. In this post-exceptional point phase, partially imaginary eigenvalues make an appearance, indicating unique quantum dynamics³¹. This transition, signifying the K-NK phase, can be likened to a quantum Zeno effect, with SO interactions contributing to decoherence. The interaction dynamics exhibit a delicate balance, where dissipation often prevails, providing a means to exert control over decoherence stemming from dissipative environments^{32;33}.

4.6 Discussion

Our study has unveiled intriguing insights into the behavior of non-Hermitian systems, shedding light on several crucial aspects that have broad implications for the understanding of quantum phases and transport phenomena.

Impact of Higher-Order Corrections and Our Perturbation Theory

First and foremost, our investigation underscores the significance of considering higher-order corrections beyond the one-loop level in non-Hermitian systems. By doing so, we have successfully introduced a novel perturbation theory that has allowed us to uncover the emergence of a spiral fixed point, a phenomenon not previously observed in this context. This finding stands in contrast to conventional Conformal Field Theory (CFT) work, where parity channels have dominated the discussions. Importantly, the inclusion of these higher-order corrections enables us to retain the parameter "g" in its original form, emphasizing its pivotal role in the system's dynamics.

Furthermore, we verified the algebraic consistency between our newly developed perturbation theory and the algebra of CFT. This provides a strong foundation for our analytical framework and enhances our confidence in the results obtained.

Role of Interactions in Exceptional Points (EPs)

One of our key motivations was to investigate the influence of interactions

on Exceptional Points (EPs). Prior research in Chapter 2 had demonstrated that EPs remained unaffected in the presence of a strong correlation. Our study, however, revealed that interactions can significantly impact the Kondo problem, manifesting in a fixed point that emerges before the breaking of \mathcal{PT} -symmetry. This phenomenon opens up intriguing avenues for more efficient tuning of the NKK phases by increasing the invariant strengths.

Conclusion

In conclusion, the study presented in the chapter advances our understanding of non-Hermitian systems by introducing a novel perturbation theory and uncovering new fixed points. It also demonstrates the influence of interactions on Exceptional Points, providing a comprehensive framework that harmonizes with existing works. These findings open up exciting prospects for further exploration in the dynamic field of non-Hermitian quantum mechanics and condensed matter physics.

4.7 Open Questions

Within the realm of open quantum systems lie several intriguing avenues for exploration. One such path involves extending the $\mathcal{T}_{kk'}$ formalism into the $g > 1$ regime, embarking on a comprehensive journey through general diagrammatic perturbation theory³⁴ within the domain of non-Hermitian strength. While the mapping of \mathcal{PT} models to PHH and anti-symmetric real models presents a tantalizing possibility for a broad range of many-body systems, it's imperative to acknowledge that the conventional equation of motion faces serious issues with non-Hermiticity, particularly at E_p . The quest for achieving two-channel behavior, reminiscent of Luttinger liquids^{35;36}, opens up exciting prospects, particularly in the context of cold atom experiments.

In our pursuit of unraveling the subtleties of \mathcal{PT} transitions within the intricate landscape of many-body systems, the development of a novel formalism emerges as an imperative task. This formalism should serve as a guiding light for precise analytic solutions, serving as benchmarks for numerical methodologies like Numerical Renormalization Group (NRG) techniques^{37;38}. NRG has earned its stripes as a potent tool for scrutinizing quantum impurity and correlated systems. By juxtaposing the outcomes of our proposed formalism with NRG results, especially in the domain of real eigenvalues, we can validate its precision and reliability. This symbiotic relationship between theoretical innovation and rigorous numerical validation propels our comprehension of \mathcal{PT} transitions in many-body systems, ushering in an era of enriched understanding in this captivating domain.

Upcoming Chapter: Avenues of Exploration

The next chapter explores how to couple to the environment, including incorporating full momentum space and using Finite-U Auxiliary-Particle methods.

Bibliography

- [1] N. Syassen, D. M. Bauer, M. Lettner, T. Volz, D. Dietze, J. J. Garcia-Ripoll, J. I. Cirac, G. Rempe, and S. Dürr, *Science* **320**, 1329 (2008).
- [2] B. Zhu, B. Gadway, M. Foss-Feig, J. Schachenmayer, M. L. Wall, K. R. A. Hazzard, B. Yan, S. A. Moses, J. P. Covey, D. S. Jin, J. Ye, M. Holland, and A. M. Rey, *Phys. Rev. Lett.* **112**, 070404 (2014).
- [3] G. Barontini, R. Labouvie, F. Stubenrauch, A. Vogler, V. Guarrera, and H. Ott, *Phys. Rev. Lett.* **110**, 035302 (2013).
- [4] M. J. Mark, E. Haller, K. Lauber, J. G. Danzl, A. Janisch, H. P. Büchler, A. J. Daley, and H.-C. Nägerl, *Phys. Rev. Lett.* **108**, 215302 (2012).
- [5] Y. Takasu, T. Yagami, Y. Ashida, R. Hamazaki, Y. Kuno, and Y. Takahashi, *arXiv preprint arXiv:2004.05734* (2020).
- [6] J. Malecki, *Journal of Statistical Physics* **129**, 741 (2007).
- [7] M. Zarea, S. E. Ulloa, and N. Sandler, *Phys. Rev. Lett.* **108**, 046601 (2012).
- [8] D. Mastrogiuseppe, A. Wong, K. Ingersent, S. E. Ulloa, and N. Sandler, *Phys. Rev. B* **90**, 035426 (2014).
- [9] M. Zarea and N. Sandler, *Phys. Rev. B* **79**, 165442 (2009).
- [10] R. Žitko, *Phys. Rev. B* **81**, 241414 (2010).
- [11] C. M. Bender, D. C. Brody, and H. F. Jones, *Phys. Rev. Lett.* **89**, 270401 (2002).
- [12] C. M. Bender, D. C. Brody, and H. F. Jones, *Phys. Rev. Lett.* **92**, 119902 (2004).
- [13] I. Rotter, *Journal of Physics A: Mathematical and Theoretical* **42**, 153001 (2009).
- [14] M. M. Sternheim and J. F. Walker, *Physical Review C* **6**, 114 (1972).

- [15] M. Müller and I. Rotter, Physical Review A **80**, 042705 (2009).
- [16] H. Eleuch and I. Rotter, The European Physical Journal D **69**, 1 (2015).
- [17] V. M. Kulkarni, A. Gupta, and N. Vidhyadhiraja, Physical Review B **106**, 075113 (2022).
- [18] I. Affleck and A. W. Ludwig, Physical review letters **68**, 1046 (1992).
- [19] I. Affleck, A. W. W. Ludwig, and B. A. Jones, Phys. Rev. B **52**, 9528 (1995).
- [20] J. A. S. Lourenço, R. L. Eneias, and R. G. Pereira, Phys. Rev. B **98**, 085126 (2018).
- [21] A. A. Abrikosov, Physics Physique Fizika **2**, 5 (1965).
- [22] A. C. Hewson, *The Kondo problem to heavy fermions*, Vol. 2 (Cambridge university press, 1997).
- [23] P. Anderson, Journal of Physics C: Solid State Physics **3**, 2436 (1970).
- [24] J. Sólyom and A. Zawadoswki, Journal of Physics F: Metal Physics **4**, 80 (1974).
- [25] J. Sólyom, Journal of Physics F: Metal Physics **4**, 2269 (1974).
- [26] M. A. Abrikosov A.A., Low. Temp. Phys. **3**, 519 (1970).
- [27] P. Phillips, *Advanced solid state physics* (Cambridge University Press, 2012).
- [28] I. Affleck and A. W. Ludwig, Physical Review B **48**, 7297 (1993).
- [29] S. Han, D. J. Schultz, and Y. B. Kim, Phys. Rev. B **106**, 155155 (2022).
- [30] G. Y. Cho and E.-G. Moon, Scientific Reports **6**, 19198 (2016).
- [31] C. M. Bender and S. Boettcher, Phys. Rev. Lett. **80**, 5243 (1998).
- [32] Y. Kondo, Y. Matsuzaki, K. Matsushima, and J. G. Filgueiras, New Journal of Physics **18**, 013033 (2016).
- [33] T. Carle, H. J. Briegel, and B. Kraus, Phys. Rev. A **84**, 012105 (2011).
- [34] R. D. Mattuck, *A guide to Feynman diagrams in the many-body problem* (Courier Corporation, 1992).

- [35] A. Furusaki and N. Nagaosa, Physical review letters **72**, 892 (1994).
- [36] D.-H. Lee and J. Toner, Physical review letters **69**, 3378 (1992).
- [37] R. Bulla, T. A. Costi, and T. Pruschke, Rev. Mod. Phys. **80**, 395 (2008).
- [38] K. G. Wilson, Rev. Mod. Phys. **47**, 773 (1975).

Chapter 5

Flow Equation and Finite-U Parton Boson Analysis of \mathcal{PT} -SIAM with RSO and DSO interactions

This chapter investigates Anderson's models, both Hermitian and non-Hermitian, uncovering interaction-induced exceptional points in Hermitian models. We propose a novel generator for the flow equation method to address the convergence issues around the exceptional points. Furthermore, we bridge non-Hermitian and isospectral Hermitian models to compare the conventional flow equation method and later one. Our study illuminates the intriguing interplay of interactions and exceptional points, with physical implications beyond Anderson models.

Manuscript under preparation.

5.1 Introduction

In this chapter, we will explore the impact of Hermitian and non-Hermitian perturbations on breaking parity and time-reversal symmetries, focusing on the Dresselhaus and Rashba spin-orbit interactions. We'll use examples to illustrate how these interactions disrupt symmetries and relate to exceptional points. Additionally, we'll investigate the repercussions of these interactions and exceptional points in interacting many-body systems using a three-dimensional angular momentum basis and the path integral Grassmann formalism.

Recent experiments¹ have observed oscillations in the expectation values of specific non-Hermitian operators, and we will explore their relation to the theoretical framework.

5.2 Derivation of the Angular Momentum Basis Model

In spherically symmetric systems, the field operator can be expanded using spherical harmonics. Consider a system with a Fermi momentum vector, k , in three dimensions and an impurity at the origin. Here, the quantum number l represents the orbital angular momentum, and m takes values from $-l$ to l .

Expanding the field operator in terms of spherical harmonics allows us to express the system's wave function spatially and describe the orbital angular momentum of particles. This method is a powerful tool for analyzing particle behavior, providing insights into the system's spatial distribution, orbital structure, and angular momentum properties. The interplay between the Fermi vector, impurity, and quantum numbers l and m can thus be effectively explored, aiding in the study of spherically symmetric systems.

$$c_{\vec{k}} = \sum_{lm} e^{im\phi} P_l(\cos \theta) \tilde{c}_{\vec{k}} \quad (5.1)$$

In Equation 5.1, P_l are associated Legendre polynomials the variables l and m represent the angular and azimuthal quantum numbers, respectively. These quantum numbers arise from the momentum vector \vec{k} , which takes values from zero to the magnitude of the Fermi vector, denoted as k_f and ϕ, θ correspond to azimuthal and polar angles respectively.

The tilde notation on the expanded operators in Equation 5.1 is redundant and can be dropped for notational simplicity. To show there exist exceptional points in certain transformed Angular Momentum basis we consider the following Hamiltonian.

$$\begin{aligned}
H = & \sum_{k\sigma} \epsilon_{k\sigma} c_{k\sigma}^\dagger c_{k\sigma} + \sum_{\sigma} \epsilon_d d_{\sigma}^\dagger d_{\sigma} + \sum_{k\sigma} V_{k\sigma} (c_{k\sigma}^\dagger d_{\sigma} + hc) \\
& + \sum_k i \vec{\lambda}_2 \cdot c_k^\dagger (\vec{k} \times \vec{\sigma}) c_k + \sum_k \lambda_1 c_k^\dagger (\vec{k} \cdot \vec{\sigma}) c_k \\
& + U n_{d\uparrow} n_{d\downarrow} \\
& \text{where } c_k^\dagger = \begin{pmatrix} c_{k\uparrow}^\dagger & c_{k\downarrow}^\dagger \end{pmatrix}, \quad \vec{\lambda}_2 = 0\hat{i} + 0\hat{j} + \lambda_2\hat{k}
\end{aligned} \tag{5.2}$$

In Equation 5.2, upon expanding the bath operators and substituting Equation 5.1, a noteworthy observation emerges: \mathcal{PT} -symmetric bands manifest following a unitary rotation within the model. This finding underscores the role of unitary transformations in elucidating the emergence of \mathcal{PT} -symmetry in the system.

In Appendix E, we present an alternative derivation by considering the full range of quantum numbers, from $-m$ to m , and general θ values for the associated Legendre polynomials. It is important to note that, for the Kondo problem, focusing on the lowest quantum number, specifically $l = 0$, is sufficient to capture essential aspects of the physics.

In the comprehensive expansion, we encounter trigonometric functions as hybridization coefficients. It is worth mentioning that the resulting exceptional points (EPs) are influenced by the sign-reversion of these $P_l(\cos \theta)$ polynomials. To address this intricacy and emphasize the interaction-induced emergence of EPs, we opt not to incorporate these polynomials, allowing for a clearer examination of the phenomenon.

5.3 Emergence of \mathcal{PT} -bands in DSO case

In a three-dimensional model, the Rashba spin-orbit (RSO) and Dresselhaus spin-orbit (DSO) interactions drive a coupled system, involving mode coupling where the number of coupled modes depends on the specific interaction. The RSO interaction couples $m+1$ modes, while the DSO interaction couples $m-1$ modes. This mode coupling significantly influences the behavior and properties of the system, leading to phenomena such as mode hybridization,

spin-momentum correlations, and the emergence of topological effects and EPs.

$$H_{SO} = \sum_{\mathbf{k}, m} \frac{\lambda_1}{2\pi} (c_{\mathbf{k}, m+1, \uparrow}^\dagger c_{\mathbf{k}, m, \downarrow} + hc) + \sum_{\mathbf{k}, m} \frac{\lambda_2}{2\pi} (c_{\mathbf{k}, m-1, \uparrow}^\dagger c_{\mathbf{k}, m, \downarrow} + hc) \quad (5.3)$$

In above equation 5.3 parameters λ_1 and λ_2 are RSO and DSO interactions respectively. It is possible to absorb the off-diagonal terms introduced by spin-orbit interactions in the kinetic energy of the bath by unitary operation in the following basis, i.e. $H = H_{kin} + H_{SO}$, where $H_{kin} = \sum_{m\mathbf{k}\sigma} \epsilon_{\mathbf{k}} c_{m\mathbf{k}\sigma}^\dagger c_{m\mathbf{k}\sigma}$ can be written as follows,

$$\sum_{\mathbf{k}m} \psi_{\mathbf{k}m}^\dagger \begin{pmatrix} \epsilon_{\mathbf{k}} & \lambda_1 & 0 \\ \lambda_1 & \epsilon_{\mathbf{k}} & -i\lambda_2 \\ 0 & i\lambda_2 & \epsilon_{\mathbf{k}} \end{pmatrix} \psi_{\mathbf{k}m}, \text{ where } \psi_{\mathbf{k}m} = \begin{pmatrix} c_{\mathbf{k}m+1, \downarrow} \\ c_{\mathbf{k}m, \uparrow} \\ c_{\mathbf{k}m-1, \uparrow} \end{pmatrix}, \quad (5.4)$$

Eigenvalues of H_{kin} are $\epsilon_{\mathbf{k}}, \epsilon_{\mathbf{k}} \pm \sqrt{\lambda_1^2 + \lambda_2^2}$

A unitary operator that diagonalizes the kinetic part with the SO interactions can be found as follows,

$$\mathcal{U} = \begin{pmatrix} \frac{ie^{\frac{i\pi}{3}} \lambda_2}{\Delta} & 0 & \frac{e^{\frac{i\pi}{3}} \lambda_1}{\Delta} \\ -\frac{ie^{\frac{i\pi}{3}} \lambda_1}{\sqrt{2}\Delta} & \frac{ie^{\frac{i\pi}{3}}}{\sqrt{2}} & \frac{e^{\frac{i\pi}{3}} \lambda_2}{\sqrt{2}\Delta} \\ -\frac{ie^{\frac{i\pi}{3}} \lambda_1}{\sqrt{2}\Delta} & -\frac{ie^{\frac{i\pi}{3}}}{\sqrt{2}} & \frac{e^{\frac{i\pi}{3}} \lambda_2}{\sqrt{2}\Delta} \end{pmatrix}, \text{ where } \Delta = \sqrt{\lambda_1^2 + \lambda_2^2} \quad (5.5)$$

After finding this unitary, we can find the following transformed operators in terms of the original ones,

$$\psi_{\mathbf{k}m} = \begin{pmatrix} \tilde{c}_{\mathbf{k}m+1,0} \\ \tilde{c}_{\mathbf{k}m,-} \\ \tilde{c}_{\mathbf{k}m-1,+} \end{pmatrix} = \begin{pmatrix} \frac{ie^{\frac{i\pi}{3}} \lambda_2}{\Delta} & 0 & \frac{e^{\frac{i\pi}{3}} \lambda_1}{\Delta} \\ -\frac{ie^{\frac{i\pi}{3}} \lambda_1}{\sqrt{2}\Delta} & \frac{ie^{\frac{i\pi}{3}}}{\sqrt{2}} & \frac{e^{\frac{i\pi}{3}} \lambda_2}{\sqrt{2}\Delta} \\ -\frac{ie^{\frac{i\pi}{3}} \lambda_1}{\sqrt{2}\Delta} & -\frac{ie^{\frac{i\pi}{3}}}{\sqrt{2}} & \frac{e^{\frac{i\pi}{3}} \lambda_2}{\sqrt{2}\Delta} \end{pmatrix} \begin{pmatrix} c_{\mathbf{k}m+1, \downarrow} \\ c_{\mathbf{k}m, \uparrow} \\ c_{\mathbf{k}m-1, \uparrow} \end{pmatrix} \quad (5.6)$$

Now we write explicitly these operators in emergent angular momentum quantum numbers and 3-chiral bands,

$$\begin{aligned} c_{0\uparrow} &= -\frac{i}{\sqrt{2}} e^{\frac{i\pi}{3}} \tilde{c}_{jm-} + \frac{i}{\sqrt{2}} e^{\frac{i\pi}{3}} \tilde{c}_{jm+} \\ c_{0\downarrow} &= -\frac{i\lambda_2}{\Delta} e^{-\frac{i\pi}{3}} \tilde{c}_{jm0} + \frac{\lambda_1}{\Delta} \frac{i}{\sqrt{2}} e^{-\frac{i\pi}{3}} \tilde{c}_{jm-} + \frac{\lambda_1}{\Delta} \frac{i}{\sqrt{2}} e^{-\frac{i\pi}{3}} \tilde{c}_{jm+} \\ c_{-1\uparrow} &= \frac{i\lambda_1}{\Delta} e^{-\frac{i\pi}{3}} \tilde{c}_{jm0} + \frac{\lambda_2}{\Delta} \frac{1}{\sqrt{2}} e^{-\frac{i\pi}{3}} \tilde{c}_{jm-} + \frac{\lambda_2}{\Delta} \frac{1}{\sqrt{2}} e^{-\frac{i\pi}{3}} \tilde{c}_{jm+} \end{aligned} \quad (5.7)$$

In the above equations 5.7 k is implicit and is considered later. Since the dot only couples to the $m = 0$ subspace, we only need $c_{0\uparrow}$ and $c_{0\downarrow}$ for the hybridization, which splits into three channels as follows:

$$\begin{aligned}
H_{hyb}^0 &= \sum_{\mathbf{k}j_m} V_k \frac{\lambda_2}{\Delta} (-ie^{-\frac{i\pi}{3}} d_{\downarrow}^{\dagger} \tilde{c}_{\mathbf{k}j_m 0} + h.c) \\
H_{hyb}^{-} &= \sum_{\mathbf{k}j_m} V_k \frac{\lambda_1}{\Delta} \left(\frac{i}{\sqrt{2}} e^{-\frac{i\pi}{3}} d_{\downarrow}^{\dagger} \tilde{c}_{\mathbf{k}j_m -} + h.c \right) + V_{\mathbf{k}} \left(\frac{i}{\sqrt{2}} e^{-\frac{i\pi}{3}} d_{\uparrow}^{\dagger} \tilde{c}_{\mathbf{k}j_m -} + h.c \right) \\
H_{hyb}^{+} &= \sum_{\mathbf{k}j_m} V_k \frac{\lambda_1}{\Delta} \left(\frac{i}{\sqrt{2}} e^{-\frac{i\pi}{3}} d_{\downarrow}^{\dagger} \tilde{c}_{\mathbf{k}j_m +} + h.c \right) + V_{\mathbf{k}} \left(\frac{i}{\sqrt{2}} e^{-\frac{i\pi}{3}} d_{\uparrow}^{\dagger} \tilde{c}_{\mathbf{k}j_m +} + h.c \right)
\end{aligned} \tag{5.8}$$

Where j_m is the angular quantum number that takes values of $j_m = m \pm \sigma$, and we absorb the bare hybridization in Spin-Orbit (SO) couplings as $\lambda_1 V_k \rightarrow \lambda_1$ and $\lambda_2 V_k \rightarrow \lambda_2$. After all the above expansion transformations full model will appear as follows,

$$\begin{aligned}
H &= \sum_{\mathbf{k}j_m h=0,\pm} \epsilon_{\mathbf{k}} c_{\mathbf{k}j_m h}^{\dagger} c_{\mathbf{k}j_m h} + H_{hyb}^0 + H_{hyb}^{+} + H_{hyb}^{-} \\
&\quad \sum_{\sigma} \epsilon_d d_{\sigma}^{\dagger} d_{\sigma} + U n_{d\uparrow} n_{d\downarrow}
\end{aligned} \tag{5.9}$$

5.4 Derivation of spectral function

The equation of motion for the model is laborious to close in this problem. However, the Grassmann action provides a powerful method to handle the Fermionic degrees of freedom by formulating a path-integral description.

Using the Grassmann action, we describe the impurity dynamics through functional integrals over Grassmann variables. This allows us to get spectral functions.

While deriving spectral functions involves complex calculations, the Grassmann approach offers a systematic framework to analyze impurity dynamics. This method reveals the interaction between impurities, non-Hermitian effects, and the system's underlying physics.

We begin by considering the transformed model in equation 5.9. To obtain the spectral functions in the non-interacting case, we express the action as follows:

$$\begin{aligned}
\mathcal{S}_0 = & \int d\tau d_\sigma^\dagger \left(\partial_\tau - \epsilon_d \right) d_\sigma + \sum_{\mathbf{k}j_m} c_{\mathbf{k}j_m h}^\dagger \left(\partial_\tau - \epsilon_{kh} \right) c_{\mathbf{k}j_m h} \\
& + \sum_{\mathbf{k}j_m} \frac{\lambda_2}{\Delta} (-ie^{-\frac{i\pi}{3}} d_\downarrow^\dagger \tilde{c}_{\mathbf{k}j_m 0} + h.c) \\
& + \sum_{\mathbf{k}j_m} \frac{\lambda_1}{\Delta} \left(\frac{i}{\sqrt{2}} e^{-\frac{i\pi}{3}} d_\downarrow^\dagger \tilde{c}_{\mathbf{k}j_m -} + h.c \right) + V_0 \left(\frac{i}{\sqrt{2}} e^{-\frac{i\pi}{3}} d_\uparrow^\dagger \tilde{c}_{\mathbf{k}j_m -} + h.c \right) \\
& + \sum_{\mathbf{k}j_m} \frac{\lambda_1}{\Delta} \left(\frac{i}{\sqrt{2}} e^{-\frac{i\pi}{3}} d_\downarrow^\dagger \tilde{c}_{\mathbf{k}j_m +} + h.c \right) \\
& + \sum_{\mathbf{k}j_m} V_0 \left(\frac{i}{\sqrt{2}} e^{-\frac{i\pi}{3}} d_\uparrow^\dagger \tilde{c}_{\mathbf{k}j_m +} + h.c \right) + \mathcal{S}_{int} \\
\text{where } \mathcal{S}_{int} = & \int d\tau U d_\uparrow^\dagger d_\downarrow^\dagger d_\uparrow d_\downarrow
\end{aligned} \tag{5.10}$$

After integrating out the bath operators $\mathcal{Z} = \int \mathcal{D}[\bar{c}c d\bar{d}] e^{-\mathcal{S}_0} \rightarrow \mathcal{Z} = \int \mathcal{D}[\bar{d}d] e^{-\tilde{\mathcal{S}}_0}$ we get the impurity effective action as the following,

$$\begin{aligned}
\mathcal{S}_0 = & \int d\tau \\
& d^\dagger \begin{pmatrix} \omega^+ - \epsilon_d - \sum_{kh} \frac{V_0^2}{\omega^+ - \epsilon_{kh}} & - \sum_{kh} \frac{V_0 \lambda_1}{\Delta(\omega^+ - \epsilon_{kh})} \\ - \sum_{kh} \frac{V_0 \lambda_1}{\Delta(\omega^+ - \epsilon_{kh})} & \omega^+ - \epsilon_d - \sum_{kh} \frac{\lambda_2^2}{\Delta(\omega^+ - \epsilon_{kh})} - \sum_k \frac{\lambda_1^2}{\Delta(\omega^+ - \epsilon_{k0})} \end{pmatrix} d \\
& + \mathcal{S}_{int} \\
\text{where } \mathcal{S}_{int} = & \int d\tau U d_\uparrow^\dagger d_\downarrow^\dagger d_\uparrow d_\downarrow \text{ and } d^\dagger = \begin{pmatrix} d_\uparrow^\dagger & d_\downarrow^\dagger \end{pmatrix}
\end{aligned} \tag{5.11}$$

After integrating all the bath operators and performing an analytic continuation by substituting ∂_τ with ω^+ , the path integral yields the Green function matrix. This matrix encapsulates the system's propagator and provides valuable information about its dynamics and properties.

$$\begin{aligned}
\mathcal{G}_d^{-1} = & \begin{pmatrix} \omega^+ - \epsilon_d - \sum_{kh} \frac{V_0^2}{\omega^+ - \epsilon_{kh}} & - \sum_{kh} \frac{V_0 \lambda_1}{\Delta(\omega^+ - \epsilon_{kh})} \\ - \sum_{kh} \frac{V_0 \lambda_1}{\Delta(\omega^+ - \epsilon_{kh})} & \omega^+ - \epsilon_d - \sum_{kh} \frac{\lambda_2^2}{\Delta(\omega^+ - \epsilon_{kh})} - \sum_k \frac{\lambda_1^2}{\Delta(\omega^+ - \epsilon_{k0})} \end{pmatrix} \\
\text{where } \epsilon_{kh} = & \epsilon_k + h\Delta \text{ and } h = \pm
\end{aligned} \tag{5.12}$$

To investigate the existence of exceptional points, we have introduced explicit parity and time reversal symmetry-breaking interactions, which make the above \mathcal{G}_d^{-1} matrix non-Hermitian. To diagonalize this matrix, we can express it as $\tilde{\mathcal{G}}_d^{-1} = U\mathcal{G}_d^{-1}U^\dagger$, where U is a unitary matrix. As we discuss in the section "Mathematical Digression" in Appendix E, in Schur's triangularization theorem it is justified for such unitary operation to diagonalize the Green function matrix while η is chosen as a small number. This diagonalization process allows us to analyze the eigenvalues and eigenvectors of \mathcal{G}_d^{-1} in a more convenient form.

$$\tilde{\mathcal{G}}_d^{-1} = \begin{pmatrix} G^{-1} + A(\omega) & 0 \\ 0 & G^{-1} - A(\omega) \end{pmatrix}$$

where $G^{-1} = \omega^+ - \epsilon_d - \frac{1}{2} \sum_{kh=\pm} \frac{V_0^2}{\omega^+ - \epsilon_{kh}} - \frac{1}{2} \sum_{kh=\pm} \frac{\lambda_2^2}{\Delta(\omega^+ - \epsilon_{kh})} - \frac{1}{2} \sum_k \frac{\lambda_1^2}{\Delta(\omega^+ - \epsilon_{k0})}$ (5.13)

In the equation presented above (Equation 5.13), it's important to note that the determinant is given by $(G^{-1})^2 - (A(\omega))^2$. This determinant can become zero under certain parameter sets, indicating what we refer to as the Hermitian defectiveness of spectral functions, where the matrix becomes singular due to the determinant crossing zero. To investigate this singular point more closely, we conduct a detailed analysis of the function $A(\omega)$ in Equation 5.13 to demonstrate the presence of Exceptional Points (EPs).

$$A(\omega) = \frac{1}{2} \sqrt{\left(\sum_k \frac{\lambda_1^2}{\Delta(\omega^+ - \epsilon_{k0})} \right)^2 + 4 \left(\sum_{kh} \frac{V_0 \lambda_1}{\Delta(\omega^+ - \epsilon_{kh})} \right)^2} \quad (5.14)$$

We get the 4 roots of the function $A(\omega) = 0$ while $\omega^+ \rightarrow \omega$ as the following,

$$\omega \rightarrow \pm \sqrt{\Delta^2 \lambda_1^2 \pm 4 \sqrt{\Delta^4 (-V_0^2) (\lambda_1^2 - 4V_0^2) - 8\Delta^2 V_0^2}}, \quad (5.15)$$

As mentioned earlier, exceptional points, which occur when two or more eigenvalues coalesce in the parameter space, are a crucial aspect of our investigation. Upon a more detailed examination of $A(\omega)$, it becomes apparent that it will vanish as λ_1 tends towards zero, and any changes in λ_2 will not lead to the emergence of fixed points. It becomes evident that achieving exceptional points requires the participation of both λ_1 and λ_2 .

In light of this prior explanation, we can now delve into the presence of these exceptional points in figure 5.1 within the framework of a Hermitian

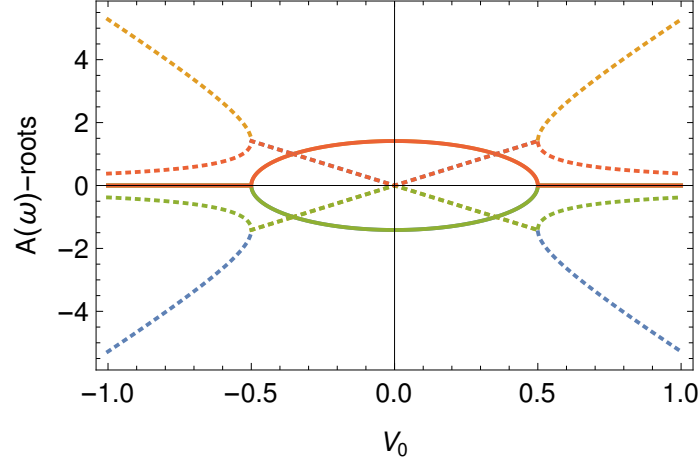


Figure 5.1: The plot illustrates the roots of $A(\omega)$, which encompass both real and imaginary components, showcasing Exceptional Points (EPs). Solid lines in different colors represent real parts of the roots, while dotted lines depict the imaginary roots as functions of V_0 . Throughout these computations, we maintain a constant value of $\lambda_2 = 1.0$, and λ_1 can be adjusted. A higher λ_1 value signifies increased strength of V_0 and a greater likelihood of encountering EPs.

problem. To do so, we derive the exact Green function from a quadratic action. Exceptional points, specific to situations where eigenvalues converge, can profoundly impact the system's behavior. By individually setting $\omega^+ \rightarrow \omega$ in the Green functions, we can observe the convergence of points in the ω roots and gain deeper insights into the existence and characteristics of these exceptional points in the considered Hermitian problem. It's important to note that these exceptional points will no longer be present once we take the trace over $Tr(\hat{\mathcal{G}}_d^{-1})$. It is important to note that this analysis focuses solely on the sums in \hat{A} at $k = 0$, and aims to introduce a more complex set of exceptional points.

5.4.1 Finite-U Auxiliary Particle -Boson Analysis

In Chapter 2, we introduced the finite- U Slave-Boson method as a versatile tool for analyzing various systems. We first applied it to investigate exceptional points in Hermitian models with onsite interactions, then extended it to explore their effects in non-Hermitian systems.

By using this approach, we examined the interplay between onsite interactions and exceptional points, enhancing our understanding of non-Hermitian

systems. Our research aims to uncover new phenomena arising from the co-existence of interactions and exceptional points, particularly in the context of chiral Green functions.

We also adapted the Slave-Boson operators to account for chiral operators, ensuring an accurate treatment of probability non-conservation. This allowed for a more comprehensive analysis of the non-Hermitian Anderson model. Although our current analysis focuses on a Hermitian problem that explicitly breaks \mathcal{PT} symmetry, we still maintain the general applicability of our method.

The effective action is given by:

$$\mathcal{S}_{eff} = \int d\tau \ln \tilde{G}_{0+} \tilde{G}_{0-} + U d^\dagger d + \lambda^{(1)} P + \lambda_h^{(2)} Q_h, \quad (5.16)$$

where the inverse Green's functions are:

$$\tilde{G}_{0\pm}^{-1} = (G^{-1} \pm \tilde{A}) z^2. \quad (5.17)$$

The RISB constraints are:

$$\begin{aligned} z &= \frac{(e^\dagger p + p^\dagger d)}{\sqrt{(1 - d^\dagger d - p^\dagger p)(1 - e^\dagger e - p^\dagger p)}}, \\ P &= e^\dagger e + \sum_h p_h^\dagger p_h + d^\dagger d - 1 = 0, \\ Q_h &= n_{dh} - p_h^\dagger p_h - d^\dagger d = 0. \end{aligned} \quad (5.18)$$

Here, z is the Boson weight, and P and Q are constraints for filling and charge, respectively. e , p , and d are spinless pseudo-Bosons, with p_h as the chiral Boson.

The corresponding free energy functional is:

$$f_0 = \ln \left(\prod_h \tilde{G}_{0h}^{-1} \right) + U d^2 + \lambda^{(1)} P + \lambda_h^{(2)} Q_h. \quad (5.19)$$

We can derive saddle-point equations by taking derivatives with respect to the Lagrange multipliers:

$$\frac{\partial f_0}{\partial \lambda^{(1)}} = 0, \quad \frac{\partial f_0}{\partial \lambda_h^{(2)}} = 0, \quad \frac{\partial f_0}{\partial d^2} = 0, \quad \frac{\partial f_0}{\partial e^2} = 0. \quad (5.20)$$

These calculations allow us to determine the Auxiliary Particle-Boson scale, which we later compare with results from the Flow equation method. We now turn our attention to the Flow equation method and discuss the need for a new generator.

5.5 Illustration of Proposed Flow Generator for Diagonal Non-Hermiticity in a Simple Model

One of our motivations in doing flow equations with the modified generator is the breakdown of Poorman's scaling when there is diagonal non-Hermiticity. This becomes evident when we compute Poorman's corrections encounter with complex poles and, consequently, an unconventional breakdown of unitarity. We initiate our study with a fundamental single-particle Hamiltonian and then proceed to derive flow equations for our model. In our research, we illustrate that when the generator used in these flow equations belongs to a specific category of pseudo-Hermitian Hamiltonians (PHH), our model yields the correct and expected outcomes. This highlights the significance of using such pseudo-Hermitian Hamiltonian in our work to obtain accurate results.

$$\begin{aligned}
H &= \sum_k \left((\epsilon + i\mu) c_{k\uparrow}^\dagger c_{k\uparrow} + (\epsilon - i\mu) c_{k\downarrow}^\dagger c_{k\downarrow} + \gamma (c_{k\uparrow}^\dagger c_{k\downarrow} + h.c) \right) \\
&= \sum_k \begin{pmatrix} c_{k\uparrow}^\dagger & c_{k\downarrow}^\dagger \end{pmatrix} \begin{pmatrix} \epsilon + i\mu & \gamma \\ \gamma & \epsilon - i\mu \end{pmatrix} \begin{pmatrix} c_{k\uparrow}^\dagger \\ c_{k\downarrow}^\dagger \end{pmatrix}
\end{aligned} \tag{5.21}$$

In above equation 5.21 will have eigenvalues $\epsilon \pm \sqrt{\gamma^2 - \mu^2}$. Building upon our previous proof through conjugate eigenvalues and the trace flow, we select a generator with the property of pseudo-Hermitian Hamiltonian (PHH), defined as $\mathcal{PT}\eta\mathcal{PT}^\dagger = \eta^\dagger$. Consequently, we express η as $\eta = [H, H_{int}^\dagger] + [H^\dagger, H_{int}]$. This will give us the following form of the generator,

$$\eta = \sum_k \left(\frac{\gamma_k^r}{\epsilon + i\mu} c_{k\uparrow}^\dagger c_{k\downarrow} - \frac{\gamma_k^r}{\epsilon - i\mu} c_{k\downarrow}^\dagger c_{k\uparrow} \right) \tag{5.22}$$

Where in the equation 5.22 γ_k^r corresponds to a reference value of hybridization which is a free parameter. Continuing with the previously mentioned generator in equation 5.22, we derive the following flow equations.

$$\begin{aligned}
\frac{dH}{dl} &= [H, \eta] \\
&= \sum_k \frac{\gamma_k \gamma_k^r}{\epsilon + i\mu} c_{k\uparrow}^\dagger c_{k\uparrow} + \sum_k \frac{\gamma_k \gamma_k^r}{\epsilon - i\mu} c_{k\downarrow}^\dagger c_{k\downarrow} + \sum_k \gamma_k^r (c_{k\uparrow}^\dagger c_{k\downarrow} + h.c) \\
&\quad + \sum_{k \neq k'} \left(\frac{\gamma_k \gamma_{k'}^r}{\epsilon - i\mu} c_{k\uparrow}^\dagger c_{k'\downarrow}^\dagger c_{k\downarrow} c_{k'\uparrow} + \frac{\gamma_{k'} \gamma_k^r}{\epsilon + i\mu} c_{k'\uparrow}^\dagger c_{k\downarrow}^\dagger c_{k'\downarrow} c_{k\uparrow} \dots \right)
\end{aligned} \tag{5.23}$$

At the one-loop level, we compare the operator structures, resulting in the following RG equations.

$$\begin{aligned}\frac{d\gamma_k}{dl} &= \gamma_k^r \\ \frac{d(\epsilon_k + i\mu)}{dl} &= \frac{\gamma_k \gamma_k^r}{\epsilon + i\mu} \\ \frac{d(\epsilon_k - i\mu)}{dl} &= \frac{\gamma_k \gamma_k^r}{\epsilon - i\mu}\end{aligned}\tag{5.24}$$

The solution for the above set of equations 5.24 will be found out as follows which we call flow equation invariant,

$$\tilde{\epsilon}_k = \pm \sqrt{\tilde{\gamma}_k^2 - \tilde{\mu}^2} + \text{constant}\tag{5.25}$$

By utilizing Equation 5.25, we were able to restore the initial model's eigenvalues, which validates our suggestion. Moving forward, we'll adopt our proposed generator's structure in a non-Hermitian SIAM. It's worth noting that we have off-diagonal non-Hermiticity in non-Hermitian SIAM, which is distinct from this section.

5.5.1 Deriving Flow Equations for Non-Hermitian Single Impurity Anderson Models using a Novel Generator

As discussed in Appendix E, the theorems on continuous unitary transformations (CUT) provide us with a bound on imaginary weight until we reach a defective point or encounter the non-diagonalizability of a generic square matrix. This guidance helps us in selecting a generator with specific properties. Additionally, it's important to note that the negative trace flow is a crucial criterion for the flow equations to diagonalize the effective model. Therefore, we need to select pseudo antihermitian generators to perform unitary operations.

Now, let's shift our focus to the consideration of the following non-Hermitian model as we proceed with the derivation of the flow equations:

$$\begin{aligned}H &= \sum_{\alpha k \sigma} \epsilon_{\alpha k \sigma} c_{k \sigma}^\dagger c_{k \sigma} + \sum_{\sigma} \epsilon_{d \sigma} d_{\sigma}^\dagger d_{\sigma} + \sum_{\alpha k \sigma} V_{\alpha k} e^{i \xi_{\alpha} \phi} (c_{\alpha k \sigma}^\dagger d_{\sigma} + h.c) \\ &+ U d_{\uparrow}^\dagger d_{\downarrow}^\dagger d_{\uparrow} d_{\downarrow}\end{aligned}\tag{5.26}$$

where $\alpha = R, L$ $\xi_{\alpha} = \pm$ for L/R

The chosen generator should possess the symmetry $\mathcal{PT}\eta\mathcal{PT}^\dagger = \eta^\dagger$ and also exhibit anti-Pseudo Hermitian behavior, expressed as $\mathcal{PT}^\dagger\eta\mathcal{PT} = -\mathcal{PT}^\dagger\eta^\dagger\mathcal{PT}$ or in other terms it is equivalent of $\eta = [H_0, H_{int}^\dagger] + [H_0^\dagger, H_{int}]$.

$$\begin{aligned}
\eta = & \sum_{k\sigma} (\epsilon_k - \epsilon_d) V_k^r e^{i\phi} (c_{L\sigma}^\dagger d_\sigma + hc) - (\epsilon_k - \epsilon_d) V_k^r e^{-i\phi} (c_{R\sigma}^\dagger d_\sigma + hc) \\
& + \sum_{kq\sigma\alpha\alpha'} V_k V_q^r e^{i\xi_\alpha\phi} e^{i\xi_{\alpha'}\phi} (c_{\alpha k\sigma}^\dagger c_{\alpha' q\sigma} - hc) \\
& + \sum_{kq\sigma\alpha\alpha'} V_k V_q^r e^{-i\xi_\alpha\phi} e^{-i\xi_{\alpha'}\phi} (c_{\alpha k\sigma}^\dagger c_{\alpha' q\sigma} - hc) \\
& + \eta^2 (c_{\alpha k\sigma}^\dagger d_\sigma^\dagger d_{\sigma'} d_\sigma)
\end{aligned} \tag{5.27}$$

In the previously mentioned Equation 5.27, the term η^2 takes on the form of a quartic operator and it will have coefficient $UV_q^r e^{i\xi_\alpha\phi}$. This quartic operator is integrated into the subsequent loop, where it contributes to more complex calculations involving combinations of six and four-operator commutators within the context of normal ordering.

The flow will be generated by calculating the commutators $\frac{dH}{dl} = [H, \eta]$. We will compare the bare Hamiltonian with the flowed one, and for the one-loop case, we have the following results.

$$\begin{aligned}
\frac{d\epsilon_k}{dl} &= \sum_{\alpha\alpha'} (\epsilon_k - \epsilon_d) V_{\alpha'k} V_{\alpha k}^r e^{i\xi_\alpha\phi} e^{i\xi_{\alpha'}\phi} \\
\frac{dV_{\alpha k}}{dl} e^{i\xi_\alpha} &= -V_{\alpha k}^r e^{i\xi_\alpha\phi} (\epsilon_k - \epsilon_d)^2 \\
&+ V_{\alpha k} e^{i\xi_\alpha\phi} \sum_{p\alpha\alpha'} V_{\alpha p} V_{\alpha' p}^r e^{i\xi_\alpha\phi} e^{i\xi_{\alpha'}\phi} \\
&- V_{\alpha k}^r e^{i\xi_\alpha} \sum_{p\alpha} V_{p\alpha}^2 e^{2i\xi_\alpha\phi} \\
\frac{d\epsilon_d}{dl} &= \frac{\sum_{k\alpha\alpha'} (\epsilon_d - \epsilon_k)^2 f(k) V_{k\alpha} V_{k\alpha'}^r e^{i\xi_\alpha\phi} e^{i\xi_{\alpha'}\phi}}{(1 - U \frac{dn_d}{d\epsilon_d})} \\
&+ \frac{U \sum_{k\alpha\alpha'} f(k) V_{k\alpha} V_{k\alpha'}^r e^{i\xi_\alpha\phi} e^{i\xi_{\alpha'}\phi} (n_d - n_k)}{(1 - U \frac{dn_d}{d\epsilon_d})} \\
\frac{dU}{dl} &= U \sum_{k\alpha\alpha'} V_{k\alpha} V_{k\alpha'}^r e^{i\xi_\alpha\phi} e^{i\xi_{\alpha'}\phi}
\end{aligned} \tag{5.28}$$

Next, we proceed to take the analytic limits of the equations 5.28 mentioned above and derive the Kondo scale for the problem. We will then compare this result with the solution obtained from the Slave-Boson approach. Firstly we

will solve ϵ_d and U equations by doing k-sum to integral and replacing the $\Delta_2 = \frac{\sum_{k\alpha\alpha'} (\epsilon_d - \epsilon_k)^2 f(k) V_{k\alpha} V_{k\alpha'}^r e^{i\xi_{\alpha}\phi} e^{i\xi_{\alpha'}\phi}}{\sum_{k\alpha\alpha'} V_{k\alpha} V_{k\alpha'}^r e^{i\xi_{\alpha}\phi} e^{i\xi_{\alpha'}\phi}}$ and $\Delta = \frac{\sum_{k\alpha\alpha'} f(k) V_{k\alpha} V_{k\alpha'}^r e^{i\xi_{\alpha}\phi} e^{i\xi_{\alpha'}\phi} (n_d - n_k)}{\sum_{k\alpha\alpha'} V_{k\alpha} V_{k\alpha'}^r e^{i\xi_{\alpha}\phi} e^{i\xi_{\alpha'}\phi}}$ with such substitutions we get ϵ_d, U equations as $\frac{d\epsilon_d}{dU} = \frac{\epsilon_d^2 \Delta_2}{U} + \Delta$ which has following closed form solution.

$$\tilde{\epsilon}_d = - \frac{U \sqrt{\Delta_2 \Delta} \left(-\frac{c_1 J_1(2\sqrt{\Delta_2 \Delta} \sqrt{U})}{\sqrt{U}} - \frac{2\sqrt{\Delta_2 \Delta} Y_1(2\sqrt{U})}{\sqrt{U}} \right)}{a \left(c_1 J_0 \left(2\sqrt{\Delta_2 \Delta} \sqrt{U} \right) + 2Y_0 \left(2\sqrt{\Delta_2 \Delta} \sqrt{U} \right) \right)} \quad (5.29)$$

In the equation, 5.29, the functions J and Y represent Bessel functions of the first and second kind, respectively, and the constant c_1 is an integral constant.

Now, let's discuss the limit of single occupancy and a large impurity site energy. In this limit basically $\Delta \rightarrow 0$ and RG equation will reduce to $\frac{d\epsilon_d}{dU} = \frac{\epsilon_d^2 \Delta_2}{U}$, which have solution as follows:

$$U = U_0 e^{-\Delta_2 / (\epsilon_d \Delta_{02})}$$

We can use this expression for U in the flow equation, replacing the effective bandwidth with the Kondo Temperature T_K . This allows us to demonstrate that the Kondo scale follows the form:

$$T_K = T_{K0} e^{-\Delta_2 / (\tilde{\epsilon}_d \Delta_{02})}$$

This scaling relationship can also be compared with the work of F. D. M. Haldane² on the asymmetric Anderson model in the limit as $\phi \rightarrow 0$.

5.6 Mapping of non-Hermitian model to isospectral Hermitian models

The process of mapping non-Hermitian models to equivalent isospectral Hermitian models presents a notable complexity, as exemplified in Swanson's oscillator problems³⁻⁵. Our objective here is to derive a comprehensive set of eigenvectors while preserving their normalization. From this, we gain insights into the scaling behavior of different operators and fundamental parameters within the non-Hermitian model. Remarkably, this transformation leads us to an equivalent Hermitian model with real eigenvalues, a characteristic that persists until we reach an exceptional point.

We introduce a scaling procedure to transform the non-Hermitian model into an equivalent Hermitian model. For such a case, we can use the method since one can show the flow of the trace is negative. This procedure allows us to map the non-Hermitian Hamiltonian to a Hermitian form by redefining the energy parameter and the hybridization term.

For the energy parameter, we use the scaled value $\tilde{\epsilon}_k = \frac{e^{-i\theta}}{\sqrt{\cos(2\theta)}}$, where $\theta = \arctan\left(\frac{\omega \sin(\phi)}{v + \omega \cos(\phi)}\right)$. This scaling factor modifies the original energy parameter to preserve certain system properties while ensuring Hermiticity.

Similarly, the hybridization term X_k which was originally $X_{\eta k} = V_k + \omega e^{i\zeta_\eta \phi}$ can be written as $\tilde{X}_k = \sqrt{V_k^2 + \omega_k^2} \sqrt{\cos(2\theta)}$. This modification considers the scaling transformation's effects on the hybridization strength, ensuring that the transformed Hamiltonian remains Hermitian.

By applying these scaling transformations, we can establish an equivalent Hermitian model that captures similar physics as the original non-Hermitian model. This allows us to analyze the system using established techniques and concepts from Hermitian quantum mechanics.

We have derived the flow equations by Wegner's generator with appropriate modifications as discussed in section 5.6. The flow trace is well-defined even at the spectral singularity,

$$\tilde{\eta} = [\tilde{H}_0, \tilde{H}_{int}] \quad (5.30)$$

To compute the generator $\tilde{\eta}$, we reexpress the off-diagonal hybridization terms, which can be regarded as \tilde{H}_{int} , and employ them to evaluate commutators.

$$\begin{aligned} H_{hyb}^0 &= \sum_k \frac{\lambda_2}{\Delta} (-ie^{-\frac{i\pi}{3}} d_{\downarrow}^{\dagger} \tilde{c}_{kjm0} + h.c) \\ H_{hyb}^{-} &= \sum_k \frac{\lambda_1}{\Delta} \left(\frac{i}{\sqrt{2}} e^{-\frac{i\pi}{3}} d_{\downarrow}^{\dagger} \tilde{c}_{jm-} + h.c \right) + \sum_k V_{0k} \left(\frac{i}{\sqrt{2}} e^{-\frac{i\pi}{3}} d_{\uparrow}^{\dagger} \tilde{c}_{jm-} + h.c \right) \\ H_{hyb}^{+} &= \sum_k \frac{\lambda_1}{\Delta} \left(\frac{i}{\sqrt{2}} e^{-\frac{i\pi}{3}} d_{\downarrow}^{\dagger} \tilde{c}_{jm+} + h.c \right) + \sum_k V_{0k} \left(\frac{i}{\sqrt{2}} e^{-\frac{i\pi}{3}} d_{\uparrow}^{\dagger} \tilde{c}_{jm+} + h.c \right) \\ \tilde{H}_{int} &= H_{hyb}^0 + H_{hyb}^{-} + H_{hyb}^{+} \end{aligned} \quad (5.31)$$

Now we can calculate the commutators for the generator using the unitary

transformed $H_0 = \sum_{khj_m} \epsilon_{kh} c_{khj_m}^\dagger c_{khj_m}$

$$\begin{aligned}
\tilde{\eta} &= [\tilde{H}_0, \tilde{H}_{int}] \\
&= \left[\sum_{kj_m h=0, \pm} \epsilon_{kh} \tilde{c}_{khj_m}^\dagger \tilde{c}_{khj_m}, \sum_{k'} \lambda_2^r (-ie^{-\frac{i\pi}{3}} d_\downarrow^\dagger \tilde{c}_{kj_m 0}) \right] \\
&+ \left[\sum_{kj_m h=0, \pm} \epsilon_{kh} \tilde{c}_{khj_m}^\dagger \tilde{c}_{khj_m}, \sum_{k'} \lambda_1^r \left(\frac{i}{\sqrt{2}} e^{-\frac{i\pi}{3}} d_\downarrow^\dagger \tilde{c}_{k'j'_m -} \right) \right] \\
&+ \left[\sum_{kj_m h=0, \pm} \epsilon_{kh} \tilde{c}_{khj_m}^\dagger \tilde{c}_{khj_m}, \sum_{k'} \lambda_0^r \left(\frac{i}{\sqrt{2}} e^{-\frac{i\pi}{3}} d_\uparrow^\dagger \tilde{c}_{k'j'_m -} \right) \right] \\
&+ \left[\sum_{kj_m h=0, \pm} \epsilon_{kh} \tilde{c}_{khj_m}^\dagger \tilde{c}_{khj_m}, \sum_{k'} \lambda_1^r \left(\frac{i}{\sqrt{2}} e^{-\frac{i\pi}{3}} d_\downarrow^\dagger \tilde{c}_{k'j'_m +} \right) \right] \\
&+ \left[\sum_{kj_m h=0, \pm} \epsilon_{kh} \tilde{c}_{khj_m}^\dagger \tilde{c}_{khj_m}, \sum_{k'} \lambda_0^r \left(\frac{i}{\sqrt{2}} e^{-\frac{i\pi}{3}} d_\uparrow^\dagger \tilde{c}_{k'j'_m +} \right) \right] \\
&+ U[d_\uparrow^\dagger d_\downarrow^\dagger d_\uparrow d_\downarrow, \tilde{H}_{int}] \\
\tilde{\eta} &= \sum_{kj_m} (\epsilon_{k2} - \epsilon_d) \lambda_2 \lambda_2^r (-ie^{-\frac{i\pi}{3}} d_\downarrow^\dagger \tilde{c}_{kj_m 0} - ie^{\frac{i\pi}{3}} \tilde{c}_{kj_m 0}^\dagger d_\downarrow) \\
&+ \sum_{kj_m} (\epsilon_{k1} - \epsilon_d) \lambda_1 \lambda_1^r \left(\frac{i}{\sqrt{2}} e^{-\frac{i\pi}{3}} d_\downarrow^\dagger \tilde{c}_{k'j'_m -} + \frac{i}{\sqrt{2}} e^{\frac{i\pi}{3}} \tilde{c}_{k'j'_m +}^\dagger d_\downarrow \right) \\
&+ \sum_{kj_m} (\epsilon_{0k} - \epsilon_d) V_{0k} V_{0k}^r \left(\frac{i}{\sqrt{2}} e^{-\frac{i\pi}{3}} d_\uparrow^\dagger \tilde{c}_{k'j'_m -} + \frac{i}{\sqrt{2}} e^{\frac{i\pi}{3}} \tilde{c}_{k'j'_m +}^\dagger d_\uparrow \right) \\
&+ \sum_{qh} \eta^2 (d_\uparrow^\dagger d_\downarrow^\dagger d_\uparrow c_{qhj_m h}) \dots
\end{aligned} \tag{5.32}$$

With the above-derived generator, we can derive the flow equations as

$\frac{dH}{dl} = [H, \eta]$ for the effective model after the unitary transformations.

$$\begin{aligned}
\frac{d\lambda_{kh}}{dl} &= -\lambda_{kh}^r (\epsilon_{kh} - \epsilon_d)^2 + \lambda_{kh} \sum_p \lambda_{ph'} \lambda_{ph''}^r - \lambda_{kh}^r \sum_p \lambda_{ph'}^2 - U^2 n_d (1 - n_d) \lambda_{kh}^r \\
\frac{dV_{0k}}{dl} &= -V_{0k}^r (\epsilon_{0k} - \epsilon_d)^2 + V_{0k} \sum_{ph} V_{0p} \lambda_{ph}^r - V_{0k}^r \sum_p V_{0p}^2 - U^2 n_d (1 - n_d) \lambda_{kh}^r \\
\frac{d\epsilon_{kh}}{dl} &= 2(\epsilon_{kh} - \epsilon_d) \lambda_{kh} \lambda_{kh'}^r + 2(\epsilon_{kh} - \epsilon_d) V_{0k} \lambda_{kh}^r \\
\frac{d\epsilon_d}{dl} &= \frac{2 \sum_{kh} (\tilde{\epsilon}_d - \epsilon_k)^2 \lambda_{kh} \lambda_{kh'}^r + 2U \sum_{khh'} \lambda_{kh} \lambda_{kh'}^r (n_d - n_k)}{(1 - U \frac{dn_d}{d\epsilon_d})} \\
&\quad + \frac{2 \sum_{kh} (\tilde{\epsilon}_d - \epsilon_k)^2 V_{0k} \lambda_{kh'}^r + 2U \sum_{khh'} V_{0k} \lambda_{kh'}^r (n_d - n_k)}{(1 - U \frac{dn_d}{d\epsilon_d})} \\
\frac{dU}{dl} &= 4U \sum_k \lambda_{k+} \lambda_{k+}^r + 4U \sum_k \lambda_{k0} \lambda_{k0}^r + 4U \sum_k \lambda_{k-} \lambda_{k-}^r \\
&\quad + 4U \sum_{kh} V_{0k} \lambda_{kh}^r
\end{aligned} \tag{5.33}$$

In the context of the equations provided in 5.33, it's essential to recognize that the coupling parameters λ represent distinct channel hybridizations.

To observe Exceptional Points (EPs) within the framework of equations 5.33, we embark on solving the hybridization flow equations. This investigation leads to a remarkable finding: the parameter λ_{kh} remains invariant. Furthermore, in equations 5.34 and 5.35, we highlight the presence of singular points in the effective hybridization as a consequence of the renormalization process.

It's important to emphasize that all possible permutations of h and h' must be taken into account when expanding the succinctly expressed equations mentioned above. This comprehensive approach necessitates solving seven matrix differential equations, which will subsequently be compared with appropriately scaled model equations in the subsequent section.

$$\frac{\log(\lambda_{1,2})}{\epsilon_d^2 \Delta^2} - \frac{\log(\lambda_{1,2} - \epsilon_d \Delta)}{\epsilon_d^2 \Delta^2} - \frac{1}{\epsilon_d \Delta (\lambda_{1,2} - \epsilon_d \Delta)} = \text{Invariant} \tag{5.34}$$

With the incorporation of interaction terms, we can find renormalization of

the above couplings as,

$$\begin{aligned}
& - \frac{\log \left(\left(\epsilon_d - \frac{\lambda_{1,2}}{\Delta} \right)^2 - U^2 n_d (1 - n_d) \right) + \frac{2\epsilon_d \tan^{-1} \left(\frac{\epsilon_d - \frac{\lambda_{1,2}}{\Delta}}{\sqrt{-U^2 n_d (1 - n_d)}} \right)}{\sqrt{-U^2 n_d (1 - n_d)}} - 2 \log \left(-\frac{\lambda_{1,2}}{\Delta} \right)}{2(\epsilon_d^2 - U^2 n_d (1 - n_d))} \\
& = \text{Invariant}
\end{aligned} \tag{5.35}$$

Usual hybridization will also show invariance as $\frac{1}{\epsilon_d} \ln V_0$ which remain constant under flow. The exact solution of parity and time symmetry breaking in some chiral channels can be seen as follows,

$$\begin{aligned}
& - \frac{1}{2(k-2)^3} \left(\frac{2\epsilon_d (4\epsilon_d^2 (k^2 + 4k - 4) - k(k^2 + 2k - 8)) \tan^{-1} \left(\frac{(k-2)\Delta - \epsilon_d k}{\sqrt{(k-2)k - 4\epsilon_d^2 (k-1)}} \right)}{\sqrt{(k-2)k - 4\epsilon_d^2 (k-1)}} \right. \\
& - k(-8\epsilon_d^2 + k - 2) \log(\epsilon_d^2 (k-2) - 2\epsilon_d k \Delta + k\Delta^2 + k - 2\Delta^2) \\
& \left. + 8\epsilon_d (k-2)\Delta + (k-2)^2 \Delta^2 \right) = \frac{\lambda_2^2}{2} + \text{constant}
\end{aligned}$$

where $k = U^2 n_d (1 - n_d)$ and $\Delta = \sqrt{\lambda_1^2 + \lambda_2^2}$

(5.36)

In order to check the exact diagonalization results obtained earlier we can take the limit $k \rightarrow 0$ this can happen in two limits one is single occupancy $\langle n_d \rangle = \langle n_{d\uparrow} \rangle + \langle n_{d\downarrow} \rangle = 1$ or non-interacting limit, we take finite U limit and set $\epsilon_d = -\frac{U}{2}$.

$$\left(\epsilon_d^2 \tan^{-1} \left(\frac{\Delta}{\epsilon_d} \right) - \epsilon_d \Delta + \frac{\Delta^2}{4} \right) = \frac{\lambda_2^2}{2} + \text{constant} \tag{5.37}$$

In the above equation 5.37 contains invariant which is nothing but the renormalized hybridization function \tilde{V}_{0k} . Now we can analyze the zeros of this function and identify the EPs, particularly in the limit of large U in equation 5.37. one can show RG invariant along $\frac{U}{2}\Delta + \frac{\Delta^2}{4} - \frac{\lambda_2^2}{2} = 0$ implying vanishing of effective interaction and formation of free local moment when $\lambda_1 = \lambda_2$.

5.6.1 Unitary Operator for \mathcal{PT} -SIAM

Through the utilization of operator transformations, we have exhibited the representation of eigenvectors as novel operators that uphold commutation

relations, as also expounded⁶ across diverse problem sets. Scaling both left and right operators, and employing a simplified model for the density of states, enables the identification of eigenvalue degeneracies by locating the zeros of these functions. This analytical approach provides invaluable insights into the system's behavior, contributing significantly to our comprehension of non-Hermitian models within the realm of condensed matter physics.

The exploration of these mapping techniques and the recognition of crucial features, such as eigenvalue degeneracies, unveils the fundamental physics underlying non-Hermitian systems. To demonstrate how the mapping works we will consider resonant level non-Hermitian Anderson Model (NHAM) as follows,

$$H_{NHAM} = \sum_{\alpha k \sigma} c_{\alpha k \sigma}^\dagger c_{\alpha k \sigma} + \sum_{\sigma} \epsilon_d d_{\sigma}^\dagger d_{\sigma} + \sum_{\alpha k \sigma} |X_k| e^{i\xi_{\alpha}\phi} (c_{\alpha k \sigma}^\dagger d_{\sigma} + hc), \quad (5.38)$$

where $|X_k| = \sqrt{V_k^2 + \omega_k^2}$

The above model in equation 5.38 can be written in matrix for for 3-site problem similar to the zero bandwidth problem of appendix C in Hewson textbook⁷.

$$\begin{aligned} H_{NHAM}^{3-site} &= \psi^\dagger \hat{H} \psi \\ &= \begin{pmatrix} c_{Lk}^\dagger & d_{\sigma}^\dagger & c_{Rk}^\dagger \end{pmatrix} \begin{pmatrix} \epsilon_{Lk} & |X_k| e^{-i\phi} & 0 \\ |X_k| e^{-i\phi} & \epsilon_d & |X_k| e^{i\phi} \\ 0 & |X_k| e^{i\phi} & \epsilon_{Rk} \end{pmatrix} \begin{pmatrix} c_{Lk\sigma} \\ d_{\sigma\sigma} \\ c_{Rk\sigma} \end{pmatrix} \quad (5.39) \end{aligned}$$

For the above form of the model in equation 5.39 we can find the following

\mathcal{PT} -Unitary operator θ which satisfies the relation $(\mathcal{PT}\theta)^\dagger\theta = \mathcal{I}$.

$$\begin{aligned}
\mathcal{U}\hat{H}\mathcal{U}^\dagger &= \theta \begin{pmatrix} \epsilon_{Lk} & |X_k|e^{-i\phi} & 0 \\ |X_k|e^{-i\phi} & \epsilon_d & |X_k|e^{i\phi} \\ 0 & |X_k|e^{i\phi} & \epsilon_{Rk} \end{pmatrix} (\mathcal{PT}\theta^\dagger) \\
|0\rangle &= \frac{1}{\sqrt{N_0}} \begin{pmatrix} |X_k|e^{i\phi} \\ 0 \\ -|X_k|e^{-i\phi} \end{pmatrix} |\pm\rangle = \frac{1}{\sqrt{N_\pm}} \begin{pmatrix} |X_k|e^{-i\phi} \\ \frac{(\epsilon_0 - \epsilon)}{2} \pm \sqrt{\Delta} \\ |X_k|e^{i\phi} \end{pmatrix} \\
\theta_k &= \begin{pmatrix} \frac{|X_k|e^{-i\phi}}{\sqrt{N_+}} & \frac{((\epsilon_0 - \epsilon)/2 + \sqrt{\Delta})}{\sqrt{N_+}} & \frac{|X_k|e^{i\phi}}{\sqrt{N_+}} \\ \frac{|X_k|e^{i\phi}}{\sqrt{N_0}} & 0 & -\frac{|X_k|e^{-i\phi}}{\sqrt{N_0}} \\ \frac{|X_k|e^{-i\phi}}{\sqrt{N_-}} & \frac{(\epsilon_0 - \epsilon)/2 - \sqrt{\Delta}}{\sqrt{N_-}} & \frac{|X_k|e^{i\phi}}{\sqrt{N_-}} \end{pmatrix} \\
N_{\pm,0} &= \langle \pm, 0 | (\mathcal{PT} | \pm, 0 \rangle), \quad \Delta = \frac{(\epsilon_0 - \epsilon)^2 + 8|X_k|^2 \cos(2\phi)}{4} \\
\begin{pmatrix} c_{Lk} \\ d \\ c_{Rk} \end{pmatrix} &\Rightarrow \begin{pmatrix} \tilde{c}_{k+} \\ \tilde{d} \\ \tilde{c}_{k-} \end{pmatrix} \\
\tilde{c}_{k\pm} &= \frac{1}{\sqrt{N_\pm}} (|X_k|e^{-i\phi} c_{Lk} + ((\epsilon_0 - \epsilon)/2 \pm \sqrt{\Delta}) d + |X_k|e^{i\phi} c_{Rk}) \\
\tilde{d} &= \frac{1}{\sqrt{N_0}} (|X_k|e^{i\phi} c_{Lk} - |X_k|e^{-i\phi} c_{Rk})
\end{aligned} \tag{5.40}$$

When we compare the unitary obtained in equation 5.5 to equation 5.40, we can see that the normalization factors $N_{\pm,0}$ of the \mathcal{PT} vectors help us create a new basis for the transformed operators. This results in an effective Hermitian model that has the same eigenvalues as the original \mathcal{PT} -AM. In this new basis, the effective hybridization is represented by $\tilde{X} = |X_k| \sqrt{\cos(2\phi)}$, which is equal to $\sqrt{X_{k\text{real}}^2 - X_{k\text{im}}^2}$.

In the scaled model with the transformed Hamiltonian \tilde{H} , one can conveniently apply the Heisenberg equation of motion, even without the need to determine the left-right states in advance. This allows us to establish the Green functions and subsequently derive their corresponding Lehmann representation. The scaled model is given by $\tilde{H} = \sum_{\eta k} \epsilon_{\eta k} \tilde{c}_{\eta k}^\dagger \tilde{c}_{\eta k} + H_d + \sum_{\eta k} \tilde{X} (\tilde{c}_{\eta k}^\dagger d + \text{h.c.})$. In the scaled model, the H_d part remains unaffected since the \mathcal{PT} -symmetric hybridization arises from the bath itself. This allows for an open condition where the number of bath electrons can vary. However, a unitary transformation is performed at the impurity site, preserving the original information. The eigenvalues of the Resonant Anderson Model (AM) for a system with $X_{\mathbf{k},\mathbf{k}'} = X$ and n bands can be determined. In

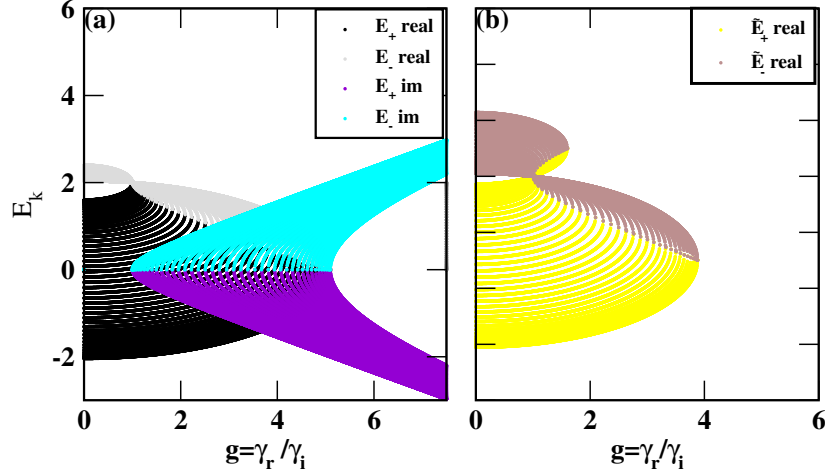


Figure 5.2: The figure displays a comparison between the original non-Hermitian resonant level Anderson model (NHAM) and the Anderson model after mapping. In plot (a), you can observe the eigenvalues of NHAM, while plot (b) showcases the eigenvalues of the mapped Anderson model.

this case, the eigenvalues are given by $\lambda_{2,3,\dots,n} = \epsilon_{\mathbf{k}2}, \epsilon_{\mathbf{k}3} \dots \epsilon_{\mathbf{k}n}$, while λ_1 takes the form of $(\epsilon_{\mathbf{k}1} + \epsilon_d) \pm \sqrt{(\epsilon_{\mathbf{k}1} - \epsilon_d)^2 + 4V^2}$.

Similarly, for the \mathcal{PT} -AM with $\omega_{\mathbf{k},\mathbf{k}'} = \omega$ and $\epsilon_{L\mathbf{k}n} = \epsilon_{R\mathbf{k}n}$, the eigenvalues are $\lambda_{2,3,\dots,n} = \epsilon_{\mathbf{k}2}, \epsilon_{\mathbf{k}3} \dots \epsilon_{\mathbf{k}n}$, and the eigenvalue ϵ is given by $\frac{(\epsilon_d - \epsilon_{\mathbf{k}h})}{2} \pm \frac{1}{2} \sqrt{(\epsilon_d - \epsilon_{\mathbf{k}h})^2 + 8(X_{real}^2 - X_{im}^2)}$.

Incorporating spin-orbit coupling (SO) modifies the energy levels E_p , expressed as $\frac{X_{im}}{X_{real}} = \pm \sqrt{1 - \frac{(\epsilon_{\mathbf{k}h} - \epsilon_d)^2}{8V_{real}^2}}$. During the transition, a pair of eigenvalues become complex. Figure 5.2 below illustrates the \mathcal{PT} transition for $\epsilon_{\mathbf{k}} \neq \epsilon_d$ with different values of g . *The \mathcal{PT} -unitary operation we identified serves the purpose of determining the phase factors associated with bath operators, enabling their scaling to transform the system into a Hermitian model. It's important to note that this mapping operation is not actually unitary in nature. Despite this, it achieves the remarkable result of preserving the same spectrum in the real regime of eigenvalues in the mapped model. This approach can be interpreted as a form of scaling the gauge operators, allowing us to reformulate conventional quantum mechanical problems in the framework of first quantization⁸. Transformed Hamiltonian will be of the in the scaled operators and can be written as follows,*

$$\tilde{H}_{AM} = \sum_{\alpha k \sigma} \epsilon_{\alpha k \sigma} \tilde{c}_{\alpha k \sigma}^\dagger \tilde{c}_{\alpha k \sigma} + \sum_{\sigma} \epsilon_d d_\sigma^\dagger d_\sigma + \sum_{\alpha k \sigma} |X_k| \sqrt{\cos \phi} (e^{i\xi_\alpha \phi} \tilde{c}_{\alpha k \sigma}^\dagger d_\sigma + hc) \quad (5.41)$$

Below, we illustrate how the transformation operates on the model for discrete k-points, as presented. It's important to note that in this particular case, we have assumed that ϕ remains independent of k. Nevertheless, it's worth mentioning that the concept can be readily extended to more general scenarios.

$$\begin{array}{c}
 \begin{bmatrix}
 \ddots & & \vdots & & \ddots \\
 \dots & \epsilon_{Lk_1} & |X_{Lk_1}|e^{-i\phi} & 0 & \dots \\
 \dots & |X_{Lk_1}|e^{-i\phi} & \epsilon_d & |X_{Rk_1}|e^{i\phi} & \dots \\
 \dots & 0 & |X_{Rk_1}|e^{-i\phi} & \epsilon_{Rk_1} & \dots \\
 \ddots & & \vdots & & \ddots
 \end{bmatrix} \\
 \downarrow \\
 \text{Transformation} \\
 \begin{bmatrix}
 \ddots & & \vdots & & \ddots \\
 \dots & \epsilon_{Lk_1} & |X_{Lk_1}|\sqrt{\cos\phi}e^{-i\phi} & 0 & \dots \\
 \dots & |X_{Lk_1}|\sqrt{\cos\phi}e^{i\phi} & \epsilon_d & |X_{Rk_1}|\sqrt{\cos\phi}e^{-i\phi} & \dots \\
 \dots & 0 & |X_{Rk_1}|\sqrt{\cos\phi}e^{i\phi} & \epsilon_{Rk_1} & \dots \\
 \ddots & & \vdots & & \ddots
 \end{bmatrix}
 \end{array}$$

The plot in figure 5.2 illustrates the comparison between the original non-Hermitian resonant level Anderson model in the equation 5.41 and the mapped Anderson model. The \mathcal{PT} Resonant Anderson model can be represented in matrix form. Spin-orbit coupling introduces time-reversal-invariant chiral channels, resulting in spin-dependent hybridization and modified dispersion. In the first case, these modifications arise from the k-dependence of the energy levels E_p . By performing a unitary transformation, such as $c_{\pm} = (c_{Rk} \pm c_{Lk})/\sqrt{2}$, the scaled Hamiltonian transforms into a single impurity Anderson model (SIAM) with two flavors. This transformation enables the calculation of spectral functions. The retarded Green's function for the scaled Hamiltonian can be determined from these calculations.

$$\begin{aligned}
 \tilde{\mathcal{G}}_{c_{\eta}^{\dagger}c_{\eta}}^{-1} &= \frac{1}{N_{\eta}} \left(\omega^{+} - \epsilon - \sum_{k\eta=\pm} \frac{\tilde{V}_{\eta}^2}{\omega^{+} - \epsilon_d - \sum_{k\eta=\pm} \frac{\tilde{V}_{\eta}^2}{\omega^{+} - \epsilon}} \right) \\
 \tilde{\mathcal{G}}_{d^{\dagger}d}^{-1} &= \frac{1}{N_0} \left(\omega^{+} - \epsilon_d - \sum_{\eta k} \frac{\tilde{V}_{\eta k}^2}{\omega^{+} - \epsilon_{k\eta=\pm}} \right)
 \end{aligned} \tag{5.42}$$

5.6.2 Flow equations For Scaled PTSIAM

An essential benefit demonstrated in the previous section regarding mapping or complex scaling is its capability to transform a problem into a Hermitian one. This proves especially advantageous because it simplifies the intricate task of normal ordering in non-Hermitian systems, particularly when handling left-right states. Normal ordering can be quite challenging in such scenarios; however, by employing mapping, we can apply conventional normal ordering techniques to derive the flow equations, making the calculation process more straightforward and efficient. In the equation 5.30, the Hamiltonian \tilde{H}_0 represents the kinetic component in a new basis, which is parameterized by scaled parameters derived from the bare model:

$$\tilde{\epsilon}_k = \frac{e^{-i\theta_k}}{\sqrt{\cos(2\theta_k)}} \theta_k = \arctan\left(\frac{\omega_k \sin(\phi_k)}{v_k + \omega_k \cos(\phi_k)}\right) \quad \tilde{V}_k = \sqrt{V^2 + \omega_k^2} \sqrt{\cos(2\theta_k)}$$

For the derivatives, we calculate:

$$\begin{aligned} \frac{d\tilde{\epsilon}_{Lk}}{dl} &= \frac{e^{-2i\theta_k}}{\cos(2\theta_k)} \frac{d\tilde{\epsilon}_k}{dl} - 2i \frac{e^{-2i\theta_k}}{\cos^2(2\theta_k)} \sin(2\theta_k) \frac{d\theta_k}{dl} \\ \frac{d\tilde{\epsilon}_{Rk}}{dl} &= \frac{e^{2i\theta_k}}{\cos(2\theta_k)} \frac{d\tilde{\epsilon}_k}{dl} + 2i \frac{e^{2i\theta_k}}{\cos^2(2\theta_k)} \sin(2\theta_k) \frac{d\theta_k}{dl} \end{aligned}$$

The derivative for the scaling angle θ_k is given by:

$$\frac{d\theta_k}{dl} = \frac{V_k \frac{d\omega_k}{dl}}{V_k^2 + \omega_k^2} - \frac{\omega_k \frac{dV_k}{dl}}{V_k^2 + \omega_k^2}$$

Substituting these derivatives into the flow equations, we obtain:

$$\frac{d\tilde{V}_k}{dl} = \frac{V_k^3 - V_k \omega_k^2 - 2V_k \omega_k^2}{\sqrt{V_k^2 - \omega_k^2}(V^2 + \omega_k^2)} \frac{dV_k}{dl} + \frac{-\omega_k^3 + \omega_k V_k^2 + 2\omega_k V_k^2}{\sqrt{V_k^2 - \omega_k^2}(V^2 + \omega_k^2)} \frac{d\omega_k}{dl}$$

$$\begin{aligned}
\frac{d\tilde{V}_k}{dl} &= \frac{V_k^3 - V_k\omega_k^2 - 2V_k\omega_k^2}{\sqrt{V_k^2 - \omega_k^2}(V^2 + \omega^2)} \frac{dV_k}{dl} \\
&+ \frac{-\omega_k^3 + \omega_k V_k^2 + 2\omega_k V_k^2}{\sqrt{V_k^2 - \omega_k^2}(V^2 + \omega^2)} \frac{d\omega_k}{dl} \\
\frac{V_k^3 - V_k\omega_k^2 - 2V_k\omega_k^2}{\sqrt{V_k^2 - \omega_k^2}(V^2 + \omega^2)} \frac{dV_k}{dl} &= -V_k^r(\epsilon(k) - \epsilon(\tilde{d}))^2 + V_k \sum_p V_p V_p^r - V_k^r \sum_p V_p^2 \\
&- U^2 n_d(1 - n_d) V_k^r \\
\frac{-\omega_k^3 + \omega_k V_k^2 + 2\omega_k V_k^2}{\sqrt{V_k^2 - \omega_k^2}(V^2 + \omega^2)} \frac{d\omega_k}{dl} &= -\omega_k^r(\epsilon(k) - \epsilon(\tilde{d}))^2 + \omega_k \sum_p \omega_p \omega_p^r - \omega_k^r \sum_p \omega_p^2 \\
&- U^2 n_d(1 - n_d) \omega_k^r \\
\frac{d\epsilon_k}{dl} &= 2(\epsilon(k) - \epsilon(\tilde{d})) V_k V_k^r + 2(\epsilon(k) - \epsilon(\tilde{d})) \omega_k \omega_k^r \\
\frac{d\tilde{\epsilon}_d}{dl} &= \frac{2 \sum_k (\tilde{\epsilon}_d - \epsilon_k)^2 V_k V_k^r + 2 \sum_k (\tilde{\epsilon}_d - \epsilon_k)^2 \omega_k \omega_k^r}{(1 - U \frac{dn_d}{d\epsilon_d})} \\
&+ \frac{2U \sum_k V_k V_k^r (n_d - nk)}{(1 - U \frac{dn_d}{d\epsilon_d})} \\
&+ \frac{2U \sum_k \omega_k \omega_k^r (n_d - nk)}{(1 - U \frac{dn_d}{d\epsilon_d})} \\
\frac{dU}{dl} &= 4U \sum_k V_k V_k^r + 4U \sum_k \omega_k \omega_k^r
\end{aligned} \tag{5.43}$$

The condition for \mathcal{PT} -symmetry holds true only when $\epsilon_k = \epsilon_d$. Furthermore, we establish the conditions for explicit Parity-time reversal breaking in the Hermitian model and derive the flow equations for the non-Hermitian model. To effectively implement the Runge-Kutta method and capture the \mathcal{PT} -transition in the equations where $V_k = \omega_k$, we commence by formulating the scaled PTSIAM (Parity-Time Symmetric Impurity Anderson Model) equations. These equations characterize the system and must be appropriately structured for numerical integration.

Once we have derived the equations, we proceed to implement the Runge-Kutta method. This numerical integration technique enables us to approximate the solutions of the equations over time. It entails breaking down the time interval into smaller steps and successively updating the system's variables based on the derivatives of the equations.

In addition to the scaled PTSIAM equations, it is imperative to verify the

\mathcal{PT} -transition equation for the scenario when $V_k = \omega_k$. This equation encapsulates the transition between \mathcal{PT} -preserved and \mathcal{PT} -broken states of the system. By tracing this condition, we ensure that the flow of V_k is accurately represented in the simulation.

5.6.3 Conventional Flow Equations For Non-Hermitian SIAM

We derive conventional flow equations for the symmetry-preserved model. We expect the failure of conventional flow equations at the spectral singularity.

$$\begin{aligned}
f(k) &= \frac{V_k^3 - V_k \omega_k^2 - 2V_k \omega_k^2}{\sqrt{V_k^2 - \omega_k^2}(V^2 + \omega^2)}, \quad g(k) = \frac{-\omega_k^3 + \omega_k V_k^2 + 2\omega_k V_k^2}{\sqrt{V_k^2 - \omega_k^2}(V^2 + \omega^2)} \\
\frac{dU}{dl} &= 4U \sum_k f(k) V_k V_k^r + 4U \sum_k g(k) \omega_k \omega_k^r \\
g(k) \frac{d\omega_k}{dl} &= -\omega_k^r (\epsilon(k) - \epsilon(\tilde{d}))^2 + \omega_k \sum_p g(p) \omega_p \omega_p^r - \omega_k^r \sum_p f(p) \omega_p^2 \\
&\quad - U^2 n_d (1 - n_d) \omega_k^r \\
\frac{d\tilde{\epsilon}_d}{dl} &= \frac{2 \sum_k (\tilde{\epsilon}_d - \epsilon_k)^2 f(k) V_k V_k^r + 2 \sum_k (\tilde{\epsilon}_d - \epsilon_k)^2 g(k) \omega_k \omega_k^r}{(1 - U \frac{dn_d}{d\epsilon_d})} \\
&\quad + \frac{2U \sum_k f(k) V_k V_k^r (n_d - nk)}{(1 - U \frac{dn_d}{d\epsilon_d})} \\
&\quad + \frac{2U \sum_k g(k) \omega_k \omega_k^r (n_d - nk)}{(1 - U \frac{dn_d}{d\epsilon_d})} \\
f(k) \frac{dV_k}{dl} &= -V_k^r (\epsilon(k) - \epsilon(\tilde{d}))^2 + V_k \sum_p f(p) V_p V_p^r - V_k^r \sum_p f(p) V_p^2 \\
&\quad - U^2 n_d (1 - n_d) V_k^r \\
\frac{d\epsilon_k}{dl} &= 2(\epsilon(k) - \epsilon(\tilde{d})) V_k V_k^r + 2(\epsilon(k) - \epsilon(\tilde{d})) \omega_k \omega_k^r
\end{aligned} \tag{5.44}$$

We can use the Runge-Kutta method and schematics shown in figures 5.5 and 5.6 to solve these differential equations in 5.43 and 5.44 respectively. After numerical solutions, We found the \mathcal{PT} transition for $V_k = \omega_k$ as shown in figure 5.4. All three regimes unitary, Exceptional Point, and non-unitary regimes are shown with labels as $V_k > W_k$, $V_k = W_k$, and $W_k > V_k$ respectively. We successfully achieved convergence in all the regimes from the

complex scaling and new generator calculations for non-Hermitian problems. While the quantitative comparison needs further investigations however we did necessary comparisons with Kehrein's work⁹ as shown in figure 5.3 at particle-hole symmetry ($\epsilon_d = -\frac{U}{2}$) and away from it ie., ($\epsilon_d \neq -\frac{U}{2}$).

In a recent paper by Budich et al.¹⁰, the flow equation method has undergone significant advancements. These developments include a new generator suggestion and an efficient algorithm, which have greatly improved the field of dissipative flow equations. The improvements made by Budich et al. have surpassed those made by Kehrein¹¹, especially in examining time-dependent scenarios, as shown by Thomson et al.¹².

Moreover, the flow equation method has been successfully applied to various specific systems, such as impurities in Bose gases¹³, periodically driven systems¹⁴, the sine-Gordon model¹⁵, and interaction quenches in the Hubbard model¹⁶. These applications demonstrate the versatility and broad applicability of the flow equation approach in investigating diverse physical systems and phenomena.

The recent advancements in the flow equation method¹⁰ have brought about a revolutionary breakthrough in the field of dissipative flow equations. With its efficient algorithm, it provides a powerful tool for studying the dynamics and properties of complex systems.

A significant improvement in the flow equation method has been made with the introduction of a new generator¹⁷. This innovation has greatly enhanced the accuracy and efficacy of the flow equation method, particularly in exploring non-Hermitian spin-Boson models and conducting more precise calculations for quantum systems.

The flow equation method builds upon Kehrein's original framework¹¹, which has proven to be especially adept at handling time-dependent scenarios¹². This approach has provided us with valuable insights into the dynamics and behavior of quantum systems when subjected to time-dependent perturbations.

Moreover, the flow equation method has demonstrated its versatility and applicability to various systems. Its successful use in exploring periodically driven systems¹⁴, impurities in Bose gases¹³, the sine-Gordon model¹⁵, and interaction quenches in the Hubbard model¹⁶ illustrates the broad range of phenomena that can be explored using this method. The growing significance of the flow equation method in the field of quantum physics is evident.

The recent developments in the flow equation method, including the new generator suggestion and efficient algorithm, hold much promise for deeper insights and exciting advancements in the study of dissipative flow equations and quantum systems.

5.7 Discussion and Conclusion

In the first part of our work, we explored the intriguing emergence of exceptional points in the impurity subspace when the bath features explicit parity-time-breaking interactions. Leveraging the analytical scale provided by the Finite U Slave-Boson method, we conducted a comprehensive comparison with the Flow equations method. This analysis allowed us to delve deeply into the potential interplay between perturbations and strong interaction effects on subsystems.

One of the pivotal accomplishments of this project is the development of an efficient generator tailored for the non-Hermitian model, seamlessly integrated into the standard flow equations method. Successfully achieving numerical convergence with non-Hermitian terms, our results proved highly satisfactory. Figures 5.3 and 5.5 represent the crowning achievement of our research, vividly illustrating the convergence of nonlinear flow equations in the presence of non-Hermiticity. This outcome underscores the robustness and reliability of our approach in elucidating the behavior of the system, even under the influence of non-Hermitian effects.

The presence of interaction-induced exceptional points within Hermitian models stands as a noteworthy highlight of our study. Our investigation has unraveled these exceptional points, shedding light on the intricate interplay between interactions and system behavior.

Additionally, we introduced an innovative generator within the context of the flow equation method, offering fresh insights into the dynamics of the model and the genesis of exceptional points.

Moreover, our work extends to the mapping of non-Hermitian models to isospectral Hermitian models. This mapping technique constitutes a pivotal stride in expanding our comprehension of these intricate systems, serving as a bridge between two seemingly disparate domains. It empowers us to harness the analytical tools of Hermitian models for the study of non-Hermitian systems, enriching our understanding of their underlying principles.

Bibliography

- [1] G. Nirala, S. N. Sahoo, A. K. Pati, and U. Sinha, Phys. Rev. A **99**, 022111 (2019).
- [2] F. D. M. Haldane, Phys. Rev. Lett. **40**, 416 (1978).
- [3] M. S. Swanson, Journal of Mathematical Physics **45**, 585 (2004).

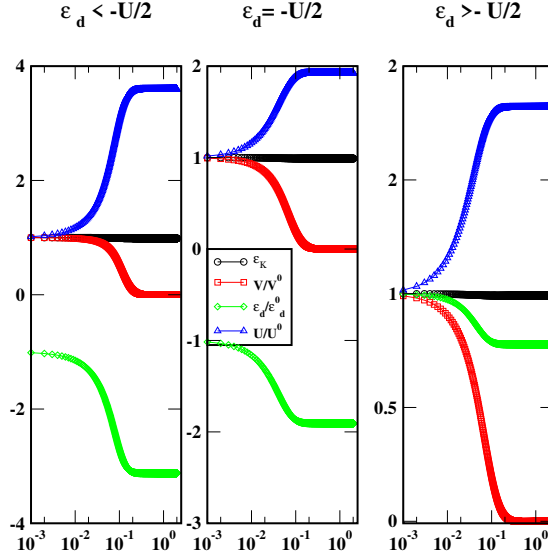


Figure 5.3: The plot for comparing the original flow equations with the new generator flow equations when parity-time breaking interactions are absent.

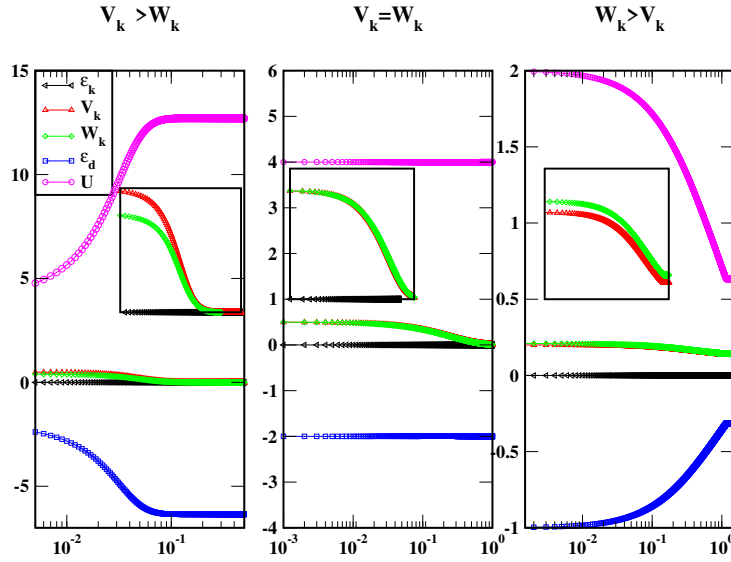


Figure 5.4: The plot for comparing the original flow equations with the new generator flow equations when parity-time breaking interactions are absent.

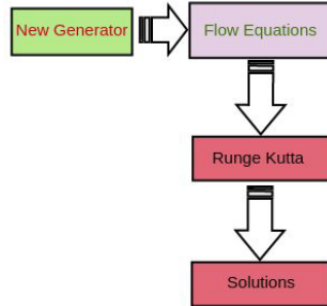


Figure 5.5: To compare the flow equation results we derive flow equations from the new generator and then implement them in the standard algorithm as shown above.

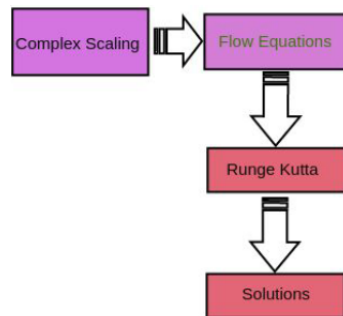


Figure 5.6: Conventional flow equations are derived and implemented as shown in the above protocol.

- [4] M. S. Swanson, *Path integrals and quantum processes* (Courier Corporation, 2014).
- [5] R. Sohn and M. S. Swanson, Journal of Physics A: Mathematical and General **38**, 2511 (2005).
- [6] K. Kawabata, Y. Ashida, H. Katsura, and M. Ueda, Phys. Rev. B **98**, 085116 (2018).
- [7] A. C. Hewson, *The Kondo problem to heavy fermions*, Vol. 2 (Cambridge university press, 1997).
- [8] N. Moiseyev, *Non-Hermitian quantum mechanics* (Cambridge University Press, 2011).
- [9] S. Kehrein, Physical Review Letters **83**, 4914 (1999).
- [10] G. Schmiedinghoff and G. S. Uhrig, SciPost Phys. **13**, 122 (2022).
- [11] S. Kehrein, *The flow equation approach to many-particle systems*, Vol. 217 (Springer, 2007).
- [12] S. Thomson and M. Schiró, Physical Review B **97**, 060201 (2018).
- [13] F. Brauneis, H.-W. Hammer, M. Lemoshko, and A. G. Volosniev, SciPost Physics **11**, 008 (2021).
- [14] M. Vogl, P. Laurell, A. D. Barr, and G. A. Fiete, Physical Review X **9**, 021037 (2019).
- [15] S. Kehrein, Nuclear Physics B **592**, 512 (2001).
- [16] M. Moeckel and S. Kehrein, Phys. Rev. Lett. **100**, 175702 (2008).
- [17] L. Rosso, F. Iemini, M. Schiró, and L. Mazza, SciPost Phys. **9**, 091 (2020).

Chapter 6

Anderson Impurities In Edge States with Nonlinear Dispersion

In this chapter, we explore how the Kondo problem can be affected by a non-linear dispersion, resulting in anomalous effects on electronic transport. By analyzing a specific bath with a 3-fold symmetry in momentum or a $\theta = \frac{\pi}{3}$ symmetry rotation in the Brillouin zone(BZ), we derive an effective spin-spin interacting model. When combining the anisotropic Dzyaloshinskii-Moriya (DM) interaction with non-linear dispersion, exceptional points (E_p) can occur in a Hermitian model. Our renormalization group (RG) analysis shows that the spin relaxation time has the signature of coalescence in momentum-resolved couplings and an ideal logarithmic divergence in resistivity over a range of nonlinearity (β). The effective model at the impurity subspace has a Lie group structure of Dirac matrices. We show nontrivial renormalization within a Poorman approximation with the inclusion of potential scattering, and the invariant obtained will not be altered by potential scattering. We then expand the model to a two-impurity Kondo model and investigate the Kondo destruction and anomalous spin transport signature by calculating the spin-relaxation time (τ). Analysis of RG equation zeros and poles shows that a "Sign Reversion" (SR) regime exists for a Hermitian problem with a critical value of nonlinear coupling J_{k3} . Our results show the existence of an out-of-phase RKKY oscillation above and below the critical value of the chemical potential. The interplay of the interaction and emergence of exceptional points is the key ingredient of the chapter.

Manuscript under Review.

6.1 Introduction

Recent studies have explored non-Hermiticity in open quantum systems^{1;2}, but its implications in condensed matter systems are less well understood. In this work, we investigate how anisotropy can induce exceptional points under perturbative renormalization. Rather than introducing *ad hoc* non-Hermitian terms based solely on symmetry considerations, we incorporate nonlinear corrections that lead to emergent anisotropic interactions.

We examine anisotropic interactions analogous to those found in quantum Hall states with C_4 symmetry³⁻⁵, which demonstrate strong interaction-induced anisotropy and support non-equilibrium states. Building on these insights, we investigate C_3 symmetric bath scatterings with impurities, which exhibit intriguing non-equilibrium steady states. Poddubny's analysis⁶ highlights interaction-induced non-Hermiticity(NH), revealing phenomena such as bound states, edge states, and flat bands.

Experimentally observed third-order exceptional points in \mathcal{PC} symmetric systems⁷ underscore the necessity of additional degrees of freedom(DoF) to achieve higher-order exceptional points. Recent research also suggests that boundary conditions can induce openness, similar to potential scattering terms in impurity-bath interactions. Moreover, nonlinear eigenvalue problems have shown the emergence of auxiliary eigenvalues for small nonlinear interactions⁸. Analogous exceptional points have been considered in real materials and tunable calculations^{9;10}, indicating that finite nonlinear dispersion can lead to complex solutions. A recent study demonstrated the formation of exceptional points in the presence of Hermiticity-breaking terms due to perturbation¹¹. It was also shown that non-Hermitian terms vanish in the strong coupling limit. In this work, we show that certain non-Hermitian scatterings are relevant for weak to intermediate interaction regime in a model having anisotropic \mathcal{DM} interactions. We find novel fixed points in this regime with various supporting analyses of the effective model from perturbative Poorman scaling with potential scattering, Fock-space diagonalization, and transport calculations.

We begin with a generic model¹²⁻¹⁴ for a topological bath with nonlinear dispersion coupled to interacting impurity(dot). Projecting onto the singly occupied subspace of the dot results in an effective Hamiltonian with anisotropic interactions. The analysis reveals emergent pseudo-chiral symmetry through anisotropy and additional DoF, and the model displays topological features in its spectrum near the critical points of the RG treatment, including exceptional points. Incorporating pseudo-chiral symmetric scattering terms lead

to the Lie algebra structure and its connection to the conformal field theory (CFT) results by Pereira et al.¹⁵, emphasizing the model's topological properties. Then the model extended to a two-impurity case, resulting in a two-impurity Kondo (TIK) model. By perturbative RG calculations reveal the novel fixed points through analytical and numerical solutions of the RG equations. We explore the scaling nature of the impurity spin relaxation time and its relation to RG invariants.

6.2 Model and Formalism

We begin with a bath model considered in the context of topological insulators¹², and the Hamiltonian reads as:

$$\hat{H} = \alpha k_{\parallel}^2 \mathbb{I} + \beta k_{\parallel}^3 \cos(3\theta) \sigma_z + i\lambda \hat{z} \cdot (\vec{k} \times \vec{\sigma}), \quad (6.1)$$

where $\vec{k} = k_x \hat{i} + k_y \hat{j} + k_{\parallel} \hat{k}$ and $\vec{\sigma} = \sigma_x \hat{i} + \sigma_y \hat{j} + \sigma_z \hat{k}$, with $\sigma_{x,y,z}$ being Pauli matrices. The parameters α , β , and λ correspond to quadratic, cubic, and linear couplings in the topological system, respectively. The second quantized form of the Hamiltonian for spinful fermions is:

$$H = \sum_k \psi_k^{\dagger} \hat{H} \psi_k, \quad (6.2)$$

Where the basis vector is $\psi_k^{\dagger} = \begin{pmatrix} c_{k\uparrow}^{\dagger} & c_{k\downarrow}^{\dagger} \end{pmatrix}$. Introducing an impurity with on-site interaction generally regarded as the single impurity Anderson model (SIAM) and hybridization with the edge states leads to the Hamiltonian:

$$H_{\text{SIAM}} = \psi^{\dagger} \hat{H} \psi + H_d + \sum_{k\sigma} V_k (c_{k\sigma}^{\dagger} d_{\sigma} + \text{h.c.}), \quad (6.3)$$

where H_d is defined as:

$$H_d = \sum_{\sigma} \epsilon_d d_{\sigma}^{\dagger} d_{\sigma} + U n_{d\uparrow} n_{d\downarrow}.$$

To simplify the bath Hamiltonian, we use the parametrization $k_x \pm ik_y = k_{\parallel} e^{\pm i\theta}$ and apply a k -dependent unitary operation on the bath operators, preserving canonical relations. This results in a nonlinear k -dependent coefficient as shown below,

$$\mathcal{U} = \frac{1}{\sqrt{\mathcal{N}}} \begin{pmatrix} e^{i\frac{\theta}{2}} \alpha_{k1} & -ie^{i\frac{\theta}{2}} \alpha_{k2} \\ e^{-i\frac{\theta}{2}} \alpha_{k2} & ie^{-i\frac{\theta}{2}} \alpha_{k1} \end{pmatrix} \quad (6.4)$$

In above equation 6.4 coefficients $\alpha_{k1} = \sqrt{\Delta + \beta k^3 \cos 3\theta}$ and $\alpha_{k2} = \sqrt{\Delta - \beta k^3 \cos 3\theta}$. And the normalization constant is $\mathcal{N} = |\alpha_{k1}|^2 + |\alpha_{k2}|^2 = \Delta$, where $\Delta = \sqrt{\beta^2 k^6 \cos^2 3\theta + \lambda^2 k^2} = \beta k^3 \gamma \cos 3\theta$, with $\gamma = \sqrt{1 + \frac{\lambda^2}{\beta^2 k^4 \cos^2 3\theta}}$. In the limit $\lambda \rightarrow 0$ or $\beta \rightarrow \infty$, $\gamma \rightarrow 1$.

In equation 6.4 choice for α_{k2} can be $\sqrt{\beta k^3 \cos 3\theta - \Delta}$ or $i\sqrt{\Delta - \beta k^3 \cos 3\theta}$. Both forms diagonalize the bath Hamiltonian having two chiral bands with the eigenenergies $\epsilon_{k\zeta} = \alpha k^2 + \zeta \Delta$ and it's eigenvalues are shown in figure 6.1. This non-interacting spectrum is similar to Rashba study¹⁶ except from nonlinear term which serves as additional parameter to tune band touching to gapped phase in the bath.

This unitary transformation rotates the bath operators as $\tilde{\psi}_k = \mathcal{U}_k \psi_k$. Such k -dependent operations are used in the case of Weyl multiplicity^{17;18} having different nonlinear dispersion as $(k_x \pm ik_y)^3$. Basis after rotation $\tilde{\psi} = \begin{pmatrix} c_{k+} \\ c_{k-} \end{pmatrix} = \mathcal{U} \psi$ can be shown as,

$$\begin{aligned} c_{k+} &= \frac{1}{\sqrt{\beta \gamma k^3 \cos 3\theta}} \left(e^{-i\frac{\theta}{2}} \alpha_{k1} c_{k\uparrow} + e^{i\frac{\theta}{2}} \alpha_{k2} c_{k\downarrow} \right) \\ c_{k-} &= \frac{1}{\sqrt{\beta \gamma k^3 \cos 3\theta}} \left(i e^{i\frac{\theta}{2}} \alpha_{k2} c_{k\uparrow} - i e^{i\frac{\theta}{2}} \alpha_{k1} c_{k\downarrow} \right) \end{aligned} \quad (6.5)$$

Using $\psi = \mathcal{U}^{-1} \tilde{\psi}$ to express the original spin basis in terms of these new chiral basis,

$$\begin{aligned} c_{k\uparrow} &= \frac{1}{\sqrt{\beta \gamma k^3 \cos 3\theta}} \left(e^{i\frac{\theta}{2}} \alpha_{k1} c_{k+} - i e^{i\frac{\theta}{2}} \alpha_{k2} c_{k-} \right) \\ c_{k\downarrow} &= \frac{1}{\sqrt{\beta \gamma k^3 \cos 3\theta}} \left(e^{-i\frac{\theta}{2}} \alpha_{k2} c_{k+} + i e^{-i\frac{\theta}{2}} \alpha_{k1} c_{k-} \right) \end{aligned} \quad (6.6)$$

In new basis the hybridization transforms as follows:

$$\begin{aligned} \tilde{H}_{hyb}^+ &= \sum_{k\theta} \tilde{V}_k^\theta \left(e^{-i\frac{\theta}{2}} \alpha_{k1} c_{k+}^\dagger d_\uparrow + \text{h.c.} \right) \\ &\quad + \sum_{k\theta} \tilde{V}_k^\theta \left(e^{i\frac{\theta}{2}} \alpha_{k2} c_{k+}^\dagger d_\downarrow + \text{h.c.} \right) \\ \tilde{H}_{hyb}^- &= \sum_{k\theta} \tilde{V}_k^\theta \left(i e^{-i\frac{\theta}{2}} \alpha_{k2} c_{k-}^\dagger d_\uparrow + \text{h.c.} \right) \\ &\quad + \sum_{k\theta} \tilde{V}_k^\theta \left(-i e^{i\frac{\theta}{2}} \alpha_{k1} c_{k-}^\dagger d_\downarrow + \text{h.c.} \right) \end{aligned} \quad (6.7)$$

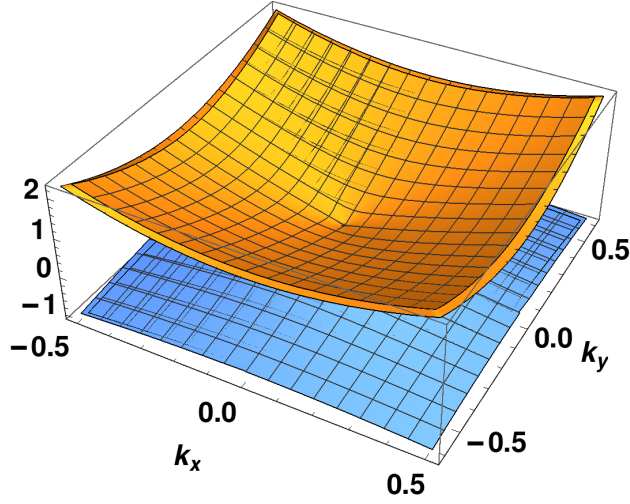


Figure 6.1: The eigenvalues of the diagonalized model in equation 6.2 around the low k points represent the emergent chiral bands. In this case, we set $\beta = 0.3$, $\lambda = 1.0$, and $\theta = \frac{\pi}{3}$. We observed that larger β values flatten the bands.

In above equation 6.7 $\tilde{V}_k^\theta = \frac{V_k}{\sqrt{\beta\gamma k^3 \cos 3\theta}}$ has k, θ dependence. A square root momentum dependent hybridization found in Rashba coupling studies^{19–22}. After the unitary rotation, we obtain the renormalized SIAM as follows:

$$\tilde{H} = \sum_{k\zeta} \epsilon_{k\zeta} c_{k\zeta}^\dagger c_{k\zeta} + H_d + \tilde{H}_{hyb}^+ + \tilde{H}_{hyb}^- \quad (6.8)$$

The above equation 6.8 satisfies the pseudo-chirality, as $\eta \tilde{H} \eta^{-1} = -\tilde{H}^\dagger$, when the couplings are complex-valued. This symmetry for Hermitian problem can be written as $\{\tilde{H}, \eta\} = 0$ the η is constructed as $\sigma_x \otimes \sigma_x$ for $U = 0$ in matrix form we can also construct in operator form¹⁶ as $\psi^\dagger \eta \psi$ where $\psi^\dagger = (c_+^\dagger \ c_-^\dagger \ d_\uparrow^\dagger \ d_\downarrow^\dagger)$. Generally the \mathcal{PT} - symmetry is associated with the NH transitions but in presence of topology and non-Hermiticity lead to additional symmetry classes²³ as follows,

$$\begin{aligned} \eta H \eta^{-1} &= H^\dagger \text{ for } \mathcal{PT} \text{ symmetry} \\ \eta H \eta^{-1} &= -H^\dagger \text{ for } \mathcal{PC} \text{ symmetry} \end{aligned} \quad (6.9)$$

These above symmetries parity-time(\mathcal{PT}) and \mathcal{PC} will be written as $[H, \eta] = 0$ and $\{H, \eta\} = 0$, when $H = H^\dagger$. These observations will guide us on how the formation of exceptional points occurs when couplings are complex-valued without altering the symmetry.

6.3 Effective Model Derivation And Poorman Scaling

To project this model in equation 6.8 onto the impurity subspace, we use projection operator method²⁴. The projection operators are defined as $P_0 = (1 - n_\uparrow)(1 - n_\downarrow)$, $P_1 = n_\uparrow(1 - n_\downarrow) + n_\downarrow(1 - n_\uparrow)$, and $P_2 = n_\uparrow n_\downarrow$ for unoccupied, singly occupied, and doubly occupied states, respectively. Using these projections, we derive the components of the effective model as $H_{\eta\eta'} = P_\eta H P_{\eta'}$ which is detailed in Appendix A. The emergent quantum numbers $\zeta = \pm$ represent chiral bands in the effective model.

$$H_{eff}^\eta = H_{\eta\eta} + \sum_{\substack{\eta' \neq \eta=0,1,2 \\ \zeta, \zeta' = \pm}} H_{\eta\eta'}^\zeta \frac{1}{E - H_{\eta'\eta'}} H_{\eta'\eta}^{\zeta'} \quad (6.10)$$

The singly occupied subspace Hamiltonian is the low-energy effective model for the Kondo regime. We show here for such a topological bath one gets an effective model which has emergent anisotropic \mathcal{DM} interactions. We adopt a specific convention for representing couplings. We utilize vector notation to denote couplings, while pseudo-spin of bath operators are represented using bold symbols. This notation allows us to distinguish between different types of operators.

$$\begin{aligned} H_{eff}^1 = H_0 &+ \sum_{kk'} J_0 s \cdot \mathbf{S}_{kk'} + i \sum_{kk'} \vec{J}_{k^3} \cdot (s \times \mathbf{S}_{kk'}) \\ &+ i \sum_{kk'} \vec{J}_k \cdot (s \times \mathbf{S}_{kk'}) \end{aligned} \quad (6.11)$$

In equation 6.11, $H_0 = \sum_{k\zeta} \epsilon_{k\zeta} c_{k\zeta}^\dagger c_{k\zeta}$ and the operator $\mathbf{S}_{kk'}$ represents the Abrikosov pseudo-spin for conduction electrons, while s corresponds to the impurity spin. The couplings are denoted as $J_0 = (\alpha_{k1}\alpha_{k'1} + \alpha_{k2}\alpha_{k'2})M_{kk'\zeta}^{\theta, \theta'}$, $\vec{J}_{k^3} = (\alpha_{k1}\alpha_{k'1} - \alpha_{k2}\alpha_{k'2})M_{kk'\zeta}^{\theta, \theta'}\hat{z}$ and $\vec{J}_k = \alpha_{k1}\alpha_{k'2}M_{kk'\zeta}^{\theta, \theta'}(\hat{x} + \hat{y})$. Here, $M_{kk'\zeta}^{\theta\theta'} = \tilde{V}_k^\theta \tilde{V}_{k'}^{\theta'} \left(\frac{1}{\epsilon_{k'\zeta} - \epsilon_d} + \frac{1}{\epsilon_d + U - \epsilon_{k\zeta}} \right)$ and $\tilde{V}_{k'}^{\theta'} = \frac{V_{k'}}{\sqrt{\beta\gamma(k')^3 \cos 3\theta'}}$. The matrix elements in this problem in general depend on polar angles and momenta are derived in Appendix A. The nonlinear dispersion introduces cross-product terms in z component and linear term will introduce x,y components of \mathcal{DM} . Poorman

RG will yield following equations,

$$\begin{aligned}
\frac{dJ_0}{dl} &= J_0^2 + J_{k^3}J_k + J_{k^3}^2 + J_k^2 \\
\frac{dJ_{k^3}}{dl} &= J_k^2 + J_0J_{k^3} \\
\frac{dJ_k}{dl} &= J_0J_k
\end{aligned} \tag{6.12}$$

The appendix B contains a detailed derivation and the complete solution to the RG equations 6.12. One of the solutions, obtained by eliminating J_0 , is given by the equation $J_k^2 - J_k = mJ_{k^3}$, where m can be a positive or negative value. The roots of this solution are expressed as $J_k = \frac{1}{2} \pm \frac{1}{2}\sqrt{1 + 4mJ_{k^3}}$. In the low-energy effective model, it plays a significant role in causing exceptional points, which will be discussed in detail in the subsequent section, along with the diagonalization.

6.4 Emergence Of Complex Solution

We performed poorman RG on Hamiltonian as in the equation 6.12 and found the invariants \tilde{J}_0, \tilde{J}_k as shown in Appendix C. Here we analyse the local Hamiltonian symmetry properties and its eigenvalue spectrum using the RG invariants for couplings and varying the J_{k^3} .

$$\begin{aligned}
\tilde{H} &= \sum_{kk'} \tilde{J}_0 s \cdot \mathbf{S}_{kk'} + i \sum_{kk'} \vec{\tilde{J}}_{k^3} \cdot (s \times \mathbf{S}_{kk'}) \\
&+ i \sum_{kk'} \vec{\tilde{J}}_k \cdot (s \times \mathbf{S}_{kk'})
\end{aligned} \tag{6.13}$$

In order to show the effective model above exhibits pseudo-chiral symmetry, we can write the local Hamiltonian at $k = 0$ as follows:

$$\begin{aligned}
\hat{\tilde{H}} &= \tilde{J}_0(\sigma_z \otimes \boldsymbol{\sigma}_z + \sigma^+ \otimes \boldsymbol{\sigma}^- + \sigma^- \otimes \boldsymbol{\sigma}^+) \\
&+ i\tilde{J}_{k^3}(\sigma_x \otimes \boldsymbol{\sigma}_y - \boldsymbol{\sigma}_y \otimes \sigma_x) \\
&+ i\tilde{J}_k(\sigma_y \otimes \boldsymbol{\sigma}_z - \boldsymbol{\sigma}_z \otimes \sigma_y) \\
&+ i\tilde{J}_k(\sigma_x \otimes \boldsymbol{\sigma}_z - \boldsymbol{\sigma}_z \otimes \sigma_x)
\end{aligned} \tag{6.14}$$

We can construct the ket vector for the above Hamiltonian as $(|\uparrow\uparrow\rangle, |\uparrow\downarrow\rangle, |\downarrow\uparrow\rangle, |\downarrow\downarrow\rangle)$. For such a state, we can show the metric operator as the following:

$$\eta = \begin{pmatrix} 0 & 0 & 0 & 1 \\ 0 & 0 & 1 & 0 \\ 0 & 1 & 0 & 0 \\ 1 & 0 & 0 & 0 \end{pmatrix} \quad (6.15)$$

In the above equation 6.14 the block symbol is for the bath spin and rest are impurity spin operators to distinguish between the two. The chiral symmetry operator can be generalized to n -dimensional matrices²⁵, is $\eta = \sigma_x \otimes \sigma_x$. This metric satisfies $\eta \hat{H} \eta^{-1} = -\hat{H}^\dagger$, indicating pseudo-chiral symmetry²³ this inherent property become very crucial after adding the potential scattering terms which is elaborated in section V. For Hermitian matrix this symmetry will be $\{\hat{H}, \eta\} = 0$. This symmetry also exists when $J_0 \rightarrow 0$ and even if all couplings are real-valued. Each of the states can be represented as follows:

$$\begin{aligned} |\uparrow\uparrow\rangle &= (1 \ 0 \ 1 \ 0) \\ |\uparrow\downarrow\rangle &= (1 \ 0 \ 0 \ 1) \\ |\downarrow\uparrow\rangle &= (0 \ 1 \ 1 \ 0) \\ |\downarrow\downarrow\rangle &= (0 \ 1 \ 0 \ 1) \end{aligned} \quad (6.16)$$

So it can be readily seen the operations as $\eta|\uparrow\uparrow\rangle \rightarrow |\downarrow\downarrow\rangle$, $\eta|\uparrow\downarrow\rangle \rightarrow |\downarrow\uparrow\rangle$, $\eta|\downarrow\uparrow\rangle \rightarrow |\downarrow\uparrow\rangle$ and $\eta|\downarrow\downarrow\rangle \rightarrow |\uparrow\uparrow\rangle$.

$$\hat{H} = \begin{pmatrix} J_0 & -J_k e^{-i\frac{\pi}{4}} & J_k e^{-i\frac{\pi}{4}} & 0 \\ -J_k e^{i\frac{\pi}{4}} & -J_0 & 2iJ_{k^3} + J_0 & -J_k e^{-i\frac{\pi}{4}} \\ J_k e^{i\frac{\pi}{4}} & -2iJ_{k^3} + J_0 & -J_0 & J_k e^{-i\frac{\pi}{4}} \\ 0 & -J_k e^{i\frac{\pi}{4}} & J_k e^{-i\frac{\pi}{4}} & J_0 \end{pmatrix} \quad (6.17)$$

The above matrix has some specific properties due to the anisotropic \mathcal{DM} interaction,

$$\begin{aligned} \eta_{\sigma_z \otimes \sigma_z} \hat{H} \eta_{\sigma_z \otimes \sigma_z}^{-1} &= H \text{ for } J_k \rightarrow -J_k \\ \eta_{\sigma_y \otimes \sigma_y} \hat{H} \eta_{\sigma_y \otimes \sigma_y}^{-1} &= H \text{ for } J_{k^3} \rightarrow 0 \end{aligned} \quad (6.18)$$

In our analysis, we examine the eigenvalues of the spin Hamiltonian defined in equation 6.17 within the (1, 1) occupancy sector. This is represented in figures 6.2 and 6.3. We observe the emergence of complex eigenvalues and the formation of exceptional points due to perturbative RG. This phenomenon is also evident in the one-loop and Poorman equations in non-Hermitian

scenarios^{15;26}. Here, we present numerical evidence of the spectral properties at these fixed points.

Using Fock-space diagonalization with $\tilde{J}_k = \frac{1}{2} \pm \frac{1}{2} \sqrt{1 + 4mJ_{k^3}}$ in the single occupancy sector(SS), we find that for $J_{k^3} < |0.5|$, the eigenvalues follow hyperbolic trajectories typical of the conventional Kondo regime. However, for values greater than the critical value, topological transitions occur in the spectrum. In the resonant level scenario depicted in figure 6.3, exceptional points emerge for large m values.

As J_0 increases, the disappearance of the Dirac cone indicates the emergence of a spectral gap. This observation underscores the role of the RG invariant $J_k = \frac{1}{2} \pm \frac{1}{2} \sqrt{1 + 4mJ_{k^3}}$ in shaping the impurity spectrum. This invariant is crucial for the appearance of coalescing points in the spectrum, revealing the complex interplay between coupling parameters and their renormalization under RG flow. These coalescing points vanish as $J_0 \rightarrow \infty$.

6.4.1 Condition Number In Fock Space

The condition number²⁷ $\kappa(A)$ of matrix A is defined as $\kappa(A) = \frac{|\lambda_{max}|}{|\lambda_{min}|}$, where λ_{max} and λ_{min} correspond to the highest and lowest eigenvalues. This number is associated with error in measurement, sensitivity, and the singular spectrum of real and complex-valued matrices. We illustrate this number in plots 6.4 and 6.5 for one and two impurities for local Hamiltonian in spin Fock space. The sensitivity of the models with J_{k^3} versus K type of \mathcal{DM} interactions is also depicted. The defectiveness in diagonalization is attributed to eigenvector becoming parallel and loss of orthogonality indicating exceptional points. However, the conclusion made here is based on the local Hamiltonian in sector one fock space, hence this is relevant to the dissipation in this subsystem and does not translate to full many-body systems. Note that dissipation in large N systems generally shown to be relevant for local system, since larger systems always tend to equilibrate.

6.5 Renormalization With Potential Scattering

We analyze the coefficients of effective model and construct the regular hexagonal boundaries of the bath as shown in figure 6.6. The spin-spin interaction model resembles the structure in work¹⁵ after including potential scattering terms. Our goal is to examine whether the invariant responsible for coalescence (Exceptional Point, EP) undergoes renormalization or remains

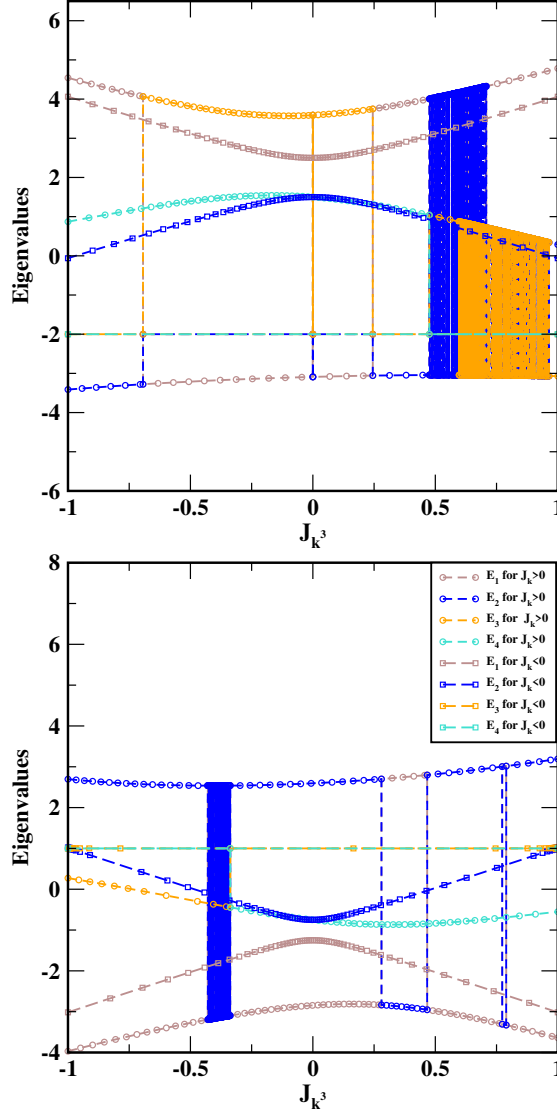


Figure 6.2: The eigenvalues of the model (equation 6.17) with $J_0 = -2.0$ (above) and $J_0 = 1.0$ (below), along with the RG invariant $m = \pm 0.01$. For small values of m and two roots denoted as $J_0 < 0$, $J_0 > 0$, the eigenvalues are denoted from E_1 to E_4 for corresponding RG root. Topological transitions occur at $J_k^3 = \pm 0.5$ and around $J_k^3 = 0.75$. At smaller values of m , there will be small imaginary weights in the eigenvalues, but no exceptional points. These topological points remain at higher values of m , but the spectrum will be gapped due to higher J_0 values.

unrenormalized with the inclusion of non-Hermitian terms, particularly at third-order RG corrections. Complex-valued potential scattering is essential

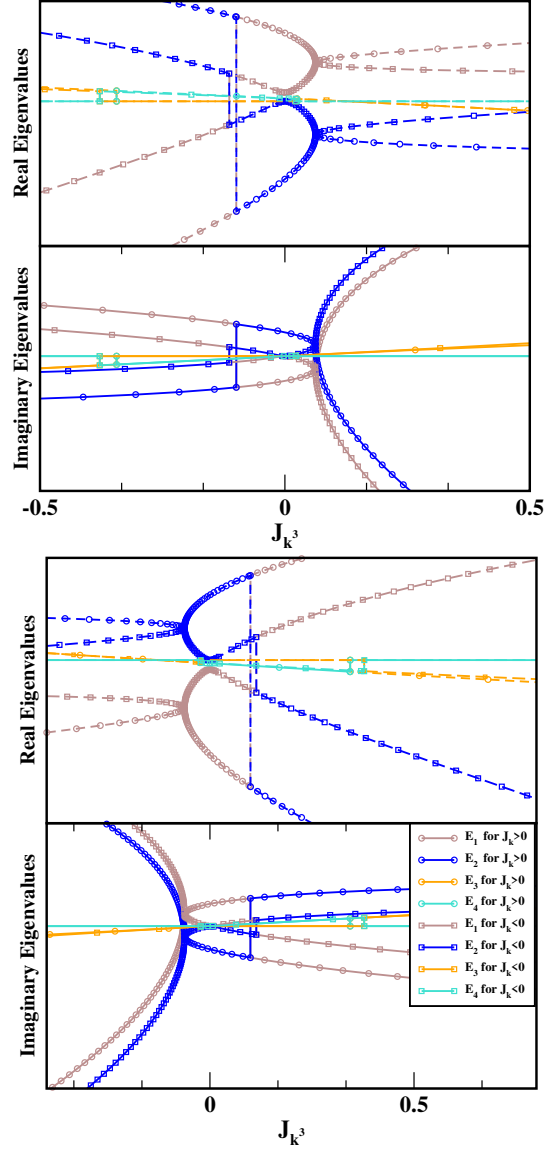


Figure 6.3: Eigenvalues of the equation 6.17 for resonant level cases (small J_0). For $J_0 = \pm 0.1$ and the RG invariant $m = \pm 4.0$. The labels E_1 to E_4 denote four different eigenvalues for positive and negative RG invariants, respectively. A Dirac cone appears in the impurity spectrum due to the topological properties of the local Hamiltonian. Larger values of m are required to observe exceptional points, and the gap in the spectrum widens with increasing J_0 .

for obtaining fixed points in the flow, corresponding to ground state topological transitions in the eigenvalue spectrum of the model. The effective model

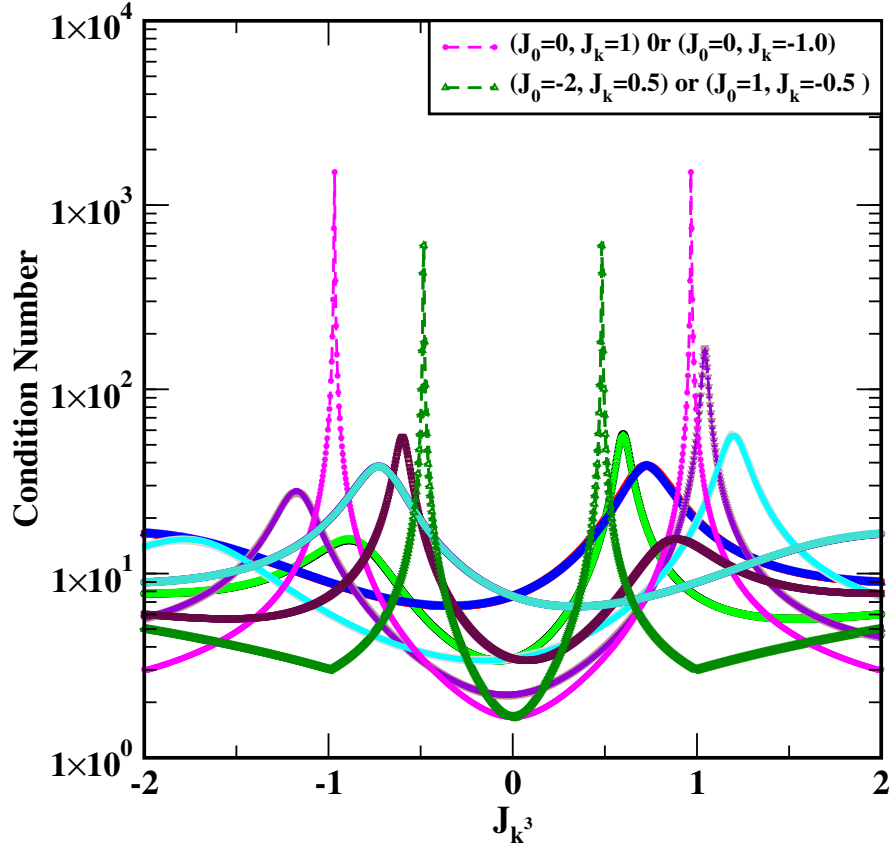


Figure 6.4: Variation of the condition number with anisotropic \mathcal{DM} coupling J_{k^3} in the model in equation 6.14, using Fock-space diagonalization in the SS of the one-impurity problem. Diverging cusp-like points indicate high condition numbers denoted in graph implies defects in diagonalization found figure 6.2.

with scattering terms can be expressed as follows:

$$\begin{aligned}
H'_{eff} = & H_0 + \sum_{kk'} J_0 s \cdot \psi^\dagger(\Sigma) \psi \\
& + i \sum_{kk'} \vec{J}_{k^3}^{0,0} \cdot (s \times \psi^\dagger(\Sigma) \psi) \\
& + i \sum_{kk'} \vec{J}_k^{(0,0)} \cdot (s \times \psi^\dagger(\Sigma) \psi) + H_{pot}
\end{aligned} \tag{6.19}$$

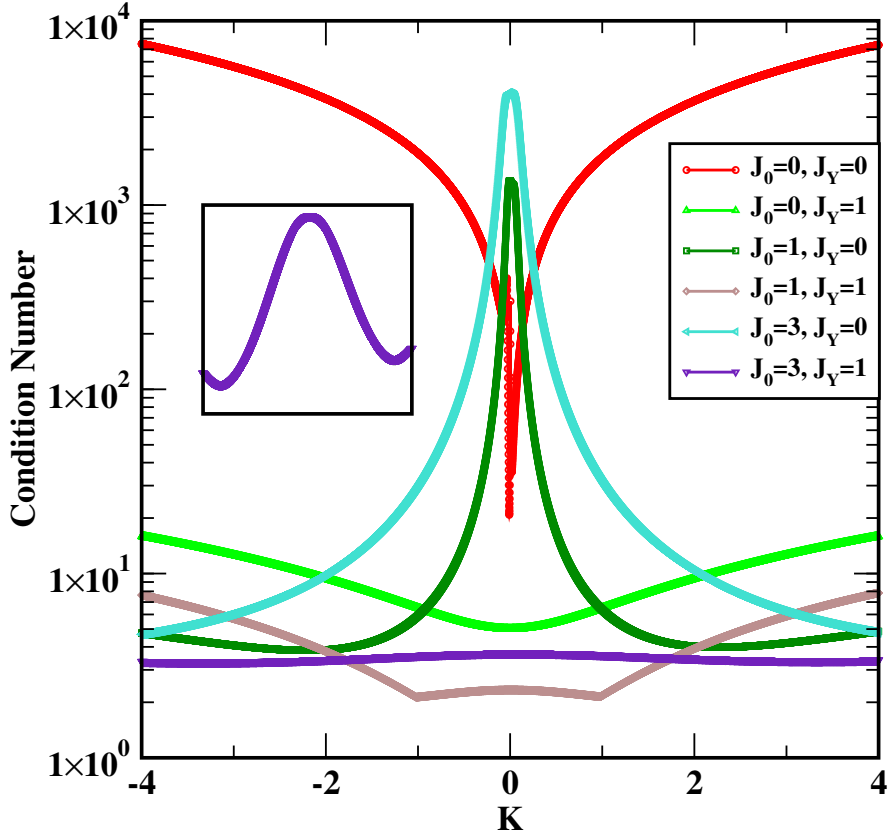


Figure 6.5: Variation of condition numbers in Fock space of the two-impurity model given in equation 6.24, and they show that the model is well conditioned for most values of K , except when K is 0. However, high condition numbers occur when the anisotropic coupling is non-zero, indicating that the model is not defective when J_{k^3} and J_k couplings are absent.

Where we add the \mathcal{PC} -symmetric potential scattering terms as shown in the figure 6.6 and represented as H_{pot} can be written as following,

$$\begin{aligned}
 H_{pot} = & \sum_{kk'} \left(\bar{J}_{k^3}^{\frac{2\pi}{3}, -\frac{\pi}{3}} + \bar{J}_k^{\frac{2\pi}{3}, -\frac{\pi}{3}} \right) \cdot (s \times \psi^\dagger(\mathbf{\Gamma})\psi) \\
 & - \sum_{kk'} \left(\bar{J}_{k^3}^{\pm \frac{2\pi}{3}, \pm \frac{\pi}{3}} + \bar{J}_k^{\pm \frac{2\pi}{3}, \pm \frac{\pi}{3}} \right) \cdot (s \times \psi^\dagger(\mathbf{\Omega})\psi)
 \end{aligned} \tag{6.20}$$

Essentially, added degrees of freedom are $\psi^\dagger = \left(c_{k\frac{2\pi}{3}+}^\dagger, c_{k\frac{\pi}{3}-}^\dagger, c_{-k-\frac{2\pi}{3}+}^\dagger, c_{-k-\frac{\pi}{3}-}^\dagger \right)$ needed to achieve the generalized Pauli matrices or the block structure of the Kondo problem and it is detailed in Appendix B3 we have shown by expanding the above model in detail to derive the RG equations and those are

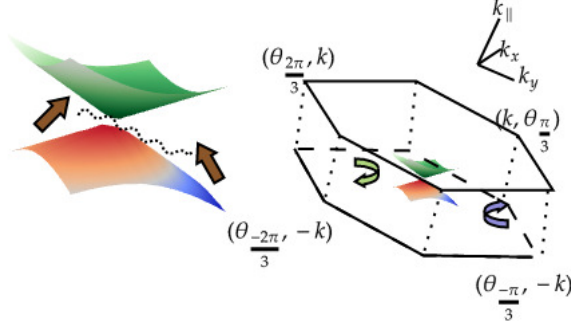


Figure 6.6: Left schematic representing two Anderson impurities in the edge states of the bath. Right one is regular hexagonal cell of bath to incorporate \mathcal{PC} symmetric potential scattering terms. The left and right scatterers are depicted with green and blue arrows, respectively. Here, $k_{\parallel} \rightarrow k$, $\sqrt{k_x^2 + k_y^2} \rightarrow k$ and $\theta \rightarrow \tan^{-1} \frac{k_y}{k_x}$. For derivations, see equations from 6.4 to 6.6. Electron and hole scatterings for (k, θ) to $(-k, \theta')$ are represented around the Dirac cone. Note that k is modulus of the vector and only its direction will decide the sign of momenta of hole or electron.

plotted in the figure 6.7. We used the simplified notations for the couplings as $(J_0, J_{k^3}^{0,0}, J_{k^3}^{\pm \frac{2\pi}{3}, \pm \frac{\pi}{3}}, J_{k^3}^{\frac{2\pi}{3}, -\frac{\pi}{3}}, J_k^{(0,0)}, J_k^{\pm \frac{2\pi}{3}, \pm \frac{\pi}{3}}, J_k^{\frac{2\pi}{3}, -\frac{\pi}{3}})$ into $(J_0, J_{k^3}, g_{1k^3}, g_{2k^3}, J_k, g_{1k}, g_{2k})$.

6.6 Generalization to Two Impurities

We extend this model to a two-impurity Kondo model with a direct spin-spin coupling and isotropic \mathcal{DM} interaction between the impurities. Similar interactions have been studied in two dots with spin-orbit coupling²⁸, which demonstrated that the \mathcal{DM} term exists only for the Y-component when there is linear dispersion in the bath. In this instance, we focus on the renormalization of anisotropic versus isotropic interactions.

$$\begin{aligned}
 H_{eff} = H_0 &+ \sum_{kk'} J_0 s_{\alpha} \cdot \mathbf{S}_{kk'} + i \sum_{kk'\zeta} \vec{J}_{k^3} \cdot (s_{\alpha} \times \mathbf{S}_{kk'}) \\
 &+ i \sum_{kk'\zeta} \vec{J}_k \cdot (s_{\alpha} \times \mathbf{S}_{kk'}) + J_Y s_1 \cdot s_2 + i \vec{K} \cdot (s_1 \times s_2)
 \end{aligned} \tag{6.21}$$

where in above equation 6.21 kinetic energy $H_0 = \sum_{k\zeta} \epsilon_{k\zeta} c_{k\zeta}^{\dagger} c_{k\zeta}$, J_Y is direct coupling between impurities, K is impurity \mathcal{DM} interaction and the bold operators represent spinor vectors as defined earlier. Since the generalized problem has many coupling, we restrict our-self to analyzing the one-loop

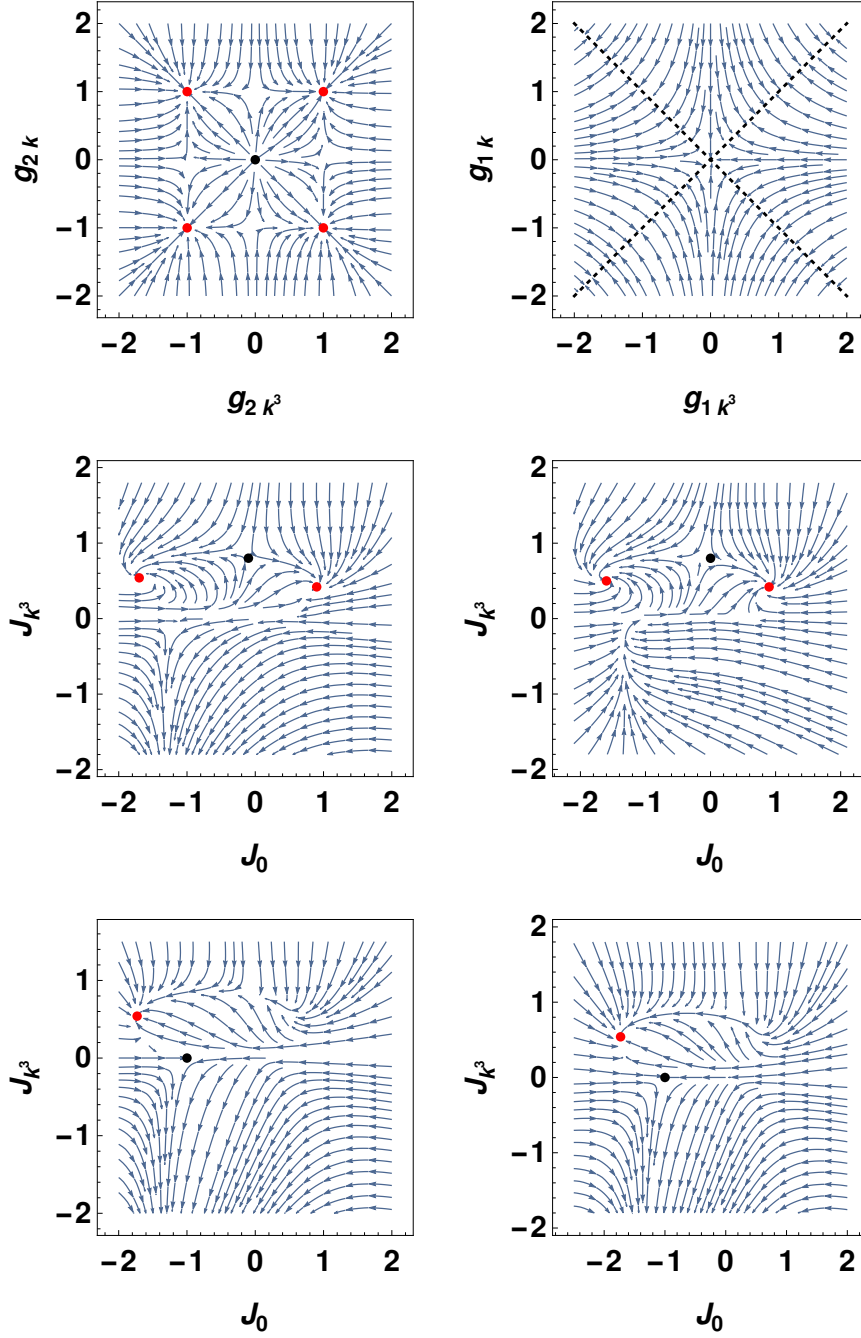


Figure 6.7: In these figures, we show the RG flow using the fixed values $g_{1k} = g_{1k^3} = 1$, which is invariant derived in the appendix B. Throughout our calculations, we use $J_{1k} = \frac{1}{2} \pm \frac{1}{2} \sqrt{1 + 4mJ_{1k^3}}$ alongside setting $m = -4$. The top row of the plots represents potential scattering, and the second row shows the real and imaginary parts of (J_{1k}) in both RG equations in x and y axes, where the notation (R^+, R^+) and $(R^+ I^+)$ denotes the real and imaginary parts on the x and y axes, respectively. Similarly, the third row is (I^-, R^-) and (I^-, I^-) . We observe at least two fixed points (FP) and two spiral points (SP) in the second row, while the third row shows one SP and one marginal point. The dotted lines in the second plot of the first row represent a family of FPs. The EP signatures figure 6.3 in RG flow can be observed here as parallel arrows at small J_0 and J_{k^3} values, representing unstable solutions. At these SP we found topological transitions in figures 6.2 and high condition numbers in figure 6.4 for $J_{k^3} = 0.5$.

RG equations.,

$$\begin{aligned}
\frac{dJ_0}{dl} &= J_0^2 + J_{k^3} J_k + J_{k^3}^2 + J_k^2 + J_Y J_0 + K J_0 \\
\frac{dJ_{k^3}}{dl} &= J_k^2 + J_0 J_{k^3} + J_Y J_{k^3} + J_Y J_k + K J_{k^3} \\
\frac{dJ_k}{dl} &= J_0 J_k + J_Y J_{k^3} + J_Y J_k + K J_k \\
\frac{dJ_Y}{dl} &= J_Y^2 + K^2 + J_0^2 + J_{k^3} J_k + J_k^2 + J_{k^3}^2 \\
\frac{dK}{dl} &= K^2 + K J_Y + J_{k^3} J_k
\end{aligned} \tag{6.22}$$

Solutions to the above equations are detailed in an appendix in various limits. The beta function zeros for Kondo destruction can be seen in the odd-even couplings are studied^{29;30}. Since we focus on the nonlinear couplings J_k, J_{k^3} , We look at the solutions around the anomalous contributions to Spin-relaxation time and the FPs in these couplings.

6.6.1 Eigenspectrum connection to fixed points

Now, we will construct the 3-spin Fock space for the two-impurity problem, investigate the spectrum, and show the connection with the RG FP's and Condition Numbers.

$$\begin{aligned}
\tilde{H}_{2imp} &= \sum_{kk'} \tilde{J}_0 s_\alpha \cdot \mathbf{S}_{kk'} + i \sum_{kk'\alpha} \tilde{J}_{k^3} \cdot (\mathbf{S}_\alpha \times \mathbf{s}_{kk'}) \\
&+ i \sum_{kk'\alpha} \tilde{J}_k \cdot (s_\alpha \times \mathbf{S}_{kk'}) + \tilde{J}_Y s_1 \cdot s_2 + i \tilde{K} \cdot (s_1 \times s_2)
\end{aligned} \tag{6.23}$$

In above equation 6.23 α takes values 1,2 correspond to two impurities. We use the Fock space for the above problem in the 3-spin (impurity-bath-impurity) system in the SS as $\psi^\dagger = (|\uparrow\uparrow\uparrow\rangle \quad |\uparrow\uparrow\downarrow\rangle \quad |\uparrow\downarrow\uparrow\rangle \quad |\downarrow\uparrow\uparrow\rangle \quad |\uparrow\downarrow\downarrow\rangle \quad |\downarrow\downarrow\uparrow\rangle \quad |\downarrow\uparrow\downarrow\rangle \quad |\downarrow\downarrow\downarrow\rangle)$
For this state vector we can write the following Hamiltonian as $\hat{\tilde{H}}_{2imp} =$

$$\langle \psi | \tilde{H}_{2imp} | \psi \rangle$$

$$\begin{aligned}
\hat{H}_{2imp} = & J_0 \sigma_z \otimes \boldsymbol{\sigma}_z \otimes \mathbb{I} + J_0 \sigma^+ \otimes \boldsymbol{\sigma}_- \otimes \mathbb{I} + J_0 \sigma^- \otimes \boldsymbol{\sigma}^+ \otimes \mathbb{I} \\
& + J_0 \mathbb{I} \otimes \sigma_z \otimes \sigma_z + J_0 \mathbb{I} \otimes \sigma^+ \otimes \sigma^- + J_0 \mathbb{I} \otimes \sigma^- \otimes \sigma^+ \\
& + i \tilde{J}_{k^3} (\sigma_x \otimes \boldsymbol{\sigma}_y \otimes \mathbb{I} - \boldsymbol{\sigma}_y \otimes \sigma_x \otimes \mathbb{I}) \\
& + i \tilde{J}_k (\sigma_y \otimes \boldsymbol{\sigma}_z \otimes \mathbb{I} - \boldsymbol{\sigma}_z \otimes \sigma_y \otimes \mathbb{I}) \\
& + i \tilde{J}_k (\sigma_x \otimes \boldsymbol{\sigma}_z \otimes \mathbb{I} - \boldsymbol{\sigma}_z \otimes \sigma_x \otimes \mathbb{I}) \\
& + i \tilde{J}_{k^3} (\mathbb{I} \otimes \sigma_x \otimes \boldsymbol{\sigma}_y - \mathbb{I} \otimes \boldsymbol{\sigma}_y \otimes \sigma_x) \\
& + i \tilde{J}_k (\mathbb{I} \otimes \sigma_y \otimes \boldsymbol{\sigma}_z - \mathbb{I} \otimes \boldsymbol{\sigma}_z \otimes \sigma_y) \\
& + i \tilde{J}_k (\mathbb{I} \otimes \sigma_x \otimes \boldsymbol{\sigma}_z - \mathbb{I} \otimes \boldsymbol{\sigma}_z \otimes \sigma_x) \\
& + J_Y \sigma_z \otimes \mathbb{I} \otimes \sigma_z + J_Y \sigma^+ \otimes \mathbb{I} \otimes \sigma_- + J_Y \sigma^- \otimes \mathbb{I} \otimes \sigma^+ \\
& + i K (\sigma_x \otimes \mathbb{I} \otimes \boldsymbol{\sigma}_y - \boldsymbol{\sigma}_y \otimes \mathbb{I} \otimes \sigma_x) \\
& + i K (\sigma_y \otimes \mathbb{I} \otimes \boldsymbol{\sigma}_z - \boldsymbol{\sigma}_z \otimes \mathbb{I} \otimes \sigma_y) \\
& + i K (\sigma_x \otimes \mathbb{I} \otimes \boldsymbol{\sigma}_z - \boldsymbol{\sigma}_z \otimes \mathbb{I} \otimes \sigma_x).
\end{aligned} \tag{6.24}$$

This results in the following matrix. We analyze the symmetry properties of this matrix as we did in the single impurity case. By constructing the metric operator as $\hat{\eta} = \sigma_x \otimes \sigma_x \otimes \sigma_x$ as chosen in the article²⁵, we verify that it possesses \mathcal{PC} symmetry, expressed as $\hat{\eta} \hat{H} \hat{\eta}^\dagger = -\hat{H}^\dagger$. We demonstrate that anisotropic \mathcal{DM} -interaction is necessary to satisfy this condition that is $J_{k^3} \neq 0$, and this Hamiltonian is not \mathcal{PC} symmetric when this is zero.

$$\hat{H} = \begin{pmatrix} 2J_0 + J_y & -e^{i\frac{\pi}{4}} J_{Kp} & 0 & 0 & e^{i\frac{\pi}{4}} J_{Kp} & 0 & 0 & 0 \\ -e^{-i\frac{\pi}{4}} J_{Kp} & -J_y & 4J_{0p} & -2e^{i\frac{\pi}{4}} J_k & 4J_{Yp} & e^{i\frac{\pi}{4}} J_{Km} & 0 & 0 \\ 0 & 4J_{0m} & -2J_0 + J_y & e^{i\frac{\pi}{4}} J_{Km} & 4J_{0p} & 0 & -e^{i\frac{\pi}{4}} J_{Km} & 0 \\ 0 & -2e^{-i\frac{\pi}{4}} J_k & e^{-i\frac{\pi}{4}} J_{Km} & -J_y & 0 & 4J_{0p} & 4J_{Yp} & -e^{i\frac{\pi}{4}} J_{Kp} \\ e^{-i\frac{\pi}{4}} J_{Kp} & 4J_{Ym} & 4J_{0m} & 0 & -J_y & -e^{i\frac{\pi}{4}} J_{Km} & -2e^{i\frac{\pi}{4}} J_k & 0 \\ 0 & e^{-i\frac{\pi}{4}} J_{Km} & 0 & 4J_{0m} & -e^{-i\frac{\pi}{4}} J_{Km} & -2J_0 + J_y & 4J_{0p} & 0 \\ 0 & 0 & -e^{-i\frac{\pi}{4}} J_{Km} & 4J_{Ym} & -2e^{-i\frac{\pi}{4}} J_k & 4J_{0m} & -J_y & e^{i\frac{\pi}{4}} J_{Kp} \\ 0 & 0 & 0 & -e^{-i\frac{\pi}{4}} J_{Kp} & 0 & 0 & e^{-i\frac{\pi}{4}} J_{Kp} & 2J_0 + J_y \end{pmatrix}$$

In above matrix we used the reduced notations which are related to original model as $J_{Kp} = J_k + K, J_{Km} = J_k - K, J_{0p} = J_0 + i\frac{J_{k^3}}{2}, J_{0m} = J_0 - i\frac{J_{k^3}}{2}, J_{Yp} = J_y + i\frac{J_{k^3}}{2}$, and $J_{Ym} = J_y - i\frac{J_{k^3}}{2}$.

6.7 Solutions for RG ODE

We calculated numerical solutions for the set of equations 6.22 and plotted them around the fixed points as initial conditions for RG ODE. The results are shown in figure 6.8. These solutions only restricted to real values, and we can observe the renormalization of J_{k^3} and J_k in line with our analytical findings. In next section we analyze the general solutions around the dissipative FP's.

6.7.1 RG Equations Zeros and Poles Analysis

The RG ODE's are analyzed by allowing the complex solution which then will be treated as RG beta functions³¹. It is known that these beta functions show single peak structure at FP's. As we have seen from various results^{15;26;31} the complex FP's will show unique features as RG reversion. As a generalization of this reversion we see that peak structure in the imaginary part of beta function should reverse sign. This has been shown in figure 6.9 specifically the SP can be identified with these feature and these are unique to such type of dissipation.

Rest of the features in RG-beta functions such as zero crossings, or no single peak structure can be attributed to unstable points. Quantitative analysis is required to classify all different type of fixed points. The analysis presented here remain unaffected with choice of method.

Consistent results from both the algebra of conformal field theory (CFT) and the renormalization group (RG) equations suggest that both approaches capture the essential physics of the problem and provide complementary insights.

6.8 Impurity Transport Calculation

We have calculated the anomalous contributions to the relaxation time in the presence of a nonlinear dispersive bath using the $\mathcal{T}_{kk'}$ formalism²⁴, and the details can be found in Appendix E.

$$\frac{1}{\tau(k)} \propto (1 - 2J\tilde{g}_\alpha - 2J_{k^3}\tilde{g}_{\alpha k^3} - 2J_k\tilde{g}_{\alpha k}) \quad (6.25)$$

In above equation 6.25 all couplings J_0, J_k, J_k^3 relates to bare model and $\tilde{g}_{0\alpha}, \tilde{g}_{\alpha k^3}$ and $\tilde{g}_{\alpha k}$ are the integrals originate from second order perturbation theory are detailed in appendix E. Here we investigate the criticality associated with such dissipative fixed points obtained from the perturbative

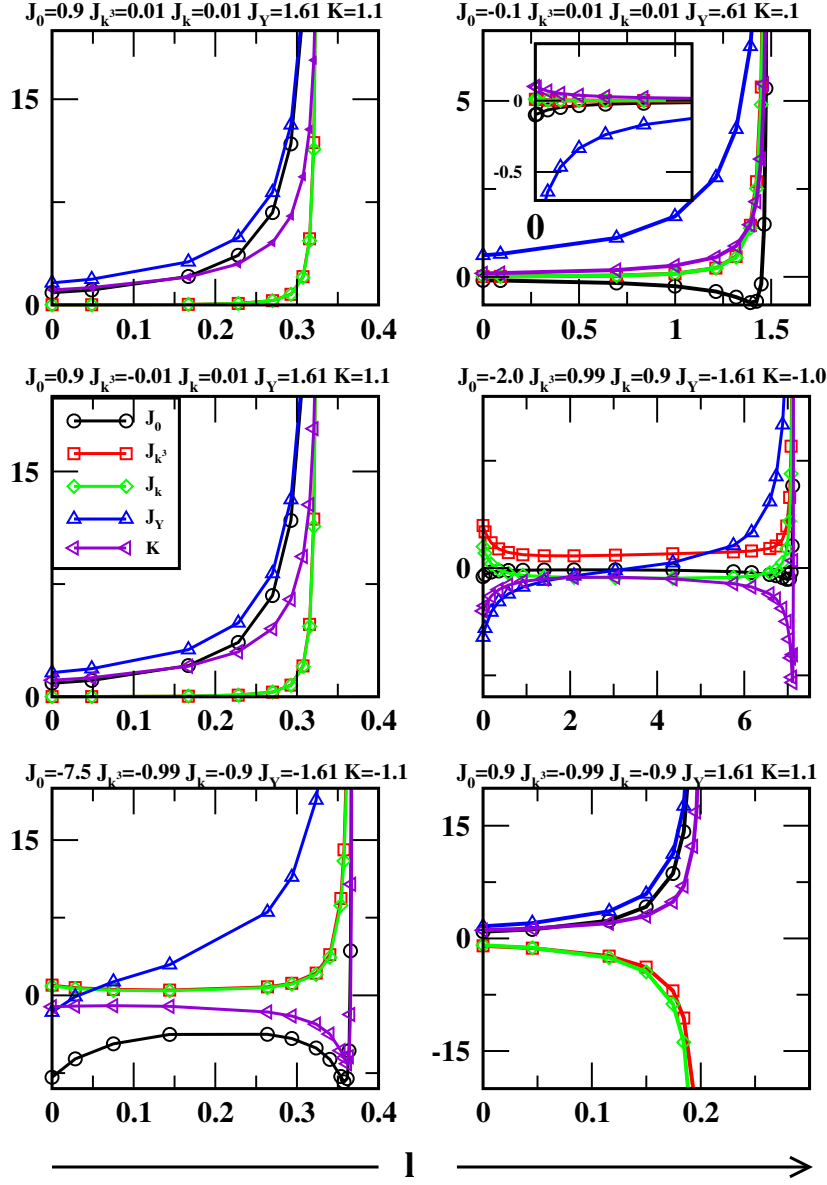


Figure 6.8: We plot numerical solutions of the RG equations (6.22) at the fixed points in the flow diagrams. The x-axis corresponds to the flow parameter, and each plot is labeled at the top with the initial conditions for evolving RG ODE. Diverging solutions correspond to the strong coupling regimes, while cusp-like features changing sign abruptly correspond to dissipative regimes. The inset graph corresponds to a large negative RKKY, while the rest are set to small values as initial conditions. The plot depicts in order to renormalize RKKY all other coupling originating from bath are necessary, hence all flows to zero.

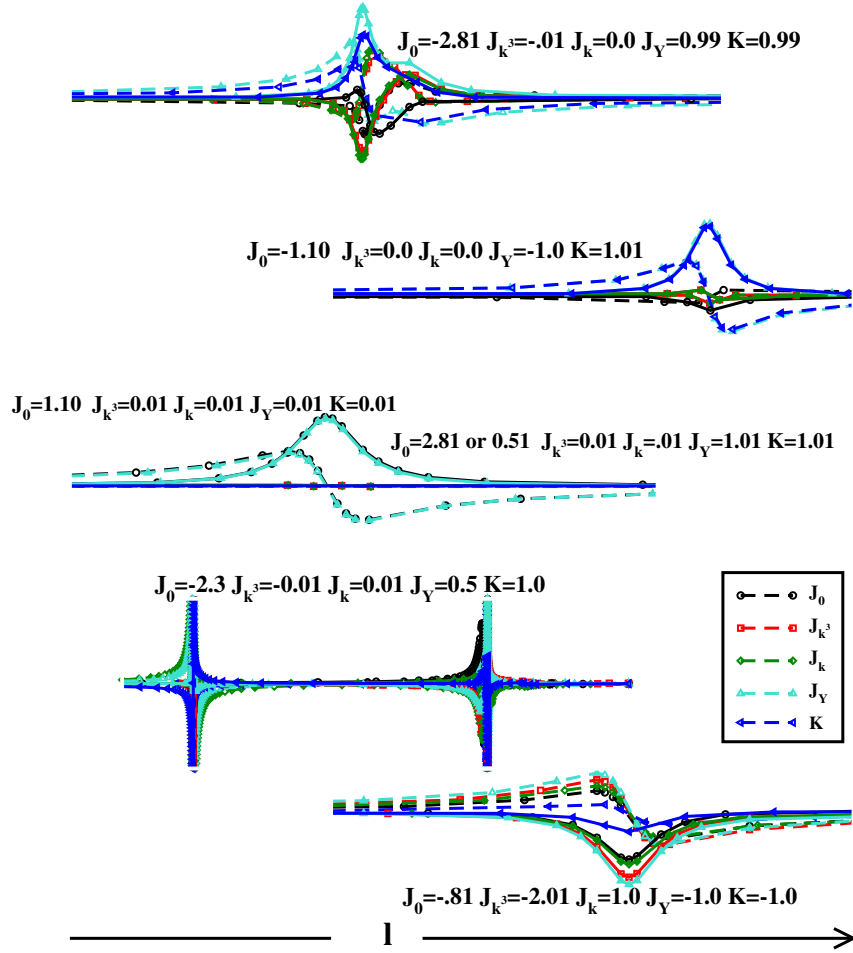


Figure 6.9: In all plots above Dotted and thick lines correspond to real and imaginary coupling values. Sign reversion occurs in all couplings for imaginary weights at $J_{k^3} = -2.0$ in bottom plot. Between two sign-reversing phases top to bottom, various 2-pole and 3-pole regimes are observed. We verified that SR in imaginary weights in both one and two impurities occur at these dissipative fixed points.

RG. We find the two scale collapse regimes as discussed in next section with a emergent invariant structure which we found in the RG.

6.8.1 Scaling Collapse In $\frac{1}{\tau}$

In a previous section, we discussed emergent coalescing points, which occur when the integrand vanishes in equation B.31 or when $q \rightarrow 0$. These points are represented by $(k^2 - \mu)^2 - \lambda^2 k^2 = 0$, resulting in the momentum roots $\frac{k}{\lambda} = \frac{1}{2} \pm \frac{1}{2} \sqrt{1 + 4 \frac{\mu}{\lambda^2}}$ and this we compare to the RG invariant $J_k = \frac{1}{2} \pm \frac{1}{2} \sqrt{1 + 4mJ_{k^3}}$ since in small β limit $J_k \propto \frac{k}{\lambda}, J_{k^3} \propto \frac{1}{\lambda^2}$ and μ can be compared to invariant m , this analysis is similar to laser induced Kondo-effect study³². Exceptional points exist only when the chemical potential $\mu \neq 0$, indicating a critical region where null momentum points arise. Beyond a certain critical value of the chemical potential, complex momentum is encountered, reflecting a complex gauge choice for momentum. These null momentum points are also evidenced through the diagonalization of the effective spin-spin Hamiltonian.

After the previous discussion, we plotted the computed functions in figure 6.10 while keeping the values of $\mu = -1.0$ and $\lambda = 1.0$ fixed and varying ϵ . We then scaled the functions and the argument of functions with the bandwidth in the momentum roots fashion, as discussed earlier, to show scaling collapse. The scaling we discussed here could also be extended to strong dissipation with complex-valued couplings, which we did not consider in this work, as we only aimed to establish that such an invariant structure emerges with these perturbations in the bath.

In the anisotropic model, scattering elements with \mathcal{PC} symmetry form a non-Hermitian Kondo problem. Under renormalization, SP's emerge, these may show complex critical phenomena. This would require further analysis may even need special treatments depending on type of dissipation. Note that the added scattering terms are not included in the transport calculations, and they can be analyzed in a separate study to better understand their impact on the transport.

6.9 Results and Discussion

The nontrivial renormalization of the impurity problem shown by revealing the dissipative fixed points of the model through perturbative RG incorporating \mathcal{PC} symmetric potential scattering. The \mathcal{PC} terms are found to be relevant in the weak and intermediate interaction regimes in contrast to the particle-hole symmetry, where it was known that these are irrelevant. Regardless of the \mathcal{PC} terms the common invariant structure is found which is responsible

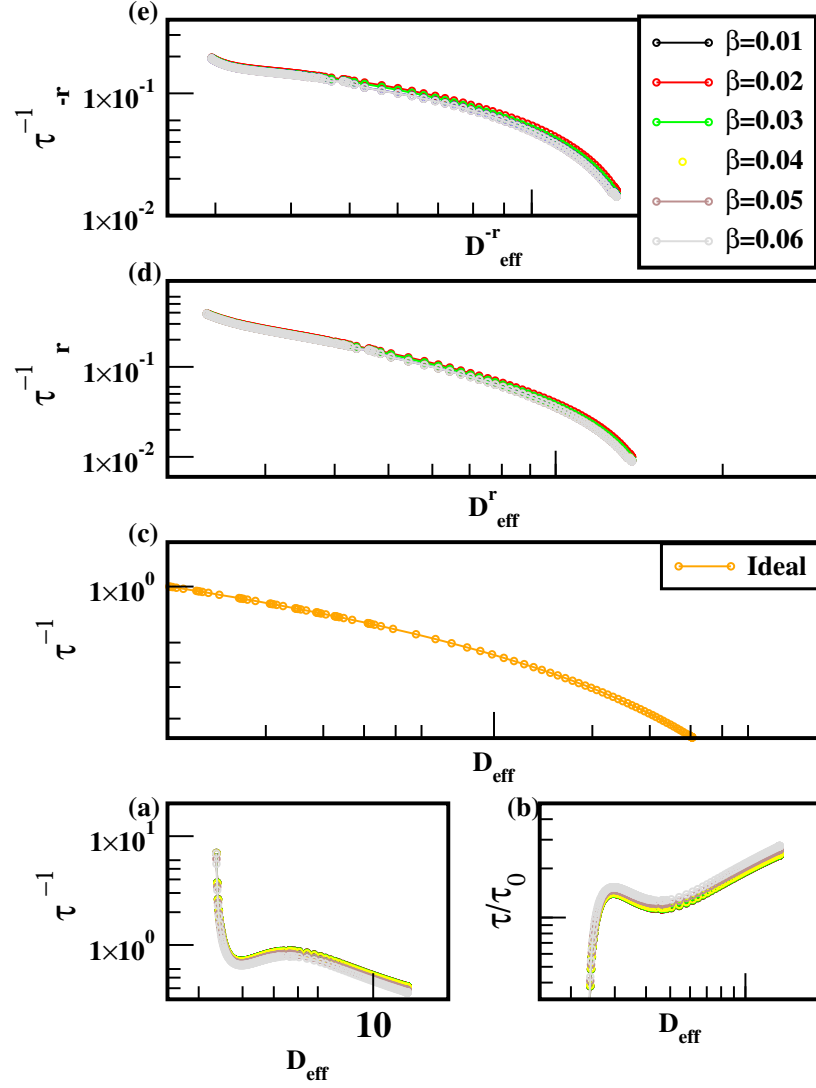


Figure 6.10: Plot (a) shows the relaxation time for different values of the nonlinear parameter (β), which is proportional to resistivity. Plot (b) is scaled from the first point of each curve shows a kink in the relaxation time (τ). We show scaling collapse, and the kink disappears in plots (e) and (d) when those are scaled from two different roots respectively for both axes as $\tau_{\pm r}^{-1} = \tau^{-1} \times (1 \pm \sqrt{4D_{\text{eff}} + 1})$ and $D_{\text{eff}}^{\pm r} = D_{\text{eff}} \times (1 \pm \sqrt{4D_{\text{eff}} + 1})$.

for dissipative(SP's) in two distinct calculations namely RG and relaxation time. The local effective Hamiltonian in single impurity shows topological transition at the FP's observed in RG flow implying the \mathcal{PC} terms are important for the problem. We show that high condition number in fock space

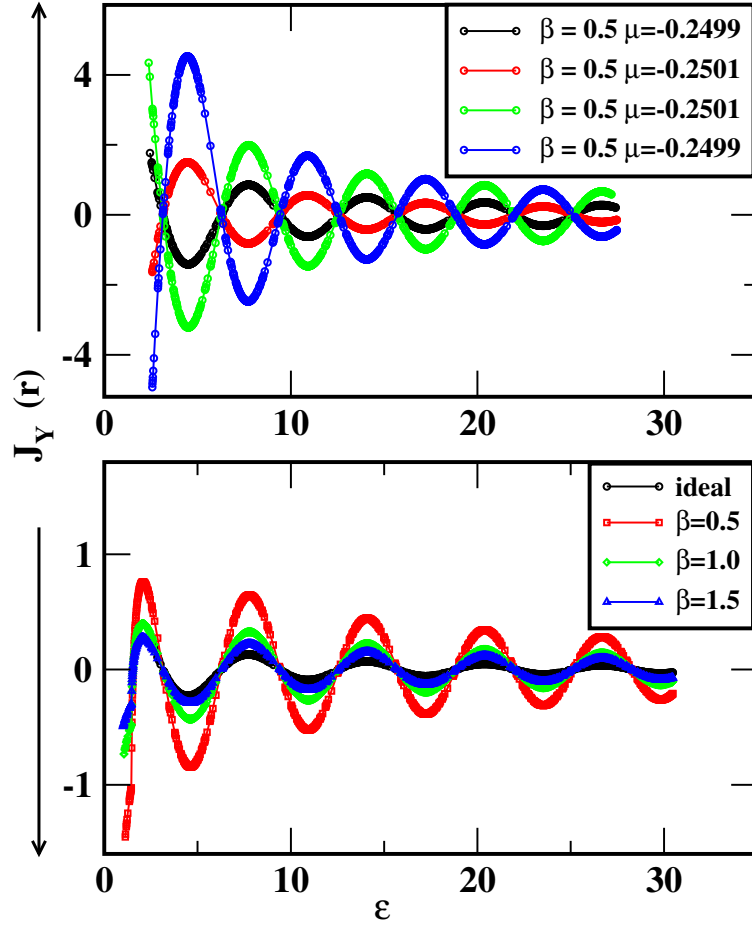


Figure 6.11: We plot RKKY interaction as function of bandwidth ϵ , for a critical value of the chemical potential ($\mu = \pm 0.25$), J_Y^{odd} changes sign and goes out of phase as shown in the figure above. The RKKY interaction is amplified for a range of $0 < \beta < 1.0$ and approaches the ideal flat band limit for $\beta > 1.0$.

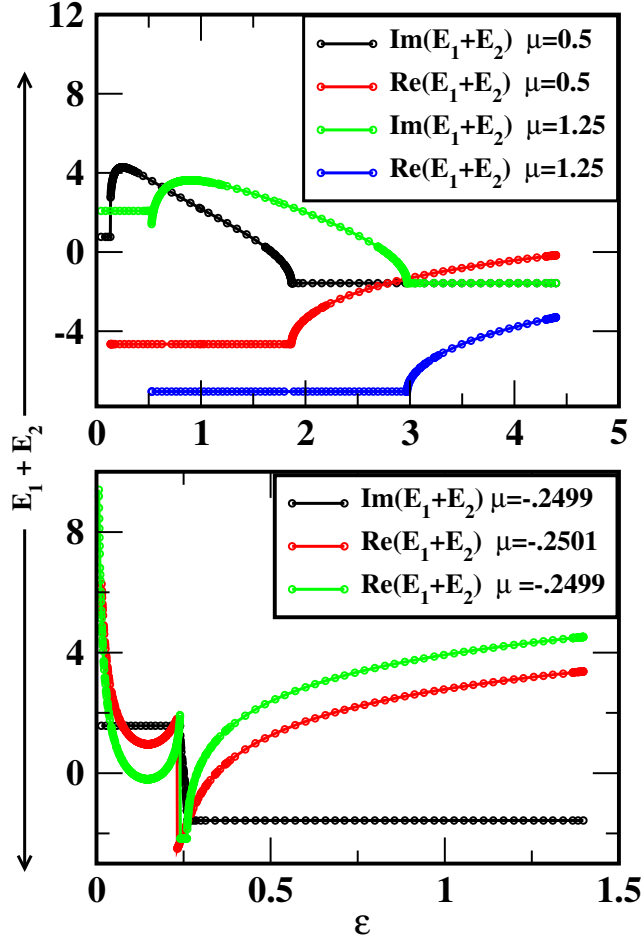


Figure 6.12: We plot the elliptic functions written in solution B.33. For negative chemical potential μ , there is discontinuity when bandwidth $\epsilon = -\mu = 0.25$ this correspond $q \rightarrow 0$ limit; elsewhere, we see exceptional points. The EPs start shifting for increasing positive μ , but there is no SR in the real part of these special functions. This odd channel shows EP or SR behavior, which is relevant in RG when dominant odd channel scattering emerges as complex FPs in such models.

local Hamiltonian for all real-valued couplings show defectiveness due to presence of anisotropy.

We analyzed RG equations for single and two impurity problems in a homogeneous bath, observing the competition between RKKY and Kondo interactions when the impurity \mathcal{DM} -interaction is absent. We found that anisotropic \mathcal{DM} interactions contribute as Hermiticity breaking terms with \mathcal{PC} Symmetry to obtain coalescing points in such Kondo models. The distinctive transport signature results from residue contributions from such a specific bath when $q \neq 0$. The numerical diagnosis showed sign reversion regimes at the fixed points obtained in flow diagrams from the perturbative analysis; however, we have shown that the added potential scattering brings openness to the problem; hence these fixed points are specific to this type of dissipation. Existence of nonlinear perturbation leads to out-of-phase oscillations in the RKKY and Exceptional point in elliptic functions. The dissipation induced by such non linearity counter intuitively enhance the RKKY oscillations but for asymptotically large nonlinearity will reach the flat band limit.

The study opens up possibility new experiments to realise the higher order exceptional points and their topology with \mathcal{PC} interactions in anisotropic vacancy-spin systems⁷. Additionally exceptional points may be realized in systems like cavity-bath and vacancy centres in diamond with a control of cubic perturbation. The study motivates to conduct advanced Numerical Renormalization Group (NRG) calculations involving complex-valued and anisotropic \mathcal{DM} -interactions to investigate critical phenomena corresponding to dissipative problems.

Bibliography

- [1] H.-P. Breuer, F. Petruccione, *et al.*, *The theory of open quantum systems* (Oxford University Press on Demand, 2002).
- [2] Y. Ashida, Z. Gong, and M. Ueda, *Advances in Physics* **69**, 249 (2020).
- [3] P. Kumar and R. Bhatt, *Physical Review B* **104**, 035147 (2021).
- [4] C. Han and Z. Liu, *Physical Review B* **105**, 045108 (2022).
- [5] T. Thakur and B. Szafran, *Scientific Reports* **13**, 1 (2023).
- [6] A. N. Poddubny, *Phys. Rev. B* **107**, 045131 (2023).

- [7] Y. Wu, Y. Wang, X. Ye, W. Liu, Z. Niu, C.-K. Duan, Y. Wang, X. Rong, and J. Du, *Nature Nanotechnology* **19**, 160 (2024).
- [8] T. Isobe, T. Yoshida, and Y. Hatsugai, *Phys. Rev. Lett.* **132**, 126601 (2024).
- [9] B. Zhen, C. W. Hsu, Y. Igarashi, L. Lu, I. Kaminer, A. Pick, S.-L. Chua, J. D. Joannopoulos, and M. Soljačić, *Nature* **525**, 354 (2015).
- [10] J. Betancourt, S. Li, X. Dang, J. Burton, E. Tsybmal, and J. Velez, *Journal of Physics: Condensed Matter* **28**, 395501 (2016).
- [11] G. A. Starkov, M. V. Fistul, and I. M. Eremin, *Phys. Rev. A* **108**, 022206 (2023).
- [12] C.-X. Liu, X.-L. Qi, H. Zhang, X. Dai, Z. Fang, and S.-C. Zhang, *Phys. Rev. B* **82**, 045122 (2010).
- [13] I. Boettcher, *Phys. Rev. Lett.* **124**, 127602 (2020).
- [14] H. Zhang, C.-X. Liu, X.-L. Qi, X. Dai, Z. Fang, and S.-C. Zhang, *Nature physics* **5**, 438 (2009).
- [15] J. A. S. Lourenço, R. L. Eneias, and R. G. Pereira, *Phys. Rev. B* **98**, 085126 (2018).
- [16] V. M. Kulkarni, A. Gupta, and N. S. Vidhyadhiraja, *Phys. Rev. B* **106**, 075113 (2022).
- [17] H.-F. Lü, Y.-H. Deng, S.-S. Ke, Y. Guo, and H.-W. Zhang, *Phys. Rev. B* **99**, 115109 (2019).
- [18] A. K. Mitchell and L. Fritz, *Phys. Rev. B* **93**, 035137 (2016).
- [19] M. Zarea, S. E. Ulloa, and N. Sandler, *Phys. Rev. Lett.* **108**, 046601 (2012).
- [20] D. Mastrogiuseppe, A. Wong, K. Ingersent, S. E. Ulloa, and N. Sandler, *Phys. Rev. B* **90**, 035426 (2014).
- [21] M. Zarea and N. Sandler, *Phys. Rev. B* **79**, 165442 (2009).
- [22] R. Žitko, *Phys. Rev. B* **81**, 241414 (2010).
- [23] P. Delplace, T. Yoshida, and Y. Hatsugai, *Phys. Rev. Lett.* **127**, 186602 (2021).

- [24] A. C. Hewson, *The Kondo problem to heavy fermions*, Vol. 2 (Cambridge university press, 1997).
- [25] A. Melkani, Phys. Rev. Res. **5**, 023035 (2023).
- [26] M. Nakagawa, N. Kawakami, and M. Ueda, Phys. Rev. Lett. **121**, 203001 (2018).
- [27] A. Van der Sluis, Numerische Mathematik **14**, 14 (1969).
- [28] D. F. Mross and H. Johannesson, Phys. Rev. B **80**, 155302 (2009).
- [29] B. A. Jones and C. M. Varma, Phys. Rev. Lett. **58**, 843 (1987).
- [30] B. A. Jones, C. M. Varma, and J. W. Wilkins, Phys. Rev. Lett. **61**, 125 (1988).
- [31] S. Han, D. J. Schultz, and Y. B. Kim, Phys. Rev. B **107**, 235153 (2023).
- [32] M. Nakagawa and N. Kawakami, Phys. Rev. Lett. **115**, 165303 (2015).

Chapter 7

Conclusions and Future perspectives

In conclusion, this journey through the realm of non-Hermitian systems has revealed a rich tapestry of extraordinary phenomena and intriguing insights. These systems, characterized by Hamiltonians featuring gain and loss terms, have demonstrated a capacity for exceptional points, spontaneous symmetry breaking, and unconventional modes of behavior. The diverse array of methodologies, encompassing analytical techniques and numerical methods, has allowed us to dissect and understand the unique attributes of non-Hermitian systems. Throughout this exploration, we've uncovered the critical roles of symmetry, interactions, and disorder in shaping their behavior. Moreover, we've gained valuable perspectives on the potential applications of these findings in various scientific and technological domains. As we conclude this chapter, we anticipate continued exploration and innovation in the field of non-Hermitian systems, promising exciting discoveries and practical advancements in the years to come.

7.1 Summary of the Thesis

We present here a concise summary and results of all work chapters from two to six.

Chapter 2 In this chapter, we delved into the complex interplay between interactions, Rashba spin-orbit coupling, and non-Hermitian coupling in the context of the Kondo effect and \mathcal{PT} -symmetry. We found that exceptional points and Kondo destruction critical points coincide under certain conditions. Moreover, our study explored the interplay of Coulomb interaction and spin-orbit interaction in preserving \mathcal{PT} symmetry. We employed exact diagonalization, Green's functions, and a slave-boson method to unravel the complex interplay. Our work raises questions about the relationship between these models and the nature of complex boson mean fields beyond the Kondo destruction critical point.

Chapter 3 In this chapter we used slave-boson methods in the Callan-Symmanzik equation serves as a valuable tool for studying strong correlations in the non-Hermitian system, each offering unique insights into different phases and phenomena. However, they come with inherent limitations and approximations. Non-equilibrium methods, particularly the Keldysh field theory, are crucial for investigating non-Hermitian systems, allowing us to delve into dynamic and non-equilibrium properties. These methods shed light on complex interactions, such as the laser-induced Kondo effect and the multichannel Anderson problem, offering a deeper understanding of the behavior of strongly correlated systems with rich phase transitions.

Chapter 4 In summary, this study offers valuable insights into non-Hermitian systems, unveiling a novel perturbation theory and shedding light on the influence of interactions on Exceptional Points (EPs). The research advances our understanding of perturbative RG and its link to \mathcal{PT} -symmetry, promising exciting avenues for future exploration in non-Hermitian quantum mechanics and condensed matter physics. The introduced method for RG with metric operators, as demonstrated in our benchmarks, presents a novel approach to studying finite interaction effects in the thermodynamic limit, adding a significant contribution to the field.

Chapter 5 The study explored the emergence of exceptional points in the impurity subsystem with parity-time-breaking interactions. We introduced an efficient generator for non-Hermitian models within the Flow Equations method, demonstrating robust numerical convergence in the presence of non-Hermiticity. This work also uncovered interaction-induced exceptional points in Hermitian models, highlighting the intricate interplay between interactions and system behavior. Moreover, our research extended to mapping

non-Hermitian models to isospectral Hermitian models, providing a bridge between these domains and enhancing our understanding of these complex systems.

Chapter 6 This Chapter delves into the coalescence of points in a bulk system with magnetic impurities, focusing on spin relaxation time calculations in different momentum directions. Key findings include the common invariant in RG solutions and the transition from Kondo to non-Kondo regimes with log divergence. The study also explores RG calculations on single and two impurity problems and the interplay between RKKY and Kondo interactions, emphasizing the significance of anisotropic \mathcal{DM} interactions for coalescing points in Hermitian Kondo models. This research offers a valuable transport signature and opens avenues for further investigations, including charge and thermal transport, impurity effects, and unitarity in different subspaces.

7.2 Future Perspectives

The study of non-Hermitian quantum many-body systems is an emerging field with several key challenges that require deeper exploration:

- *Non-Hermitian Systems with Interactions and Disorder*: A major challenge lies in understanding the behavior of non-Hermitian systems under interactions and disorder. Such systems often exhibit open dynamics, exchanging energy and particles with their environment, leading to phenomena like eigenstate localization, enhanced energy transport, and reduced dissipation.
- *Generalization of Exceptional Points to Many-Body Systems*: Exceptional points, where both eigenvalues and eigenvectors of a Hamiltonian coalesce, are pivotal in non-Hermitian physics. Extending this concept to many-body systems is complex, as interactions, disorder, and environmental noise can significantly affect the behavior of these points.
- *Advancement of Hermitianization Techniques*: Hermitianization methods¹, which map non-Hermitian Hamiltonians to Hermitian ones by introducing suitable Hermitian operators, need further development for many-body systems. The complexity of many-body interactions poses significant difficulties in designing appropriate Hermitianization schemes.
- *Impact of Non-Hermitian Hamiltonians*: Non-Hermitian Hamiltonians can give rise to unique effects, such as enhanced energy transfer, diminished dissipation, and unconventional vibrational modes. Understanding the implications of these effects in the context of many-body systems is crucial for a more complete picture of their behavior.

Addressing these challenges will advance the theoretical framework of non-Hermitian quantum many-body physics and expand its potential applications in diverse areas of physics.

7.3 Time Evolution of Non-Hermitian Systems

Krein, 3-Hilbert, or rigged Hilbert spaces are instrumental in the analysis of non-Hermitian operators, which frequently arise in open quantum systems interacting with their environments. In such systems, the Hamiltonian deviates from Hermiticity, and the corresponding inner product becomes indefinite.

A key concept in Krein space theory is the notion of self-adjoint operators. In a Krein space, a self-adjoint operator is defined as one that is equal to its Krein space adjoint. This adjoint extends the notion of the Hermitian adjoint to indefinite inner products, requiring the reversal of the inner product's order and multiplication by a fundamental symmetry operator. This operator, fundamental in Krein space theory, preserves the indefinite inner product while maintaining isometric properties, ensuring that vector norms remain conserved.

7.3.1 Lie Algebra and Renormalization Group (RG) Invariants

Lie algebras are central to many areas of physics, including non-Hermitian systems. In these systems, symmetry and its associated Lie algebra become more complex than in Hermitian systems due to the underlying non-Hermitian structure.

A useful approach to studying Lie algebra in non-Hermitian systems is through pseudo-Hermiticity, which generalizes Hermiticity via a similarity transformation. This transformation relates the non-Hermitian operator to its Hermitian counterpart, allowing the derivation of the non-Hermitian operator's Lie algebra.

In non-Hermitian quantum mechanics, Lie algebra plays an essential role in understanding symmetry breaking and phase transitions, particularly in \mathcal{PT} -symmetric systems. This concept is widely applied in fields such as optics, condensed matter physics, and quantum field theory.

In the context of the Kondo problem, Lie algebras encode the symmetries of the system, providing a framework for addressing its complexities. For example, the XXZ Kondo model is governed by a $U(1) \times SU(2)$ symmetry group, reflecting the conservation of charge and spin. The corresponding Lie algebra comprises operators that commute with the Hamiltonian, preserving these symmetries.

Lie algebraic techniques are especially useful for solving the Kondo problem, where they facilitate the expression of renormalized couplings through flow equations. These equations describe how the couplings evolve with the energy scale, which is crucial for understanding the low-energy behavior of the system. This is particularly important when studying magnetic impurities in metals, where Lie algebra helps simplify RG flow calculations and elucidate the system's behavior under various conditions.

7.4 Exploration of \mathcal{DM} interaction forms And their Group structures

According to Kogan's research² on the XXZ Kondo model, any interaction with a $U(1)$ symmetry can be expressed as a linear combination of three invariants. These invariants include the $U(1)$ -symmetric interactions $S^x \otimes \sigma^x + S^y \otimes \sigma^y$ and $S^z \otimes \sigma^z$, which involve the spin operators S^x , S^y , and S^z of the Kondo model and the Pauli matrices σ^x , σ^y , and σ^z of bath operators in Abrikosov's notation.

Using these invariants, it becomes straightforward to write down the general interaction with arbitrary couplings. However, an additional invariant is generated in this case, which changes the Lie algebra. Specifically, the invariant $S^x \otimes \sigma^z + S^y \otimes \sigma^z$ is generated.

Thus, the most general \mathcal{PT} -symmetric interaction for the XXZ Kondo model can be expressed as a linear combination of these four invariants, including the new invariant generated by the arbitrary couplings.,

$$V = J_1(S^x \otimes \sigma^x + S^y \otimes \sigma^y) + J_2(S^x \otimes \sigma^z + S^y \otimes \sigma^z) + J(S^z \otimes \sigma^z) + J_{\mathcal{DM}}(S^x \otimes \sigma^y - S^y \otimes \sigma^x) \quad (7.1)$$

7.5 DMFT for non-Hermitian systems

- DMFT is widely used to study the electronic properties of materials, mapping the lattice problem to an effective quantum impurity model coupled to a self-consistently determined bath.
- In non-Hermitian systems, e.g., with gain and loss, mapping to an effective impurity model becomes complex due to non-Hermitian terms in the Hamiltonian.
- Extending DMFT to non-Hermitian systems requires developing new formalisms and techniques to handle the non-Hermitian nature of the quantum impurity model and associated bath.

7.6 NRG for non-Hermitian systems

Robert Peters's work³ addresses the emergence of non-Hermitian phenomena in open quantum systems with gain and loss and equilibrium single-particle properties of strongly correlated systems. It distinguishes the distinct conditions required for non-Hermitian behavior in each field, notably the need for

postselection in open quantum systems but not in strongly correlated systems. The study establishes a connection between these two descriptions of non-Hermitian phenomena, demonstrating the identity of the non-Hermitian Hamiltonians involved. Furthermore, it outlines a novel method for analyzing non-Hermitian properties that obviates the necessity of postselection. While several studies have delved into this area, a number of open questions still remain.

- NRG is a numerical method used to study low-energy properties of quantum impurity models and strongly correlated many-body systems.
- In non-Hermitian systems, NRG faces challenges due to the complex energy spectrum and presence of exceptional points.
- Calculating the density of states and spectral functions in non-Hermitian NRG requires modifications to accommodate non-Hermitian operators and analysis of spectral singularities.

7.7 Self-consistency and Green's functions

- Both DMFT and NRG rely heavily on self-consistency⁴, where the impurity problem and bath are iteratively solved.
- In non-Hermitian systems, self-consistency becomes intricate due to the non-unitary nature of the non-Hermitian Hamiltonian, necessitating adapted self-consistency schemes.
- Computing Green's functions in non-Hermitian systems is challenging, as traditional definitions may not hold, requiring new methods for an accurate description of system dynamics.

7.8 Real-time dynamics

- Investigating real-time dynamics in non-Hermitian quantum many-body systems is a challenging problem.
- Non-Hermitian systems can lead to non-unitary dynamics with amplification and decay, unlike Hermitian systems where time evolution is unitary.

- Developing efficient and accurate numerical techniques for simulating real-time dynamics in non-Hermitian systems is an ongoing research direction.

Addressing these challenges and extending DMFT and NRG to non-Hermitian quantum many-body problems will significantly advance our understanding of open quantum systems and their applications in various fields, including the study of non-Hermitian topological phases, quantum dissipative systems, and open quantum dots.

Bibliography

- [1] M. Znojil, *Annals of Physics* **448**, 169198 (2023).
- [2] E. Kogan, *Journal of Physics Communications* **3**, 125001 (2019).
- [3] Y. Michishita and R. Peters, *Phys. Rev. Lett.* **124**, 196401 (2020).
- [4] Y. Nagai, Y. Qi, H. Isobe, V. Kozii, and L. Fu, *Physical review letters* **125**, 227204 (2020).

Appendix A

Derivation Of Metric Operator and RG Equations

A.1 Metric Operator in spin basis

We rewrite the $\hat{\mathcal{PT}}$ operator where it satisfies $\hat{\mathcal{PT}}^{-1} = \hat{\mathcal{PT}}^\dagger$ hence it is unitary and also it is in (m, σ) basis as the following,

$$\begin{aligned}
\hat{\mathcal{PT}} &= \sum_{k\eta} -c_{k\eta+}^\dagger c_{k\eta+} + c_{\eta-}^\dagger c_{k\eta-} - d_\uparrow^\dagger d_\uparrow + d_\downarrow^\dagger d_\downarrow \\
&= \sum_{kh} \left(-\frac{1}{2}(c_{k\uparrow}^0 + hc_{k\downarrow}^1)^\dagger (c_{k\uparrow}^0 + hc_{k\downarrow}^1) + \frac{1}{2}(c_{k\uparrow}^{-1} + hc_{k\downarrow}^0)(c_{k\uparrow}^{-1} + hc_{k\downarrow}^0)^\dagger \right) \\
&\quad - d_\uparrow^\dagger d_\uparrow + d_\downarrow^\dagger d_\downarrow = \sum_k -c_{k\uparrow}^{0\dagger} c_{k\uparrow}^0 - c_{k\downarrow}^{1\dagger} c_{k\downarrow}^1 + c_{k\uparrow}^{-1\dagger} c_{k\uparrow}^{-1} + c_{k\downarrow}^{0\dagger} c_{k\downarrow}^0 - d_\uparrow^\dagger d_\uparrow + d_\downarrow^\dagger d_\downarrow
\end{aligned} \tag{A.1}$$

We insert the operator at each vertex in order to preserve symmetry at each scattering process. This will involve calculating the following,

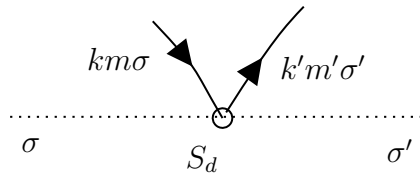
$$\begin{aligned}
[S_z, \hat{\mathcal{PT}}] &= 0, \quad [S_\pm, \hat{\mathcal{PT}}] = -S_\mp \\
[c_{k\sigma}^{0\dagger} c_{k\sigma}^0, \hat{\mathcal{PT}}] &= 0, \quad [c_{k\sigma}^{0\dagger} c_{k\bar{\sigma}}^0, \hat{\mathcal{PT}}] = -c_{k\sigma}^{0\dagger} c_{k\sigma}^0 \\
[c_{k\sigma}^{m\dagger} c_{k\sigma'}^{m'}, \hat{\mathcal{PT}}] &= (1 - \delta_{m,m'} \delta_{\sigma\sigma'}) c_{k\sigma}^{m\dagger} c_{k\sigma}^{m'}
\end{aligned} \tag{A.2}$$

The above commutators are derived by expanding them in operator basis and all the operators are in spin basis ie,

$$\begin{aligned}
[S_z, \hat{\mathcal{PT}}] &= [n_\uparrow - n_\downarrow, \sum_{k'} -c_{k'\uparrow}^{0\dagger} c_{k'\uparrow}^0 - c_{k'\downarrow}^{1\dagger} c_{k'\downarrow}^1 \\
&\quad + c_{k'\uparrow}^{-1\dagger} c_{k'\uparrow}^{-1\dagger} + c_{k'\downarrow}^{0\dagger} c_{k'\downarrow}^{0\dagger} - d_\uparrow^\dagger d_\uparrow + d_\downarrow^\dagger d_\downarrow] = 0 \\
[S^+, \hat{\mathcal{PT}}] &= [d_\uparrow^\dagger d_\downarrow, \sum_{k'} -c_{k'\uparrow}^{0\dagger} c_{k'\uparrow}^0 - c_{k'\downarrow}^{1\dagger} c_{k'\downarrow}^1 + c_{k'\uparrow}^{-1\dagger} c_{k'\uparrow}^{-1\dagger} + c_{k'\downarrow}^{0\dagger} c_{k'\downarrow}^{0\dagger} \\
&\quad - d_\uparrow^\dagger d_\uparrow + d_\downarrow^\dagger d_\downarrow] = -d_\uparrow^\dagger d_\downarrow + d_\downarrow^\dagger d_\uparrow = -2S^+ \\
[S^-, \hat{\mathcal{PT}}] &= [d_\downarrow^\dagger d_\uparrow, \sum_{k'} c_{k'\uparrow}^{0\dagger} c_{k'\uparrow}^0 - c_{k'\downarrow}^{1\dagger} c_{k'\downarrow}^1 + c_{k'\uparrow}^{-1\dagger} c_{k'\uparrow}^{-1\dagger} + c_{k'\downarrow}^{0\dagger} c_{k'\downarrow}^{0\dagger} \\
&\quad - d_\uparrow^\dagger d_\uparrow + d_\downarrow^\dagger d_\downarrow] = -d_\downarrow^\dagger d_\uparrow + d_\uparrow^\dagger d_\downarrow = -2S^- \\
[S_{kk'}^z, \hat{\mathcal{PT}}] &= [c_{km\uparrow}^\dagger c_{km\uparrow} - c_{km\downarrow}^\dagger c_{km\downarrow}, \sum_{k'} -c_{k'\uparrow}^{0\dagger} c_{k'\uparrow}^0 - c_{k'\downarrow}^{1\dagger} c_{k'\downarrow}^1 \\
&\quad + c_{k'\uparrow}^{-1\dagger} c_{k'\uparrow}^{-1\dagger} + c_{k'\downarrow}^{0\dagger} c_{k'\downarrow}^{0\dagger} - d_\uparrow^\dagger d_\uparrow + d_\downarrow^\dagger d_\downarrow] = 0 \\
[S_{kk'}^+, \hat{\mathcal{PT}}] &= [c_{k'm'\uparrow}^\dagger c_{km\downarrow}, \sum_{k'} -c_{k'\uparrow}^{0\dagger} c_{k'\uparrow}^0 - c_{k'\downarrow}^{1\dagger} c_{k'\downarrow}^1 + c_{k'\uparrow}^{-1\dagger} c_{k'\uparrow}^{-1\dagger} + c_{k'\downarrow}^{0\dagger} c_{k'\downarrow}^{0\dagger} \\
&\quad - d_\uparrow^\dagger d_\uparrow + d_\downarrow^\dagger d_\downarrow] = -c_{k\uparrow}^{0\dagger} c_{km\downarrow} \delta_{m',0} - c_{km'\uparrow}^\dagger c_{k\downarrow}^1 \delta_{m',1} \\
[S_{kk'}^-, \hat{\mathcal{PT}}] &= [c_{k'm'\downarrow}^\dagger c_{km\uparrow}, \sum_{k'} -c_{k'\uparrow}^{0\dagger} c_{k'\uparrow}^0 - c_{k'\downarrow}^{1\dagger} c_{k'\downarrow}^1 + c_{k'\uparrow}^{-1\dagger} c_{k'\uparrow}^{-1\dagger} \\
&\quad + c_{k'\downarrow}^{0\dagger} c_{k'\downarrow}^{0\dagger} - d_\uparrow^\dagger d_\uparrow + d_\downarrow^\dagger d_\downarrow] = -c_{k\downarrow}^{0\dagger} c_{km\uparrow} \delta_{m',0} - c_{km'\downarrow}^\dagger c_{k\uparrow}^1 \delta_{m',1} \\
[S_{kk'}^{\pm,0}, \hat{\mathcal{PT}}] &= S_{kk'}^{\pm,0}, \quad [S_{kk'}^{z,0}, \hat{\mathcal{PT}}] = S_{kk'}^{z,0}, \quad [S_{kk'}^\pm, S_{kk'}^z] = S_{kk'}^\pm \delta_{m,0}
\end{aligned} \tag{A.3}$$

The above commutators A.2 will be used in calculating the following respectively,

$$\begin{aligned}
:S_z: &:= \hat{\mathcal{PT}}^{-1} S_z \hat{\mathcal{PT}} = S_z, :S_\pm: := \hat{\mathcal{PT}}^{-1} S_\pm \hat{\mathcal{PT}} = -S_\mp \\
:c_{k\sigma}^{m\dagger} S_\alpha c_{k'\sigma'}^{m'}: &:= \hat{\mathcal{PT}}^{-1} (c_{k\sigma}^{m\dagger} S_\alpha c_{k'\sigma'}^{m'}) \hat{\mathcal{PT}}, = -c_{k\sigma}^{m\dagger} S_z c_{k'\sigma'}^{m'} \text{ for } \alpha = z \\
&= c_{k\sigma}^{m\dagger} S_\mp c_{k'\sigma'}^{m'} \text{ for } \alpha = \pm
\end{aligned} \tag{A.4}$$



We can expand the above diagram as the following,

$$\begin{aligned}
J : c_{k\sigma}^{m\dagger} \frac{S_d}{E - H_0} c_{k'\sigma}^{m'} &:= \mathcal{PT}^\dagger c_{k\sigma}^{m\dagger} \frac{S_d}{E - H_0} c_{k'\sigma}^{m'} \mathcal{PT} \\
[c_{k'\sigma}, \hat{\mathcal{PT}}] &= [c_{k'm\sigma}, \sum_{k'} -c_{k'\uparrow}^{0\dagger} c_{k'\uparrow}^0 - c_{k'\downarrow}^{1\dagger} c_{k'\downarrow}^1 + c_{k'\uparrow}^{-1\dagger} c_{k'\uparrow}^{-1} + c_{k'\downarrow}^0 c_{k'\downarrow}^{0\dagger} - d_\uparrow^\dagger d_\uparrow + d_\downarrow^\dagger d_\downarrow] \\
&= \sigma(c_{k\sigma}^m \delta_{m,0} + c_{k\sigma}^m \delta_{m,1}) \\
\hat{\mathcal{PT}}^{-1} \hat{\mathcal{PT}} &= \sum_{km\sigma} n_{km\sigma} + \sum_{\sigma} n_{d\sigma} = I \text{ for half filling}
\end{aligned} \tag{A.5}$$

The $T_{kk'}$ matrix calculation can be done as following,

$$\begin{aligned}
T_{kk'} &= V_{kk'} + V_{k'q} G_0(\omega, q) T_{qk} \\
&+ V_{k'q} G_0(\omega, q) T_{q,q'} G_0(\omega, q') T_{q',k} + ..
\end{aligned} \tag{A.6}$$

The perturbative expansion described above applies to specific Left-Right states. Since our propagator is already symmetric, we must maintain this symmetry in the operator $T_{qq'mm'}$. Therefore, it must satisfy the condition $[T_{qq'mm'}, \hat{\mathcal{PT}}] = 0$.

$$\begin{aligned}
&: V_{k'q} G_0(\omega, q) T_{q,q'} G_0(\omega, q') T_{q',k} := \\
&: \left(S_\alpha c_{k'm'\sigma'}^\dagger c_{qm\sigma} \frac{1}{\omega - \epsilon_{m'} - H_0} c_{qm'\sigma'}^\dagger c_{q'm\sigma} \frac{1}{\omega - \epsilon_{m'} - H_0} c_{k'm'\sigma'}^\dagger c_{q,m,\sigma} \right) :
\end{aligned} \tag{A.7}$$

As we can see from $[T_{qq'}, T_{q'k}] = T_{qk}$ one can show the contribution from the third order correction as crossing and non-crossing diagrams (topologically equivalent or equivalent) as following.

$$\begin{aligned}
&: V_{k'q} G_0(\omega, q) T_{q,q'} G_0(\omega, q') T_{q',k} :=: V_{k'q} G_0(\omega, q) (T_{qk} + T_{q',k} T_{q,q'}) G_0(\omega, k) : \\
&= -V_{k'q} G_0(\omega, q) G_0(\omega, q') T_{q'k'} + V_{kk'} G_0(\omega, q) T_{qq'} G_0(\omega, q')
\end{aligned} \tag{A.8}$$

Apart from the above topologically distinct contributions remaing all other contributions vanish these are also discussed in¹⁻⁴.

$$\begin{aligned}
\Delta T_{kk'}^{(3)} &=: S_\alpha c_k^\dagger c_q \frac{1}{\omega - \epsilon_q - H_0} S_{\alpha'} \frac{1}{\omega - \epsilon_{q'} - H_0} S_{\alpha''} c_k^\dagger c_q : \\
&+ S_\alpha c_k^\dagger c_{k'} S_{\alpha'} \frac{1}{\omega - \epsilon_q - H_0} c_k^\dagger c_{k'} \frac{1}{\omega - \epsilon_{q'} - H_0} S_{\alpha''} :
\end{aligned} \tag{A.9}$$

Where $\alpha, \alpha', \alpha''$ correspond to all values \pm and z components of impurity spin. We had dropped the m and spin index while deriving distinct diagrams.

Now we can retain and take various combinations of vertices and calculate the contributions. For example, let's calculate the one non-Hermitian contribution for third order $T_{kk'}$ as the following,

$$\begin{aligned}
\Delta T_{kk'}^{(3)} &= iJ_i S_\alpha c_{k\uparrow}^{0\dagger} c_{q\uparrow}^0 \frac{1}{\omega - \epsilon_q - H_0} iJ_i S_{\alpha'} \frac{1}{\omega - \epsilon_{q'} - H_0} iJ_i S_{\alpha''} c_{q'\uparrow}^{0\dagger} c_{k\uparrow}^0 : \\
&= iJ_i^3 \frac{1}{\omega - \epsilon_{q0} - \epsilon_{k'0} - H_0} \frac{1}{\omega - \epsilon_{q0} - \epsilon_{k'0} - H_0} \\
&= iJ_i^3 \frac{1}{D'^2} \rho'_0 |\delta D'| S_z c_{k\uparrow}^{0\dagger} c_{k\uparrow}^0 \\
&= iJ_i^3 \frac{1}{D'} \rho'_0 |\delta \ln D'| S_z c_{k\uparrow}^{0\dagger} c_{k\uparrow}^0
\end{aligned} \tag{A.10}$$

In this analysis, we are investigating the scaling properties of a third-order correction term, denoted as ρ' . This correction is closely related to the energy scale and is connected to the parameter D through the relationship $D' = D + \lambda$. We are also examining the \mathcal{PT} operation and its impact on non-flip processes. Additionally, we are studying the emergence of $\mathcal{PT} - \mathcal{DM}$ interactions and their implications for the Kondo model. Our goal is to gain insights into the non-Hermitian behavior and the physics of the model.

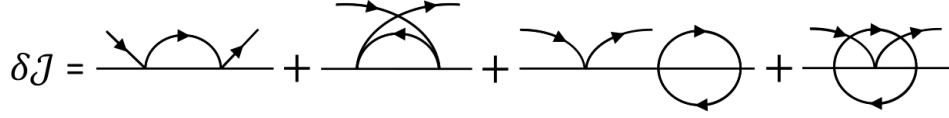


Figure A.1: δJ represents couplings' RG equations and diagrams show 1-loop and 2-loop spin-flip possibilities.

1-loop

In the conventional case, single vertex correction terms vanish for \mathcal{PT} -operations, but non-zero contributions emerge at the 2-vertex level. These contributions, expressed as $\lambda e^{2i\phi} : c_{k\downarrow}^{0\dagger} d_{\uparrow}^{\dagger} d_{\downarrow} c_{k\uparrow}^1 :: \lambda e^{2i\phi} c_{k\uparrow}^{1\dagger} d_{\downarrow}^{\dagger} d_{\uparrow} c_{k\downarrow}^0$, correspond to Kondo coupling.

For the 2-vertex level, we find contributions in the form of $\lambda^2 e^{4i\phi} : c_{k\uparrow}^{0\dagger} d_{\uparrow}^{\dagger} d_{\uparrow} c_{k\uparrow}^0$ and $\lambda^2 e^{-4i\phi} : c_{k\downarrow}^{0\dagger} d_{\downarrow}^{\dagger} d_{\downarrow} c_{k\downarrow}^0$, representing diagonal coupling contributions for $m = 0$ particles.

For $m = 1$ to $m = 0$ scattering, the γ term is affected, primarily contributing to δJ in the non-Hermitian spin-orbit coupling scenario.

Regarding non-Hermitian couplings J_r and J_i , J_r influences δJ_r , while J_i does not affect δJ due to \mathcal{PT} -symmetry.

The remaining calculations extend these observations to the two-loop level.

In summary, 2-loop corrections become significant in the strong coupling regime for non-Hermitian systems, particularly the \mathcal{DM} term, which transitions between $m = 0$ and $m = \pm 1$.

$$\begin{aligned}\frac{d\mathcal{J}}{d\ln D'} &= \mathcal{J}^3 + (\mathcal{J}^2 + \gamma^2) + \gamma^2(\mathcal{J} - \gamma) \\ \frac{d\Gamma}{d\ln D'} &= \Gamma(\mathcal{J} + \gamma - \mathcal{J}\gamma + \Gamma^2 + \gamma^2 + \mathcal{J}^2) \\ \frac{d\gamma}{d\ln D'} &= \gamma^2 + re(\Gamma^2)\gamma + re(\Gamma^2) + \gamma^3\end{aligned}\tag{A.11}$$

Expanding the compactly written RG equations we get the following,

$$\begin{aligned}\frac{dJ}{d\log D'} &= J(J - J_r) + \Lambda^2 + J^3 + J_r^2 J + J_i^2 J + \gamma^2 \Lambda \\ \frac{d\Lambda}{d\log D'} &= \Lambda((J - J_r) + \gamma + J_r^2 + J^2 + J\gamma + \gamma^2) \\ \frac{dJ_i}{d\log D'} &= J_i((J - J_r) + \gamma + J^2 + J_r^2 + J\gamma + \gamma^2 + J_i^2) \\ \frac{dJ_r}{d\log D'} &= J_i^2 - J_r^2 + \Lambda J_i + \Lambda^2 - J_r^3 + J_i^2(J_r + \gamma + \Lambda) \\ \frac{d\gamma}{d\log D'} &= \gamma^2 + \Lambda^2 - J_r\gamma + J_r^2\gamma + \gamma^3 + J_i^2\gamma\end{aligned}\tag{A.12}$$

A.1.1 Poorman scaling

Now we know the model and can proceed to calculate RG equations from 1-loop and 2-loop according to the fig A.1:

$$\begin{aligned}& : c_{k\uparrow}^{0\dagger} c_{k'\uparrow}^0 S^z J e^{2i\phi} : M_{kk'} : J e^{-2i\phi} S^z c_{k'\downarrow}^{0\dagger} c_{k\downarrow}^0 \mathcal{PT}^{-1} \\ &= - : c_{k\uparrow}^{0\dagger} c_{k'\uparrow}^0 :: S^z J e^{2i\phi} : M_{kk'} : J e^{2i\phi} S^z :: c_{k'\uparrow}^{0\dagger} c_{k\uparrow}^0 := -J^2 e^{4i\phi} M_{kk'} c_{\uparrow}^{0\dagger} c_{\uparrow}^0 S^z\end{aligned}\tag{A.13}$$

We can identify the S^z vertex goes to S^\perp under symmetry operations, but each dot $:$ consists of $\mathcal{PT}^{-1}\mathcal{PT}$ indicating that this: "ordering" does not break symmetry hence it goes back to S^z with - sign. We calculate the 2-loop in a similar way as follows;

$$\begin{aligned}& : c_{k\uparrow}^{0\dagger} :: d_{\uparrow} J e^{2i\phi} : M_{kk'} : d_{\uparrow}^\dagger :: c_{k'\uparrow}^0 :: c_{k\uparrow}^{0\dagger} c_{k'\uparrow}^0 S^z J e^{2i\phi} : M_{kk'} : J e^{-2i\phi} S^z c_{k'\downarrow}^{0\dagger} c_{k\downarrow}^0 \mathcal{PT}^{-1} \\ &= - :: c_{k\uparrow}^{0\dagger} c_{k'\uparrow}^0 :: S^z J e^{2i\phi} : M_{kk'} : J e^{2i\phi} S^z :: c_{k'\uparrow}^{0\dagger} c_{k\uparrow}^0 := -J^2 e^{4i\phi} M_{kk'} c_{\uparrow}^{0\dagger} c_{\uparrow}^0 S^z\end{aligned}\tag{A.14}$$

We can find the analytic solutions using Abel's substitution⁵ for second-order nonlinearity as the following,

A.1.2 One loop solution with γ

We have the following RG equations after bit of algebra,

$$\frac{\frac{1}{J} \frac{dJ}{dl} - \frac{1}{\gamma} \frac{d\gamma}{dl}}{\alpha^2 \frac{d\gamma}{dl} - \frac{S^2}{4} \frac{dJ_r}{dl}} = \frac{J - \gamma - \frac{S^2}{4} \frac{J^2}{\gamma}}{\alpha^2 \gamma^2 - \alpha^2 J_r \gamma + \frac{S^2}{4} J_r^2} \quad (\text{A.15})$$

In order to solve the above we substitute $\frac{J}{\gamma} = w$ and rewriting the above differential equations using separation of variables followed by partial fraction and integrating gives the two solutions,

$$\begin{aligned} \text{Sol}_1 : \log \left(w(w - \frac{2}{s^2} - \zeta)^{\frac{4a}{s^2}} (w - \frac{2}{s^2} + \zeta)^{\frac{4b}{s^2}} \right) &= \log \gamma^k, \\ \text{Sol}_2 : \gamma &= \left(\frac{\frac{J_r}{\gamma} - \zeta_1}{\frac{J_r}{\gamma}} \right)^{-\frac{1}{\zeta_1}} \end{aligned} \quad (\text{A.16})$$

$$\begin{aligned} \text{where } \zeta &= \left(\frac{4}{s^4} - \frac{4}{s^2} \right)^{\frac{1}{2}}, \quad \zeta_1 = \left(\frac{4\alpha^2}{s^2} - 1 \right), \\ a &= \frac{1}{2\zeta(\frac{2}{s^2} + \zeta)}, \quad b = \frac{-1}{2\zeta(\frac{2}{s^2} - \zeta)}, \quad \alpha = (g^2 + s^2 + gs) \end{aligned}$$

$$\begin{aligned} \gamma &= C_1 \frac{J}{\gamma} \left(\frac{J}{\gamma} + 1 - \frac{s^2}{4} \left(\frac{J}{\gamma} \right)^2 \right)^{-\frac{1}{2}}, \quad \gamma = C_2 \left\{ \frac{\frac{J_r}{\gamma}}{\alpha - \frac{s^2}{4} - \frac{s^2}{4} \left\{ \frac{J_r}{\gamma} \right\}^2} \right\}^{\frac{s^2}{4\alpha - s^2}} \\ \text{where } \tau &= \left\{ \frac{s^2 \frac{J}{\gamma} - 2 - 2\sqrt{1 + s^2}}{s^2 \frac{J}{\gamma} - 2 + 2\sqrt{1 + s^2}} \right\}^{\frac{s}{\sqrt{1 + s^2}}}, \quad C_1, C_2 \text{ integral - constants} \end{aligned} \quad (\text{A.17})$$

$$\begin{aligned} s^2 (J_r/\gamma)^2 + \left(\frac{C_2(1 + J/\gamma)}{(s^2 + C_1^2)J^2/\gamma^2} \right)^{s^2/(g^2 + gs)} (J_r/\gamma) &= \alpha \\ \text{for } g &= s, \quad J_r^2 = \text{constant}/J \end{aligned} \quad (\text{A.18})$$

A.1.3 Analytical Solution at third order non-linearity

The surprising fact of the \mathcal{PT} symmetry is that even at the 2-loop invariants $g = \frac{J_i}{J - \gamma}$ $s = \frac{\Lambda}{J - \gamma}$ It seems we can solve them analytically as follows we got

2 invariants but we still have the 3 ODE's we separate the two channels as follows,

$$\begin{aligned} \frac{d(J - \gamma)}{d(J + \gamma)} &= \frac{dJ_1}{dJ_2} \\ &= \frac{J_1 J_2 - J_r J_1 + J_r^2 J_1 + g^2 J_1^3 + J_1(J_1^2 - \frac{3}{4} J_2^2)}{J_2^2 - \frac{(J_1^2 - J_2^2)}{2} - J_r J_1 + J_r^2 J_2 + 2s^2 J_1^2 + g^2 J_2^3 + J_2^3 - \frac{3}{4} J_2(J_1^2 - J_2^2)} \end{aligned} \quad (\text{A.19})$$

In the equation referred to as A.19, we can begin by examining the different phases by considering several asymptotic limits.

A.1.4 Regime $s/g \rightarrow \infty$

$$\frac{dJ_2}{dJ_1} = \frac{2s^2}{g^2} \frac{1}{J_1} + \frac{J_2^3}{J_1^3} \quad (\text{A.20})$$

substituting $\frac{J_2^3}{J_1^3} = \frac{3\alpha}{J_1}$ and separating we get the following,

$$\frac{g^2 \alpha^{2/3} {}_2F_1\left(\frac{2}{3}, 1; \frac{5}{3}; -\frac{3g^2 \alpha}{2s^2}\right)}{4s^2} = -\frac{3}{4} J_1^{-\frac{4}{3}} + \text{const} \quad (\text{A.21})$$

A.1.5 Regime $g \rightarrow \infty$

This will give the Kondo problem for the inverse couplings $\frac{1}{J_1}, \frac{1}{J_2}$

$$\frac{dJ_1}{dJ_2} = \frac{J_1^3}{J_2^3} \implies \frac{2}{J_1^2} - \frac{2}{J_2^2} = \text{const} \quad (\text{A.22})$$

which basically shows that the $J_1 - J_2$ plane does have the separatrix and both the couplings are relevant.

A.2 Resistivity Calculation

While our RG calculations initially focused on flat bands, we extended our analysis to account for the square root divergence introduced by spin-orbit coupling (SOC). Specifically, we calculated the non-Hermitian and SOC contributions to resistivity using the scattering process described in⁶, which

involves evaluating $\langle k', \sigma | T(\epsilon) | k, \bar{\sigma} \rangle$.

$$\begin{aligned}
\tilde{\gamma}_\alpha &= \sum_\alpha \int_0^{k_f} \frac{q dq}{\frac{\epsilon}{\sqrt{k}} - \frac{\epsilon}{\sqrt{q}} + \alpha(k-q)\lambda + i\eta} \\
Re(\gamma)_+ &= \left[-\frac{2k^{5/2} \log(\sqrt{q} - \sqrt{k})}{2k^{3/2}\lambda + \epsilon} \right. \\
&\quad + \frac{(k^{3/2}\epsilon\lambda - k^3\lambda^2 + \epsilon^2) \log(\sqrt{k}\lambda q + k\lambda\sqrt{q} + \epsilon)}{\sqrt{k}\lambda^2 (2k^{3/2}\lambda + \epsilon)} \\
&\quad \left. + \frac{2\sqrt[4]{k} (-3k^{3/2}\epsilon\lambda + k^3\lambda^2 - \epsilon^2) \tan^{-1}\left(\frac{\sqrt[4]{k}\sqrt{\lambda}(\sqrt{k}+2\sqrt{q})}{\sqrt{4\epsilon-k^{3/2}\lambda}}\right)}{\lambda^{3/2}\sqrt{4\epsilon-k^{3/2}\lambda} (2k^{3/2}\lambda + \epsilon)} \right] \Big|_0^{k_f} - \frac{k}{\lambda} \Big|_0^{k_f}
\end{aligned} \tag{A.23}$$

These above integrals can be used to explore the contribution to resistivity as follows,

$$\begin{aligned}
\rho \propto \frac{1}{\tau(k)} \propto & (1 - 2J_0\tilde{\gamma}_\alpha(\epsilon_k) - 2J_0\tilde{\gamma}_\alpha^*(\epsilon_k) - 2J_r\tilde{\gamma}(\epsilon_k) \\
& - 2J_r\tilde{\gamma}^*(\epsilon_k) - 2J_i\tilde{\gamma}_{\alpha k}(\epsilon_k) - 2J_i\tilde{\gamma}_{\alpha k}^*(\epsilon_k))
\end{aligned} \tag{A.24}$$

Bibliography

- [1] P. Anderson, Journal of Physics C: Solid State Physics **3**, 2436 (1970).
- [2] J. Sólyom and A. Zawadoski, Journal of Physics F: Metal Physics **4**, 80 (1974).
- [3] J. Sólyom, Journal of Physics F: Metal Physics **4**, 2269 (1974).
- [4] M. A. Abrikosov A.A., Low. Temp. Phys. **3**, 519 (1970).
- [5] V. F. Zaitsev and A. D. Polyandin, *Handbook of exact solutions for ordinary differential equations* (CRC press, 2002).
- [6] A. C. Hewson, *The Kondo problem to heavy fermions*, vol. 2 (Cambridge university press, 1997).

Appendix B

Derivations for The Chapter 6

B.1 Projection details for deriving effective sd model

The projection operator method is a versatile technique used in single-particle quantum mechanics[?] and many-body physics[?], particularly in the study of Kondo problems. It allows for the description of many-body wavefunctions in distinct sectors based on the occupancy of the impurity subspace, such as unoccupied (ψ_0), singly occupied (ψ_1), and doubly occupied (ψ_2) sectors. The method provides a formalism for projecting the total many-body wavefunction onto these sectors, facilitating a systematic analysis of the Kondo problem.

$$\begin{aligned} & \left(\sum_{i=0}^2 |\psi_i\rangle\langle\psi_i| \right) H \left(\sum_{i=0}^2 |\psi_i\rangle\langle\psi_i| \right) \left(\sum_{i=0}^2 |\psi_i\rangle\langle\psi_i| \right) \psi \\ &= E \left(\sum_{i=0}^2 |\psi_i\rangle\langle\psi_i| \right) \psi \end{aligned} \quad (\text{B.1})$$

The identity operators can be represented as projectors onto the $(0, 1, 2)$ subspaces, corresponding to unoccupied, singly occupied, and doubly occupied states. These projectors are orthogonal.

$$\begin{pmatrix} H_{00} & H_{01} & H_{02} \\ H_{10} & H_{11} & H_{12} \\ H_{20} & H_{21} & H_{22} \end{pmatrix} \begin{pmatrix} \psi_0 \\ \psi_1 \\ \psi_2 \end{pmatrix} = E \begin{pmatrix} \psi_0 \\ \psi_1 \\ \psi_2 \end{pmatrix} \quad (\text{B.2})$$

where $P_\eta P_{\eta'} = \delta_{\eta\eta'} P_{\eta=\eta'}$ and $P^I = P$, $I \in \mathcal{Z}^+$

$$H_{\eta,\eta'=0,1,2} = P_\eta H P_{\eta'}$$

We can define the projection operators using impurity number operators satisfying the completeness relation $\sum_{\eta} P_{\eta} = \mathcal{I}$ as $P_0 = (1 - n_{\downarrow})(1 - n_{\uparrow})$, $P_1 = n_{\downarrow}(1 - n_{\uparrow}) + n_{\uparrow}(1 - n_{\downarrow})$, and $P_2 = n_{\uparrow}n_{\downarrow}$. The effective Hamiltonian for different subspaces can be obtained by eliminating the corresponding wave function in favor of the others.

$$H_{eff}^{\eta} = H_{\eta\eta} + \sum_{\substack{\eta' \neq \eta=0,1,2 \\ \zeta, \zeta'=\pm}} H_{\eta\eta'}^{\zeta} \frac{1}{E - H_{\eta'\eta'}} H_{\eta'\eta}^{\zeta'} \quad (\text{B.3})$$

In the equation B.3, the index η and $\eta' = 0, 1, 2$ corresponds to the unoccupied, singly occupied, and doubly occupied states, respectively. Computing the $P_1 H P_2$ we get the following,

$$\begin{aligned} \tilde{H}_{12}^{+} &= \sum_{k\theta} \tilde{V}_k^{\theta} \alpha_{k1} e^{-i\frac{\theta}{2}} c_{k+}^{\dagger} n_{\downarrow} d_{\uparrow} + \sum_{k\theta} e^{i\frac{\theta}{2}} \tilde{V}_k^{\theta} \alpha_{k2} c_{k+}^{\dagger} n_{\uparrow} d_{\downarrow} \\ \tilde{H}_{12}^{-} &= \sum_{k\theta} i \tilde{V}_k^{\theta} \alpha_{k2} e^{-i\frac{\theta}{2}} c_{k-}^{\dagger} n_{\downarrow} d_{\uparrow} - \sum_{k\theta} i e^{i\frac{\theta}{2}} \tilde{V}_k^{\theta} \alpha_{k1} c_{k-}^{\dagger} n_{\uparrow} d_{\downarrow} \\ \implies (H_{21}^{+} + H_{21}^{-}) &= (H_{12}^{+} + H_{12}^{-})^{\dagger} \end{aligned} \quad (\text{B.4})$$

Similarly for the $P_0 H P_1$ again only hybridization terms contribute can be shown as the following,

$$\begin{aligned} \tilde{H}_{10}^{+} &= \sum_{k\theta} \tilde{V}_k^{\theta} \alpha_{k1} e^{-i\frac{\theta}{2}} c_{k+}^{\dagger} (1 - n_{\downarrow}) d_{\uparrow} \\ &\quad + \sum_{k\theta} e^{i\frac{\theta}{2}} \tilde{V}_k^{\theta} \alpha_{k2} c_{k+}^{\dagger} (1 - n_{\uparrow}) d_{\downarrow} \\ \tilde{H}_{10}^{-} &= \sum_{k\theta} i \tilde{V}_k^{\theta} \alpha_{k2} e^{-i\frac{\theta}{2}} c_{k-}^{\dagger} (1 - n_{\downarrow}) d_{\uparrow} \\ &\quad - \sum_{k\theta} i e^{i\frac{\theta}{2}} \tilde{V}_k^{\theta} \alpha_{k1} c_{k-}^{\dagger} (1 - n_{\uparrow}) d_{\downarrow} \\ \implies (H_{01}^{+} + H_{01}^{-}) &= (H_{10}^{+} + H_{10}^{-})^{\dagger} \end{aligned} \quad (\text{B.5})$$

The components H_{02} and H_{20} will vanish since P_0 commutes and also using the orthogonality $P_0 P_2 = 0$. The remaining components can be computed as follows:

$$\begin{aligned} H_{00} &= \sum_{k\zeta} \epsilon_{k\zeta} c_{k\zeta}^{\dagger} c_{k\zeta} P_0 + \sum_{\sigma} \epsilon_d n_{\sigma} P_0, \\ H_{11} &= \sum_{k\zeta} \epsilon_{k\zeta} c_{k\zeta}^{\dagger} c_{k\zeta} P_1 + \sum_{\sigma} \epsilon_d n_{\sigma} P_1, \\ H_{22} &= \sum_{k\zeta} \epsilon_{k\zeta} c_{k\zeta}^{\dagger} c_{k\zeta} P_2 + \sum_{\sigma} \epsilon_d n_{\sigma} P_2 + U n_{\uparrow} n_{\downarrow} P_2. \end{aligned} \quad (\text{B.6})$$

We will derive the components of the Hamiltonian to obtain the effective Hamiltonian can be expressed as:

$$H_{eff}^1 = H_{11} + \sum_{\zeta, \zeta' = \pm} \left(H_{12}^{\zeta} \frac{1}{E - H_{22}} H_{21}^{\zeta'} + H_{10}^{\zeta} \frac{1}{E - H_{00}} H_{01}^{\zeta'} \right)$$

The derivation proceeds as follows:

$$\begin{aligned} \sum_{\zeta, \zeta' = \pm} H_{12}^{\zeta} \frac{1}{E - H_{22}} H_{21}^{\zeta'} &= H_{12}^+ \frac{1}{E - H_{22}} H_{21}^+ + H_{12}^+ \frac{1}{E - H_{22}} H_{21}^- + H_{12}^- \frac{1}{E - H_{22}} H_{21}^+ + H_{12}^- \frac{1}{E - H_{22}} H_{21}^- \\ &= \left(\sum_k \tilde{V}_k \alpha_{k1} e^{-i\frac{\theta}{2}} c_{k+}^{\dagger} n_{\downarrow} d_{\uparrow} + \sum_k e^{i\frac{\theta}{2}} \tilde{V}_k \alpha_{k2} c_{k+}^{\dagger} n_{\uparrow} d_{\downarrow} \right) \\ &\quad \times \frac{1}{E - H_{22}} \left(\sum_{k'} \tilde{V}_{k'} \alpha_{k'1} e^{-i\frac{\theta'}{2}} c_{k'+}^{\dagger} n_{\downarrow} d_{\uparrow} + \sum_{k'} e^{i\frac{\theta'}{2}} \tilde{V}_{k'} \alpha_{k'2} c_{k'+}^{\dagger} n_{\uparrow} d_{\downarrow} \right)^{\dagger} \\ &\quad + \left(\sum_k \tilde{V}_k \alpha_{k1} e^{-i\frac{\theta}{2}} c_{k+}^{\dagger} n_{\downarrow} d_{\uparrow} + \sum_k e^{i\frac{\theta}{2}} \tilde{V}_k \alpha_{k2} c_{k+}^{\dagger} n_{\uparrow} d_{\downarrow} \right) \\ &\quad \times \frac{1}{E - H_{22}} \left(\sum_{k'} i \tilde{V}_{k'} \alpha_{k'2} e^{-i\frac{\theta'}{2}} c_{k'-}^{\dagger} n_{\downarrow} d_{\uparrow} - \sum_{k'} i e^{i\frac{\theta'}{2}} \tilde{V}_{k'} \alpha_{k'1} c_{k'-}^{\dagger} n_{\uparrow} d_{\downarrow} \right)^{\dagger} \\ &\quad + \left(\sum_k i \tilde{V}_k \alpha_{k2} e^{-i\frac{\theta}{2}} c_{k-}^{\dagger} n_{\downarrow} d_{\uparrow} - \sum_k i e^{i\frac{\theta}{2}} \tilde{V}_k \alpha_{k1} c_{k-}^{\dagger} n_{\uparrow} d_{\downarrow} \right) \\ &\quad \times \frac{1}{E - H_{22}} \left(\sum_{k'} \tilde{V}_{k'} \alpha_{k'1} e^{-i\frac{\theta'}{2}} c_{k'+}^{\dagger} n_{\downarrow} d_{\uparrow} + \sum_{k'} e^{i\frac{\theta'}{2}} \tilde{V}_{k'} \alpha_{k'2} c_{k'+}^{\dagger} n_{\uparrow} d_{\downarrow} \right)^{\dagger} \\ &\quad + \left(\sum_k i \tilde{V}_k \alpha_{k2} e^{-i\frac{\theta}{2}} c_{k-}^{\dagger} n_{\downarrow} d_{\uparrow} - \sum_k i e^{i\frac{\theta}{2}} \tilde{V}_k \alpha_{k1} c_{k-}^{\dagger} n_{\uparrow} d_{\downarrow} \right) \\ &\quad \times \frac{1}{E - H_{22}} \left(\sum_{k'} i \tilde{V}_{k'} \alpha_{k'2} e^{-i\frac{\theta'}{2}} c_{k'-}^{\dagger} n_{\downarrow} d_{\uparrow} - \sum_{k'} i e^{i\frac{\theta'}{2}} \tilde{V}_{k'} \alpha_{k'1} c_{k'-}^{\dagger} n_{\uparrow} d_{\downarrow} \right)^{\dagger} \end{aligned} \tag{B.7}$$

In equation B.7, we simplify using commutation algebra for operators of the form $\frac{1}{E - O_1} O_2$, where $[O_1, O_2] = c O_2$. This allows us to rewrite the expression as a power series and show explicit calculations for a specific

component in H_{eff} .

$$\begin{aligned}
& \sum_{\zeta, \zeta' = \pm} H_{10}^{\zeta} \frac{1}{E - H_{00}} H_{01}^{\zeta'} \\
&= H_{10}^{+} \frac{1}{E - H_{00}} H_{01}^{+} + H_{10}^{+} \frac{1}{E - H_{00}} H_{01}^{-} + H_{10}^{-} \frac{1}{E - H_{00}} H_{01}^{+} + H_{10}^{-} \frac{1}{E - H_{00}} H_{01}^{-} \\
&= \left(\sum_k \tilde{V}_k \alpha_{k1} e^{-i\frac{\theta}{2}} c_{k+}^{\dagger} (1 - n_{\downarrow}) d_{\uparrow} + \sum_k e^{i\frac{\theta}{2}} \tilde{V}_k \alpha_{k2} c_{k+}^{\dagger} (1 - n_{\uparrow}) d_{\downarrow} \right) \\
&\quad \times \frac{1}{E - H_{00}} \left(\sum_{k'} \tilde{V}_{k'} \alpha_{k'1} e^{-i\frac{\theta'}{2}} c_{k'+}^{\dagger} (1 - n_{\downarrow}) d_{\uparrow} + \sum_{k'} e^{i\frac{\theta'}{2}} \tilde{V}_{k'} \alpha_{k'2} c_{k'+}^{\dagger} (1 - n_{\uparrow}) d_{\downarrow} \right)^{\dagger} \\
&+ \left(\sum_k \tilde{V}_k \alpha_{k1} e^{-i\frac{\theta}{2}} c_{k+}^{\dagger} (1 - n_{\downarrow}) d_{\uparrow} + \sum_k e^{i\frac{\theta}{2}} \tilde{V}_k \alpha_{k2} c_{k+}^{\dagger} (1 - n_{\uparrow}) d_{\downarrow} \right) \\
&\quad \times \frac{1}{E - H_{00}} \left(\sum_{k'} i \tilde{V}_{k'} \alpha_{k'2} e^{-i\frac{\theta'}{2}} c_{k'-}^{\dagger} (1 - n_{\downarrow}) d_{\uparrow} - \sum_{k'} i e^{i\frac{\theta'}{2}} \tilde{V}_{k'} \alpha_{k'1} c_{k'-}^{\dagger} (1 - n_{\uparrow}) d_{\downarrow} \right)^{\dagger} \\
&+ \left(\sum_k i \tilde{V}_k \alpha_{k2} e^{-i\frac{\theta}{2}} c_{k-}^{\dagger} (1 - n_{\downarrow}) d_{\uparrow} - \sum_k i e^{i\frac{\theta}{2}} \tilde{V}_k \alpha_{k1} c_{k-}^{\dagger} (1 - n_{\uparrow}) d_{\downarrow} \right) \\
&\quad \times \frac{1}{E - H_{00}} \left(\sum_{k'} \tilde{V}_{k'} \alpha_{k'1} e^{-i\frac{\theta'}{2}} c_{k'+}^{\dagger} (1 - n_{\downarrow}) d_{\uparrow} + \sum_{k'} e^{i\frac{\theta'}{2}} \tilde{V}_{k'} \alpha_{k'2} c_{k'+}^{\dagger} (1 - n_{\uparrow}) d_{\downarrow} \right)^{\dagger} \\
&+ \left(\sum_k i \tilde{V}_k \alpha_{k2} e^{-i\frac{\theta}{2}} c_{k-}^{\dagger} (1 - n_{\downarrow}) d_{\uparrow} - \sum_k i e^{i\frac{\theta}{2}} \tilde{V}_k \alpha_{k1} c_{k-}^{\dagger} (1 - n_{\uparrow}) d_{\downarrow} \right) \\
&\quad \times \frac{1}{E - H_{00}} \left(\sum_{k'} i \tilde{V}_{k'} \alpha_{k'2} e^{-i\frac{\theta'}{2}} c_{k'-}^{\dagger} (1 - n_{\downarrow}) d_{\uparrow} - \sum_{k'} i e^{i\frac{\theta'}{2}} \tilde{V}_{k'} \alpha_{k'1} c_{k'-}^{\dagger} (1 - n_{\uparrow}) d_{\downarrow} \right)^{\dagger}
\end{aligned} \tag{B.8}$$

We consider $\theta = \theta'$ $k = k'$ for now, potential scattering will be included later. From equations B.7 and B.8, we derive the following component of the effective Hamiltonian.

$$\begin{aligned}
H_{eff} &= H_{11} \\
&+ \sum_{kk'\zeta}^{\theta\theta'} M_{kk'\zeta}^{\theta\theta'} \left(e^{i\delta} \alpha_{k1} \alpha_{k'1} c_{k+}^\dagger d_{\uparrow} d_{\uparrow}^\dagger c_{k'+} + e^{-i\delta} \alpha_{k2} \alpha_{k'2} c_{k+}^\dagger d_{\downarrow} d_{\downarrow}^\dagger c_{k'+} \right. \\
&\quad \left. + e^{i\phi} \alpha_{k2} \alpha_{k'1} c_{k+}^\dagger d_{\downarrow} d_{\uparrow}^\dagger c_{k'+} + e^{-i\phi} \alpha_{k1} \alpha_{k'2} c_{k+}^\dagger d_{\uparrow} d_{\downarrow}^\dagger c_{k'+} \right) \\
&+ i \sum_{kk'\zeta}^{\theta\theta'} M_{kk'\zeta}^{\theta\theta'} \left(\alpha_{k1} \alpha_{k'1} e^{-i\phi} c_{k+}^\dagger d_{\uparrow} d_{\downarrow}^\dagger c_{k'-} - e^{-i\delta} \alpha_{k2} \alpha_{k'1} c_{k+}^\dagger d_{\uparrow} d_{\uparrow}^\dagger c_{k'-} \right. \\
&\quad \left. + e^{i\delta} \alpha_{k2} \alpha_{k'1} c_{k+}^\dagger d_{\downarrow} d_{\downarrow}^\dagger c_{k'-} - \alpha_{k2} \alpha_{k'2} e^{i\phi} c_{k+}^\dagger d_{\downarrow} d_{\uparrow}^\dagger c_{k'-} \right) \quad (B.9) \\
&- i \sum_{kk'\zeta}^{\theta\theta'} M_{kk'\zeta}^{\theta\theta'} \left(\alpha_{k1} \alpha_{k'1} e^{i\phi} c_{k-}^\dagger d_{\downarrow} d_{\uparrow}^\dagger c_{k'+} - e^{i\delta} \alpha_{k2} \alpha_{k'1} c_{k-}^\dagger d_{\uparrow} d_{\uparrow}^\dagger c_{k'+} \right. \\
&\quad \left. + e^{-i\delta} \alpha_{k1} \alpha_{k'2} c_{k-}^\dagger d_{\downarrow} d_{\downarrow}^\dagger c_{k'+} - e^{-i\phi} \alpha_{k2} \alpha_{k'2} c_{k-}^\dagger d_{\uparrow} d_{\downarrow}^\dagger c_{k'+} \right) \\
&+ \sum_{kk'\zeta}^{\theta\theta'} M_{kk'\zeta}^{\theta\theta'} \left(e^{i\delta} \alpha_{k1} \alpha_{k'1} c_{k-}^\dagger d_{\downarrow} d_{\downarrow}^\dagger c_{k'-} - e^{-i\phi} \alpha_{k2} \alpha_{k'1} c_{k-}^\dagger d_{\uparrow} d_{\downarrow}^\dagger c_{k'-} \right. \\
&\quad \left. - e^{i\phi} \alpha_{k1} \alpha_{k'2} c_{k-}^\dagger d_{\downarrow} d_{\uparrow}^\dagger c_{k'-} + e^{-i\delta} \alpha_{k2} \alpha_{k'2} c_{k-}^\dagger d_{\uparrow} d_{\uparrow}^\dagger c_{k'-} \right)
\end{aligned}$$

where in above $\delta = \frac{\theta}{2} - \frac{\theta'}{2}$ and $\phi = \frac{\theta}{2} + \frac{\theta'}{2}$. It can be seen in above equation B.9 $H_{eff} = H_{eff}^\dagger$ since the k, k' summations interchangeable. In equation B.9 the elements $M_{kk'\zeta}^{\theta\theta'} = \frac{\tilde{V}_k^\theta \tilde{V}_{k'}^{\theta'}}{-\epsilon_d + \epsilon_{k\zeta}} + \frac{\tilde{V}_k^\theta \tilde{V}_{k'}^{\theta'}}{U + \epsilon_d - \epsilon_{k\zeta}}$ and $\tilde{V}_k^\theta = \frac{V_k}{\sqrt{\beta \gamma k^3 \cos 3\theta}}$. we demonstrate how anisotropy arises in a Hermitian problem and its associated symmetry, leading to exceptional points. It's important to note that not all perturbative methods lead to exceptional points unless there are symmetries present even in the original model. In the current scenario, we have two crucial tuning parameters, denoted as k and θ , which significantly influence the local Hamiltonian properties. Additionally, the β parameter term plays a role similar to a magnetic field coupled system, such as $B * S_z$, except it is associated with dispersion in this particular problem.

Note that the edge contribution, which solely emerges in the cross-terms, particularly $\vec{s} \times \vec{S}_{kk'}$, does not contribute to $s_z S_{kk'}^z$. That is why the spin Hamiltonian in equation 6.17 show topological properties.

We simplify the above and use the Abrikosov representation[?] for spin for impurity as $s = \psi_d^\dagger \sigma \psi_d$ and $S_k = \psi_k^\dagger \sigma \psi_k$ for bath operators. In this representation, σ is the Pauli matrix, $\psi_d^\dagger = \begin{pmatrix} d_{\uparrow}^\dagger & d_{\downarrow}^\dagger \end{pmatrix}$ and $\psi_k^\dagger = \begin{pmatrix} c_{k\uparrow}^\dagger & c_{k'\downarrow}^\dagger \end{pmatrix}$.

Collecting all terms in equation B.9,

$$\begin{aligned}
H_{eff}^1 = & H_{11} + \\
& \sum_{kk'\zeta} M_{kk'\zeta}^{\theta\theta'} \left((\alpha_{k1}\alpha_{k'1}e^{i\delta} + e^{-i\delta}\alpha_{k2}\alpha_{k'2})s_z S_{kk'}^z \right. \\
& + (\alpha_{k1}\alpha_{k'1} + \alpha_{k2}\alpha_{k'2}) \left(e^{i\phi}s_- S_{kk'}^+ + e^{-i\phi}S_{kk'}^- s_+ \right) \\
& + \alpha_{k1}\alpha_{k'2} \underline{\underline{(e^{i\phi}s_- S_{kk'}^z + e^{-i\phi}S_{kk'}^z s_+)}} \\
& + i(\alpha_{k1}\alpha_{k'1} - \alpha_{k2}\alpha_{k'2}) \left(e^{i\phi}s_- S_{kk'}^+ - e^{-i\phi}S_{kk'}^- s_+ \right) \\
& \left. \underline{\underline{+ \alpha_{k1}\alpha_{k'2} \left(-ie^{i\delta}s_z S_{kk'}^- + ie^{-i\delta}S_{kk'}^+ s_z \right)}} \right)
\end{aligned} \tag{B.10}$$

A simplification in doubly underlined terms leads to anisotropic \mathcal{DM} -interaction. For symmetry properties, refer to the section III in the main article. Substituting $\alpha_{k1} = \sqrt{\Delta + \beta k^3 \cos 3\theta}$, $\alpha_{k'2} = \sqrt{\Delta - \beta(k')^3 \cos 3\theta'}$ and in limit $k \rightarrow k'$ we get simplifications as $\alpha_{k1}^2 + \alpha_{k2}^2 = \Delta$, where the $\Delta = \sqrt{\beta^2 k^6 \cos^2 3\theta + \lambda^2 k^2}$, $\alpha_1^2 - \alpha_2^2 = \beta k^3 \cos 3\theta$ and $\alpha_1 \alpha_2 = k\lambda$. This model is then rewritten in the form of anisotropic \mathcal{DM} interaction model as equation 6.11.

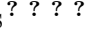
Analyzing the prefactors of $M_{kk'}^{\theta\theta'}$, which scale as $\frac{V_k}{\sqrt{\beta\gamma k^3 \cos 3\theta}} \frac{V_{k'}}{\sqrt{\beta\gamma(k')^3 \cos 3\theta'}}$, we can consider the scatterings by constructing a regular hexagon, as the $\cos 3\theta$ takes maximum values at the points of this hexagonal cell. For any given k point at band edges, these scatterings will be high-energy states and need to be integrated out. As we discussed in the main article, we proceed by constructing the new spinor as $\psi^\dagger = \left(c_{k\frac{2\pi}{3}+}^\dagger \quad c_{k\frac{\pi}{3}-}^\dagger \quad c_{k-\frac{2\pi}{3}+}^\dagger \quad c_{k-\frac{\pi}{3}-}^\dagger \right)$; in this basis, the Hamiltonian may be written in a more general form discussed in the next section.

B.2 Including the potential scattering

In the main article we discussed about the incorporated potential scattering terms, Here we expand model and detail how we can use the lie matrices algebra to compute RG equations. We can expand the above equation by expressing it in terms of magnitudes and operators in vector form, where the

spin operator components are denoted with a hat symbol.

$$\begin{aligned}
H_{eff}^1 = & H_0 + \sum_{kk'} J_0 \left(S_x \hat{\Sigma}_x + S_y \hat{\Sigma}_y + S_z \hat{\Sigma}_z \right) \\
& + i \sum_{kk'} |\vec{J}_{k^3}| (S_x \hat{\Sigma}_y - \hat{\Sigma}_x S_y) \\
& - \sum_{kk'} |\vec{g}_{1k^3}| (S_x \hat{\Omega}_y - \hat{\Omega}_x S_y) \\
& + \sum_{kk'} |\vec{g}_{2k^3}| (S_x \hat{\Gamma}_y - \hat{\Gamma}_x S_y) \\
& + i \sum_{kk'} |\vec{J}_k| \left((S_y \hat{\Sigma}_z - \hat{\Sigma}_y S_z) + (S_x \hat{\Sigma}_z - \hat{\Sigma}_x S_z) \right) \\
& - \sum_{kk'} |\vec{g}_{1k}| \left((S_y \hat{\Omega}_z - \hat{\Omega}_y S_z) + (S_x \hat{\Omega}_z - \hat{\Omega}_x S_z) \right) \\
& + i \sum_{kk'} |\vec{g}_{2k}| \left((S_y \hat{\Gamma}_z - \hat{\Gamma}_y S_z) + (S_x \hat{\Gamma}_z - \hat{\Gamma}_x S_z) \right)
\end{aligned} \tag{B.11}$$

We use the diagrams  with all permutations of vertices using the following algebra for third order perturbation theory,

$$\begin{aligned}
[\Sigma_a \Sigma_b, \Sigma_c] &= \Sigma_a [\Sigma_b, \Sigma_c] + [\Sigma_a, \Sigma_c] \Sigma_b = 0 \\
[\Sigma_a \Sigma_b, \Sigma_a] &= \Sigma_a [\Sigma_b, \Sigma_c] + [\Sigma_a, \Sigma_a] \Sigma_b = 8i \Sigma_b \\
[\Gamma_a \Gamma_b, \Gamma_a] &= \Gamma_a [\Gamma_b, \Gamma_c] + [\Gamma_a, \Gamma_a] \Gamma_b = 8i \Gamma_b \\
[\Omega_a \Omega_b, \Omega_a] &= \Omega_a [\Omega_b, \Omega_c] + [\Omega_a, \Omega_a] \Omega_b = 8i \Omega_b \\
[\Omega_a \Sigma_b, \Sigma_a] &= \Omega_a [\Sigma_b, \Sigma_c] + [\Omega_a, \Sigma_a] \Sigma_b = 8i \Sigma_b \\
[\Sigma_a \Omega_b, \Gamma_a] &= \Sigma_a [\Omega_b, \Gamma_c] + [\Sigma_a, \Gamma_a] \Omega_b = 8i \Upsilon
\end{aligned} \tag{B.12}$$

Where in above equation B.12 $\Sigma_i = \begin{pmatrix} \sigma_i & \sigma_i \\ \sigma_i & \sigma_i \end{pmatrix}$, $\Omega_i = \begin{pmatrix} \sigma_i & 0 \\ 0 & -\sigma_i \end{pmatrix}$, $\Gamma_i = \begin{pmatrix} \sigma_i & 0 \\ 0 & \sigma_i \end{pmatrix}$ and $\Upsilon = \begin{pmatrix} \mathcal{I}_{2 \times 2} & 0 \\ 0 & \mathcal{I}_{2 \times 2} \end{pmatrix}$ these conventions used earlier[?]. The subscript i refers a,b and c which are Pauli matrices. Using the algebra we derive RG equations as follows,

$$\begin{aligned}
\frac{dJ_0}{dl} &= J_0^2 + J_{k^3}^2 + J_k^2 + J_{k^3}J_k + J_k^2J_0 + J_{k^3}^2J_0 + J_0^3 \\
&\quad - J_{k^3}g_{2k} - J_{k^3}g_{2k^3} - J_kg_{2k} + g_{2k}^2J_{k^3} + g_{2k^3}^2J_k \\
&\quad - J_k^2g_{2k^3} \\
\frac{dJ_{k^3}}{dl} &= J_k^2 + J_0J_{k^3} + J_k^2J_{k^3} + J_0^2J_{k^3} + J_{k^3}^3 \\
\frac{dJ_k}{dl} &= J_0J_k + J_0^2J_k + J_kJ_{k^3}^2 + J_k^3 \\
\frac{dg_{1k^3}}{dl} &= g_{1k^3}^3 - g_{1k}^2g_{1k^3} \\
\frac{dg_{1k}}{dl} &= g_{1k}^3 - g_{1k^2}^2g_{1k} \\
\frac{dg_{2k^3}}{dl} &= -g_{2k^3}^3 + g_{1k^3}^2g_{2k^3} \\
\frac{dg_{2k}}{dl} &= -g_{2k}^3 + g_{1k}^2g_{2k}
\end{aligned} \tag{B.13}$$

From above, we identify various RG invariants as $\frac{g_{1k^3}}{g_{1k}} = m_1$, and we can notice that after adding the potential scattering terms, we still have the invariant $J_k^2 + J_k = mJ_{k^3}$ and $\frac{g_{2k}^2(g_{2k} + \sqrt{m_2})}{(g_{2k} - \sqrt{m_2})} = \frac{g_{2k^3}^2(g_{2k^3} + \sqrt{m_2/m_1})}{(g_{2k^3} - \sqrt{m_2/m_1})}$

B.3 Analytic Solution of RG Equations

A straightforward simplification of the equations 6.12 for J_{k^3} and J_k by eliminating J_0 yields the following expressions:

$$\begin{aligned}
\frac{dJ_{k^3}}{dl} - J_k^2 &= \frac{J_{k^3}}{J_k} \frac{dJ_k}{dl} \\
\frac{1}{J_{k^3}} \frac{dJ_{k^3}}{dl} - \frac{J_k^2}{J_{k^3}} &= \frac{1}{J_k} \frac{dJ_k}{dl}
\end{aligned} \tag{B.14}$$

By performing a substitution $\frac{J_k^2}{J_{k^3}} = x$, which results in $\frac{dx}{dl} = 2\frac{J_k}{J_{k^3}} \frac{dJ_k}{dl} - \frac{J_k^2}{J_{k^3}^2} \frac{dJ_{k^3}}{dl}$, and subsequently rearranging the equation, we obtain the solution $J_k = \frac{1}{2} \pm \frac{1}{2} \sqrt{1 + 4mJ_{k^3}}$. We can derive the complete solution by variable separation as follows:

$$\begin{aligned}
J_0 \frac{dJ_0}{dl} - J_0^3 &= n \\
\left(\frac{J_k^2 + J_k}{m} + J_k \frac{(J_k + 1)^2}{m^2} + J_k \right) \frac{dJ_k}{dl} &= n
\end{aligned} \tag{B.15}$$

The resulting solution will be in terms of two invariants, n and m . When we allow for complex solutions, we find that $J_k^* \rightarrow \frac{\sqrt{3}e^{i\frac{\pi}{3}}}{2}$, $J_{k^3}^* \rightarrow \frac{9e^{i\frac{\pi}{3}}}{16}$, and $m = e^{i\frac{\pi}{3}}$, with J_0^* having a \tan^{-1} quantity that vanishes for $J_0^* = \pm 1$ in both ferromagnetic and antiferromagnetic cases as $n \rightarrow 1$. Please see equations in B.16. Additionally, the logarithmic contribution to the scale vanishes when $J_0^* = -2$. These fixed points(complex) are obtained by incorporating the potential scattering terms.

$$\log \left(\frac{[m^2 + m(J_k - 1) + (J_k - 1)^2]^{3\gamma}}{J_k^{2\gamma}} \right) + \frac{(m - 2)}{\sqrt{3}(m^2 - m + 1)} \tan^{-1} \left(\frac{m + 2J_k - 2}{\sqrt{3}m} \right) = n \log D_{eff} \quad (\text{B.16})$$

Solving first equation in B.15 for J_0 as following,

$$\frac{\log(n^{2/3} + \sqrt[3]{n}(-J_0) + J_0^2) - 2 \log(\sqrt[3]{n} + J_0)}{6\sqrt[3]{n}} - \frac{-2\sqrt{3} \tan^{-1} \left(\frac{1 - \frac{2J_0}{\sqrt[3]{n}}}{\sqrt{3}} \right)}{6\sqrt[3]{n}} = \log D_{eff} \quad (\text{B.17})$$

In above equation $\gamma = \frac{-m}{6*(m^2-m+1)}$ and gamma diverges when $m = e^{\pm i\frac{\pi}{3}}$. As a result we expect complex fixed points and as exponent γ diverge.

A noteworthy similarity exists between the RG equations for a single impurity in edge states and that of two impurities having \mathcal{DM} interactions. To explore this connection, we address the two-impurity problem by simplifying the RG equations. We consider setting all couplings to zero, except for $J_0 \neq J_Y \neq K \neq 0$.

$$\begin{aligned} \frac{dJ_0}{dl} &= J_0^2 + J_Y J_0 + K J_0, \\ \frac{dJ_Y}{dl} &= J_Y^2 + J_0^2 + K^2, \\ \frac{dK}{dl} &= K^2 + K J_Y. \end{aligned} \quad (\text{B.18})$$

By solving the equations for J_0 and K , we obtain the solution $J_0 = \frac{RK}{K-1}$, where R is a constant or an invariant under renormalization. Using this solution, we proceed to solve for J_Y and K as follows:

$$J_Y \frac{dJ_Y}{dl} - J_Y^3 = R_1, \frac{dK}{dl} - K^2 = \frac{R_1}{\frac{R^2 K}{(1-K)^2} + K} \quad (\text{B.19})$$

Solution to the J_Y equation can be written as follows:

$$\frac{\sqrt[3]{R_1}(-J_Y) + J_Y^2 + R_1^{2/3}}{(J_Y + \sqrt[3]{R_1})^2} e^{2\sqrt{3} \tan^{-1} \left(\frac{\frac{2J_Y}{\sqrt[3]{R_1}} - 1}{\sqrt{3}} \right)} = D_{eff}^{6R_1^{\frac{1}{3}}} \quad (\text{B.20})$$

For K -equation has higher order nonlinearity so we have solutions in two limits,

$$\begin{aligned} & \frac{\left(\sqrt[3]{R_1}(-K) + K^2 + R_1^{2/3} \right)}{(K + \sqrt[3]{R_1})^2} e^{+2\sqrt{3} \tan^{-1} \left(\frac{\frac{2K}{\sqrt[3]{R_1}} - 1}{\sqrt{3}} \right)} \\ &= D_{eff}^{6\sqrt[3]{R_1}}, \text{ for } K \rightarrow \infty \\ & -\frac{R^2}{K-1} + R^2 \log(K-1) + \frac{1}{2}(K-1)^2 + K \\ & \quad \quad \quad R_1 \\ &= \log D_{eff}, \text{ for } K \rightarrow 0 \end{aligned} \quad (\text{B.21})$$

In a similar fashion, we will work on solving the J_0 equation with J_Y in order to separate the solutions. For $R = R_1 = 1.0$, we will illustrate the RG flow in figure B.1. We anticipate fixed points in different quadrants based on the sign chosen for these constants.

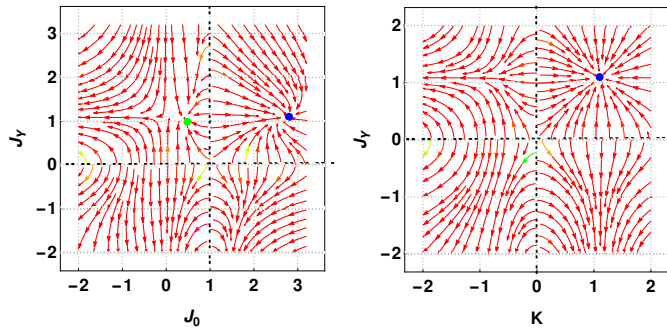


Figure B.1: RG flow of two impurity show the FP can be in different quadrants with $R_1 = -1$ and $R = 1.0$. We get around the SP($(J_Y = 1.0, J_0 = 3.0)$) existing SR regime in couplings.

B.4 RKKY Interaction

The RKKY interaction in the edge states can be expressed by expanding it in the Fourier series for the spins.

$$\begin{aligned}
J_Y(r_i - r_j) &\propto \sum_{kk'hh'} \frac{V_{ij}}{\epsilon_{kh} - \epsilon_{k'h'}} e^{ik(r_i - r_j)} V_{ij}^* e^{-ik'(r_i - r_j)} \\
&= \int_0^{2\pi} \int_0^\pi \int_0^{k_f} \frac{k^2 \sin\theta e^{ikR} dk d\theta d\phi}{\sqrt{k^6 \beta^2 \cos^2 3\theta + \lambda^2 k^2}} \\
&\quad + (k \neq k', h = h') \text{ terms}
\end{aligned} \tag{B.22}$$

We solve the above integral using the same method as in the impurity transport sections. We find that the leading contribution for J_Y can be expressed as the sum of special functions, given by $E_1(\epsilon) + E_2(\epsilon)$. With the substitution $\cos\theta = t$, we obtain the following expression. We don't set $\epsilon_k = \epsilon_{k'}$ as in the Poorman limit. Instead, we consider a chemical potential so that the integral does not diverge in this limit.

$$\begin{aligned}
J_Y &\propto \pi \int_k \frac{e^{ikR}}{k\beta} \oint \frac{q dt}{q^2 - (4t^3 - 3t)^2} \\
&\quad + \sum_{kk'} \frac{|V_{ij}|}{k^2 - (k')^2} e^{ikr} e^{-ik'r}, \\
\text{where } q &= \frac{\sqrt{(k^2 - \mu)^2 - k^2}}{\beta k^3}
\end{aligned} \tag{B.23}$$

The distinct contribution from the conventional flat band occurs when $q \neq 0$. Vanishing points for momentum or bandwidth occur at two limits: as $\beta \rightarrow \infty$ or $\frac{k}{\lambda} \rightarrow \frac{1}{2} \pm \frac{1}{2} \sqrt{1 + 4\frac{\mu}{\lambda^2}}$, with $\mu = -0.25$ as a critical value for RKKY. The second term is a standard component in various studies and can be expressed using Bessel functions[?] or elliptic functions[?]. The first term can be expressed as a sum of odd and even parts; all the odd terms can be represented using elliptic functions and the even terms are composed of transcendental functions.

B.5 Impurity Transport Calculation

We follow the $\mathcal{T}_{kk'}$ formalism for the effective Kondo model in equation 6.11 to compute the relaxation time as follows,

$$\frac{1}{\tau} \propto \left(1 - 2J\tilde{g}_\zeta - 2J_{k^3}\tilde{g}_{\zeta k^3} - 2J_k\tilde{g}_{\zeta k} \right) \tag{B.24}$$

Where the ζ correspond to chiral index and takes vales $\zeta = \pm$ for each bands in effective model bands.

$$\tilde{g}_\zeta = \int_0^{2\pi} \int_0^\pi \int_0^{k_f} \frac{k^2 \sin\theta dk d\theta d\phi}{k^2 + \zeta \sqrt{k^6 \beta^2 \cos^2 3\theta + \lambda^2 k^2} - \mu} \quad (\text{B.25})$$

where Solving the θ integral first, we get two pieces as follows,

$$\tilde{g}_\zeta = 2\pi \int_k k^2 \oint \frac{dt}{k^2 + \zeta \sqrt{k^6 \beta^2 (4t^3 - 3t)^2 + \lambda^2 k^2} - \mu} \quad (\text{B.26})$$

we rationalize the above integral and write as the following by introducing $q = \frac{\sqrt{(k^2 - \mu)^2 - \lambda^2 k^2}}{\beta k^3}$,

$$\begin{aligned} \tilde{g}_\zeta &= 2\pi \int_k \frac{1}{k} \oint \frac{q + \bar{\zeta} \sqrt{(4t^3 - 3t)^2 + \frac{\lambda^2}{\beta^2 k^4}}}{q^2 - (4t^3 - 3t)^2} dt \\ &= \int_k \frac{\pi}{kq} \left(\sum_{res} f(t, q) + \sum_{res} f(t, -q) \right) \end{aligned} \quad (\text{B.27})$$

For finding these residues, we will use the roots of the cubic equations $\beta(4t^3 - 3t) \pm q = 0$. We collect positive q roots and negative as follows for doing contour integrals,

$$t^\zeta = \begin{cases} \frac{1}{2} \left(\sqrt[3]{\sqrt{q^2 - 1}} + \zeta q + \frac{1}{\sqrt[3]{\sqrt{q^2 - 1} + \zeta q}} \right), \\ -\frac{1}{4} (1 - i\sqrt{3}) \sqrt[3]{\sqrt{q^2 - 1} + \zeta q} - \frac{1+i\sqrt{3}}{4 \sqrt[3]{\sqrt{q^2 - 1} + \zeta q}} \\ -\frac{1}{4} (1 + i\sqrt{3}) \sqrt[3]{\sqrt{q^2 - 1} + \zeta q} - \frac{1-i\sqrt{3}}{4 \sqrt[3]{\sqrt{q^2 - 1} + \zeta q}} \end{cases} \quad (\text{B.28})$$

Where in above we have $\zeta = \pm$, Similarly, the other contributions are as follows,

$$\begin{aligned} \tilde{g}_{\zeta k^3} &= 2\pi\beta \int_k k^2 \oint \frac{((4t^3 - 3t)^2)(q + \bar{\zeta}r)}{q^2 - (4t^3 - 3t)^2} dt \\ \tilde{g}_{\zeta k} &= \int_k \oint \frac{(q + \bar{\zeta}r)}{q^2 - (4t^3 - 3t)^2} dt \\ \text{where } r &= \sqrt{(4t^3 - 3t)^2 + \frac{\lambda^2}{\beta^2 k^4}} \end{aligned} \quad (\text{B.29})$$

after summing over the $\zeta = \pm$ bands we get following simplifications,

$$\begin{aligned}\tilde{g} &= 2\pi \int_k \frac{1}{k} \oint \frac{q dt}{q^2 - (4t^3 - 3t)^2} \\ \tilde{g}_{k^3} &= 2\pi\beta \int_k k^2 \oint \frac{(4t^3 - 3t)^2 q dt}{q^2 - (4t^3 - 3t)^2} \\ \tilde{g}_k &= \int_k \oint \frac{q dt}{q^2 - (4t^3 - 3t)^2}\end{aligned}\tag{B.30}$$

After contour integrals each contributes as $\oint \frac{q dt}{q^2 - (4t^3 - 3t)^2} = q$ hence sum of all g_ζ contribution as following,

$$\tilde{g}_\mu = \int (\beta q k^2 - \beta q^4 k + \frac{q}{k} - q) dk \tag{B.31}$$

We set $\epsilon \approx k^2$ and the density of states in 3D as $\rho(\epsilon) \approx \sqrt{\epsilon}$ then above integral yields,

$$\begin{aligned}\tilde{g}_\mu &= \int \left(\frac{\sqrt{(\epsilon - \mu)^2 - \lambda^2 \epsilon}}{\sqrt{\epsilon}} - \frac{((\epsilon - \mu)^2 - \lambda^2 \epsilon)^2}{\beta^3 \epsilon^{6-\frac{1}{2}}} \right. \\ &\quad \left. + \frac{\sqrt{(\epsilon - \mu)^2 - \lambda^2 \epsilon}}{\beta \epsilon^2} - \frac{\sqrt{(\epsilon - \mu)^2 - \lambda^2 \epsilon}}{\beta \epsilon^{\frac{3}{2}}} \right) d\epsilon\end{aligned}\tag{B.32}$$

Where in above μ is the chemical potential can take any values around Fermi energy. We perform this above integral exactly in terms of special functions to extract contribution to $\frac{1}{\tau}$, which indeed scales with RG invariant in the

elliptic functions.

$$\begin{aligned}
\tilde{g}_\epsilon &\propto \frac{P_1(\epsilon) + P_{\frac{3}{2}}(\epsilon) + T_1(\epsilon) + E_1(\epsilon) + E_2(\epsilon) + \log(\epsilon)}{\beta^3} \\
P_1(\epsilon) &= -\frac{3\mu^4 - 16\mu^3\epsilon + 4\mu^2\epsilon(9\epsilon - 2) + 2\epsilon^2\mathcal{K}(\epsilon)}{12\epsilon^4} \\
\mathcal{K} &= \left(2\epsilon \left(\beta^2 \sqrt{(\mu - \epsilon)^2 - \epsilon} (2\sqrt{\epsilon}(\beta - \beta\epsilon + 3) + 3) - 6\right) + 3\right) \\
P_{\frac{3}{2}}(\epsilon) &= \frac{8\mu\epsilon^2 \left(2\beta^3\epsilon^{3/2} \sqrt{(\mu - \epsilon)^2 - \epsilon} - 6\epsilon + 3\right)}{12\epsilon^4} \\
T_1(\epsilon) &= \beta^2 \tanh^{-1} \left(\frac{-2\mu + 2\epsilon - 1}{2\sqrt{(\mu - \epsilon)^2 - \epsilon}} \right) + \frac{(2\mu + 1)\beta^2 \coth^{-1} \left(\frac{2\mu\sqrt{(\mu - \epsilon)^2 - \epsilon}}{2\mu(\mu - \epsilon) - \epsilon} \right)}{2\mu} \\
E_1(\epsilon) &= \frac{i\beta^2\epsilon \sqrt{\frac{-2\mu + \sqrt{4\mu + 1} + 2\epsilon - 1}{\epsilon}} \sqrt{-\frac{2\mu + \sqrt{4\mu + 1} - 2\epsilon + 1}{\epsilon}} \Gamma(\epsilon)}{3\sqrt{2}\sqrt{-2\mu - \sqrt{4\mu + 1} - 1}\sqrt{(\mu - \epsilon)^2 - \epsilon}} \\
\Gamma(\epsilon) &= \left(AE \left(i \sinh^{-1} \left(\frac{\sqrt{-2\mu - \sqrt{4\mu + 1} - 1}}{\sqrt{2}\sqrt{\epsilon}} \right) \middle| \frac{2\mu - \sqrt{4\mu + 1} + 1}{2\mu + \sqrt{4\mu + 1} + 1} \right) \right) \\
A &= \left(2\mu + \sqrt{4\mu + 1} + 1 \right) (2\mu\beta + \beta + 6) \\
E_2(\epsilon) &= -\frac{B \left((\sqrt{4\mu + 1} + 2\mu(\sqrt{4\mu + 1} + 2) + 1) \beta + 6\sqrt{4\mu + 1} \right) \mathcal{Z}(\epsilon)}{3\sqrt{2}\sqrt{-2\mu - \sqrt{4\mu + 1} - 1}\sqrt{(\mu - \epsilon)^2 - \epsilon}} \\
\mathcal{Z}(\epsilon) &= F \left(i \sinh^{-1} \left(\frac{\sqrt{-2\mu - \sqrt{4\mu + 1} - 1}}{\sqrt{2}\sqrt{\epsilon}} \right) \middle| \frac{2\mu - \sqrt{4\mu + 1} + 1}{2\mu + \sqrt{4\mu + 1} + 1} \right) \\
B &= i\beta^2\epsilon \sqrt{\frac{-2\mu + \sqrt{4\mu + 1} + 2\epsilon - 1}{\epsilon}} \sqrt{-\frac{2\mu + \sqrt{4\mu + 1} - 2\epsilon + 1}{\epsilon}}
\end{aligned} \tag{B.33}$$

In the above solution, F is an incomplete elliptic function of the first kind, and E is an elliptic function of the second kind. P and T are polynomial and transcendental functions, respectively.

Appendix C

Derivation Of Effective Model From Lindbladian

C.1 Appendix-Development of a non-Hermitian Hamiltonian

In order to incorporate dissipation in a conventional Hermitian model, one can start with the quantum master equation¹⁻³, thereby arriving at an effective model in terms of a Lindbladian which is non-Hermitian. For spin-Hamiltonians, the Lindbladians have been constructed by Prosen and others^{4;5}. For a Hermitian Kondo model, Kawakami and co-workers⁶ utilized a similar Lindbladian approach to justify a non-Hermitian Kondo model. Lindbladians for the dissipative Bose-Hubbard model have also been considered⁷. A unique gauge transformed hamiltonian⁸ also gives rise to a \mathcal{PT} -symmetric, non-Hermitian 1-d Hubbard model.

The quantum master equation is given by the following:

$$\frac{d\tilde{\rho}}{dt} = -i[H, \tilde{\rho}] + \sum_{\sigma\sigma'} \left[\mathcal{L}_{\sigma} \tilde{\rho} \mathcal{L}_{\sigma'}^{\dagger} - \frac{1}{2} \{ \mathcal{L}_{\sigma}^{\dagger} \mathcal{L}_{\sigma'}, \tilde{\rho} \} \right] \quad (\text{C.1})$$

where \mathcal{L}_{σ} is the \mathcal{PT} -symmetric Lindbladian obeying⁹,

$$\mathcal{PT}(\mathcal{L}_{\sigma}) \rightarrow \bar{\sigma} \mathcal{L}_{\sigma} \quad (\text{C.2})$$

and $\tilde{\rho} = \mathcal{PT}|\psi\rangle\langle\psi|$ is the \mathcal{PT} -symmetric non-Hermitian density matrix. The above master equation can also be written in terms of diagonal generators of dynamical quantum groups by a unitary transformation which is discussed in the quantum master equation approach to many body systems¹⁰. The last term in eq C.1 is the recycling term, which can be absorbed in the unitary

part of the single particle effective evolution¹¹, using an effective Hamiltonian as

$$\frac{d\tilde{\rho}}{dt} = -i[H_{eff}, \tilde{\rho}] + \sum_{\sigma\sigma'} \mathcal{L}_{\sigma}^{\dagger} \tilde{\rho} \mathcal{L}_{\sigma'}, \quad (\text{C.3})$$

where the effective Hamiltonian is given by

$$H_{eff} = H + \frac{i}{2} \sum_{\sigma\sigma'} \mathcal{L}_{\sigma}^{\dagger} \mathcal{L}_{\sigma'}, \quad (\text{C.4})$$

and eq C.3 obeys \mathcal{PT} -symmetric Liouvillian dynamics as $\frac{d\tilde{\rho}}{dt} = \hat{\mathcal{L}}\tilde{\rho}$ as shown in Ref.⁵, in terms of an effective Hamiltonian given by equation C.4¹. In the next subsection, we present a possible way of deriving a non-Hermitian Hamiltonian through this formalism.

C.2 Lindbladian Derivation

The construction of the Lindbladian is based on the angular quantum number $j_m = m \pm \frac{1}{2}$. For simplifying notation, we drop the k (momentum) index for now, but one can also define a local operator by summing over the momentum $c_{0m\sigma} = \sum_k V_k c_{km\sigma}$. The Lindbladians below are in the (m, σ) basis, but they can be written equally in the (j_m, σ) basis. For these local Lindbladians, we can use the angular momentum expansion $\mathcal{L}_{\sigma} = \frac{1}{\sqrt{2\pi}} \sum_{m=-\infty}^{\infty} \mathcal{L}_{m\sigma} \exp(-im\theta)$, and so:

$$\begin{aligned} \mathcal{L}_{\sigma}^{\dagger} \mathcal{L}_{\sigma'} &= \frac{1}{2\pi} \sum_{m=-\infty}^{\infty} \mathcal{L}_{m\sigma}^{\dagger} \exp(im\theta) \sum_{m'=-\infty}^{\infty} \mathcal{L}_{m'\sigma'} \exp(-im'\theta) \\ &= \frac{1}{2\pi} \sum_{m, m'=0, \pm 1} e^{-i(m'-m)\theta} \mathcal{L}_{m\sigma}^{\dagger} \mathcal{L}_{m'\sigma'} + \text{higher } m... \\ &= \frac{1}{2\pi} \left(\mathcal{L}_{0\sigma}^{\dagger} \mathcal{L}_{0\sigma'} + e^{-i2\theta} \mathcal{L}_{1\sigma}^{\dagger} \mathcal{L}_{-1\sigma'} + e^{i2\theta} \mathcal{L}_{-1\sigma}^{\dagger} \mathcal{L}_{1\sigma'} \right. \\ &\quad + \mathcal{L}_{-1\sigma}^{\dagger} \mathcal{L}_{-1\sigma'} + \mathcal{L}_{1\sigma}^{\dagger} \mathcal{L}_{1\sigma'} + e^{-i\theta} \mathcal{L}_{0\sigma}^{\dagger} \mathcal{L}_{1\sigma'} \\ &\quad \left. + e^{i\theta} \mathcal{L}_{1\sigma}^{\dagger} \mathcal{L}_{0\sigma'} + e^{i\theta} \mathcal{L}_{-1\sigma}^{\dagger} \mathcal{L}_{0\sigma'} + e^{-i\theta} \mathcal{L}_{0\sigma}^{\dagger} \mathcal{L}_{-1\sigma'} \dots \right) \end{aligned} \quad (\text{C.5})$$

From the above, we can see multiplicative phase factors for $m \neq m'$, and it is enough to proceed with retaining only the operator structures. However, one can also start with generic expansion C.5 and start eliminating interactions that do not preserve the global number to get gain-loss terms.

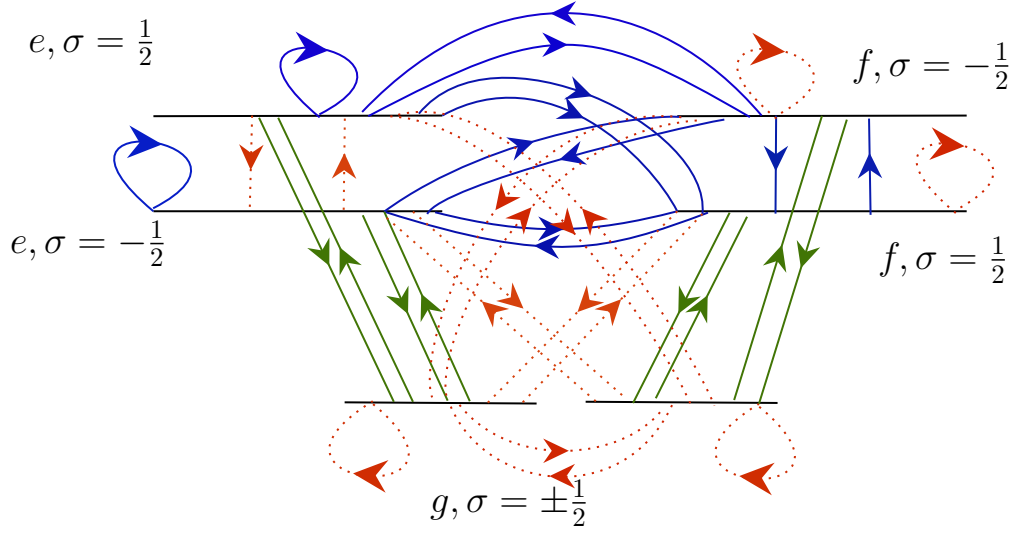
We choose Lindbladian for ground state and excited states as $\mathcal{L}_{g\sigma} = |m = 0, \sigma\rangle_k + |m = \pm 1, \sigma\rangle_k + |0, \sigma\rangle_d$, $\mathcal{L}_{e\sigma} = |m = 0, \sigma\rangle$, or $|m = \pm 1, \bar{\sigma}\rangle$, $\mathcal{L}_{f\downarrow} = |m = 0, \downarrow\rangle$ and $\mathcal{L}_{f\uparrow} = |m = -1, \uparrow\rangle$. Here k is the bath index, and d represents impurity states. This choice is based on the low-energy physical picture of the Anderson model, where the ground state can be composed of the bath and dot states. Excited states are only bath states with lifted degeneracy due to spin-orbit interaction. Also, all Lindbladians satisfy symmetry operations $\mathcal{PT}\mathcal{L}_{m\uparrow} \rightarrow -\mathcal{L}_{m\downarrow}$, and we consider only single fermion states. To incorporate dissipation with varying number scenarios with essential inclusion of the excited states and out of them, only certain kinds of electron scattering to these states will be gain-loss balancing. There is definitely an ambiguity in choosing these states, but we can derive various Hamiltonians and show that gauge transformation connects these various choices.

$$\begin{aligned}
\mathcal{L}_{g\uparrow} &= c_{\frac{1}{2}\uparrow} + c_{-\frac{1}{2}\uparrow} + d_{\uparrow} \\
\mathcal{L}_{g\downarrow} &= -c_{\frac{1}{2}\downarrow} - c_{-\frac{1}{2}\downarrow} - d_{\downarrow} \\
\mathcal{L}_{e\uparrow} &= c_{\frac{1}{2}\uparrow} \\
\mathcal{L}_{e\downarrow} &= -c_{\frac{1}{2}\downarrow} \\
\mathcal{L}_{f\uparrow} &= c_{-\frac{1}{2}\uparrow} \\
\mathcal{L}_{f\downarrow} &= -c_{-\frac{1}{2}\downarrow}
\end{aligned} \tag{C.6}$$

We rewrite the sum in equation C.5 as $\mathcal{L}_{\sigma}^{\dagger}\mathcal{L}_{\sigma'} = \sum_{m,m'=g,e,f} \mathcal{L}_{m\sigma}^{\dagger}\mathcal{L}_{m'\sigma'}$. A similar convention has also been used in the supplementary information of Nakagawa et al⁶ for two body losses. This deviates from earlier approaches⁸ like forward and backward hopping having opposite phases of each other with finite real parts in 1D tight-binding models.

The above Lindbladians C.6 give a total of 36 terms (which can be identified in C.5; each of the 9 terms will have implicit 4 terms with $\sigma = \pm\frac{1}{2}$, $\sigma' = \pm\frac{1}{2}$) which are represented below pictorially. We can see several ways to derive minimal terms that preserve symmetry. We also verified, in general, that there is a possibility to derive \mathcal{PT} -symmetric representations if we find coefficients those commute with the total number operator (at a single particle level). Here we see it is not easy due to the angular momentum and spin indices, but this method works nicely when only the spin index is present.

$$\begin{aligned}
\text{Green lines} &= \mathcal{L}_{e\uparrow}^\dagger \mathcal{L}_{g\uparrow} + \mathcal{L}_{f\downarrow}^\dagger \mathcal{L}_{g\uparrow} + \mathcal{L}_{e\downarrow}^\dagger \mathcal{L}_{g\downarrow} + \mathcal{L}_{f\uparrow}^\dagger \mathcal{L}_{g\downarrow} + \mathcal{L}_{g\uparrow}^\dagger \mathcal{L}_{e\uparrow} + \mathcal{L}_{g\uparrow}^\dagger \mathcal{L}_{f\downarrow} \\
&\quad + \mathcal{L}_{g\downarrow}^\dagger \mathcal{L}_{f\uparrow} + \mathcal{L}_{g\downarrow}^\dagger \mathcal{L}_{e\downarrow} \\
\text{Blue lines} &= -2\mathcal{L}_{e\uparrow}^\dagger \mathcal{L}_{e\uparrow} - \mathcal{L}_{f\uparrow}^\dagger \mathcal{L}_{e\uparrow} - \mathcal{L}_{f\downarrow}^\dagger \mathcal{L}_{e\uparrow} - 2\mathcal{L}_{e\downarrow}^\dagger \mathcal{L}_{e\downarrow} - \mathcal{L}_{f\uparrow}^\dagger \mathcal{L}_{e\downarrow} - \mathcal{L}_{f\downarrow}^\dagger \mathcal{L}_{e\downarrow} \\
&\quad - \mathcal{L}_{e\uparrow}^\dagger \mathcal{L}_{f\uparrow} - \mathcal{L}_{e\downarrow}^\dagger \mathcal{L}_{f\uparrow} - 2\mathcal{L}_{f\downarrow}^\dagger \mathcal{L}_{f\uparrow} - \mathcal{L}_{e\uparrow}^\dagger \mathcal{L}_{f\downarrow} - \mathcal{L}_{e\downarrow}^\dagger \mathcal{L}_{f\downarrow} - 2\mathcal{L}_{f\uparrow}^\dagger \mathcal{L}_{f\downarrow} \\
&\quad \quad \quad (C.7)
\end{aligned}$$



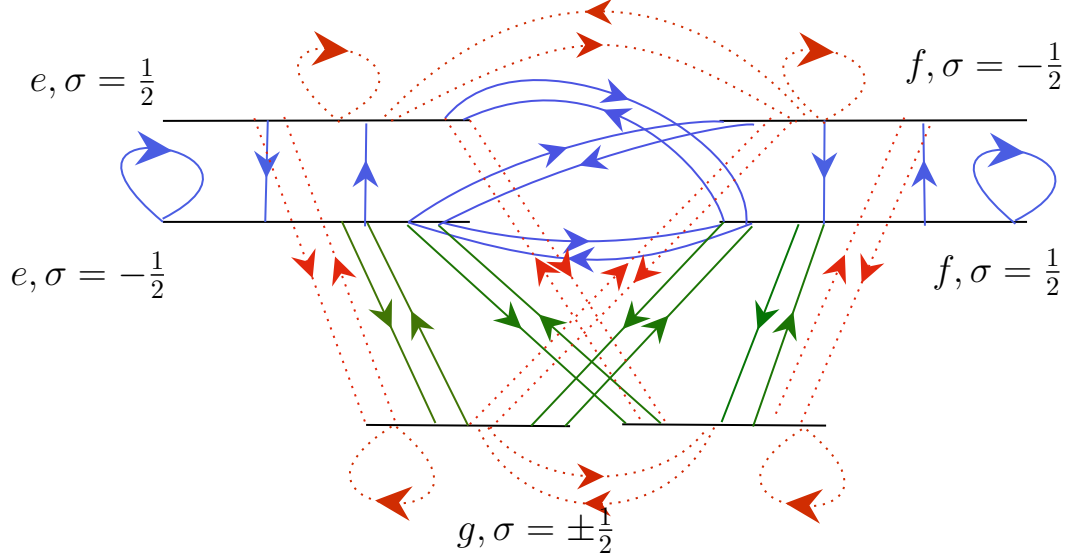
Scatterings in I method

This choice of interactions also yields us the only hybridization terms we considered in our model.

$$\begin{aligned}
&d_{\uparrow\frac{1}{2}}^\dagger c_{\frac{1}{2}\uparrow} + d_{\downarrow\frac{1}{2}}^\dagger c_{\frac{1}{2}\downarrow} - d_{\downarrow\frac{1}{2}}^\dagger c_{-\frac{1}{2}\uparrow} - d_{\uparrow\frac{1}{2}}^\dagger c_{-\frac{1}{2}\downarrow} \\
&+ c_{\frac{1}{2}\uparrow}^\dagger d_{\uparrow} + c_{\frac{1}{2}\downarrow}^\dagger d_{\downarrow} - c_{-\frac{1}{2}\uparrow}^\dagger d_{\downarrow} - c_{-\frac{1}{2}\downarrow}^\dagger d_{\uparrow}
\end{aligned} \tag{C.8}$$

$$\begin{aligned}
\text{Green lines} &= \mathcal{L}_{e\uparrow}^\dagger \mathcal{L}_{g\downarrow} + \mathcal{L}_{g\downarrow}^\dagger \mathcal{L}_{e\uparrow} + \mathcal{L}_{f\downarrow}^\dagger \mathcal{L}_{g\downarrow} \\
&\quad + \mathcal{L}_{g\downarrow}^\dagger \mathcal{L}_{f\downarrow} + \mathcal{L}_{e\uparrow}^\dagger \mathcal{L}_{g\uparrow} + \mathcal{L}_{g\uparrow}^\dagger \mathcal{L}_{e\uparrow} \\
&\quad + \mathcal{L}_{f\downarrow}^\dagger \mathcal{L}_{g\uparrow} + \mathcal{L}_{g\uparrow}^\dagger \mathcal{L}_{f\downarrow} \\
\text{Blue lines} &= -\mathcal{L}_{e\uparrow}^\dagger \mathcal{L}_{e\downarrow} - \mathcal{L}_{e\downarrow}^\dagger \mathcal{L}_{e\uparrow} - \mathcal{L}_{f\downarrow}^\dagger \mathcal{L}_{e\downarrow} \\
&\quad - \mathcal{L}_{e\downarrow}^\dagger \mathcal{L}_{f\downarrow} - 2\mathcal{L}_{f\downarrow}^\dagger \mathcal{L}_{e\uparrow} - 2\mathcal{L}_{e\uparrow}^\dagger \mathcal{L}_{f\downarrow} \\
&\quad - \mathcal{L}_{f\uparrow}^\dagger \mathcal{L}_{e\uparrow} - \mathcal{L}_{e\uparrow}^\dagger \mathcal{L}_{f\uparrow} - 2\mathcal{L}_{e\uparrow}^\dagger \mathcal{L}_{e\uparrow} \\
&\quad - \mathcal{L}_{f\uparrow}^\dagger \mathcal{L}_{f\downarrow} - \mathcal{L}_{f\downarrow}^\dagger \mathcal{L}_{f\uparrow} - 2\mathcal{L}_{f\downarrow}^\dagger \mathcal{L}_{f\downarrow}
\end{aligned} \tag{C.9}$$

The above Lindbladian construction may be seen graphically as the following,



Scatterings in II method

The above preserves the total number in Kondo-relevant angular momentum channels since we find the coefficients by calculating the commutators as $[(\text{Green lines} + \text{Blue lines})_{no-flip}, (n_{j_m\sigma} + n_{d\sigma})] = 0$ and since the flip terms are odd under parity, their coefficients are evaluated as $\{(\text{Green lines} + \text{Blue lines})_{flip}, (n_{j_m\sigma} + n_{d\sigma})\} = 0$. All blue lines correspond to the negative sign scattering terms, and green corresponds to positive scattering terms. Red dots are the terms left out because we preserve number in $j_m = \pm \frac{1}{2}$. On the dot, dissipation is absent. Hence we did not consider the onsite dissipation for the dot operators and non-flip terms, which will introduce non-Hermitian spin-orbit interaction on the dot, which is out of the scope of the current work. These terms may arise in controlled dissipation, and these signs by this way of calculation also tell us about even and odd under parity, which also ensures commutation with the metric operator.

$$\begin{aligned} \text{Green lines} + \text{Blue lines} = & -d^\dagger_{\uparrow} c_{-\frac{1}{2}\downarrow} + d^\dagger_{\uparrow} c_{-\frac{1}{2}\downarrow} + d^\dagger_{\uparrow} c_{\frac{1}{2}\uparrow} - d^\dagger_{\downarrow} c_{\frac{1}{2}\uparrow} \\ & -c^\dagger_{-\frac{1}{2}\downarrow} d_{\uparrow} + c^\dagger_{-\frac{1}{2}\downarrow} d_{\downarrow} + c^\dagger_{\frac{1}{2}\uparrow} d_{\uparrow} - c^\dagger_{\frac{1}{2}\uparrow} d_{\downarrow} \end{aligned} \quad (\text{C.10})$$

Following a slightly laborious but straightforward calculation of commutators and anticommutators, this hybridization can be written as the following: multiplying a prefactor as $(iV + \omega)$ to get the following terms. We also bring

back the k-index for bath operators and coefficients.

$$\begin{aligned}
H^{hyb} &= \sum_k V_k (c_{k\frac{1}{2}\uparrow}^\dagger d_\uparrow + c_{k-\frac{1}{2}\downarrow}^\dagger d_\downarrow + h.c) \\
\frac{i}{2} \sum_{\sigma\sigma'} \mathcal{L}_\sigma^\dagger \mathcal{L}_{\sigma'} &= \sum_k \left(-\frac{V_k}{2} + \frac{i}{2} \omega_k \right) \left(c_{k\frac{1}{2}\uparrow}^\dagger d_\uparrow + c_{k-\frac{1}{2}\downarrow}^\dagger d_\downarrow - c_{k\frac{1}{2}\uparrow}^\dagger d_\downarrow - c_{k-\frac{1}{2}\downarrow}^\dagger d_\uparrow + h.c \right) \\
&\implies H^{hyb} + \frac{i}{2} \sum_{\sigma\sigma'} \mathcal{L}_\sigma^\dagger \mathcal{L}_{\sigma'} = H_{\text{flip}}^{\text{hyb}} + H_{\text{nflip}}^{\text{hyb}}
\end{aligned} \tag{C.11}$$

Out of the two possibilities C.8 and C.10, although we have chosen the first one in this work on the lines of the real space non-Hermitian Anderson model¹², nevertheless, we have considered both these hybridization terms below, which are \mathcal{PT} -symmetric and also yield the same eigenvalues.

I Method

$$\begin{aligned}
H_{nflip}^{hyb} &= \sum_k X_k \left(c_{k,+\frac{1}{2}\uparrow}^\dagger d_\uparrow + c_{k,\frac{1}{2}\downarrow}^\dagger d_\downarrow + h.c \right) \\
H_{flip}^{hyb} &= - \sum_k X_k^* \left(c_{k,-\frac{1}{2}\uparrow}^\dagger d_\downarrow + c_{k,-\frac{1}{2}\downarrow}^\dagger d_\uparrow + h.c \right)
\end{aligned} \tag{C.12}$$

II method

$$\begin{aligned}
H_{nflip}^{hyb} &= \sum_k X_k \left(c_{k,+\frac{1}{2}\uparrow}^\dagger d_\uparrow + c_{k,-\frac{1}{2}\downarrow}^\dagger d_\downarrow + h.c \right) \\
H_{flip}^{hyb} &= \sum_k X_k^* \left(c_{k,\frac{1}{2}\uparrow}^\dagger d_\downarrow + c_{k,-\frac{1}{2}\downarrow}^\dagger d_\uparrow + h.c \right)
\end{aligned} \tag{C.13}$$

So, we can see that the **method-I** compares well with Lourenco et al¹², while **method-II** is indeed consistent with the work of Zarea et al¹³. However, the additional terms brought through Lindbladian dynamics are to explore the interplay between dissipation and parity-breaking interactions. Only in bath this parity breaking can be verified with commutation of only bath S_z operator $[(n_{\pm\frac{1}{2}\uparrow} - n_{\pm\frac{1}{2}\downarrow}), H_{nflip}^{hyb} + H_{flip}^{hyb}] \neq 0$. This condition is satisfied by both hybridization terms, and they yield the same eigenvalues since there is no angular momentum-dependent coefficient for hybridization. However, from **I method**, it is convenient to find simpler metric operators (no-phase attached to d operators in eigenvector) to map to the non-Hermitian studied version of the model and to compare the results. Here we show from the

following gauge choices that the C.12 and C.11 are equivalent:

$$\begin{aligned}
&\text{for no-flip : } c_{k\frac{1}{2}\uparrow} = e^{i\theta} c_{kL\uparrow} \\
&\quad c_{k-\frac{1}{2}\downarrow} = e^{-i\theta} c_{kL\downarrow} \\
&\text{for flip : } c_{k\frac{1}{2}\uparrow} = -e^{-i\theta} c_{kR\uparrow} \\
&\quad c_{k-\frac{1}{2}\downarrow} = -e^{i\theta} c_{kR\downarrow}
\end{aligned} \tag{C.14}$$

From this choice, we get the following unitary which shows that both the hybridization terms yield equivalent models which we used for various calculations.

$$\begin{aligned}
\mathcal{U} &= \frac{1}{\sqrt{2}} \begin{pmatrix} e^{-i\theta} & e^{i\theta} \\ e^{-i\theta} & -e^{i\theta} \end{pmatrix} \\
\mathcal{U} \begin{pmatrix} d_{\uparrow} \\ d_{\downarrow} \end{pmatrix} &= \begin{pmatrix} d_{+} \\ d_{-} \end{pmatrix}
\end{aligned} \tag{C.15}$$

Thus, the full non-Hermitian Hamiltonian in the angular momentum basis then becomes

$$H_{\text{SIAM}}^{\text{NH}} = H_0 + H_{\text{flip}}^{\text{hyb}} + H_{\text{nflip}}^{\text{hyb}} + H_{\text{RSO}} + H_d. \tag{C.16}$$

Equation 2.6 is off-diagonal in the 'm' basis, but a simple transformation to the total angular momentum basis, namely $j_m = m + \sigma$ gives the following:

$$H_{\text{RSO}} = \lambda \sum_{kj_m} \left(c_{kj_m\uparrow}^{\dagger} c_{kj_m\downarrow} + \text{h.c.} \right) \tag{C.17}$$

which is diagonal in the j_m basis. The kinetic energy term and the hybridization terms may also be rewritten in the same way, and we get the following:

$$H_0 = \sum_{kj_m\sigma} \tilde{\epsilon}_k c_{kj_m\sigma}^{\dagger} c_{kj_m\sigma} \tag{C.18}$$

$$H_{\text{nflip}}^{\text{hyb}} = \sum_k X_k \left(c_{k,+\frac{1}{2}\uparrow}^{\dagger} d_{\uparrow} + c_{k,\frac{1}{2}\downarrow}^{\dagger} d_{\downarrow} + \text{h.c.} \right) \tag{C.19}$$

$$H_{\text{flip}}^{\text{hyb}} = - \sum_k X_k^* \left(c_{k,-\frac{1}{2}\uparrow}^{\dagger} d_{\downarrow} + c_{k,-\frac{1}{2}\downarrow}^{\dagger} d_{\uparrow} + \text{h.c.} \right) \tag{C.20}$$

where $X_k = (V_k + i\omega_k)/2\sqrt{k}$. Note that the Lindbladian formalism allows us to choose coefficients of the hybridization in a specific way, that maintains the \mathcal{PT} -symmetry of the Hamiltonian. The RSOC term (equation C.17)

is off-diagonal in the spin-index, so we can combine it with equation C.18 through a unitary rotation of the σ_z basis into a ‘chiral’ basis, namely,

$$c_{kjmh} = \frac{1}{\sqrt{2}}(c_{kj\uparrow} + hc_{kj\downarrow}) \quad (\text{C.21})$$

where $h = \pm$, to a form that is diagonal in the chiral quantum number (h). So, we get

$$H_0 + H_{\text{RSO}} = \sum_{kjmh} \tilde{\epsilon}_{kh} c_{kjmh}^\dagger c_{kjmh} \quad (\text{C.22})$$

where $\tilde{\epsilon}_{kh} = \tilde{\epsilon}_k + h\lambda$. The coupling of only the $m = 0$ lead states in hybridization follows in a straightforward way by combining the Fourier transform, and the angular momentum expansion, and is a consequence of the dot states being independent of k ¹³. In this rotated basis ($j_m\sigma \rightarrow j_mh$), and with the identification of $j_m = \pm 1/2$ as the left (L) and right (R) channels respectively, the model may be interpreted as a system with one interacting quantum dot hybridizing with two conduction electron baths. The full Hamiltonian written below reflects such an interpretation.

$$\begin{aligned} H = & \sum_{kh\eta} \tilde{\epsilon}_{kh} c_{kh\eta}^\dagger c_{kh\eta} \\ & + \sum_k X_k \left[\left(c_{kL+}^\dagger + c_{kL-}^\dagger \right) d_\uparrow + \left(c_{kL+}^\dagger - c_{kL-}^\dagger \right) d_\downarrow + \text{h.c.} \right] \\ & - \sum_k X_k^* \left[\left(c_{kR+}^\dagger + c_{kR-}^\dagger \right) d_\downarrow + \left(c_{kR+}^\dagger - c_{kR-}^\dagger \right) d_\uparrow + \text{h.c.} \right] \\ & + \sum_\sigma \epsilon_d n_{d\sigma} + U n_{d\uparrow} n_{d\downarrow} \end{aligned} \quad (\text{C.23})$$

where $\eta = L, R$ is the channel index. Defining a rotation of the spin basis on the dot $(d_+ \ d_-)^T = U (d_\uparrow \ d_\downarrow)^T$, where the unitary rotation is given by $U = (\sigma_z + \sigma_x)/\sqrt{2}$, the model Hamiltonian may be condensed into a form that appears very similar to a conventional Anderson impurity model connected to two baths, namely:

$$\begin{aligned} H = & \sum_{kh\eta} \tilde{\epsilon}_{kh} c_{kh\eta}^\dagger c_{kh\eta} + \sum_{k\eta h} X_{k\eta h} \left(c_{k\eta h}^\dagger d_h + \text{h.c.} \right) \\ & + \epsilon_d \sum_h n_{dh} + U n_{d+} n_{d-} \end{aligned} \quad (\text{C.24})$$

where $X_{kLh} = \sqrt{2}|X_k|e^{i\phi_k}$ and $X_{kRh} = -hX_{kLh}^*$.

Bibliography

- [1] V. Gorini, A. Kossakowski, and E. C. G. Sudarshan, Journal of Mathematical Physics **17**, 821 (1976).
- [2] A. J. Daley, Advances in Physics **63**, 77 (2014).
- [3] J. Dalibard, Y. Castin, and K. Mølmer, Phys. Rev. Lett. **68**, 580 (1992), URL <https://link.aps.org/doi/10.1103/PhysRevLett.68.580>.
- [4] T. Prosen, Journal of Statistical Mechanics: Theory and Experiment **2010**, P07020 (2010).
- [5] T. Prosen, Physical Review A **86**, 044103 (2012).
- [6] M. Nakagawa, N. Kawakami, and M. Ueda, Phys. Rev. Lett. **121**, 203001 (2018), URL <https://link.aps.org/doi/10.1103/PhysRevLett.121.203001>.
- [7] D. Dast, D. Haag, H. Cartarius, and G. Wunner, Physical Review A **90**, 052120 (2014).
- [8] V. Tripathi and V. Vinokur, Scientific reports **10**, 1 (2020).
- [9] T. c. v. Prosen, Phys. Rev. Lett. **109**, 090404 (2012), URL <https://link.aps.org/doi/10.1103/PhysRevLett.109.090404>.
- [10] H.-P. Breuer, F. Petruccione, et al., *The theory of open quantum systems* (Oxford University Press on Demand, 2002).
- [11] A. J. Daley, Advances in Physics **63**, 77 (2014).
- [12] J. A. S. Lourenço, R. L. Eneias, and R. G. Pereira, Phys. Rev. B **98**, 085126 (2018), URL <https://link.aps.org/doi/10.1103/PhysRevB.98.085126>.
- [13] M. Zarea, S. E. Ulloa, and N. Sandler, Phys. Rev. Lett. **108**, 046601 (2012), URL <https://link.aps.org/doi/10.1103/PhysRevLett.108.046601>.

